

**Characterization of bacteria,  
antibiotics of the fluoroquinolone type  
and their biological targets DNA and gyrase  
utilizing the unique potential of vibrational  
spectroscopy**

**Dissertation**

zur Erlangung des akademischen Grades *doctor rerum naturalium*  
(Dr. rer. nat.)

vorgelegt dem Rat der Chemisch-Geowissenschaftlichen Fakultät der  
Friedrich-Schiller-Universität Jena

von Dipl.-Chemikerin Ute Neugebauer  
geboren am 23. November 1978 in Erfurt

Gutachter:

1. Prof. Dr.

2. Prof. Dr.

Tag der öffentlichen Verteidigung:

# Contents

<b>1</b>	<b>Introduction</b>	<b>1</b>
<b>2</b>	<b>Theoretical fundamentals</b>	<b>7</b>
2.1	Vibrational Spectroscopy . . . . .	7
2.2	Atomic force microscopy (AFM) . . . . .	22
2.3	Statistical evaluation methods: Multivariate data analysis . . . . .	24
<b>3</b>	<b>Material and Methods</b>	<b>29</b>
3.1	Spectroscopic instrumentation . . . . .	29
3.2	Biological samples . . . . .	38
3.3	Data treatment . . . . .	46
3.4	Statistical data analysis . . . . .	47
3.5	DFT calculation . . . . .	50
<b>4</b>	<b>Bacteria</b>	<b>53</b>
4.1	Vibrational spectroscopic characterization . . . . .	54
4.2	Vibrational spectroscopic discrimination of bacteria . . . . .	62
4.3	Bacterial metabolism: Vibrational spectroscopic study of bacterial growth . . . . .	63
4.4	Conclusion . . . . .	73
<b>5</b>	<b>Tip-enhanced Raman spectroscopy (TERS) of complex biological surfaces</b>	<b>75</b>
5.1	Biological fundamentals: Cell wall structure of Gram-positive bacteria . . . . .	75
5.2	TERS while scanning the bacterial surface with AFM . . . . .	77
5.3	TERS on selected points on the sample surface . . . . .	78
5.4	Dynamics on the bacterial cell surface probed by TERS . . . . .	84
5.5	TERS of bacteria under special conditions: Cells under argon . . . . .	85
5.6	Estimation of the enhancement factor . . . . .	86
5.7	Possible problems . . . . .	87
5.8	Summary and outlook . . . . .	88
<b>6</b>	<b>Fluoroquinolones – important antibiotics</b>	<b>91</b>
6.1	Background and history . . . . .	91
6.2	Structural characteristics of the fluoroquinolones . . . . .	92
6.3	Proposed mode of action of the fluoroquinolones . . . . .	94
6.4	UV/vis absorption spectra . . . . .	96
6.5	DFT calculations . . . . .	97
6.6	Raman spectra of the bulk substances . . . . .	98
6.7	IR absorption spectra of the bulk substances . . . . .	103
6.8	Raman spectra of the quinolones in hydrated environment . . . . .	105

## Contents

6.9	Raman spectra in solution, pH-dependence . . . . .	108
6.10	Surface-enhanced Raman spectra . . . . .	109
6.11	Resonance Raman spectra . . . . .	111
6.12	Conclusion . . . . .	112
<b>7</b>	<b>The biological target: DNA</b>	<b>113</b>
7.1	The DNA building blocks: nucleic acid bases, nucleoside and nucleotides . . . . .	113
7.2	Primary and secondary structure of DNA . . . . .	134
7.3	The plasmid-DNA pBR322 . . . . .	135
7.4	Spectroscopic characterization of DNA . . . . .	135
7.5	Tertiary structure of DNA: supercoiling . . . . .	141
7.6	Intercalation of ethidium bromide . . . . .	145
7.7	Summary and outlook . . . . .	150
<b>8</b>	<b>The biological target: DNA-gyrase</b>	<b>151</b>
8.1	Structure and biological function of the enzyme gyrase . . . . .	151
8.2	The protein building blocks: the amino acids . . . . .	154
8.3	Spectroscopic characterization of the enzyme . . . . .	158
8.4	Interactions with DNA and the drug . . . . .	160
8.5	Summary . . . . .	164
<b>9</b>	<b>Influence of fluoroquinolone drugs on bacterial growth</b>	<b>165</b>
9.1	Minimal inhibition concentration . . . . .	165
9.2	Effect of moxifloxacin on <i>Staphylococcus epidermidis</i> . . . . .	166
9.3	Effect of ciprofloxacin on <i>Bacillus pumilus</i> . . . . .	178
9.4	Summary and Conclusion . . . . .	179
<b>10</b>	<b>Summary and Outlook</b>	<b>181</b>
<b>11</b>	<b>Zusammenfassung und Ausblick</b>	<b>187</b>
	<b>Appendix</b>	<b>193</b>
<b>A</b>	<b>Chemicals and Media</b>	<b>195</b>
A.1	Antibiotics . . . . .	195
A.2	Cellular Components . . . . .	195
A.3	Bacteria . . . . .	196
A.4	Buffer . . . . .	197
A.5	Gel electrophoreses . . . . .	200
A.6	Further biological assays . . . . .	202
<b>B</b>	<b>Additional spectra and tables</b>	<b>203</b>
B.1	DNA and DNA building blocks . . . . .	203
B.2	Gyrase and amino acids . . . . .	218
	<b>Abbreviations</b>	<b>221</b>
	<b>Bibliography</b>	<b>227</b>

<b>Publication list</b>	<b>243</b>
<b>Conference Contributions</b>	<b>245</b>
<b>List of figures</b>	<b>252</b>
<b>List of tables</b>	<b>254</b>
<b>Danksagung</b>	<b>255</b>
<b>Selbständigkeitserklärung</b>	<b>257</b>
<b>Lebenslauf</b>	<b>259</b>



# 1 Introduction

Bacteria are ubiquitous. They grow on the skin and inside the human being as e. g. the gut flora. But they are also abundant in soil and water. Some of them can be used in the water and waste industry for a biological cleaning of waste water. Also other industrial branches, such as the food, the pharmaceutical and the chemical industry make use of different bacteria when producing cheese, vinegar, yoghurt, antibiotics, hormones, lactic acids, and many other products. However, most of the people might think of infectious diseases when thinking of bacteria. There are many different diseases caused by bacteria and each year many thousand people die as a consequence. Growing resistances of the bacteria against the common drugs make the research for new effective and powerful drugs necessary. The knowledge base for a target oriented drug search is a detailed understanding of the structure and the function of bacteria on a molecular level.

Bacteria are single cell organisms whose cell size can range between 0.2 and 10  $\mu\text{m}$ , most of them having an average size of 1-5  $\mu\text{m}$ . They are procaryotes, which means they do not have a nucleus, however their DNA is found in circular form within the cell (genomic DNA and smaller plasmid DNA). Other cell constituents within the cytoplasm are proteins such as for example the ribosomes and mesosomes and storage granules. Around the cytoplasm membrane a cell wall made of murein (peptidoglycan) is found which gives the bacteria its characteristic shape: round cocci, rods of different length, spirals or commas. According to the structure of the cell wall bacteria can be divided into Gram-negative and Gram-positive. Gram-negative bacteria, such as e. g. *Escherichia coli* possess a thin (2 nm) peptidoglycan (murein) layer which is embedded in a periplasmatic gel between the cytoplasm membrane and an outer membrane. Gram-positive bacteria, such as e. g. *Staphylococcus epidermidis* form a thick (20-40 nm) peptidoglycan (murein) layer which surrounds the cell. Between the cytoplasm membrane and the peptidoglycan a thin slit filled with periplasma is found. Within the cell wall different teichoic acids, lipo-teichoic acids and surface proteins are embedded and pervade the cell wall. Some bacteria also have a sugar-rich slime layer or capsule around them. This additional layer facilitates the attachment of bacteria to surfaces and plays an important role in biofilm formation. It also acts as a protective layer against chemicals from outside such as antibiotics. For an understanding of the mechanisms of adhesion of cells to surfaces, biofilm formation, growing resistances and the mode of action of cell wall attacking drugs (such as  $\beta$ -lactams, penicillins and glycopeptides) it is indispensable to know the exact, spatially resolved structure of the outer bacteria layer and the dynamics occurring on it.

Beside the inhibition of the cell wall synthesis antibiotics may perturb the permeability of the cytoplasm membrane (polypeptide antibiotics), block the protein synthesis (amino glycosides, tetra-

## 1 Introduction

cycline, chloramphenicol) or suppress the nucleic acid synthesis (gyrase inhibitors, rifampicin, sulfonamides) [168]. Among the variety of antibiotic agents special focus is set on the gyrase inhibitors of the fluoroquinolone type within this work. In 1994 those gyrase inhibitors made up approx. 25% of all prescribed drugs against bacterial infections. Since their discovery in the early 1960s the basic structure of the quinolones was modified to increase their antibacterial spectrum and potency, as well as to improve their bioavailability making the quinolones useful agents for the treatment of urinary, systemic and respiratory tract infections. The target of the fluoroquinolones is the bacterial enzyme gyrase. This essential enzyme catalyzes the introduction of negative supercoils into the DNA and is therefore responsible for the maintenance of the DNA topology within the bacterial cell. By binding to the gyrase-DNA complex the quinolones block the transcription, the DNA replication and storage which results in cell death [18]. The release of broken DNA ends has been reported to accompany the quinolone action [162]. Currently, there is no definitive model for the detailed interaction of the quinolones with the gyrase-DNA complex, although mutation experiments localized the interaction area within the N-terminal domain of the GyrA subunit close to the Tyr122 which is involved in the cleavage of the DNA double strands [98]. Also parts of the GyrB subunit may be involved in stabilizing the ternary complex of gyrase, DNA and quinolone [18, 97]. Shen et al. proposed a model for this ternary complex [239], which was later modified by Morrissey et al. [163]. However, the molecular details of the interaction of the fluoroquinolones with DNA and gyrase remain until now largely conjectural [162]. Continued study of gyrase and its inhibitors at a molecular level as well as their impact on whole bacterial cells is necessary to understand the action of existing drugs and to provide the knowledge base to enable the understanding of the action of emerging compounds.

Since bacteria are so small it is impossible to distinguish by eye between the useful and harmless ones and the unwanted and toxic ones. Fast and reliable identification methods for bacteria are therefore of greatest interest. Furthermore, it is necessary to have a detailed knowledge about the structure and composition of bacteria, as well as about the bacterial metabolism including the processes of bacterial growth and biofilm formation in order to identify new target structures for new and effective drugs. A detailed understanding of the mode of action of antibiotics on a molecular level could help to understand the mechanisms of resistances and open new ways for overcoming them.

Traditional microbiological diagnoses often take several days up to weeks to provide results [81, 215, 214, 216, 217] while vibrational spectroscopy with its multitude of variations as a non-invasive technique results complex and precise information from the inside composition as well as from the surface structure of living bacterial cells in an extremely brief time span. Therefore, vibrational spectroscopic methods such as IR absorption spectroscopy and Raman spectroscopy already gained importance for the investigation of biological systems and the characterization of bacteria in the past years [151, 152, 172]. Rich "fingerprint"-like spectral information about the complex chemical composition of the cell and the cell components in their natural entity are obtained while only little sample volume (down to a single cell) is required. Since no labelling



is necessary the sample preparation is quite easy. The spectroscopic techniques are applicable to virtually all microorganisms with only a minimal amount of sample preparation and within an extremely brief time span precise results can be presented. Highly specific and multidimensional spectral signatures have been obtained from bacteriophages [191, 271], whole bacterial cells and fungi [150, 217, 229].

With micro-Raman spectroscopy the laser light can be focused down to about 1  $\mu\text{m}$ , which is roughly the size of bacterial cells. The assignment of vibrational bands to specific functional groups, cellular compounds or substructures in the complex bacterial spectrum allows the characterization of metabolic changes accompanied with growth and aging processes [180, 280], culture conditions [151, 149, 230], the influence of exposed pollutants [242], and specific cell-drug interactions [146, 179] by means of vibrational spectroscopy in combination with statistical pattern recognition methods like hierarchical cluster analysis (HCA) and principal component analysis (PCA). Furthermore, Raman spectra recorded from single bacterial cells have been used for a fast and reliable differentiation and identification of microorganisms [86, 96, 103, 145, 218, 229, 284], e. g. of contaminations or early infections.

Furthermore, it is possible to specially focus on selected components or regions of the biological system. IR absorption spectroscopy is especially suited to probe vibrations which involve a change in the dipole moment. Therefore, CO stretching vibrations, e. g. of the amide bonds of peptides and proteins, carbonic acids or organic esters being present in lipids, give rise to very intense absorption bands in the IR spectrum. Raman spectroscopy with excitation in the visible wavelength region also provides rich spectral information about the overall chemical composition of the bacteria with particular sensitivity to chemical groups exhibiting a high polarizability.

The high potential of Raman spectroscopy for the study of biological and biomedical problems [172] arises also from the possibility to probe samples in all states of aggregation and all solvents, including water. Since Raman spectroscopy is a marker-free technique it bears high potential for clinical diagnostics and for food quality controls. It possesses also some advantages over other high-resolution structural methods such as X-ray or NMR, because Raman spectroscopy is not restricted to a certain size of the molecules. Raman spectroscopy and its variations offer a good prerequisites for the investigation of large biomolecules, such as genomic DNA and their interactions with large proteins or drugs. Thereby, conventional Raman spectroscopy, UV-resonance Raman spectroscopy and polarized Raman microspectroscopy can fulfil complementary and important roles in such a research [23]. Vibrational spectroscopy has already successfully been employed to investigate DNA structures [26, 39, 62], the complexation of DNA with ions [6], the structures of small peptides [232] and proteins [235], as well as protein-DNA binding [278], drug-protein binding [57] and drug-DNA [135, 148] interactions.

When dealing with complex biological samples the data set (of spectra) tends to increase very quickly. In order to extract the significant and characteristic information from such large data sets and to visualize subtle differences in the spectra often make the use of multivariate analysis methods such as principal component, discriminant analysis and hierarchical cluster analysis [145]

## 1 Introduction

necessary. For instance, the application of classification techniques allows the rapid and accurate identification and classification of very diverse microbial species and whole bacterial cells based on their vibrational spectra [107, 152, 218]. For classification tasks the entire spectral information can be used. However, certain spectral regions may be irrelevant for the problem under study. Selecting a few wavenumbers which perform particularly well for classifying the data into relevant categories (i.e. bacteria treated/untreated with antibiotics) can highlight potentially important structural features and structural changes in the system under study.

The general drawback of Raman spectroscopy, the low scattering efficiency, can be overcome by special Raman signal enhancing techniques such as resonance Raman (RR) spectroscopy or surface-enhanced Raman spectroscopy (SERS). In resonance Raman spectroscopy the excitation wavelength lies within an electronic absorption of the molecule of interest causing a resonance enhancement of up to  $10^8$  for the vibration coupling to this electronic transition [152]. This results in a second advantage of resonance Raman spectroscopy: depending on the selected excitation wavelength different chromophores can be selectively enhanced and make it possible to focus on selected traits of interest in the presence of many other molecules. In case UV light with a wavelength of 244 nm is chosen for Raman excitation the aromatic amino acids and the purine and pyrimidine bases of the nucleic acids [281, 280, 78] are in resonance. With excitation wavelengths around 200 nm the protein backbone vibrations will be selectively enhanced. The resonance Raman spectrum is therefore dominated by those components, despite the presence of other higher concentrated molecules in the cell [145, 280]. This allows for tracking selected metabolites within the cells, e. g. during bacterial growth. Extensive UV-resonance Raman studies have been performed to analyze protein and peptide secondary structure [12, 13, 37, 50, 58, 141, 161].

In SERS the signal enhancement is achieved by exciting surface plasmon oscillations of a roughened metal surface or metal colloid solution in the close vicinity of the sample. These surface plasmon oscillations generate a high local electromagnetic field causing enhanced Raman signals exhibiting scattering cross sections of 3 to 15 orders of magnitude larger than those for normal Raman scattering [182, 119]. A recently developed technique, called tip-enhanced Raman spectroscopy (TERS) combines surface-enhanced Raman spectroscopy (SERS) with atomic force microscopy (AFM). The SERS active metal is reduced to the size of an AFM tip with apex sizes of less than 50 nm in diameter [247]. This tip is moved across the sample to record the surface features (AFM). At the same time, that part of the sample which is in the close vicinity of the tip apex experiences the strong enhanced electromagnetic field. This evanescent electromagnetic field decays very rapidly with increasing distance from the metal surface, so that at only 50 nm away from a metal tip no Raman scattering enhancement can be observed anymore [184, 211]. Thus with TERS one obtains simultaneously detailed chemical information with high sensitivity from the Raman spectra with a high spatial resolution below the diffraction limit [63, 202, 184]. This approach was already applied successfully to study DNA components [205], single-walled carbon nanotubes [94, 93], and just recently within the frame of this work also for the first time to investigate bacterial surfaces [178, 180]. TERS not only overcomes the low scattering efficiency

but also the finite spatial resolution due to the diffraction limit of micro-Raman spectroscopy. It opens the way for a detailed spatially resolved study of smaller structures, such as the bacterial surface and might lead to an understanding of the adhesion of cells to surfaces, biofilm-formation, and the mode of action of antibiotics like  $\beta$ -lactams, penicillins or glycopeptides which attack the cell wall and interfere with its synthesis.

The goal of this work is to use different vibrational spectroscopic techniques to comprehensively characterize bacteria and to investigate the metabolic changes upon bacterial growth. The influence of drugs on the vibrational spectra should be studied in order to gain a deeper insight into the molecular mechanism of antibiotic action. Special focus is put on the antibiotics of the fluoroquinolone type. They interfere with the action of the vitally important enzyme gyrase by attacking the gyrase-DNA complex. In order to correlate the observed changes in the vibrational spectra of the bacteria upon drug addition to the molecular changes the biological targets of the fluoroquinolones, the DNA and the gyrase, those molecular components have been extracted from the bacteria and were characterized by *in vitro* vibrational spectroscopy.

As vibrational spectroscopic techniques the above mentioned ones are used: IR absorption spectroscopy, micro-Raman spectroscopy, UV-resonance Raman spectroscopy as well as surface-enhanced and tip-enhanced Raman spectroscopy. The combination of those methods leads to an understanding of the structure and composition of the bacteria. Based on this knowledge the metabolism within the bacteria can be explored providing a key stone to fight the pathogens. The metabolic changes of the bacteria during different growth phases of a batch culture are investigated by means of IR absorption, micro-Raman (bulk and single cells) and UV-resonance Raman spectroscopy with excitation at 244 nm. Statistical methods are used to identify the subtle wavenumber changes which reflect changes in the chemical composition or structural changes on the cellular components during the growth process.

Special focus is put on the outermost bacterial surface when using tip-enhanced Raman spectroscopy (TERS). TERS as a non-invasive technique is applied to obtain detailed chemical and topographical information simultaneously with nanometric resolution of biological surfaces (bacteria). Due to short measuring times also variations in time within seconds are possible to resolve.

Before adding the fluoroquinolone drugs to the bacterial culture *in vitro* experiments have been performed with the pure drug substances. For a profound interpretation of the complex bacterial spectra with the addition of the drug, it is necessary to have a clear understanding of the spectra of the pure drug in different chemical environments. Therefore, a detailed vibrational spectroscopic characterization of the fluoroquinolone drugs is required. DFT calculations were incorporated for the assignment of the vibrational modes. In order to support the tentative assignment and to learn more about the complex drug interaction, the biological targets of the fluoroquinolone drugs, the bacterial enzyme gyrase and the bacterial DNA, have been extracted from the bacteria and were characterized by *in vitro* experiments. The small protein and DNA building blocks, the amino acid and nucleic acid bases have been included in the comprehensive study.

## *1 Introduction*

Finally, the influence of different fluoroquinolone drugs on the bacterial metabolism is investigated using the different vibrational spectroscopic techniques mentioned above (IR absorption and micro-Raman spectroscopy with excitation in the visible, as well as UV-resonance Raman spectroscopy). With the help of statistical methods the spectral changes due to the action of the drug are pointed out and assigned to biological features within the cell. That way the actual model for the mode of action of the fluoroquinolone drugs can be supported, demonstrating once again the power of vibrational spectroscopy for biomedical and pharmaceutical problems.

## 2 Theoretical fundamentals

### 2.1 Vibrational Spectroscopy

Each molecule is performing vibrations, even at zero Kelvin (uncertainty relation). The vibrational frequency depends on the type of atoms (mass) and how they are connected (single bond, double bond, triple bond, hydrogen bond). For a rough approximation the classical model of the harmonic oscillator can be used to estimate the vibrational frequency  $\nu_0$  (in Hz):

$$\nu_0 = \frac{1}{2\pi} \sqrt{\frac{k}{\mu}} \quad (2.1)$$

with  $k$  (in  $\text{Nm}^{-1}$ ) being the force constant describing the bond strength between the two atoms with mass  $m_1$  and  $m_2$ . The reduced mass  $\mu$  can be calculated from the individual masses by  $\mu = \frac{m_1 m_2}{m_1 + m_2}$ . The permitted vibrational energy levels  $E_{vib}$  for a harmonic oscillator as calculated from quantum mechanics are:

$$E_{vib} = h\nu_0 \left( n + \frac{1}{2} \right) \quad (2.2)$$

where  $h$  is Planck's constant and  $n$  the vibrational quantum number having integral values starting from 0 and characterizing the eigenstates of the harmonic oscillator. As higher excited vibrational levels are reached, the harmonic oscillator only poorly describes the real systems, and it completely fails when it comes to the dissociation of bonds. Therefore, anharmonicity has to be included. One way to do so is by using a Morse potential for the potential energy which results in the following permitted energy levels:

$$E_{vib} = h\nu_0 \left[ \left( n + \frac{1}{2} \right) - x_e \left( n + \frac{1}{2} \right)^2 \right] \quad (2.3)$$

where  $x_e$  is the anharmonicity constant.

Typical energies necessary for a vibrational transitions within molecules are in the wavenumber region between 400 and 4000  $\text{cm}^{-1}$  which corresponds to a wavelength of 25 to 2.5  $\mu\text{m}$ .

If the molecule consists of  $N$  atomic nuclei it has  $3N$  degrees of freedom, because the total number of coordinates needed to specify the location of each atom is  $3N$ . Out of these, three coordinates are needed to specify the location of the center of mass of the molecule (translational displacement). To define angles (rotation of the molecule) two coordinates are needed for a linear molecule and three coordinates for a non-linear molecule. This leaves a total number of  $3N-5$

## 2 Theoretical fundamentals

independent modes of vibration for a linear molecule and  $3N-6$  independent vibrational modes for a non-linear molecule.

The vibrational modes can be divided into valence vibrations (stretching vibrations) and different types of deformation vibrations. The stretching vibration ( $\nu$ ) changes the distance along the bond between the involved atoms. This vibration takes place along the nucleus-nucleus-connection line and can either be symmetric or antisymmetric with respect to the other involved vibrations. The different deformation vibrations change the bond angles. It can be differentiated between scissoring, wagging ( $\omega$ ), rocking ( $\rho$ ), twisting ( $\gamma$ ), torsion ( $\tau$ ) and bending ( $\delta$ ) vibrations.

At comparable mass of the vibrating molecules the activation energy for bond angle deformation is much smaller than for changes in bond length. Therefore, the valence modes are found at higher frequencies than the corresponding deformation modes, e.g. CH stretching vibrations can be found in the wavenumber region between  $3300$  and  $2800\text{ cm}^{-1}$ , while the CH deformation modes show up between  $1540$  and  $650\text{ cm}^{-1}$ .

Characteristic group frequencies allow the application of vibrational spectroscopy for structure elucidation. The sensitivity of the vibrational modes for changes in their chemical environment make the different vibrational spectroscopic techniques well suited and widely used analytical techniques both in research and in industry.

There are two vibrational spectroscopic techniques (and their variations) to probe the molecular vibrations: IR absorption spectroscopy where the vibrational transitions are directly excited and Raman spectroscopy where the vibrational transitions are probed via an inelastic scattering process. Both techniques are used within the frame of this work and should be introduced briefly in the next sections.

### 2.1.1 IR absorption spectroscopy

As mentioned above, molecular vibrations can be excited with radiation in the infrared (IR). If the incident electromagnetic (IR) radiation matches a vibrational transition which involves a change in the electromagnetic dipole moment of the molecule, the molecule gets excited into a higher vibrational level  $\nu$  and photons of the matching electromagnetic frequency get absorbed from the incident radiation (figure 2.1). Since at room temperature most of the molecules are in their vibrational ground states, the dominant spectral transition will be the fundamental transition, marked black in figure 2.1.

The first-order IR absorption intensity of the  $k^{\text{th}}$  mode is proportional to the square of the change of the electric dipole moment  $\mu$  caused by the normal mode coordinate  $q$ :

$$I_{IR}^k \propto \left( \frac{\delta\mu}{\delta q_k} \right)^2. \quad (2.4)$$

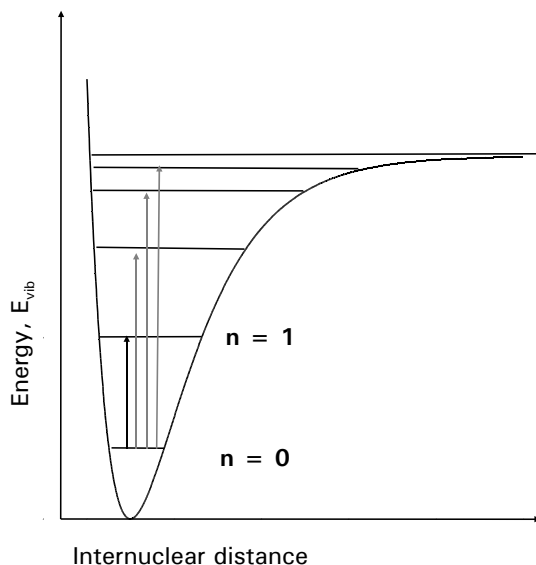


**Figure 2.1:** Energy levels and transitions for an anharmonic oscillator (black: fundamental, grey: overtones).

That means a strong change in the electromagnetic transition dipole causes high IR absorption intensity. This is e.g. observed for polar groups such as carbonyl, nitrosyl and hydroxyl groups. Non-polar groups, such as homonuclear diatomic molecules are IR inactive.

Each vibrational transition is accompanied by a change in the state of rotation of the molecule. Therefore, the IR absorption spectrum represents a rotational-vibration spectrum. Due to the superposition of the numerous individual vibrational transitions, especially in the solid and liquid phase no sharp lines but rather broad bands are detected. Position, band shape and intensity of the vibrational band contain useful information about the system under investigation.

IR absorption spectroscopy evolved to a well established technique for the identification of unknown organic compounds. In the last years IR spectroscopy also gained importance for the study of biological problems. Useful information about the constitution and chemical environment of the chemical compounds can be gained from the characteristic absorption frequencies for different structural elements.

### 2.1.2 Raman spectroscopy

Raman spectroscopy, named after the Indian scientist Sir Chandrasekhara Venkata Raman, is based on inelastic light scattering by matter. Figure 2.2 depicts the basic transitions involved in the spontaneous Raman scattering:

The Raman effect is a two photon process. A photon of the incident monochromatic light with energy  $h\nu_L$  transfers the molecule into a virtual state. The second photon is the released scattered photon. Most of the times (1 out of  $10^3$  photons [109]) the incident light gets scattered

## 2 Theoretical fundamentals

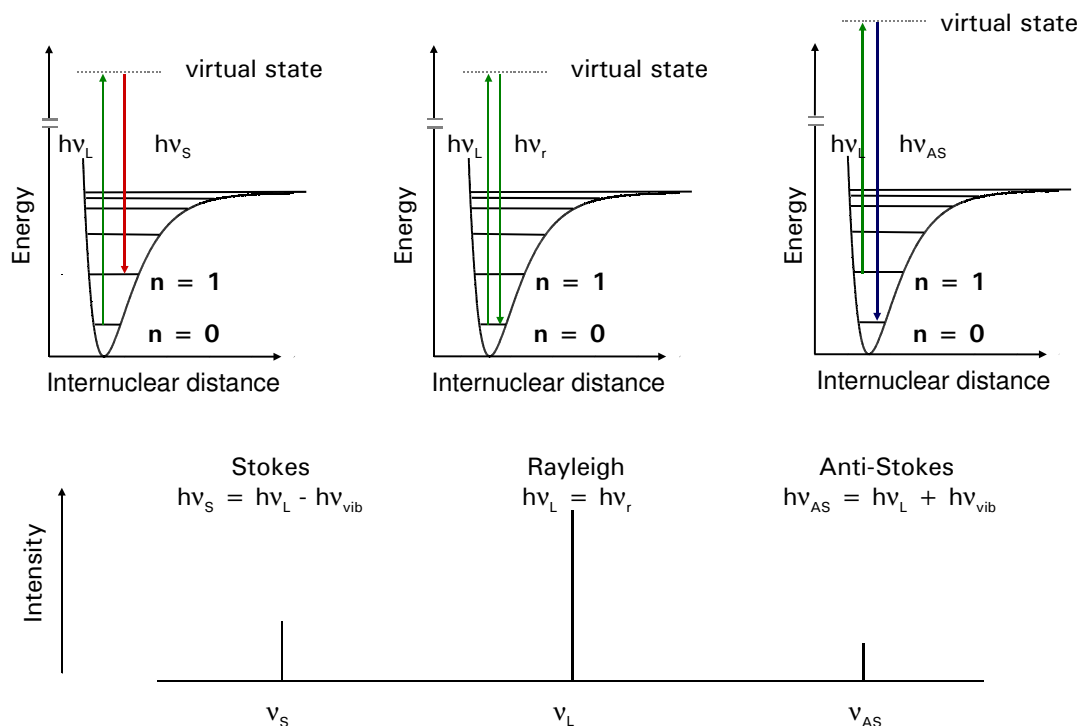


**Figure 2.2:** Energy level diagram showing the basic transitions involved in the spontaneous Raman scattering.

only elastically (Rayleigh scattering) where the molecular transition starts and finishes at the same vibrational level. However, in rare cases (1 out of  $10^7$  photons [109]) the light gets scattered inelastically, i.e. the scattered light gets modulated by the frequencies of the molecular vibrations  $\nu_{vib}$ . It can be distinguished between Stokes Raman scattering where the molecule ends up in an excited vibrational state and the energy of the scattered photon is reduced by the vibrational frequency, and between Anti-Stokes Raman scattering, where the initial state of the molecule was already a vibrationally excited state and where the molecule ends up in a lower vibrational level. At ambient temperatures ( $kT/hc \approx 200 \text{ cm}^{-1}$ ) most molecular vibrations are in the ground state and thus the Stokes transitions are more likely to occur.

In the classical description the Raman effect is due to the secondary radiation of an induced electromagnetic dipole moment. The electromagnetic dipole moment

$$\mu_{ind} = \alpha \cdot E \quad (2.5)$$

is induced by the incident electromagnetic field

$$E = E_0 \cdot \cos(\omega t) \quad (2.6)$$



with  $\alpha$  being the polarizability tensor of the molecule. This polarizability tensor is modulated by the frequency  $\nu_{vib,k}$  of the  $k^{th}$  vibrational mode:

$$\alpha_k = \alpha_0 + \left( \frac{\delta \alpha}{\delta q_k} \right)_0 \cdot q_k^0 \cdot \cos(2\pi \nu_{vib,k} t) + \dots \quad (2.7)$$

which results in the following equation for the induced electromagnetic dipole moment:

$$\mu_{ind} = \alpha_0 \cdot E_0 \cdot \cos(2\pi \nu_L t) + \left( \frac{\delta \alpha}{\delta q_k} \right)_0 \cdot q_k^0 \cdot \cos(2\pi \nu_{vib,k} t) \cdot E_0 \cdot \cos(2\pi \nu_L t) + \dots \quad (2.8)$$

When higher order terms are neglected trigonometric conversions results in:

$$\begin{aligned} \mu_{ind} = & \alpha_0 \cdot E_0 \cdot \cos(2\pi \nu_L t) && \text{Rayleigh scattering} \\ & + \frac{1}{2} \cdot \left( \frac{\delta \alpha}{\delta q_k} \right)_0 \cdot q_k^0 \cdot E_0 \cdot \cos(2\pi(\nu_L - \nu_{vib,k})t) && \text{Stokes scattering} \\ & + \frac{1}{2} \cdot \left( \frac{\delta \alpha}{\delta q_k} \right)_0 \cdot q_k^0 \cdot E_0 \cdot \cos(2\pi(\nu_L + \nu_{vib,k})t) && \text{Anti-Stokes scattering.} \end{aligned} \quad (2.9)$$

From equation 2.9 it becomes obvious, that the polarizability  $\alpha$  of a molecule must change during the vibration in order for that vibration to be Raman active:

$$\left( \frac{\delta \alpha}{\delta q_k} \right)_0 \neq 0. \quad (2.10)$$

The different selection rules for IR absorption (equation 2.4) and Raman scattering (equation 2.10) make those two vibrational spectroscopic techniques complementary.

The total intensity of a Stokes Raman band of a vibrational frequency of  $\nu_{vib}$  between the initial vibronic state  $i$  to a final state  $f$  scattered over a solid angle of  $4\pi$  by a randomly oriented molecule perturbed by electromagnetic radiation of intensity  $I_L$  and frequency  $\nu_L$  is given by:

$$I_{Stokes} = const \cdot I_L (\nu_L - \nu_{vib})^4 \sum_{\rho\sigma} |(\alpha)_{\rho\sigma} |_{fi}|^2 \quad (2.11)$$

where  $\alpha_{\rho\sigma}$  represents the components of the polarizability tensor associated with the transition  $f \leftarrow i$ . Since only 1 out of  $10^7$  photons gets scattered inelastically [109] while the others form the elastically scattered Rayleigh light, Raman spectroscopy suffers from a low scattering efficiency. This is one of the largest drawbacks of the technique. Nowadays, there are several methods to overcome this disadvantage, as will be seen in the next sections (resonance Raman (section 2.1.3.1), surface-enhanced (section 2.1.3.2) and tip-enhanced Raman scattering (section 2.1.3.3)).

Nevertheless, Raman spectroscopy enjoys high popularity for both research and industrial applications. Various advantages of Raman spectroscopy, some of them superior to other major structure elucidation methods such as NMR or X-ray, allow wide spread applications in medicine, biology, and material sciences. In the following those advantages are listed:

## 2 Theoretical fundamentals

- samples in all states of aggregation can be used (solid, liquid, gaseous, hydrated films or crystalline or polycrystalline state),
- all solvents can be used, also water (in contrast to IR absorption spectroscopy),
- no labelling is required since the probed vibrations are an intrinsic property of the substance under investigation,
- minimal or no sample preparation,
- high specificity (the position and intensity of the Raman bands strongly depends on the type of atoms and their chemical environment),
- only very small amounts of sample are required,
- good spatial resolution (especially when using micro-Raman or tip-enhanced Raman spectroscopy) can be achieved,
- Raman spectroscopy is a non-invasive and non-destructive technique,
- no limitation is placed on the size of the investigated structures (it is also possible to study native DNA and large proteins),
- biomolecules and their reactions can be investigated in their natural environment,
- can be done quantitative (for concentration determination when using calibration measurements).

### 2.1.3 Raman enhancing techniques

Since Raman scattering is an intrinsically weak process (only one out of  $10^7$  incident photons gets scattered inelastically [109]) methods are desired to increase the Raman scattering cross section. By looking at equation 2.11 several possibilities to increase the Raman scattering intensity can be thought of:

- increasing the intensity  $I_L$  of the incident electromagnetic field, e.g. by increasing the laser power or by local field enhancement (e.g. SERS, TERS, see section 2.1.3.2 and 2.1.3.3.)
- choosing higher excitation frequencies  $\nu_L$ , and
- excitation within resonance of an electronic transition in order to increase the magnitude of the polarizability tensor  $\alpha$ , i.e. resonance Raman spectroscopy (see next section 2.1.3.1).

### 2.1.3.1 Resonance Raman spectroscopy

**Sum-over-state description (time independent)** Kramers and Heisenberg (1925) and Dirac (1927) derived a quantum mechanical expression for the transition polarizability tensor  $\alpha$  (KHD dispersion theory). The individual matrix elements  $\alpha_{\rho\sigma}$  of the polarizability tensor for a transition  $f \leftarrow i$  can be calculated from:

$$(\alpha_{\rho\sigma})_{fi} = \frac{1}{\hbar} \sum_{r \neq i, f} \left( \frac{\langle f | \mu_{\rho} | r \rangle \langle r | \mu_{\sigma} | i \rangle}{\omega_{ri} - \omega_L - i\Gamma_r} + \frac{\langle f | \mu_{\sigma} | r \rangle \langle r | \mu_{\rho} | i \rangle}{\omega_{rf} + \omega_L + i\Gamma_r} \right) \quad (2.12)$$

with  $\mu_{\rho}$  and  $\mu_{\sigma}$  being the transition dipole moments and  $\Gamma$  a damping factor which can be related to the life time of the excited vibronic state  $|r\rangle$ .  $\hbar$  relates to Planck's constant as  $\hbar = h/2\pi$  and  $\omega$  to the frequency as  $\omega = 2\pi\nu$ .

This equation describes Raman scattering as a two-photon process with a transition from the initial state with the vibronic wavefunction  $i$  to the entire manifold of eigenstates with the wavefunction  $r$  of the unperturbed molecule, followed by a transition to the final state with the wavefunction  $f$  as depicted in figure 2.3. For normal Raman scattering ( $\omega_{ri} \gg \omega_L$ , figure 2.3A) the weighted summation over all possible states results in no information about the eigenstates  $|r\rangle$ . The initial  $|i\rangle$  and final state  $|f\rangle$  play the determining role.

That changes, when the incident laser frequency  $\omega_L$  matches the energy gap  $\omega_{ri}$  to an electronically excited eigenstate  $|r\rangle$  (figure 2.3B). This electronic eigenstate will dominate the whole sum: the denominator of the first term in the sum in equation 2.12 becomes really small, causing the first term to become very large. This explains the signal enhancement up to six to eight orders of magnitude that is observed for resonance Raman compared to normal Raman scattering. The second term in the sum, where the incident frequency  $\omega_L$  and the transition frequency  $\omega_{ri}$  are additively linked becomes negligible and equation 2.12 reduces to:

$$(\alpha_{\rho\sigma})_{fi} = \frac{1}{\hbar} \sum_{r \neq i, f} \left( \frac{\langle f | \mu_{\rho} | r \rangle \langle r | \mu_{\sigma} | i \rangle}{\omega_{ri} - \omega_L - i\Gamma_r} \right). \quad (2.13)$$

**Time-dependent theory** Since it is very tedious (and for large molecules almost impossible) to sum up over all possible eigenstates of the molecule, the time-dependent theory, explained in the following, holds a lot of advantages.

Through mathematical transformations (as explained in more detail in Myers et al. [170]) the Kramers-Heisenberg-Dirac relation can be transformed into an integral over time. The equation for the polarizability tensor  $\alpha_{fi}$  then reads as:

$$\alpha_{fi} = \frac{1}{\hbar} \int_0^{\infty} \langle f | i(t) \rangle \exp \left\{ -\frac{\Gamma t}{\hbar} \right\} \exp \left\{ \frac{i(E_i + E_L)t}{\hbar} \right\} dt \quad (2.14)$$

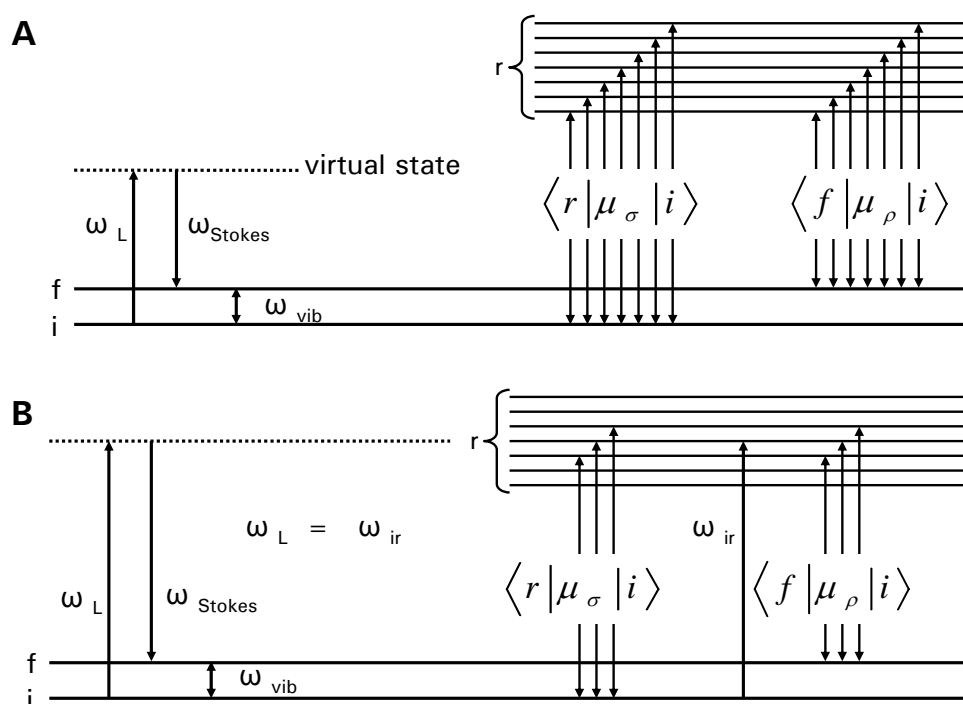


**Figure 2.3:** Energy level diagram illustrating the sum-over-state description of the Raman scattering, **A)** non-resonance Raman scattering, **B)** the exciting laser frequency  $\omega_L$  matches an actual electronic transition of the molecule (resonance Raman).

with  $\exp \left\{ \frac{i(E_i + E_L)t}{\hbar} \right\}$  being the phase factor and  $\exp \left\{ -\frac{\Gamma t}{\hbar} \right\}$  being the damping factor. The term  $\langle f | i(t) \rangle$  describes the overlap integral, the time-dependent Franck-Condon factor between the final state and the initial wavefunctions propagating on the electronic surface.

A graphic interpretation of equation 2.14 is given in figure 2.4 (adopted from Ref. [169] and Ref. [228]). The resonance Raman scattering process starts at time  $t = 0$  in the vibrational eigenstate  $|i\rangle$  of the electronic ground state. A vertical transition to the excited electronic surface is initiated by the interaction of the electronic transition dipole moment with the incident electromagnetic field  $E_L$ . Under the influence of the Hamiltonian  $H$  the wavepacket evolves and oscillates between the inner and outer turning points of the potential (dotted line in figure 2.4A) until it gets damped by the function  $\exp \left\{ -\frac{\Gamma t}{\hbar} \right\}$ . While moving back and forth on the excited state surface the wavefunction  $|i(t)\rangle$  passes regions with high overlap with the wavefunction  $|f\rangle$  in the electronic ground state and a photon of energy  $E_S$  is emitted. The Raman overlap  $\langle f | i(t) \rangle \exp \left\{ -\frac{\Gamma t}{\hbar} \right\}$  as a function of time is depicted in figure 2.4B. Maximal overlap is reached a few femtoseconds after the initial propagation (point 1 in figure 2.4A) and then again due to the damping with less amplitude on the

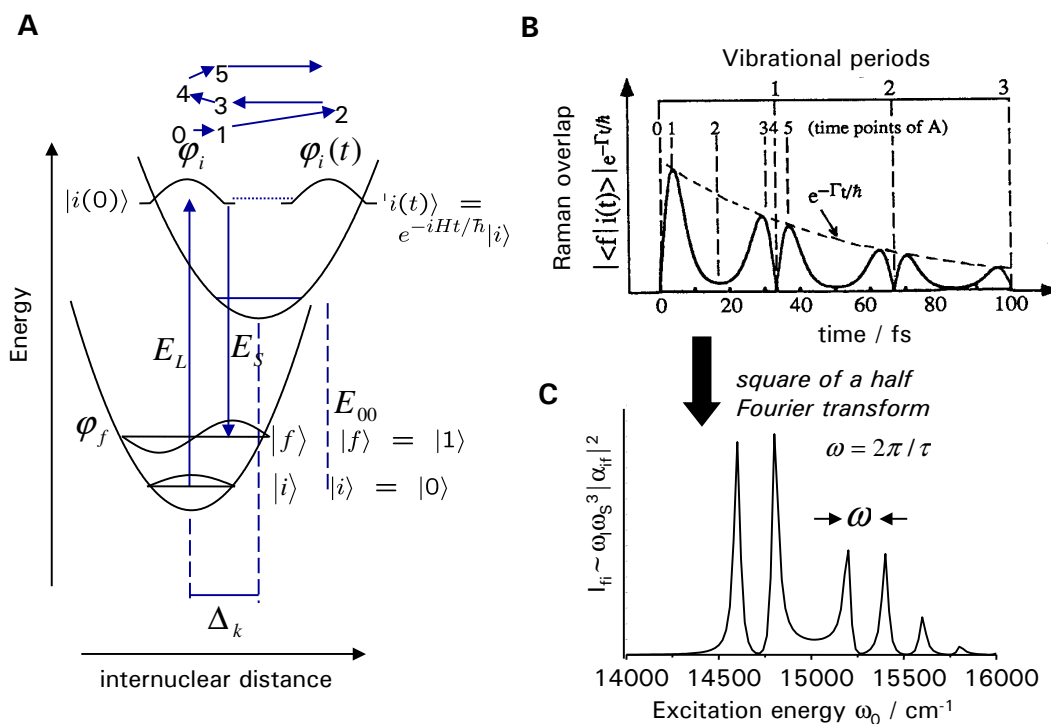


**Figure 2.4:** Time dependent picture of resonance Raman scattering **A)** Energy level diagram **B)** Raman overlap as a function of time **C)** Raman excitation profile (adapted from [169, 228].

return trip (point 3 in figure 2.4A). A full propagation cycle is completed at point 4 and the process starts over again until  $|i(t)\rangle$  is damped out.

By a half Fourier transformation the Raman excitation profile  $I_{fi} = I_{fi}(\omega_0)$  can be calculated from the Raman overlap function (depicted in figure 2.4C). The influence of the damping constant reflects on the line shape in the excitation profile: a small damping constant results in narrow lines in the excitation profile, while a large damping constant causes broad lines.

**Advantages and applications of resonance Raman spectroscopy** Since resonance Raman scattering occurs via enhanced scattering involving an excited electronic state the technique can be used to gain information about the molecular structure and dynamic of the excited electronic state. From the excitation profile one can determine the strength of the interactions between the electronic excited state and the vibrational modes, the atomic displacement between ground and excited state, and thus the change in bond length and bond angles when going from the ground to the excited state. From the overtone progression of totally symmetric vibrations or combinations with them the anharmonicity constant and harmonic frequencies of the appropriate vibrations can be calculated [52, 113].

## 2 Theoretical fundamentals

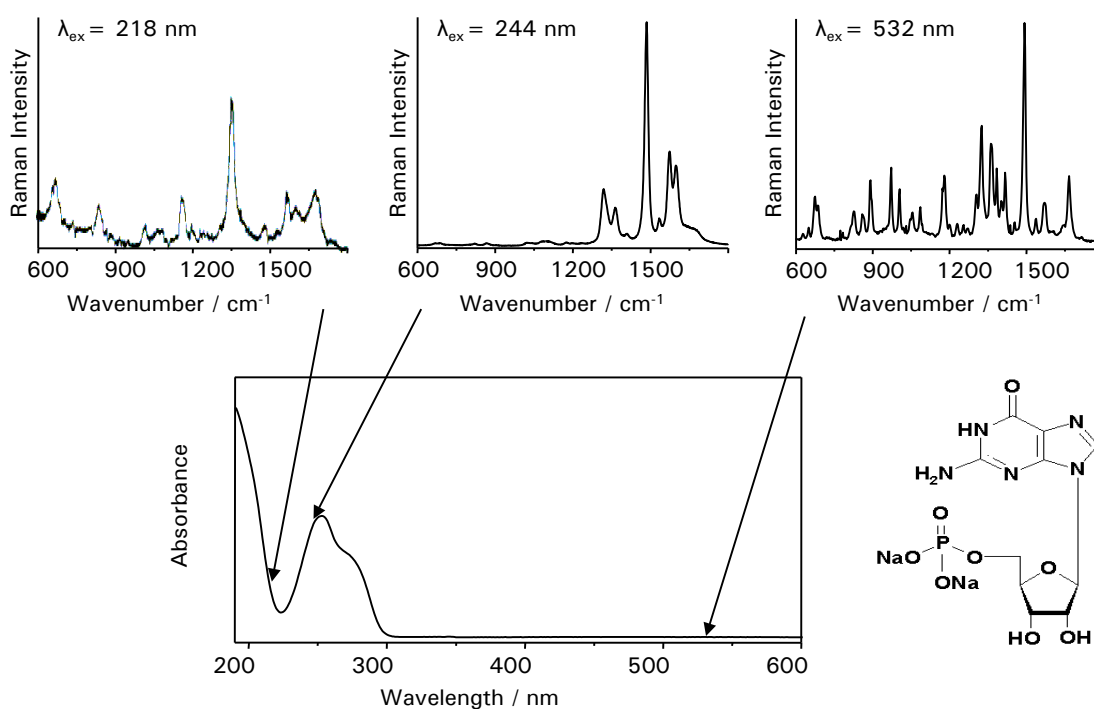


**Figure 2.5:** Selectivity of resonance Raman spectroscopy. **Bottom**) UV/vis absorption spectrum of guanosine-5'-monophosphate (structure shown on the right). The arrows mark three different excitation wavelengths applied to record the Raman spectra shown in the **Top**) the off-resonance Raman spectrum excited at 532 nm on the right, and the resonance Raman spectra excited at 244 nm (middle) and 218 nm (left) involving two different electronic transitions (spectrum excited at 218 nm taken from Ref. [77]).

However, in this work resonance Raman spectroscopy is not used because of its high power for photochemical analysis, but rather because of its high sensitivity and selectivity. By electronic resonance enhancement the intensity of the scattered light can be increased by a factor of  $10^6$  compared to non-resonant Raman excitation. This improves the signal-to-noise ratio and allows the detection of substances in solution at low concentrations ( $10^{-3} - 10^{-5}$  M).

As the enhancement results from a coupling of the vibrational modes (most of the time totally symmetric vibrational modes) to an electronically excited state it is possible to exclusively select vibrational modes from certain chromophores by choosing an appropriate wavelength Figure 2.5 illustrates this selectivity for guanosine-5'-monophosphate as an example. By varying the Raman excitation wavelength to be resonant with different electronic transitions selective excitation of different chromophores is possible. The off-resonance Raman spectrum excited at 532 nm (top right in figure 2.5) shows a very complex vibrational structure, since all Raman active vibrations contribute to this spectrum. When exciting at 244 nm only those vibrational bands are enhanced

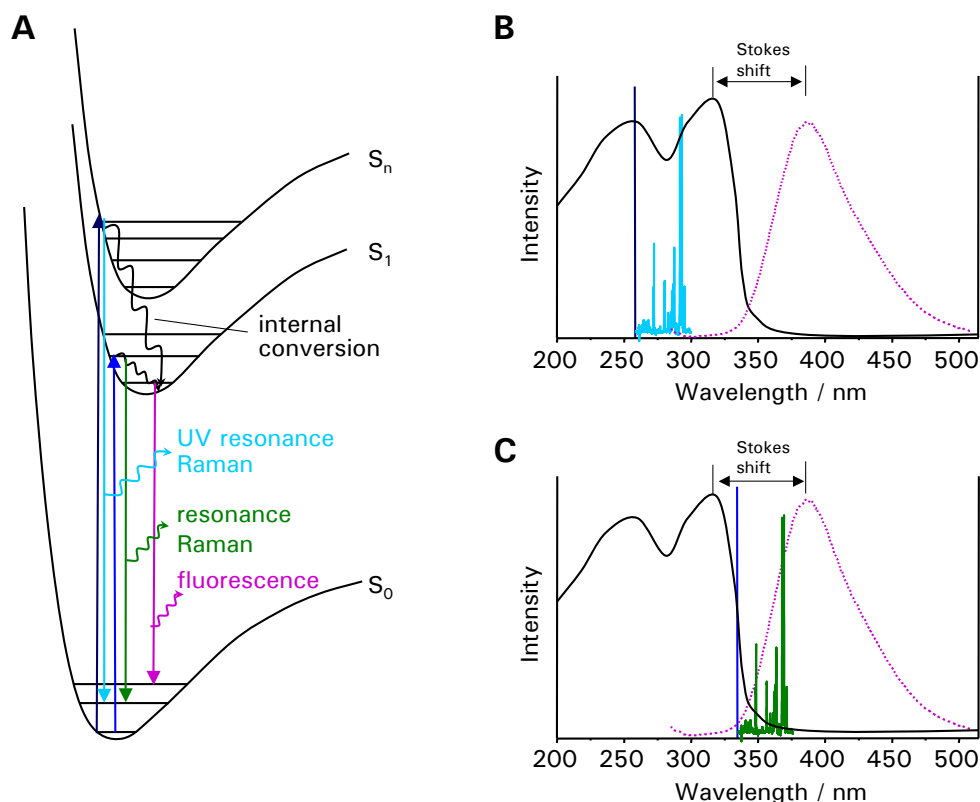


**Figure 2.6:** Resonance Raman spectroscopy and fluorescence. **A)** Energy level diagram (dark blue arrows: excitation, light blue and green arrow: Raman scattering, red: fluorescence), **B)** Excitation to higher electronic states. Fluorescence and Raman signals do not interfere. **C)** Excitation at the high wavelength edge of the absorption band. The Stokes shift is small and therefore the Raman and fluorescence signal overlap.

that couple to the  $\pi - \pi^*$  transition centered around 253 nm. The spectrum is much simpler and special focus can be put selectively on those enhanced vibrations. A different enhancement pattern is found in the resonance Raman spectrum excited at 218 nm allowing one to investigate a different site within the molecule. This site-specificity due to the application of different Raman excitation frequencies allows the study of smaller subunits in larger assemblies, as e.g. probing the active center in proteins which is pivotal for the function of the respective molecules, or the selective excitation of macromolecules such as proteins or DNA in the presence of other molecules, as e.g. in whole cells. The simplification of rich vibrational spectra from complex systems can also reduce the overlap of vibrational bands.

When using excitation wavelengths in the deep UV ( $< 250$  nm) fluorescence which is often a problem in biological samples is energetically far enough away from the scattered light and does not interfere with the Raman signal. This is illustrated in figure 2.6.

In case resonance Raman spectroscopy occurs via the same electronic excited states where the fluorescence emission originates (figure 2.6A), the Raman signals are often masked by the

## 2 Theoretical fundamentals

broad and featureless fluorescence spectra. This is especially the case when the Stokes shift, i.e. the energy difference between the absorption maximum and the fluorescence maximum, is only small (figure 2.6C). In UV-resonance Raman spectroscopy energy-rich UV-light is used, so that higher electronic excited states are incorporated. Raman scattering occurs within the first few femtoseconds ( $10^{-15}$  s) directly from the high electronic state. The fluorescence process occurs only on a time scale of nanoseconds ( $10^{-9}$  s), and therefore the molecule can relax to the lowest excited electronic state via radiationless processes. Since fluorescence consequently in most cases occurs from the lowest-energy excited state (Kasha's rule), the Raman and fluorescence signals are well separated on the energy scale as shown in figure 2.6B.

The high sensitivity, selectivity and the absence of interfering fluorescence brought forth various applications of the resonance Raman technique in biological, biochemical and medicinal research in the last years. The techniques was successfully applied to study DNA conformation, native structures of proteins and peptides, the local environment of biological chromophores (such as hemoglobin, bacterio rhodopsin, carotinoids, just to name some of them) [11, 23, 67, 114, 115, 117, 116, 231, 245, 246, 252, 277] in-situ and in dilute aqueous solutions, and for the differentiation and identification of various bacteria, fungi and algae [82, 108, 145].

Despite all the advantages experimental difficulties arise due to strong absorption of the excitation light which can cause thermal decomposition and unwanted photoreactions of the sample. Reabsorption of the scattered light makes a quantitative evaluation of the Raman intensity difficult and internal standards have to be used [272].

In this work the high sensitivity and selectivity of resonance Raman spectroscopy are used to investigate metabolic changes within bacterial cells during bacterial growth and under the influence of antibiotics. Furthermore, the biological targets of the drugs, namely DNA and the bacterial enzyme gyrase, are study in aqueous solutions at biological relevant concentrations.

### 2.1.3.2 Surface-enhanced Raman spectroscopy (SERS)

For the investigation of surfaces special techniques like surface-enhanced Raman spectroscopy (SERS) showed to have a high potential. In 1974 Fleischmann et al. [73] first reported huge Raman signals from pyridine adsorbed onto electrochemically roughened silver electrodes. Some years later, Albrecht and Creighton [7], and Jeanmaire and van Duyne [110] independently explained this high increase (up to six orders of magnitude) of the Raman scattering cross section of the adsorbed molecule by complex electromagnetic interactions of the adsorbate with the metal surface. This surface enhancing Raman effect provides another way to overcome the drawback of normal Raman spectroscopy: the low scattering efficiency.

**Mechanisms of surface enhancement** The Raman intensity of normal Raman scattering is proportional to the square of the induced electric transition dipole moment  $\mu$ . According to equation 2.5 there are two ways to increase the Raman scattering intensities: first by increasing the electromagnetic field  $E$  and second by enhancing the transition polarizability tensor  $\alpha$ . The first



is named electromagnetic field enhancement mechanism, the second charge transfer, or chemical enhancement mechanism. Discussions over the relative contributions to the total enhancement of the two mechanisms are still ongoing [190, 121, 10, 164, 189].

**Electromagnetic enhancement mechanism** The local increase of the electromagnetic field at metal surfaces is due to the excitation of surface plasmon resonance. Plasmons are the quanta of the collective oscillations of the free electron gas (conduction electrons) against the positive ion cores of the metal at optical frequencies. One differentiates between bulk plasmons which denote electron fluctuations inside the bulk and surface plasmons which are collective charge density fluctuations at the metal-vacuum or metal-dielectric interface. If the metal surface is roughened the plasmons are no longer confined and the electric field can radiate both in parallel and perpendicular direction to the surface. It is possible to excite the plasmons in metal particles as has been reported for various metals [125]. Because of its resonant character the oscillation may result in a polarization and an electric field exceeding that of the exciting light, often referred to as field enhancement. For metals such as Ag, Au and Cu, the plasmon resonances are in the visible region of the electromagnetic spectrum. Particle size and shape (morphology) were found to have a strong influence on the resonance frequency. The field enhancement should be most intense at edges where the curvature of the particle is high, and therefore, the density of the electric flux is highest (lightning rod effect).

If a sample is brought into close contact with a rough metal surface, usually silver, gold or copper, and the surface plasmons of the metal are excited with a laser, the enhanced evanescent electromagnetic field causes an enhanced Raman signal with a scattering cross section of 3 to 15 orders of magnitude larger than those for normal Raman scattering [119].

The range of the electromagnetic field of the excited surface plasmons quickly decreases with distance  $d$  from the surface of the spherical metal particle with radius  $r$ . A single molecule close to the metal surface experiences the following distance dependence of the electromagnetic enhancement  $EM_{enhance}$  [190] as was obtained as a result of the dipolar plasmon approximation for silver spheres by McCall [159]:

$$EM_{enhance} \propto \left( \frac{r}{r+d} \right)^{12}. \quad (2.15)$$

For a monolayer of molecules the equation changes to [190]:

$$EM_{enhance} \propto \left( \frac{r}{r+d} \right)^{10}. \quad (2.16)$$

as was experimentally determined by Cotton et al. using Langmuir-Blodgett monolayers and well defined spacers [56]. Besides the strong distance dependence of the enhancement, equation 2.15 and 2.16 show furthermore, that larger metal particles produce an electromagnetic enhancement with further spatial range.

## 2 Theoretical fundamentals

**Charge transfer enhancement mechanism** The charge-transfer enhancement is thought of to result from the direct chemisorption of the adsorbate on the metal surface forming a surface complex. This interaction with the conduction and/or valence bands of the metal surface (ligand to metal and/or metal-to-ligand charge transfer interactions) causes changes in the electronic structure of the analyte. If the exciting laser light fits the charge-transfer energy gap, resonance Raman scattering occurs (see section 2.1.3.1). As the mechanism depends on a metal-adsorbate bond, it effectively operates only on the first layer of adsorbates (absolute first-layer enhancement). Compared to the normal Raman spectra the surface-enhanced Raman spectra might exhibit shifted vibrational bands and a changed intensity pattern due to the selective enhancement of the vibrational modes coupling to the excited electronic transitions of the analyte-metal complex.

**Applications and limitations** SERS is a very sensitive technique capable to obtain rich chemical information from the surfaces of substances in close contact to the metal. Due to the surface enhancement the sensitivity is increased compared to normal Raman by 3 to 15 orders of magnitude. This lowers the detection limit and analytes at very low concentrations down  $10^{-11}$  M (e.g. Rhodamine6G at silver colloid [120]) can be detected. It was even possible to record surface-enhanced Raman spectra from single molecules [122, 120, 285, 154, 182, 225].

For the interpretation of the spectra surface selection rules have to be applied and also Raman inactive bands may become observable. In their simplest form, and assuming no specific symmetry selection rules, those Raman bands that originate from vibrations with an induced polarization of the adsorbate electron cloud perpendicular to the metal surface are predicted to show the highest intensity [60, 165]. This allows useful conclusions about the relative orientation of adsorbed molecules and helps to gain insights into the molecular basis of a number of surface problems. Exemplarily, this was shown for benzene and monosubstituted benzene by Gao et al. [80].

Various biomedical applications simplifying medical diagnostics and biological imaging have been developed using SERS techniques. It is possible to identify DNA and detect DNA biotargets (e.g. gene sequences, bacterial and viral DNA fragments) [266, 105] via hybridization to DNA sequences complementary to that probe [265, 267], to determine the secondary structure of DNA (helical vs. denatured) [171], and also to differentiate and identify single bacterial cells [202].

Despite all the advances, the technique still suffers from limitations. Up to now the main drawback is the rather poor quantitative reproducibility, since the SERS signal is extremely sensitive to the nature and shape of the metal surface roughness, and a number of factors involving the adsorption process such as the orientation at the metal surface and the extent of adsorption. Great research effort is put into the development of reproducible SERS substrates [127, 240, 290, 137, 89, 87, 31]. The very high sensitivity of SERS (enhancement factors up to  $10^{15}$  [182]) allows single molecule detection. However, it can also be possible that an impurity within a sample or a species formed by surface photochemistry is preferentially enhanced. The exclusion of such unwanted signals can sometimes be difficult since the specific selection rules of SERS might make it complicated to relate the SER spectra to the Raman scattering from the parent species before adsorption. Fur-

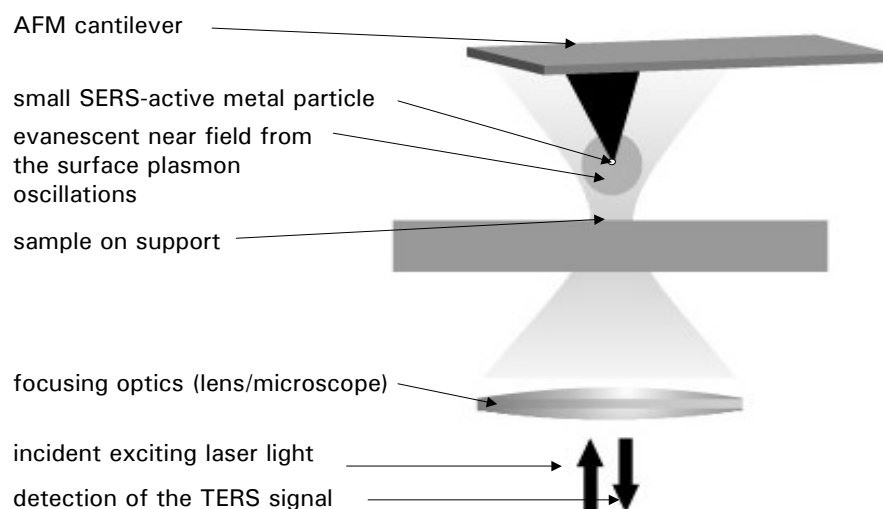


**Figure 2.7:** Tip-enhanced Raman spectroscopy (TERS) configuration: the exciting laser is focused on the SERS active particle at the tip apex of the AFM tip and excites there the surface plasmons in the metal. The evanescent near-field causes an enhanced Raman signal in the close vicinity of the tip apex (Fig. slightly adapted from ref. [204]).

thermore, since the analyte requires to be in close proximity to a suitable roughened surface, one has to be aware of contamination of the sample with metal colloid.

### 2.1.3.3 Tip-enhanced Raman spectroscopy (TERS)

Some of the drawbacks of surface-enhanced Raman spectroscopy can be overcome when moving to tip-enhanced Raman spectroscopy (TERS). Here, the enhancing metal surface is reduced to a small tip of ideally one metal particle. Illumination of the tip with a laser beam excites confined localized surface plasmons of the metal which cause an enhanced electromagnetic near field. Significant enhancement of the Raman signal is observed in a small area in close vicinity of the tip apex (figure 2.7). Since no colloidal solution of metal particles is used contamination of the sample with metal is avoided. In order to control the position of the enhancing metal tip over the sample surface, the scanning tip is combined with an atomic force microscope (AFM) (see next section 2.2). This combination of SERS and AFM allows simultaneously the investigation of the surface structure by AFM and the detailed chemical characterization of those surface structures from the vibrational information of the (tip-enhanced) Raman spectra.

Using this near field technique the Rayleigh criterion of the Abbe diffraction limit [204]

$$d = 0.61 \frac{\lambda}{NA} \quad (2.17)$$

## 2 Theoretical fundamentals

with  $\lambda$  denoting the wavelength of the exciting light and  $NA$  the numerical aperture of the lens, can be overcome and the smallest distinguishable distance  $d$  between two adjacent objects is only determined by the size  $s$  of the enhancing metal particle:

$$d \approx s \quad (2.18)$$

Usually the tip sizes are in the range between 10 and 50 nm providing a spatial resolution in  $x$ - $y$ -direction below the diffraction limit [247]. Also the information obtainable in  $z$ -direction is confined to a few nanometer due to the rapidly decaying evanescent field [184, 211].

TERS provides increased sensitivity, selectivity and spatial resolution over conventional Raman spectroscopy. So far, this technique has been applied to small pure substances like CN-ions adsorbed at gold surfaces [196], malachite green isothiocyanate [197, 198], benzenethiol [210], Rhodamine6G [270], single walled carbon nanotubes [94, 93], and DNA components [205]. Within the scope of this work TERS spectra from surfaces of complex biological systems, such as whole bacterial cells have been recorded for the first time (chapter 5).

### 2.2 Atomic force microscopy (AFM)

Atomic force microscopy is an imaging technique that is based on the measurement of very small forces between two approaching atoms, that is the probing tip and the sample (figure 2.8) [32]. Those interaction forces show a very large distance dependence, so that a good spatial resolution of the sample surface is obtained when using sharp probes. The probing tip is mounted on the free vibrating end of a flexible cantilever which is held on a fixed support with the other end. The tip is brought into close contact to the sample and scanned across the surface. The local attractive or repulsive forces  $F$  between the tip and the sample cause a deflection  $s$  of the cantilever towards or away from the substrate according to Hooke's Law:

$$F = -k \cdot s \quad (2.19)$$

with  $k$  being the force constant. This (vertical) deflection  $s$  is detected by a laser beam which is reflected from the back of the cantilever onto a photo-detector. A small change in the bending angle of the cantilever gets converted into a measurable deflection of a reflected laser spot on the photodetector (optical lever principle), which again is used to calculate a 3-dimensional topographic image of the scanned surface.

#### Imaging modes

There are two main modes to probe the sample surface: one direct feedback mode where the static feedback of the cantilever is measured while scanning over the surface and one dynamic mode where the cantilever vibrates and the slight changes in the oscillation of the cantilever upon

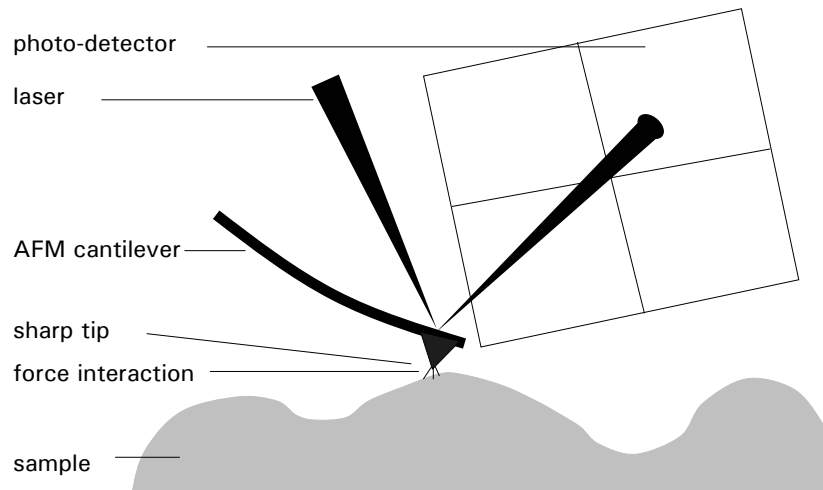


**Figure 2.8:** Atomic force microscopy: The AFM cantilever with the very sharp tip is scanned above the sample surface. Due to force interactions between the tip and the sample the cantilever bends which is monitored by the deflection of the laser beam on the photo-detector.

interaction with the sample are used to image the sample surface. The first one is known as "contact-mode" (figure 2.9A). It can be run in constant-height mode, where the height of the cantilever is kept constant and the change in force is recorded, or in the more often used constant-force mode. In the latter, the cantilever is moving up and down via a feedback loop over high and low parts of the sample so that all parts of the sample experience the same force.

The dynamic modes can be distinguished according to the amount of oscillation cycles the tip is in contact with the surface. If the tip is vibrating well above the surface without getting in touch with the surface it is called "non-contact mode" (figure 2.9B). The opposite of this mode is the "force modulation mode" (figure 2.9C) where the tip does not leave the surface at all during the oscillation cycle. This can be thought of a dynamic version of the "contact mode". The probably most popular mode is the "intermittent contact mode" ("tapping mode") where the tip gets in (repulsive) contact with the sample at its lowest point of oscillation (figure 2.9D).

### Cantilevers

Cantilevers are especially designed for either imaging mode. For the contact mode cantilevers have to have a low spring constant and a low resonant frequency in order to image the surface without getting damaged or damaging the sample due to too high applied forces. Cantilevers designed for the intermittent contact mode have to be stiffer and have to have a higher force constant and a higher resonant frequency (ideally between 200 and 300 kHz). Those cantilevers are usually shorter and thicker than the non-contact ones.

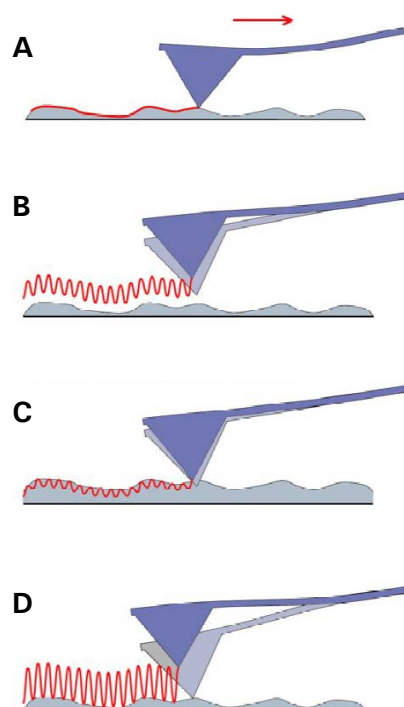


**Figure 2.9:** Imaging modes of an atomic force microscope: **A)** contact mode, **B)** non-contact mode, **C)** force modulation mode, **D)** intermittent contact mode (figure adapted from the jpk user manual).

### Advantages of AFM

Since there is no need of staining or coating the sample atomic force microscopy has grown to a very powerful technique for the investigation of biological surfaces. Single cells as well as single molecules, such as DNA and proteins have been studied so far [5, 28, 43, 68, 91, 158, 224, 237].

## 2.3 Statistical evaluation methods: Multivariate data analysis

Investigating dependencies quite often covers the analysis of a multidimensional problem, that is the variable of interest depends on not only one, but several factors. Also analyzing spectral data, as is done within the scope of this work, involves the evaluation and classification of complex data sets with a multidimensional dependence, such as the intensity at different wavenumbers, and additionally the age of the bacterial culture (chapter 4), or the concentration of added drugs (chapter 9). For a proper data assessment and to recognize correlations the use of statistical methods such as multivariate data analysis is necessary.

The aim of multivariate data analysis is to display the intrinsic data structure, to allow the discrimination and classification of groups of data and also to use it for regression and prediction.

Among the large variety of statistical methods hierarchical cluster analysis and principal component analysis have been used successfully within this work. These two methods are unsupervised classification methods, which means that no information about the affiliation of the individual objects is required for the data analysis. Unsupervised techniques are mainly used for the search for natural similarities in a data set [22]. Supervised statistical methods such as linear discriminant analysis (LDA), artificial neural networks (ANN) or support vector machines (SVM) take from the beginning the class affiliation into account. With known objects (spectra in this case) a model is created, validated and can then be used to identify unknown objects (spectra).

### 2.3.1 Hierarchical cluster analysis (HCA)

The hierarchical cluster analysis is an unsupervised method that arranges the individual objects according to their similarity in groups (clusters). The result of a hierarchical cluster analysis (HCA) is presented in a dendrogram which shows some similarity to the genealogical tree in taxonomy.

As a measure for the similarity of the individual spectra serves the heterogeneity, or spectral distance. The smaller the spectral distance the more similar are the spectra. Two identical spectra have the spectral distance of zero. To calculate the spectral difference several methods are possible. In the following the algorithm of the "standard method" and the "factorization method" will be explained shortly.

The standard method uses the euclidian distance between the intensities of the spectra  $a$  and  $b$  for all data points  $k$  in the chosen spectral range to calculate the spectral distance  $D$ :

$$D = \sqrt{\sum_k (a(k) - b(k))^2} \quad (2.20)$$

When using the factorization method first a principal component analysis (PCA) is performed (see section 2.3.2) and the spectrum is expressed as a linear combination of score coefficient and loadings. The spectral distance is then also calculated from the euclidian distance using equation 2.20, but instead of the intensities of the raw spectra the scores of the PCA are used.

It showed to be useful to perform a vector normalization of the spectra prior to calculating the spectral distance by standard or factorization method.

After having calculated the distance matrix the individual objects are grouped into clusters, first merging the two most similar spectra into a cluster. In a next step the spectral distances between all objects (clusters and spectra) are recalculated, and again the two most similar objects are united to form a cluster. This procedure goes on until all spectra are incorporated in the cluster. There are several methods how the two closest clusters are identified and the third object is added. The most common algorithms are single, complete, average and weighted average linkage as well as median, centroid and Ward's technique. In this work Ward's technique has been exclusively used to minimize intra class variances and maximize inter class variances.

## 2 Theoretical fundamentals

Ward's linkage uses an analysis of variance approach to evaluate the distances between clusters in order to form as homogeneous as possible clusters. Therefore, always the two subclusters are merged that cause the smallest increase in heterogeneity  $H$  which is calculated as:

$$H(r,i) = D(r,i) = \frac{\{n_p + n_i\} \cdot D(p,i) + \{n_q + n_i\} \cdot D(q,i) - n_i \cdot D(p,q)}{n_p + n_q + n_i} \quad (2.21)$$

with  $r$  being the cluster composed of  $p$  and  $q$  to which the object  $i$  has to be added. The variable  $n$  accounts for the number of spectra in the respective cluster.

Ward's algorithm is regarded as very efficient and proofed to be especially suited for the cluster analysis of bacterial spectra [2].

### 2.3.2 Principal component analysis (PCA)

Principal component analysis (PCA) has been widely adopted to extract abstract features and to reduce dimensionality in many pattern recognition problems. Also in spectroscopy where one has to deal with large amount of data PCA proofed to be useful to develop smaller and straightforward, clear models that describe the data, allow the detection of outliers and classify the objects of investigation. This is achieved by calculating a new coordinate system. The new orthogonal and independent axis of this coordinate systems are the principal components (PC). The first PC (PC1) is positioned along the direction of maximum variance in the data set, the second PC (PC2) lies in a direction orthogonal to the first PC and in the direction of the second largest variance. This continues until all PCs are determined. The total number of PCs is limited to either the number of objects minus one, or the number of variables, depending on which is the smaller number. Since the higher order principal components will lie along directions where there is only very little spread in the objects, these directions can progressively thought of as "noise" directions. Therefore, by performing the principal component analysis the data set is decomposed into a structured part which is described by the first PCs and a noise part, which is described by the higher order PCs. If the samples under investigation are connected by any correlation the number of "useful" principal components will be much less than the initial variables or objects and the dimension of the multivariate data is reduced whilst most of the variance is preserved. The number of principal components that are needed to reliably described the data set can be estimated with the Scree-test after Cattell [100]. Here the variance of the residues is plotted against the number of PCs and only those PCs are further investigated that still significantly decrease the variance of the residues.

Any PC can also be thought of as a linear combination of the original variables  $p$  of the data set  $X$ . The PC-vector will contain  $p$  coefficients, one for each of the  $p$  vectors. These coefficients are called loadings. The loadings from all the principal components constitute a matrix  $P$  which can be thought of a transformation matrix between the original variable space and the space spanned by the PCs. In the space spanned by the principal components the investigated objects will have



new coordinates with respect to the individual PCs which are called scores. The scores for all objects form together the score matrix  $T$ . The columns of this score matrix  $T$  describe the scores for one PC. They are orthogonal and are called score vectors  $t$ . A graphical description of the spectra in the PC space is called scores plot.

In this work the principal component analysis was performed using the program "The Unscrambler" (CAMO Process AS, Version 9.2) which calculates the PCs following the NIPALS algorithm (Nonlinear Iterative Projections by Alternating Least Squares) and is sketched briefly below:

1. Centering of the data matrix  $X_i$
2. The first score vector  $t_i$  is selected as a column from the  $X$ -matrix.
3. The corresponding loadings  $p_i$  are calculated and normalized:  $p_i = \frac{X^T t_i}{|X^T t_i|}$ .
4. For these new scores the loadings are calculated:  $t_{i,new} = X p_i$ .
5. Check the convergence: if  $|t_{i,new} - t_{i,old}| > \text{criterion}$ , go back to step 2, otherwise continue.
6. Updating (deflation):  $X_{i+1} = X_i - t_i p_i^T$  The first principal component is subtracted from the data matrix.
7. Step 2 through 6 are repeated until enough PCs have been calculated.

### 2.3.3 Further multivariate data analysis methods

Besides hierarchical cluster analysis and principal component analysis two more multivariate data analyzing methods were applied in this work and should be explained briefly in the following.

A supervised classification method is the **linear discriminant analysis (LDA)**. It seeks to find a linear transformation by maximizing the between-class variance and minimizing the within-class variance. It has proved to be a suitable technique for discriminating different pattern classes and was applied in this work as an objective function in the reverse elimination tabu search.

The **Reverse elimination tabu search (REM-TS)** is a variable selection process. Following special search routines variables are selected and those selected models are evaluated with objective functions and cross validation. The objective function might be a classification or a regression method. At the end a model is obtained with variables that show the lowest error rate for that objective function. This technique has been applied in chapter 4.3 and 9 to select the wavenumbers of high importance for the discrimination of the spectra of bacteria in different growth phases or under the influence of different drug concentration. More details on the method are given in the experimental section 3.4.



## 3 Material and Methods

In this chapter a description of the used instruments and applied methods is given. A detailed list of the chemical composition of buffers and media (especially for the extraction procedures) as well as the origin of the commercially obtained chemicals can be found in the appendix under the chapter "Chemicals and media" (chapter A).

### 3.1 Spectroscopic instrumentation

#### 3.1.1 UV/vis absorption spectroscopy

UV/vis absorption spectra of the fluoroquinolones were recorded on a Perkin Elmer UV/vis spectrometer Lambda 16 at 20°C. Also the temperature dependent measurements of the DNA (denaturation) have been performed with this spectrometer.

The growth of the bacterial cultures was monitored by measuring the absorption at 630 nm using a Spekol 1100 UV/vis spectrometer (Carl Zeiss Technology).

A Cary5000 UV-Vis-NIR absorption spectrophotometer (Varian) was used to record the UV/vis absorption spectra of the nucleic acids, DNA bases, proteins and amino acids.

#### 3.1.2 Raman spectroscopy

Micro-Raman spectra were obtained with an excitation wavelength of 532 nm from a frequency doubled Nd:YAG laser, 633 nm from a HeNe-laser and 830 nm from a diode laser, using a LabRam HR spectrometer (Jobin Yvon, Horiba). The laser light was focused by means of a 100x microscope objective onto the sample down to a spot diameter of approximately 1 µm having a laser power of circa 10 mW incident on the sample when using the 532 nm laser, 2 mW when using the 633 nm laser and 4 mW when exciting with 830 nm. The 180° back-scattered Raman signal was detected with a CCD camera (1024 x 512 pixels) operating at 220 K.

The Raman spectra of the fluoroquinolones excited at 1064 nm (Nd:YAG laser) laser light were recorded with a Fourier transform (FT) spectrometer (Bruker, Model IFS120HR) equipped with a Raman module (Model FRA106). Detection was achieved with a liquid nitrogen cooled Ge detector.

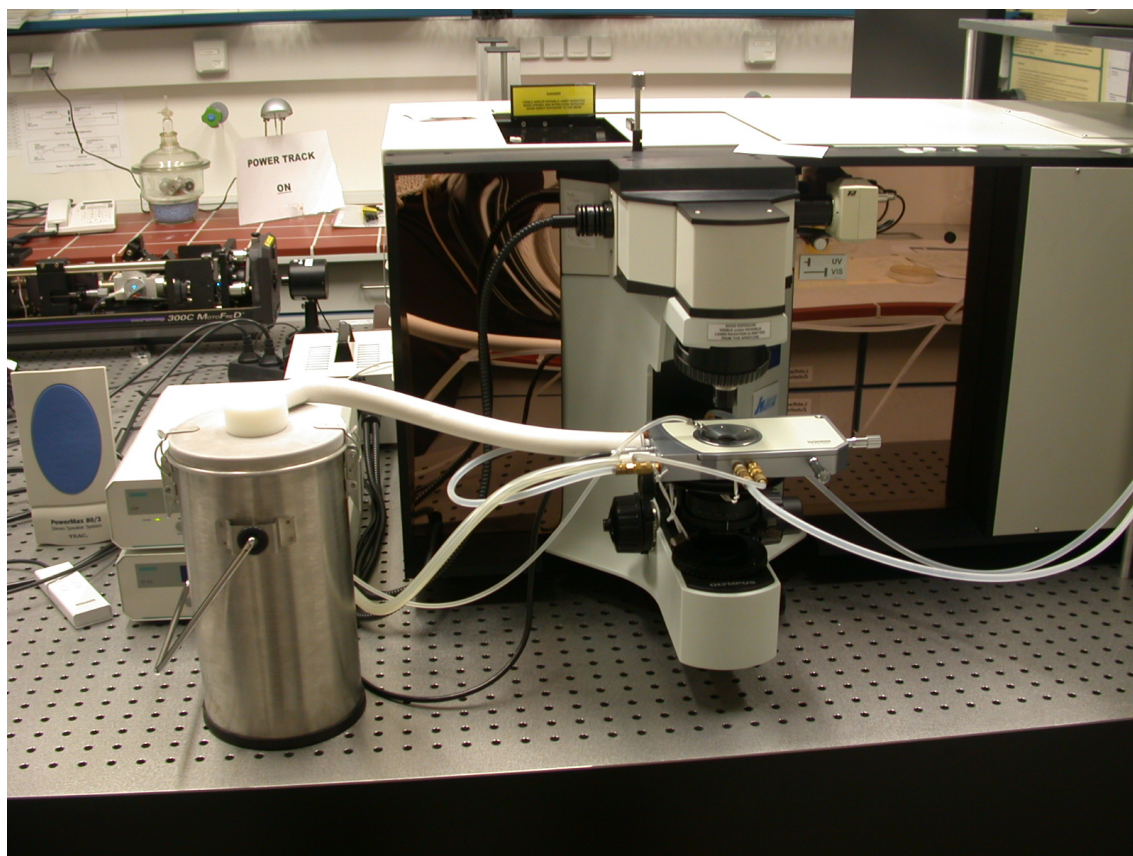


**Figure 3.1:** Experimental setup of the resonance Raman experiments when cooling the sample (Linkam stage).

#### 3.1.3 UV-resonance Raman spectroscopy

Ultra-violet (UV) resonance Raman (RR) experiments were performed with excitation at 244 nm and 257 nm from an intracavity frequency doubled argon-ion laser (Innova 300, MotoFreD, Coherent Inc.). The output power at the laser head ranged between 32 and 45 mW, the laser power at the microscope objective (LMU-40x-UVB, OFR) before hitting the sample was about 1.5 mW. A micro-Raman setup (HR800, Horiba/Jobin-Yvon) with a focal length of 800 mm and a 2400 lines/mm grating was used. The signal was recorded with a liquid N<sub>2</sub> cooled CCD camera. Calibration of the wavenumber axis was performed using the known Raman signals from teflon.

To avoid combustion or photo (and thermal) degradation the sample was rotated on a moved table. The UVRR spectra of the samples showed no significant time dependence, indicating no appreciable photodecomposition during data collection protocols. Some experiments (bulk samples of fluoroquinones, DNA) were performed at lowered temperatures of -80°C and -20°C which were achieved with a liquid nitrogen cooled and moved table (Linkam stage, figure 3.1).

For most experiments an integration time of 120 s was found to give spectra with a good signal-to-noise ratio.

Resonance Raman experiments of the fluoroquinolones with excitation at 275 nm were performed with an argon-ion laser (Spectra Physics Model 2085). A rotating cell in a 90° scattering arrangement was used to investigate the aqueous solutions of the quinolones. The scattered light was collected with an  $f = 50$  mm (1:1.3) quartz lens and analyzed with a Spex 1404 double monochromator equipped with a 2400 lines/mm gratings. The dispersed Raman straylight was detected with a Photometrics model RDS 200 CCD Raman detector system.

### 3.1.4 IR absorption spectroscopy

IR absorption spectra were recorded on a Bruker IFS66 spectrometer with  $4\text{ cm}^{-1}$  resolution. For each FT-IR spectrum 128 interferograms were coadded and averaged. A DTGS (doped triglycinerinsulfate) detector was used.

IR spectra of the pure substances of the fluoroquinolones and the DNA bases were recorded solid in KBr. IR transmission spectra of the solid nucleic acids (lyophilized powder) and the crystalline nucleic acid bases were recorded using a microscope. The sample was placed on a silicon waver. For convenient presentation the transmission spectra have been converted to IR absorption spectra using the OPUS software package.

IR absorption spectra of bacteria were recorded from dried suspension on KRS-5<sup>TM</sup> plates. KRS-5 is a crystal of 42 mol% TlBr and 58 mol% TlI with a maximum transmission of 75%. It is only poorly soluble in water (at 300 K  $5 \cdot 10^{-2}$  g/100 g H<sub>2</sub>O) and an ideal support for transparent bacterial films [172].

For each sampling mode a one-beam reference spectrum with the pure support (KBr, silicon or KRS-5) was recorded in order to account for the moisture and impurities in the optical material.

### 3.1.5 Tip-enhanced Raman spectroscopy (TERS)

The experiments using tip-enhanced Raman spectroscopy were performed in the laboratory of PD Dr. Volker Deckert at the Institute for Analytical Sciences (ISAS) in Dortmund.

#### 3.1.5.1 Experimental TERS set-up

The experimental set-up is shown in figure 3.2. A commercially available atomic force microscope (NanoWizard atomic force microscopy, JPK Instrument AG, Germany) is mounted onto an inverted Raman microscope (HR LabRam, Horiba Jobin Yvon, France; 800 mm focal length, 600 lines/mm grating). The ultra sharp silver coated AFM tip with an apex size of less than 50 nm (NSG10, ATOS GmbH, Germany) was placed above the sample and used in non-contact mode. The laser beam (568 nm, krypton-ion, Coherent, Santa Clara, USA) was focused from below onto the silver-coated tip via an oil immersion objective (60x, NA 1.45, Olympus) to excite the surface plasmons at the point of the tip apex. The laser power at sample was 1.5 mW. The specimen was moved in xy-direction via a piezo controlled sample stage, while the xy-position of the AFM-tip was fixed to the position of the laser spot. Defocusing in z-direction due to height changes during

### 3 Material and Methods

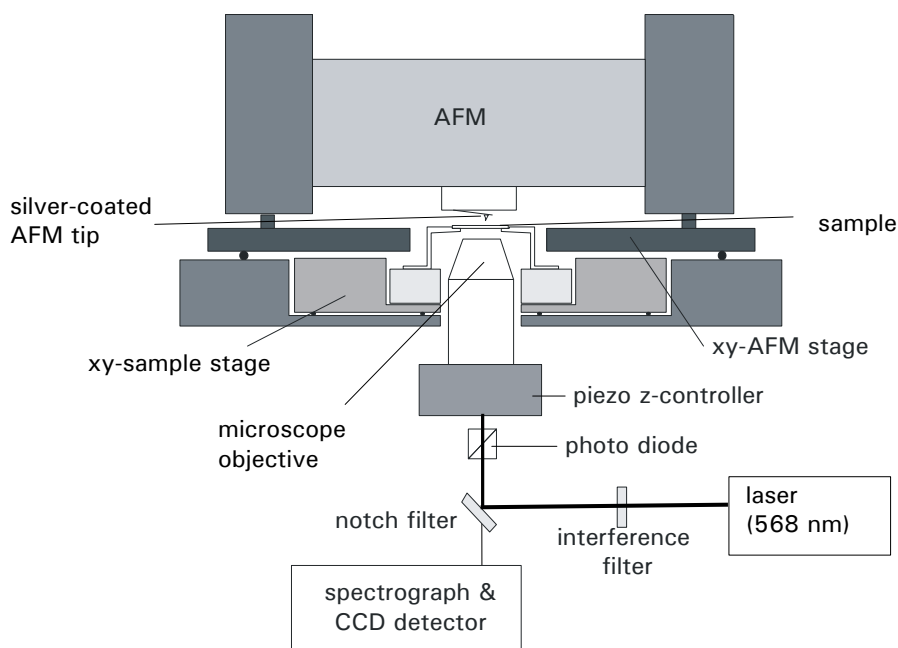


**Figure 3.2:** Experimental set-up of the TERS experiments (reproduced from ref. [205]).

a scan was avoided by a synchronized movement of tip and microscope objective. That way, a topographic image of the sample was recorded. Special, well defined points on the sample were then selected to record TERS spectra at different positions on the cell and, for reference purposes, at positions where no cells were present. The enhanced Raman signal stems from only a very small area in the vicinity of the probe point, which can be roughly estimated by the tip radius. In our case the tip radius is assumed to be less than 50 nm. The detection of the Raman signal was performed in  $180^\circ$  back-scattering geometry through the same oil immersion objective. Due to the strong signal enhancement an acquisition time of one second was sufficient. This facilitates revealing dynamics on the cell surface on a reasonable time scale. For such measurements the probe was kept on a fixed position at the cell and spectra were recorded continuously. The integrity of the bacterial cells was checked before and after the TERS experiment by AFM measurements. No changes in the bacterial surface structure could be detected. Also the probing tip did not contain any material from the cell surface or combustion products as was checked in control experiments. Therefore, it can be assumed that the cells did not get damaged in the experiment.

The AFM was operated in the instrument's intermittent contact mode, a variety of non-contact methods (see section 2.2). That way a proper measurement of the specimen was possible and shifting of the bacteria (*S. epidermidis*) on the glass substrate could be avoided as was not the case when using the contact mode. However, it was found that the smaller *E. coli* cells can be investigated in the contact mode.

### 3.1.5.2 Enhancing AFM tips

Ultrasharp AFM tips were commercially obtained from ATOS GmbH, Germany, and later from NT-MDT, Netherlands. The non-contact AFM tips NSG-10 have a curvature radius of 10 nm, a force constant between 5.5 - 22.5 N/m and a resonance frequency between 190 and 325 kHz. The contact mode AFM tips CSG-10 have a force constant between 0.03 and 0.2 N/m and a resonance frequency between 14 and 28 kHz (manufacturer information).

In order to obtain a SERS active particle at the tip apex for the field enhancement the tips were evaporated with 20 nm of silver. This was done under an argon atmosphere of about  $10^4$  mbar, starting from an initial vacuum of  $2 - 5 \cdot 10^{-7}$  mbar. The silver was evaporated at a rate of 0.02-0.07 nm/s applying a current of 30-36 A at a voltage of 4 V.

To produce small silver islands some of the silver-coated tips have been annealed (60 s at 300°C). Figure 3.3 shows the scanning electron microscope (SEM) images of a silver coated tip (A) and a silver coated tip that has been annealed (B) from three different viewing angles: (1) from top, where the tip is coming out of the cantilever and facing the observer, (2) from the side, and (3) a magnification of the tip apex. The tip apex after silver evaporation is less than 50 nm in diameter. Clearly the silver islands are visible on the cantilever of the annealed tip.

**Characterization of the plasmon resonant frequency of the silver coated AFM tips** The plasmon resonance of the tip was characterized by light microscopy. Figure 3.4A and B show the bright and dark field microscope images of a silver coated AFM tip, respectively. Figure 3.4C-F represent the absorption curves at different positions on the tip and cantilever. At the tip apex the plasmon oscillation has a maximum around 560 nm. The laser at 568 nm used in these TERS experiments excites those plasmons slightly on the red side of the maximum and therefore should cause a maximum enhancement. However, it should be noted that with this technique only macroscopic, far-field characteristics of the enhancing tip are probed. In the TERS experiment ideally a single silver particle is causing the signal enhancement about which nothing is learnt in this experiment.

**Tuning of the AFM tips** Intermittent contact-mode cantilevers have to be excited to oscillations. To give a reasonable amplitude for the oscillation the driving frequency has to be close to the resonant frequency of the cantilever. The resonant frequency  $f$  of a cantilever depends on its mass  $m$  and spring constant  $k$ :

$$f = \frac{1}{2\pi} \sqrt{\frac{k}{m}} . \quad (3.1)$$

The parameters are adjusted before the experiment and figure 3.5 shows such a tuning curve. After silver evaporation the resonant frequency of the non-contact mode are found in a range of 230 and 330 kHz. The phase of the cantilever oscillation (blue curve) can provide additional sample information such as stiffness and adhesion.

### 3 Material and Methods

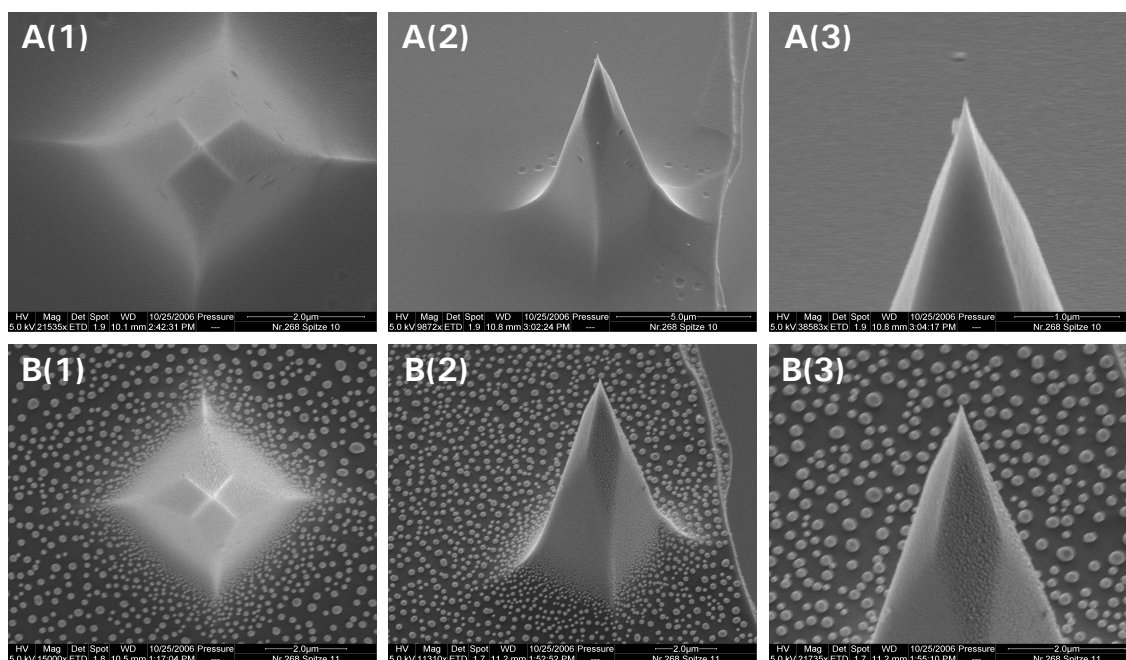


**Figure 3.3:** Scanning electron microscope images of the silver-coated AFM-tips for the TERS experiments **A)** non-contact tip covered with 20 nm of silver, **B)** non-contact AFM-tip covered with 20 nm of silver and annealed (60s at 300°C) at three different viewing angles **(1)** from top, where the tip is coming out of the cantilever and facing the viewer, **(2)** from the side, **(3)** a magnification of the tip apex.

**Sensitivity calibration** The topography of the surface is measured by recording the deflection of the reflected (AFM) laser beam from the back of the cantilever with a photodiode (figure 2.8). When there are rises or declines on the surface, the cantilever bends and thereupon the position of the reflected laser on the photodiode changes. In order to convert the photodetector signal of the cantilever deflection into a quantitative value of force and to determine the oscillation amplitude of the cantilever in nanometer, force-distance measurements have been performed with the tip. The plain cantilever tip is approached to a bare hard surface until the deflection of the cantilever rises steeply in the repulsive contact region. For a hard surface and tip this slope in deflection (in Volts) rises linearly with the piezo height (in nm) and can therefore be used to calculate the sensitivity of the cantilever spring. The oscillation amplitude of the free cantilever was set to 10 nm whereas the setpoint for feedback was set to 60% of that value. All these values vary around 10% from tip to tip.



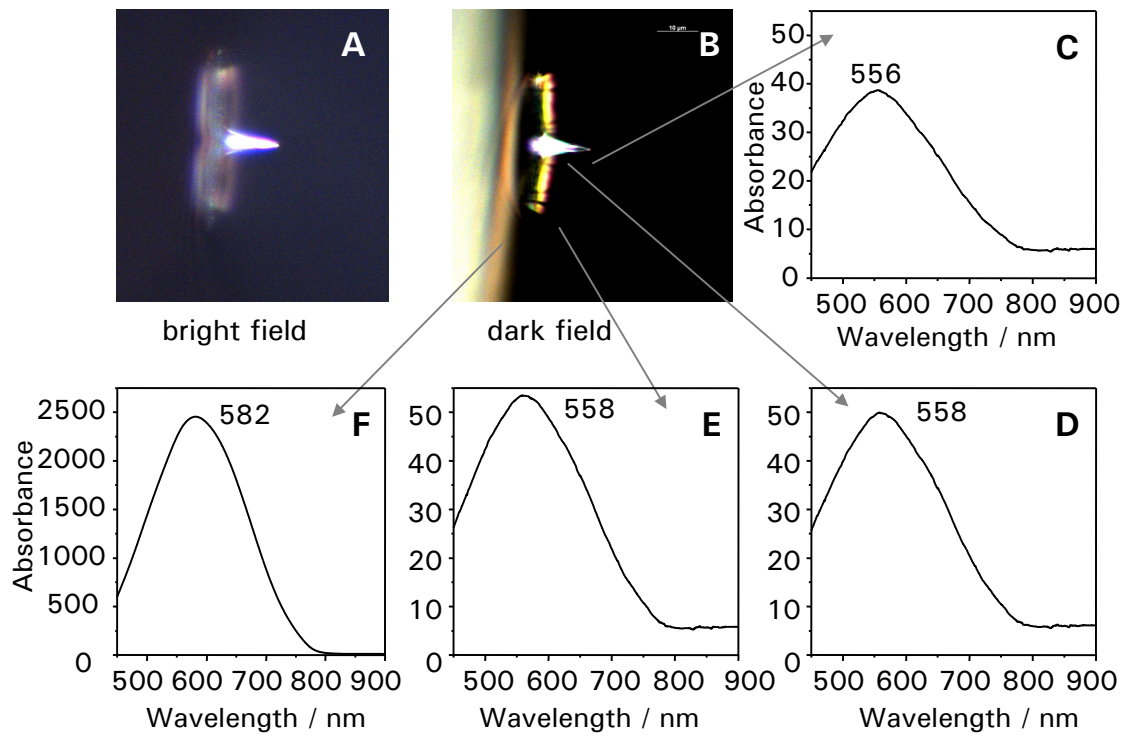


**Figure 3.4:** Plasmon resonance of the silver-coated AFM-tips for the TERS experiment **A)** light microscope image of the tip, **B)** dark field microscope image of the same tip **C-F)** spectra of the scattered light from different positions on and near the tip apex as indicated in figure B.

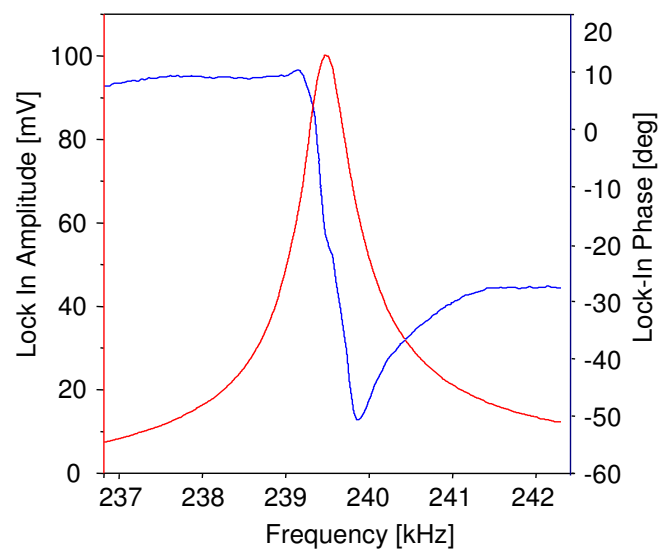


**Figure 3.5:** Tuning curve of the non-contact AFM tips, red curve: frequency, blue curve: phase.

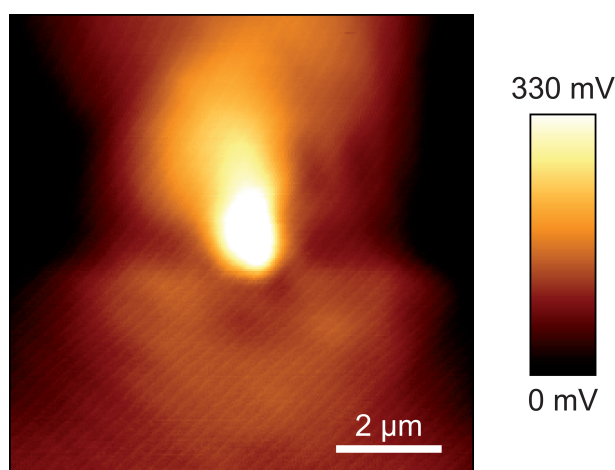


**Figure 3.6:** Optical response (reflectivity image) when scanning the silver-coated AFM tip through the laser focus.

#### 3.1.5.3 Practical tip placement / focal spot adjustment

For the maximum enhancement of the Raman signal the tip has to be positioned with the tip apex inside the laser focus. After a coarse adjustment of the entire AFM-head, the tip scans in the tip-scanning mode of the AFM through the laser focus and the reflected signal is detected by a simple photodiode (figure 3.2). If there is a silver particle at the apex of the tip a bright signal (high reflectivity) is recorded in the optical response as shown in figure 3.6.

The diameter of the tip apex after silver evaporation is expected to be well below 50 nm. However, the spot size of the tip response in the picture (figure 3.6) is larger and can be explained by a convolution of the effective tip area and the size of the laser spot (the diffraction limited diameter of the focused laser should be around 500 nm). The point of highest response marks the optimal alignment for the TERS experiment as was proven by recording tip-enhanced Raman spectra from a homogeneously thick reference sample in the area of highest reflectivity and surrounding spots. At the position of highest tip-enhanced Raman intensity, which is also the point of highest reflectivity, the tip was fixed and subsequently the AFM was operated in the sample-stage-scanning mode to address regions or points of interest on the sample. A closed loop capacitive feedback system of the AFM preserved the position of the tip within the laser focus with a precision of 1 nm. Thermal drift was avoided as far as possible by letting the system equilibrate prior to the actual measurements.

#### 3.1.5.4 Spectrometer calibration

Each day before starting the experiments a Raman spectrum of BSB (Bis-2-methylstyryl-1,4-benzene) has been recorded to check the instrument performance. The Raman spectrum of this substance together with its molecular structure is shown in figure 3.7.

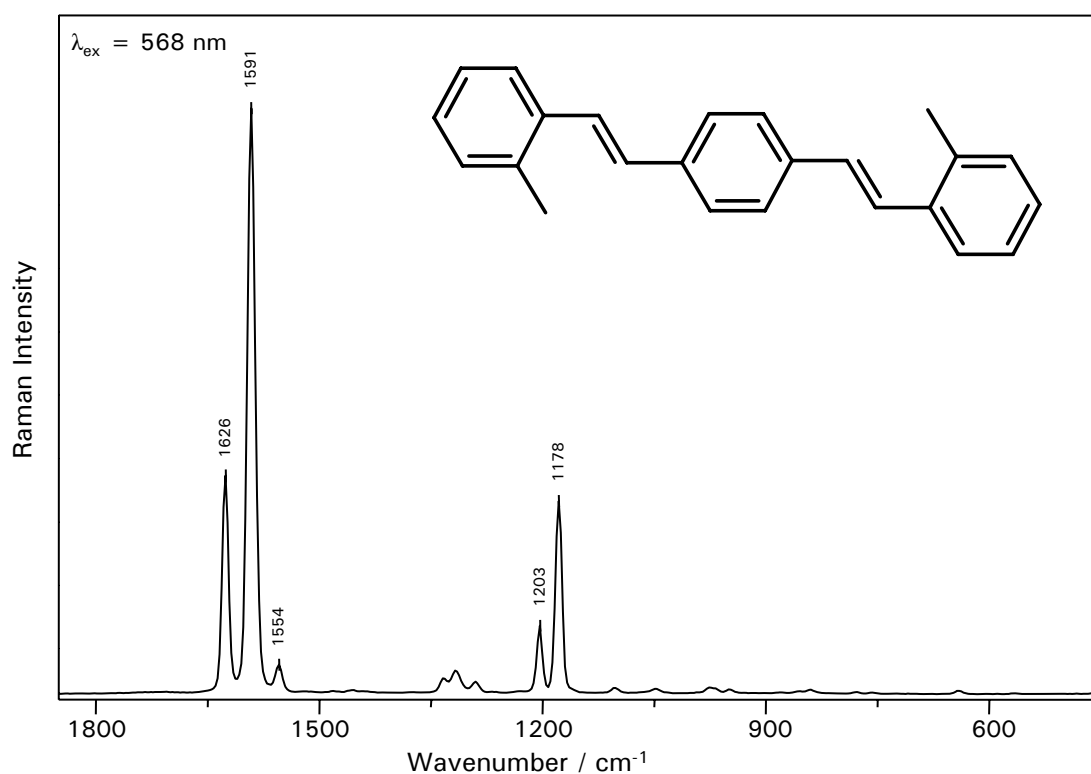


**Figure 3.7:** Raman spectrum of BSB (Bis-2-methylstyryl-1,4-benzene).

### 3.1.5.5 Sample preparation

As a sample organism the Gram-positive bacteria *Staphylococcus epidermidis* ATCC 35984 have been investigated. The cells were grown on casein-peptone-soy meal-peptone (CASO, Merck) agar plates at 37°C. After three days one colony of bacteria was suspended in 1 ml of pure water and 10  $\mu\text{l}$  of that dilute suspension were placed onto a clean glass plate. The glass plate was dried in light vacuum for 10 minutes to give well separated individual cells, being used for the TERS experiments.

As the bacterial cell wall is composed of peptidoglycan and surrounded by PIA (polysaccharide intercellular adhesin) and teichoic acids, which all contain N-acetylglucosamine as a building block, TERS spectra of N-acetylglucosamine were recorded for comparison. For this purpose, 4  $\mu\text{l}$  of a concentrated aqueous solution of N-acetylglucosamine were placed onto a clean glass plate and dried to provide a homogeneous film.

## 3.2 Biological samples

### 3.2.1 Bacteria

Within this work the following bacterial strains have been investigated by micro-Raman, UV-resonance Raman, and IR absorption spectroscopy. The location in brackets assigns the origin of the bacteria.

<i>Bacillus pumilus</i> DSM 27	(DSMZ, Braunschweig)
<i>Bacillus pumilus</i> DSM 361	(DSMZ, Braunschweig)
<i>Bacillus subtilis</i> DSM 10	(DSMZ, Braunschweig)
<i>Bacillus subtilis</i> DSM 347	(DSMZ, Braunschweig)
<i>Escherichia coli</i> DSM 423	(DSMZ, Braunschweig)
<i>Staphylococcus epidermidis</i> RP62A (ATCC 35984)	(Universität Würzburg)

For *S. epidermidis* RP62A (ATCC 35984) additionally tip-enhanced Raman spectra have been recorded.

*Bacillus pumilus* and *Bacillus subtilis* were grown in batch culture in liquid media (nutrient broth, Merck) at 30°C with shaking or on agar plates of the same media at 30°C in the incubator.

*Escherichia coli* DSM 423 was also grown in nutrient broth (Merck) or on nutrient agar at a temperature of 37°C.

*Staphylococcus epidermidis* require for optimal growth 37°C. They were cultivated in liquid media in casein-peptone - soy meal-peptone (CASO, Merck) broth with shaking or on agar plates in the incubator.

The bacterial growth in a batch culture in liquid media was monitored by measuring the absorption at 630 nm which is directly related to the amount of biomass.

#### 3.2.1.1 Sample preparation for the vibrational spectroscopic investigations

The cells were harvested from liquid culture by centrifugation. In order to remove the medium the cells were washed two or three times with water. The centrifugate was resuspended in water and a droplet of that bacterial suspension was given onto the support to dry and give a homogenous film. The substrates were CaF<sub>2</sub>, fused silica or KRS-5 plates for the micro-Raman, the UV-resonance Raman or the IR absorption experiments, respectively. For the single cell micro-Raman analysis and the TERS measurements a highly diluted suspension was dried on a CaF<sub>2</sub> or a glass plate to give well separated individual cells.

When using cultures grown on agar plates the cells were harvested with a dilution loop and directly smeared on the support. For single cell analysis a diluted bacterial suspension was prepared as well.

CaF<sub>2</sub> was found to be an ideal substrate for the Raman spectroscopic investigations because it gives no background signal, has a single Raman band at 322 cm<sup>-1</sup> [71] and therefore, does not interfere with the bacterial Raman bands.



**Figure 3.8:** Antibiotic susceptibility test of norfloxacin against *B. pumilus* DSM 361.

### 3.2.1.2 Antibiotics susceptibility tests

The minimal inhibition concentration (MIC) of various drugs for different bacteria was determined in drug dilution series. Therefore, bacteria have been incubated for 4 hours after inoculation with an overnight-culture (1:100). The culture (being in the exponential growth phase) was diluted to McFarland-Standard 0.5 and further diluted (1:200) to result in suspensions with about  $10^5 - 10^6$  cells/ml [1]. One milliliter of this bacterial suspension was added to one milliliter of different concentrated antibiotic solutions in the broth, prepared in a dilution series. The concentration range of the drug was between 0.1 and 200  $\mu\text{g/ml}$  for norfloxacin, ciprofloxacin and vancomycin. For the highly active new drug moxifloxacin the dilution series covered concentrations between 30 and 0.0001  $\mu\text{g/ml}$ . The individual test-tubes are incubated for 18 hours at the ideal growth temperature of the bacterial strain (30°C for *Bacillus pumilus*, and 37°C for *Staphylococcus epidermidis* and *Escherichia coli*). The minimal inhibition concentration (MIC) denotes the lowest antibiotic concentration at which no bacterial growth is observed. Figure 3.8 shows such a dilution series for norfloxacin against *B. pumilus* DSM361. In tube number 1 the reference solution without any drug is found, tube number 2 contains the highest drug concentration of 200  $\mu\text{g/ml}$ . Tube number 6 containing 12  $\mu\text{g/ml}$  is the lowest drug concentration at which the bacterial growth is completely inhibited. Therefore the MIC for norfloxacin on *B. pumilus* DSM361 is less than 12  $\mu\text{g/ml}$ .

### 3 Material and Methods

#### 3.2.1.3 Bacterial growth curves

In order to characterize the bacterial growth, growth curves have been recorded for *B. pumilus* and *S. epidermidis*. The bacteria were grown in batch culture in liquid media. At different growth times aliquots of the bacterial suspension were taken and the biomass density was determined by measuring the absorption at 630 nm.

To record the micro-Raman, UV-resonance Raman and IR absorption spectra, the cells were washed twice with water to remove the last traces of the medium, and transferred onto a CaF<sub>2</sub>, fused silica or KRS-5 plate to form a homogeneous bacterial film, as described above (section 3.2.1.1).

#### 3.2.1.4 Characterizing bacterial growth under the influence of antibiotics

The bacteria were grown in a batch culture in liquid media as described for the recording of the growth curves (section 3.2.1.3). At different times after the inoculation different concentrations of antibiotics were added to the bacterial suspension. During the growth process aliquots were taken from the suspensions and the cell mass was determined by turbidity measurements. Within the used interval the optical density at 630 nm is proportional to the cell mass present in the suspension. The further proceeding is identical to the one described above.

The largest effect on the growth of the bacterial culture was observed when the drug was added to the culture during the exponential growth phase. During this growth phase the cells were found to be most susceptible to changes in their environment. Therefore, most of the experiments were performed by adding different drug concentrations to the bacterial culture at the beginning of the exponential growth phase (1 to 4 hours after inoculation) and only those experiments will be discussed in chapter 9.

### 3.2.2 DNA

DNA is one of the major targets of the fluoroquinolone drugs. In order to study the interactions *in vitro* bacterial plasmid DNA has been extracted from *E. coli*, as well as amplified from precursors by polymerase chain reaction (PCR). Additionally, DNA and synthetic nucleotides with different composition were commercially obtained to study the effect of the primary DNA structure (sequence and composition) on the vibrational spectra.

#### 3.2.2.1 DNA-Extraction from *E. coli*: plasmid DNA pBR322

The plasmid pBR322 was chosen as a major study object because it has a length of 4361 base pairs which is still small enough to separate in an electrophoretic gel the different topoisomers (relaxed, superhelical and open circle), but also large enough to provide a large enough working surface for the enzyme gyrase.

The plasmid pBR322 was isolated from with pBR322 DNA transformed *E. coli* K12, JM109, following a modified method of the alkaline/SDS lysis by Birnboim and Doly [33] and using the Nucleobond AX Set from Macherey-Nagel. A detailed description of the used buffers and chemicals is given in the appendix in section A.4.1. *E. coli* cells were grown at 37°C in 2 liters of LB medium containing 100 µg/ml ampicillin. The cells were harvested from an overnight culture by centrifugation (7500 rfc, 10 min, Sorvall Evolutin RC superspeed centrifuge, rotor SLC1500) and resuspended in 24 ml of a RNase containing Tris/HCl - EDTA solution. Cell lysis was initiated by adding 24 ml of the lysis buffer which contained NaOH and SDS (Nucleobond AX Set, Macherey-Nagel, incubation time 5 min, not longer!). From the slimy solution the chromosomal DNA was precipitated by adding 24 ml of a KAc containing neutralization buffer (Nucleobond AX Set, Macherey-Nagel) and removed together with the other bacterial debris by centrifugation (>12000 rfc, 4°C, 40 min, rotorSS34, Sorvall centrifuge). The clear, slightly yellow supernatant was purified by column chromatography using an equilibrated column from the Nucleobond AX Set (Macherey-Nagel) and two washing steps. From the 15 ml elute the plasmid DNA was precipitated with 11 ml of isopropanol. After centrifugation (>15000 rfc, 4°C, 30 min, rotor SS34, Sorval centrifuge) the DNA pellet was washed twice with ethanol to remove excess salt, dried and resuspended in pure water to give a DNA solution of 1.1 mg pBR322/ml.

**Relaxation of the supercoiled DNA** Half of the isolated (supercoiled) DNA was converted into the relaxed form using topoisomerase I from calf thymus, incubating for 90 minutes at 37°C .

The reaction mixture (500 µl) contained:

100 µl TNE II 5x

50 µl pBR322

100 µl topoisomerase I (purified from calf thymus by FPLC [44, 249])

250 µl bidistilled H<sub>2</sub>O.

**Purification of DNA: Phenolization and precipitation** Both pBR322 solutions, the relaxed and the supercoiled form, were purified from remaining proteins by phenol/chloroform/isoamyl alcohol extraction. Therefore, 1 volume share phenol/chloroform (Roth) were added, the solution was vortexed and 2-3 minutes centrifuged. The upper aqueous phase was transferred to a new tube and the process repeated until no protein precipitated at the interphase anymore. The remaining dissolved phenol in the aqueous solution was removed by washing with chloroform/isoamylalcohol (1 volume element, Roth). The plasmid was precipitated in the cold (-20°C) with 0.1 volume share of 3 M sodium acetate and 2 volume shares of absolute ethanol. The pellet was washed with 70% ethanol to remove excess salt and resuspended in pure water to give DNA solutions of 1.5 mg pBR322/ml which were used for the UV-resonance Raman experiments.

**Determination of the concentration** The DNA concentration was determined by UV absorbance measurements using an extinction coefficient of 20 L · g<sup>-1</sup> · cm<sup>-1</sup> at 260 nm with a BioPhotome-

### 3 Material and Methods

ter (Eppendorf). The ratio of the absorbance between 260 and 280 nm was determined to be 1.8 for the relaxed and the supercoiled form. Values between 1.8 and 2.0 were manifested for pure DNA [160], ensuring high optical and biological purity of the extracted DNA.

**Gel electrophoresis** The purity and the success of the relaxation of the plasmid DNA were assessed by agarose gel electrophoresis. The horizontal agarose gel was prepared by dissolving 0.4 g agarose in TAE buffer (Beutenberg recipe) to give 40 ml solution. A mixture of 1  $\mu$ l plasmid DNA, 14  $\mu$ l distilled H<sub>2</sub>O and 2  $\mu$ l glycerin-bromine phenolblue were loaded onto the 1% gel. The gel was run in TAE-buffer at room temperature for 8 hours applying a voltage of 20 V. After being stained with ethidium bromide the gel was illuminated with ultraviolet radiation and photographed as shown in figure 7.12 in section 7.5.1. Clearly the two different topoisomers are separated: the fast migrating supercoiled DNA in the left lane (S) and the slower migrating relaxed form in the right lane (R) of figure 7.12.

**Lyophilization of DNA** In order to keep the DNA over a longer time span and to transform it into a state of highest concentration, the DNA solutions were lyophilized. The white solid was used to record micro-Raman and IR absorption spectra.

#### 3.2.2.2 DNA synthesis by polymerase chain reaction (PCR)

DNA synthesis by polymerase chain reaction (PCR) was performed at the Institut für medizinische Mikrobiologie (Simmelweisstrasse 4, Jena) to obtain two DNA sequences of similar size but with a different GC content. For 4 samples 50  $\mu$ l of a master mix and 5  $\mu$ l template were used.

The reaction mixture consisted of:

- 108  $\mu$ l distilled water
- 20  $\mu$ l buffer
- 20  $\mu$ l MgCl<sub>2</sub>
- 20  $\mu$ l dNTP mix
- 4  $\mu$ l primer (forward, U1)
- 4  $\mu$ l primer (backwards, U2a)
- 4  $\mu$ l Taq polymerase
- 2  $\mu$ l of the DNA fragment (CPG or ATOX).

The PCR was run in 30 cycles following the temperature program listed in Table 3.1.

To check for a successful PCR the DNA fragments (PCR products) were run in a 2% agarose gel (4 g agarose in 200 ml H<sub>2</sub>O) for 50 minutes applying a voltage of 100 V and with a current of 250 mA.

The purification of the PCR products was performed by phenol/chloroform extraction as described above.



**Table 3.1:** Temperature program for the PCR of the DNA segments ATOX and CPG, the program between the two horizontal lines was repeated for 30 cycles.

ATOX		CPG	
temperature in °C	time in minutes	temperature in °C	time in minutes
95	3	95	5
95	30	95	30
50	30	60	30
72	90	72	90
4	7	72	10
4	∞	4	∞

### 3.2.3 Gyrase

The bacterial enzyme gyrase introduces negative supercoils into the DNA. This is a vital process for the bacteria and therefore, the gyrase-DNA-complex is an ideal target for antibiotics such as the fluoroquinolones. In order to move a step towards an understanding of those drug-target-interactions the enzyme has been extracted from *Escherichia coli* and characterized by means of vibrational spectroscopy.

#### 3.2.3.1 Extraction of gyrase from *E.coli*

*E. coli* DSM 436 were grown from a starting culture over night in liquid LB media at 37°C while shaking. The cells were harvested and separated from the medium by centrifugation (10 min, 7000 rpm, rotor SLC1500, Sorvall centrifuge). From about 8 L of media roughly 30-40 g of bacteria were obtained. In order to facilitate subsequent cell lysis the cells were kept in the freezer for at least 4 hours.

For lysis the frozen *E.coli* cells were resuspended in a minimal amount of lysis buffer (ca. 50-60 ml). After adding lysozyme (150 mg in 15 ml of lysis buffer) the cells were incubated for 1 hour at 4°C. The lysate was centrifuged over night at 4°C with >1800 rpm. The supernating protein solution was loaded onto a HiTrap-Heparin column and washed with distilled water until the filtrate was free from protein as was assured by testing with Bradford's reagent. Subsequent, unspecific bound proteins were removed from the column with 0.05 M KCl solution, again until no reaction with Bradford's reagent was observed anymore. Both gyrase subunits GyrA and GyrB were eluted with a 0.45 M KCl solution. The column was cleaned from remaining protein by purging with concentrated (>1 M) KCl, followed by distilled water and finally rinsed with 20% ethanol before keeping in the fridge.

**Gel electrophoreses** To separate the protein and check for the right molecular weight an SDS polyacrylamide gel electrophoresis (PAGE) was run with the gyrase extract. The preparation details for the gel are described in the appendix (section A.5).

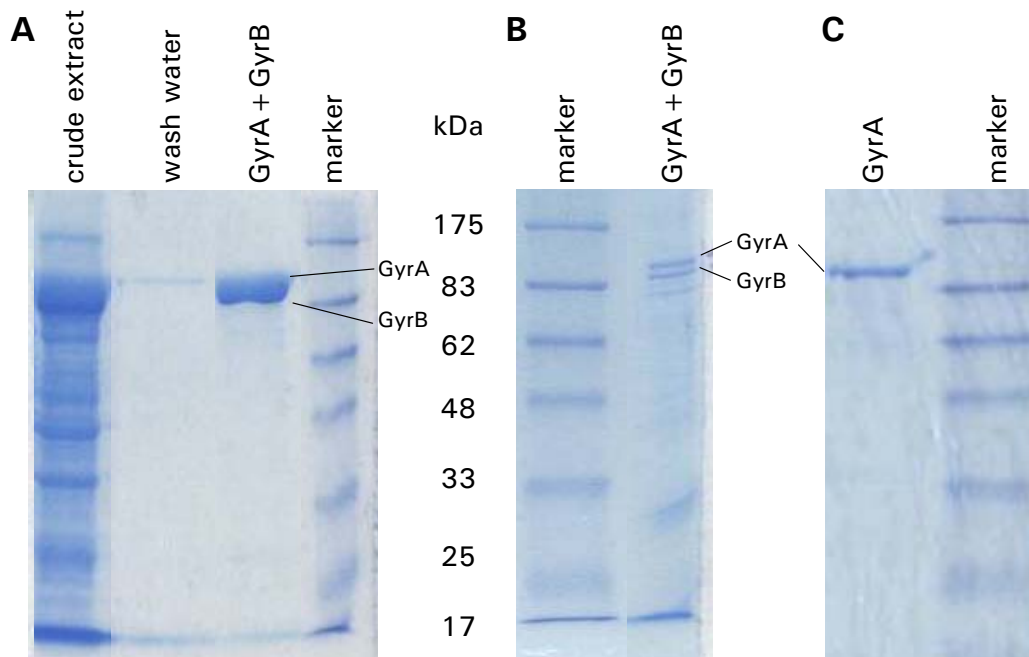


**Figure 3.9:** Coomassie-blue stained poly(acrylamide) gels of extracted gyrase, **A** and **B**) full enzyme with both subunits GyrA and GyrB, **C**) only GyrA subunit. The marker in all three gels contains protein fragments of different sizes denoted between A and B.

The protein was denatured by adding excess sodium dodecyl sulfate (SDS) and heating to 95°C. The anionic SDS compensated the negative charge of the proteins so that the proteins had a constant charge distribution. This solution was loaded on a 10% polyacrylamide gel and run for 1 hour at 130 V and about 40 mA.

Figure 3.9A and B show the polyacrylamide gel of gyrase stained with coomassie blue (slot GyrA+GyrB). The two subunits GyrA and GyrB have a molecular weight of 97 kDa and 90 kDa, and can be found above the protein marker band of 83 kDa. In figure 3.9A also protein crude extract (first slot) and the protein-free wash water were loaded on the gel for comparison. The protein loading of gyrase is quite high and therefore no clear separation between the two subunits GyrA and GyrB is achieved as is the case in figure 3.9B.

**Separation of the subunits GyrA and GyrB** For a further purification of the gyrase crude extract the gyrase solution was filtered over a coupled novobiocin-sepharose column which was equilibrated with KCl. Unspecifically bound proteins were washed away with 0.05 M KCl buffer followed by ATP buffer (0.1102 g ATP, 0.0536 g Mg-acetat, 149 g KCl dissolved in 10 ml). The GyrA subunit of the enzyme was eluted with 0.8M KCl solution, the GyrB subunit with urea in

buffer B (see appendix section A.4). To concentrate the protein and to remove excess urea the protein solutions were dialyzed against KCl.

### 3.2.3.2 Extraction of the gyrase subunit GyrA from amplified *E. coli*

The 97 kDa GyrA subunit of gyrase was also extracted from *E. coli* M15. This bacterial strain overproduces the 6xHis-tagged protein (His)<sub>6</sub>GyrA. These additional six histidine moieties at the N- or C-terminal end of the protein do not interfere with the structure or function of the protein, but can act as a label during the extraction procedure. The 6-His tag specifically binds with high efficiency to Ni<sup>2+</sup>-NTA agarose which is used for affinity chromatography in the purification step. The protein which is immobilized on the matrix can be washed easily and then recovered with a high homogeneity by elution with imidazol.

The gene for (His)<sub>6</sub>GyrA was generated from the original GyrA gen by in-frame insertion of six histidine codons in the 5' block of the encoding region. It is inducible under the control of the T5 promoter and by two *lac* operator sequences. The gene for (His)<sub>6</sub>GyrA sits together with an ampicillin resistance gene on the plasmids pQE30/GyrAliv and pQE30/GyrAnou, respectively. Furthermore the *E. coli* strain M15 holds the plasmid pREP4 which carries a kanamycin resistance gene and is responsible for the constructive overproduction of the *lac* repressor protein.

The bacterial cells of *E. coli* M15 were grown in LB media with 70 µg/ml ampicillin and 25 µg/ml kanamycin from an overnight culture at 37°C while shaking. When the cells were in the exponential growth phase (after about 30 minutes) the induction of the gene for (His)<sub>6</sub>GyrA was carried out by adding IPTG (isopropyl-β-D-thiogalactopyranoside) solution. After 60 minutes of further growth the cells were harvested by centrifugation as described above. The pellet was resuspended in a native lysis buffer (see appendix section A.4 for composition) and gently stirred for 30 minutes. The suspension was put in an ice bath and treated with ultrasound (200-300 W) for 2-3 minutes in 10 s intervals. The cell debris was separated from the cleared lysate by centrifugation (10 minutes with 12000-15000 rpm). To this cleared lysate the 50% Ni-NTA agarose was added. The solution was stirred gently for 30 minutes on ice so that the coupling between the (His)<sub>6</sub>-protein and the agarose matrix could occur. The mixture was loaded into a column and washed with the washing buffer until the filtrate was free of protein (test with Bradford reagent). The protein was eluted in 0.2 ml portions of the elution buffer. An SDS-PAGE was run to confirm the right molecular weight of the protein.

To be able to record resonance Raman spectra of the protein, the imidazol has to be removed from the solution by dialysis against KCl. As an additional advantage dialysis achieves also a concentrating of the protein solution.

**Lyophilization of gyrase** In order to keep the enzyme over a longer time span and to transform it into a state of highest concentration, the dialyzed GyrA solutions were lyophilized. The white solid (fluffy powder) was used to record micro-Raman and IR absorption spectra. However,

### 3 Material and Methods

lyophilization should be used with care when the gyrase should be kept in a biological active state (see section 8.4).

#### 3.2.4 Antibiotics

The fluoroquinolones were purchased from Sigma and Aldrich, or were kind gifts of the group of Prof. Dr. Ulrike Holzgrabe from the University of Würzburg (see appendix section A.1). The hydrated compounds were prepared by mixing the anhydrous fluoroquinolones (FQ) with water in a ratio of FQ:6H<sub>2</sub>O. Figure 6.1 in chapter 6 shows the chemical structure of the investigated quinolones and figure 6.2 the chemical structures of the investigated precursors.

### 3.3 Data treatment

If necessary, the vibrational wavenumbers of the individual spectra have been corrected against vibrational wavenumbers of the standard (TiO<sub>2</sub> for micro-Raman, teflon for UV-resonance Raman spectra and BSB for TERS).

For the multivariate statistical data analysis the individual spectra have to be comparable, i.e. irrelevant, random or systematic variations such as fluctuating laser power, noise, fluorescence background etc. should ideally be removed prior to subjecting to statistical evaluation. Spectra with spikes in the relevant spectral region have been omitted from analysis. A constant value was subtracted from the spectra, so that the Raman intensity of the baseline level is zero.

Normalization was applied in order to remove systematic intensity variations as can be caused by different laser powers on different days, by slightly changed focus adjustments or by a variable thickness of the sample. In order to perform a vector normalization the spectrum was centered around the abscissa, which is done by subtracting the mean intensity value of the whole spectrum from each individual intensity value. Afterwards, the length of the data vector of the spectrum is normalized to one by dividing all  $k$  points of the centered spectrum with the intensities  $I_z$  by the length of the data vector (the square root of the sum of all squared intensity values):

$$I_{norm} = \frac{I_z}{\sqrt{\sum_k I_z^2}} \quad . \quad (3.2)$$

#### Curve fitting

For the determination of the ratio of the nucleic acid and protein content in section 4.3, the Raman spectra were baseline corrected in the spectral region from 1800 to 1400 cm<sup>-1</sup>. To fit the resonance Raman spectra of *Bacillus pumilus* in this region six Voigt profiles, centred at 1650, 1634, 1607, 1570, 1523, and 1480 cm<sup>-1</sup> were used. The area of the bands at 1480 cm<sup>-1</sup> and 1607 cm<sup>-1</sup> were used to calculate the nucleic acid/protein ratio.

Also for *S. epidermidis* the intensity ratios of the nucleic acid (1475 cm<sup>-1</sup>) content vs. the protein (1609 cm<sup>-1</sup>) content for different growth times was calculated from the resonance Raman

spectra using the LabSpec software package. The experimental resonance Raman spectra of *S. epidermidis* were fitted in the spectral region between 1850 and 1250  $\text{cm}^{-1}$  with seven Lorentzian profiles centered at 1651, 1609, 1564, 1521, 1475, 1370 and 1316  $\text{cm}^{-1}$ . The number of bands is in agreement with the number of zero points in the first derivative of the spectra and also with the vibrational bands assigned in the spectrum (see figure 4.3 (lowest spectrum) and table 4.2 in section 4.1). The two bands at 1370 and 1316  $\text{cm}^{-1}$  do not reproduce the experimental data perfectly. However, this does not affect the quality of the fit of the Raman bands at 1475, 1521 and 1609  $\text{cm}^{-1}$ .

Furthermore, the area under the curve of the Raman bands at 1521 and 1475  $\text{cm}^{-1}$  was used to estimate the GC-content (in combination with the relation given by Nelson, Manoharan and Sperry in Reference [177]).

### 3.4 Statistical data analysis

#### 3.4.1 Hierarchical cluster analysis

The bacterial spectra from the growth experiments (section 4.3) and from the experiments with the fluoroquinolones (chapter 9) were evaluated with the OPUS software package (Bruker Optik GmbH). If necessary, the first derivatives of the individual spectra was calculated to remove the influence of baseline drifts on the classification and to reveal slight differences otherwise masked in broad bands (especially for the IR spectra) [51]. In order to determine whether it is possible to extract growth specific information from the spectra hierarchical cluster analysis (HCA) was performed. The spectral distances were calculated by the standard method (IR and micro-Raman spectra) or by the factorization method (resonance Raman spectra), and the clusters were prepared following Ward's technique. For the IR spectra the wavenumber region 500-1900  $\text{cm}^{-1}$  was used, while for the analysis of the micro-Raman spectra the wavenumber regions 600-1800  $\text{cm}^{-1}$  and 2740-3130  $\text{cm}^{-1}$  were applied. The UV-resonance Raman spectra were evaluated within the wavenumber region 500-1850  $\text{cm}^{-1}$ .

#### 3.4.2 Principal component analysis

Principal component analysis (PCA) was performed with the program "The Unscrambler" (CAMO Process AS, Version 9.2) using centered spectra and complete cross validation for the same spectral range as used for the hierarchical cluster analysis. From the loadings of the principal components the wavenumbers having the highest variance can be identified.

#### 3.4.3 Between-group variance (B) and the within-group variance (W)

The wavenumbers having the most discriminative power can be determined by calculating the ratio of the between-group variance (B) and the within-group variance (W) for each single wavenumber

### 3 Material and Methods

[282]. This ratio is referred to as B/W-ratio. The wavenumbers corresponding to the largest B/W-ratio are mainly responsible for separating the clusters. For calculating the B/W-ratio the background was removed by computing the first derivative of the spectra (Savitzky-Golay, 2<sup>nd</sup> order polynomial, 21 points). This statistical method was applied to the UV-resonance Raman spectra of *B. pumilus* under the influence of ciprofloxacin (section 9.3).

#### 3.4.4 Reverse elimination tabu search (REM-TS)

Wavenumbers with high importance for the discrimination of the spectra can be found with the help of a data-driven variable selection procedure (each wavenumber represents an independent variable in the classification problem). The reverse elimination tabu search (REM-TS) was used to search for highly discriminatory variables [20] within the vibrational spectra of different aged bacteria (section 4.3) and bacteria under the influence of different drug concentrations (chapter 9). REM-TS was coupled to Fisher's discriminant analysis which was used to classify the data based on the tentatively selected variable subsets generated by REM-TS. At each stage of the search one variable is either added to the model or removed from the model according to the largest decrease in the classification error. If only non-improving moves are possible, the mildest detrimental move is accepted. In order to avoid that one and the same solution is visited more than once, the method records recent moves in a tabu list. Hence, moves that lead to a previously visited solution are forbidden and cannot be executed again. The only user defined parameter for REM-TS is a termination criterion. For this study it was specified that the search was terminated when either six variables were included in the model or when the classification error could not be decreased by more than 3% in two consecutive iterations. The classification error was assessed by leave-multiple-out cross-validation (LMO-CV) as objective function. In particular, the training data set was divided into a construction set (75 %) and a validation set (25%) where the construction set is used to build the model while the validation set is used to assess this model. The average classification error for 50 splits into construction set and test set is then used to assess the internal predictivity of each variable subset generated during the search. It is this internal predictivity that REM-TS optimizes. The number of variables was restricted and the early stopping rule (stop if decrease is smaller than 3%) was applied to LMO-CV in order to avoid overfitting and to keep the external predictivity (test set predictivity) high [19]. To evaluate the model externally the entire data set was split into a training set (67%) and a test set (33%). This second split, which is done before REM-TS operates on the training set, is carried out to allow an external assessment (i.e. a test set prediction) of the classification performance that is independent of the model selection step by REM-TS. The split into a different training set and test set is also 100 times to obtain a stringent assessment of the external predictivity. The actual test set predictivity was computed such as in bagging [40, 279], i.e. the class assignment for a particular spectrum is based on the major vote of all models where this spectrum was part of the test set (i.e. on average 33 models because each spectrum has 33% probability to end up in the test set). Major voting has commonly the effect

of improving test set predictivity [64]. The occurrence of every variable in the 100 best variable subsets was calculated to assess the relevance of the wavenumbers and consequently changes of cellular components depending on interactions with different moxifloxacin concentrations. Baseline subtraction was done prior to variable selection by fitting a straight line to the baseline of the spectra using half-quadratic minimization [157]. This method automatically identifies the relevant baseline regions for the fit and ignores peak areas. Intercept and slope were then used to subtract the estimated linear background from the spectra. An alternative to background correction by robust curve-fitting could be using the first derivative of the spectrum instead of the raw data. However, variable selection with the first derivative is expected to be disadvantageous, as the spectral peaks are displaced in relation to the raw spectra. Apart from that the peak maxima in the raw data represent the zero crossing in the first derivative which results in a loss of information about the peak intensities. Due to the huge number of possible six variable models (combinatorial explosion), many can lead to equally good solutions. To improve the interpretability of the models, only those regions of wavenumbers that can be assigned to spectral signals of cellular components were considered for the search.

This method was applied for the analysis of the growth phenomena of the bacteria in section 4.3. Based on the band assignment given in table 4.1 the following wavenumber regions have been selected from the IR absorption spectra for the analysis: 1742  $\text{cm}^{-1}$ , 1695-1675  $\text{cm}^{-1}$ , 1654  $\text{cm}^{-1}$ , 1639  $\text{cm}^{-1}$ , 1548  $\text{cm}^{-1}$ , 1452  $\text{cm}^{-1}$ , 1396  $\text{cm}^{-1}$ , 1300-1240  $\text{cm}^{-1}$ , 1239  $\text{cm}^{-1}$ , 1085  $\text{cm}^{-1}$  and 720  $\text{cm}^{-1}$ . For the micro-Raman spectra the wavenumber regions around 1660  $\text{cm}^{-1}$ , 1614-1607  $\text{cm}^{-1}$ , 1575  $\text{cm}^{-1}$ , 1450  $\text{cm}^{-1}$ , 1370-1375  $\text{cm}^{-1}$ , 1337  $\text{cm}^{-1}$ , 1314  $\text{cm}^{-1}$ , 1242-1240  $\text{cm}^{-1}$ , 1128  $\text{cm}^{-1}$ , 1092  $\text{cm}^{-1}$ , 1001  $\text{cm}^{-1}$ , 899  $\text{cm}^{-1}$ , 855  $\text{cm}^{-1}$ , 782  $\text{cm}^{-1}$ , 731  $\text{cm}^{-1}$ , 723  $\text{cm}^{-1}$ , 663  $\text{cm}^{-1}$ , 642  $\text{cm}^{-1}$ , 621  $\text{cm}^{-1}$ , have been chosen (for an assignment see also 4.1. For the analysis of the UV-resonance Raman spectra following wavenumbers have been selected based on the assignment given in table 4.2: 1639  $\text{cm}^{-1}$ , 1609  $\text{cm}^{-1}$ , 1567  $\text{cm}^{-1}$ , 1521  $\text{cm}^{-1}$ , 1475  $\text{cm}^{-1}$ , 1359  $\text{cm}^{-1}$ , 1324  $\text{cm}^{-1}$ , 1307  $\text{cm}^{-1}$ , 1229  $\text{cm}^{-1}$ , 1168  $\text{cm}^{-1}$ . Each central wavenumber and approximately ten neighboring wavenumbers were boxaveraged and constitute one spectral region.

The programs for variable selection were written and validated for Matlab™ (The Mathworks, Inc.) by Ulrike Schmid and Knut Baumann.

### 3.4.5 Removing spectral contribution by orthogonalization

For the analysis of vibrational spectra of complexes where both partner in the complex tribute spectral contributions in the wavenumber region of interest the raw data have to be pre-treated to perform a meaningful multivariate data analysis. This involves two steps: First, to obtain consistent spectra across all measurements, the spectra had to be normalized and second, the spectral contributions of the complex partner of lesser interest had to be removed. This was done by orthogonalizing the spectra with respect to the spectrum of the pure partner of lesser interest. The procedure described in the following was applied to the analysis of the DNA intercalation exper-

### 3 Material and Methods

iments with ethidium bromide where the spectral contributions of pure ethidium bromide to the UV-resonance Raman spectra was eliminated. The results are discussed in section 7.6.

The UV-resonance Raman spectra of relaxed, supercoiled, and supercoiled DNA with the addition of different concentrations of ethidium bromide (referred to as matrix  $\mathbf{X}$ ) were row wise scaled to unit vector length. In order to investigate the effect of the intercalating drug ethidium bromide on the DNA topology, spectral contributions of pure ethidium bromide to the spectra of the drug-DNA-complexes have to be eliminated. This is done by orthogonalization of the spectra with respect to the ethidium bromide spectrum. This step was inspired by the first step of the direct orthogonalization method [8], which was developed to remove irrelevant variation from data in calibration experiments. In the following it is described how orthogonalization can be applied to subtract spectral information originating from the pure ethidium bromide spectrum. In the algorithm given below,  $\mathbf{X}$  denotes an  $m$  by  $n$  matrix of measured UV-resonance Raman spectra with  $m$  representing the number of spectra and  $n$  representing the number of wavenumbers. The ethidium bromide spectrum is designated by  $\mathbf{y}$  ( $n \times 1$ ), which is generated by calculating the mean spectrum of replicates of a single ethidium bromide concentration (solution of 0.02% ethidium bromide). In the next step it is necessary to estimate the amount of spectral features within each spectrum in  $\mathbf{X}$  correlating with  $\mathbf{y}$  (i.e. the pure ethidium bromide spectrum). This amount (proportion) of  $\mathbf{y}$  in  $\mathbf{X}$  can then be subtracted from  $\mathbf{X}$  in the final step. This is done as follows: In step 1, the data matrices are column mean centred. In step 2, the vector  $\hat{\mathbf{w}}$  ( $m \times 1$ ) constitutes the properly scaled row wise covariation between  $\mathbf{X}_C$  and  $\mathbf{y}_C$ . The values of  $\mathbf{y}_C$  weighted with the values of  $\hat{\mathbf{w}}$  are then subtracted from the centred raw data. As a result  $\mathbf{X}_{CO}$  is obtained, which is row wise orthogonal to  $\mathbf{y}_C$ . Put differently,  $\mathbf{X}_{CO}$  represents the original data matrix reduced by information correlating with the pure ethidium bromide spectrum  $\mathbf{y}_C$ . It should be noted that even spectra that do not contain any ethidium bromide lead to a non-zero weight because the ethidium bromide spectrum is unlikely to be orthogonal (i.e. completely unrelated) to the spectra under scrutiny.

1.  $\mathbf{X}$  and  $\mathbf{y}$  are column wise centered to give  $\mathbf{X}_C$  and  $\mathbf{y}_C$ .

2.  $\mathbf{X}_C$  is orthogonalized with respect to  $\mathbf{y}_C$

$$\hat{\mathbf{w}} = \mathbf{X}_C \cdot \mathbf{y}_C \cdot (\mathbf{y}_C^T \cdot \mathbf{y}_C)^{-1}$$

$$\mathbf{X}_{CO} = \mathbf{X}_C - \hat{\mathbf{w}} \cdot \mathbf{y}_C^T$$

The orthogonalization was computed in Braunschweig by Knut Baumann and Ulrike Schmid with an in-house written MATLAB (7.1) script.

### 3.5 DFT calculation

Density functional theory (DFT) has been used to calculate the geometries, energies and vibrational spectra (Raman and IR) of the fluoroquinolones, DNA bases, nucleoside and nucleotides as well as of the simple amino acids.

All calculations of harmonic wavenumbers and Raman scattering activities were performed by using a fully optimized geometry as reference geometry. The DFT geometry optimizations were



performed with the program Gaussian 98 [83] using the hybrid functionals B3LYP and B3PW91. Both functionals use Beckes' three parameter exchange functional [21] and while B3LYP uses the Lee-Yang-Parr correlation functional [132], B3PW91 calculates the correlation with the Perdew-Wang 91 gradient corrected correlation functional [193]. The Gaussian type split valence basis sets 6-31G and 6-311G in combination with d polarization functions on heavy atoms (d) and p polarization functions on hydrogen atoms (p) were employed for all atoms for the geometry optimization. In order to describe anions, molecules with lone pairs of electrons and very electronegative atoms accurately diffuse functions were added on heavy atoms (+). The geometry optimization was followed by a normal coordinate analysis at the same level of theory. All calculated wavenumber values are positive, indicating that the optimized structure is indeed a true minimum on the energy hypersurface. The calculated wavenumbers were scaled with a factor of 0.9614 [233, 206] when using the B3PW91 method, otherwise used as obtained.

To be able to construct a calculated spectrum the Raman scattering intensity  $I_{Raman}$  needs to be calculated from the polarization tensor  $\left(\frac{\delta\alpha}{\delta q}\right)^2$  obtained from the frequency calculations taking the  $\nu^4$  dependency into account [263]:

$$I_{Raman,k} = \frac{2\pi^2 h}{c} \frac{(\tilde{\nu}_0 - \tilde{\nu})^4}{\tilde{\nu}[1 - \exp(-hc\tilde{\nu}/kT)]} \left(\frac{\delta\alpha}{\delta q_k}\right)^2, \quad (3.3)$$

with  $h$  being Planck's constant,  $c$  the speed of light,  $\tilde{\nu}_0$  the excitation wavenumber,  $\tilde{\nu}$  the wavenumber of the vibration of interest,  $k$  Boltzmann's constant and  $T$  the temperature.

To simulate the spectra the calculated lines were convoluted with a 1:1 Gaussian-Lorentzian-profile with fixed line width of  $10 \text{ cm}^{-1}$  at half maximum.

In order to use the DFT calculation of the vibrational modes for a detailed band assignment a potential energy distributions (PED) analysis was performed using the program gar2ped [153]. The PED gives the percentage of potential energy localized in a particular bond for a given mode.



## 4 Bacteria

Bacteria are the cause of many infectious diseases and medical problems. Increasing resistances of many bacterial strains against common drugs raise the steady demand for new and powerful antibiotics. For a target-oriented design of new and effective drugs the metabolic pathways within the bacterial organisms need to be understood on a molecular level. Furthermore, bacteria play an important role in the clean room production, but also in the pharmaceutical and food industry. Since many biotechnological production processes depend on an optimized functioning of the used biocatalysts which are living microorganisms [229], a detailed understanding of the bacterial metabolism is of greatest interest.

To gain a better insight into the metabolism of the bacteria and to learn more about the action of antibiotics special non-destructive, highly sensitive characterization methods are needed. During the last years vibrational spectroscopic techniques have been proven to have a high potential for the study of biological problems [152, 175, 243]. It is, for example, possible to rapidly discriminate and identify microorganism at the genus, species and strain level by different spectroscopic methods such as Fourier-transformed infrared (FT-IR) spectroscopy [173, 174], and micro-Raman spectroscopy with excitation in the visible [218], near-infrared [104, 151] and ultraviolet [145, 280], as well as by special Raman techniques, like surface enhanced Raman spectroscopy (SERS) [66, 107, 106]. The vibrational spectra of the microorganisms consist of signal contributions of all components present in the cell and therefore reflect their overall molecular composition and provide information on the environment in which these molecules are found within the cell and therefore on their molecular interactions [51, 146]. While FT-IR and Raman spectroscopy with excitation in the visible and infrared result in spectra with contributions from all components, excitation with UV light introduces a selective enhancement of the Raman bands of the UV-absorbing molecules due to the resonance Raman effect. This enhancement might increase the Raman band intensity of those chromophores by a factor of  $10^3$ - $10^5$  [145], which allows the detection of molecules that occur only at low concentrations. When applying 244 nm as excitation wavelength especially the spectral features of the aromatic amino acids, as well as of the DNA/RNA bases are enhanced [57]. Furthermore, fluorescence is usually energetically far enough away from the wavelength region where the Raman signal is recorded. This enables the specific focussing of changes in the chemical composition within bacteria due to metabolic pathways (synthesis of proteins, translation of DNA) as well as changes in the micro-environment of the DNA and the enzymes that occur upon drug binding within the bacterial cell. In this chapter, the bacterial growth in undisturbed bacterial batch cultures is investigated by means of different vibrational

spectroscopic techniques (IR absorption, micro-Raman and UV-resonance Raman spectroscopy). The observed subtle spectral changes are interpreted by means of statistical methods. As an example, such a comprehensive vibrational spectroscopic characterization is shown for *Staphylococcus epidermidis* in this chapter. Additionally, *Bacillus pumilus* and its bacterial growth is characterized by means of UV-resonance Raman spectroscopy. The results from this chapter will be used later in chapter 9 when interpreting the vibrational changes occurring in bacteria upon drug addition.

### 4.1 Vibrational spectroscopic characterization

In classical microbiology morphological parameters are used for a first differentiation between microorganisms. Those parameters include size, shape, color of the bacteria as well as of the colonies.

More detailed information about the chemical composition for a deeper understanding and a profound characterization of the bacteria is gained in a non-invasive manner by vibrational spectroscopy. In the following, a detailed vibrational band assignment is given exemplarily for two different bacterial strains which enables in the second part of the discussion the correlation of observed wavenumber changes with growth time with the metabolic changes within the bacteria (section 4.3).

#### 4.1.1 *Staphylococcus epidermidis*

*Staphylococcus epidermidis* is a common constituent of healthy human skin and mucosal surfaces with a low pathogenic potential. However, in recent decades the species emerged also as a leading cause of medical-device associated nosocomial infections in immuno-compromised patients and got into the focus of research interest [36]. The establishment of *S. epidermidis* as an opportunistic pathogen is due to the ability of certain strains to form multilayered bacterial biofilms on inert surfaces of medical devices (figure 4.1). These biofilms consist of staphylococcal cells embedded into an extracellular matrix containing mainly a polysaccharide intercellular adhesin (PIA), teichoic acids and cell surface-associated proteins. The extracellular matrix of biofilm-growing cells acts thereby as a glue that mediates both cell-cell contacts between bacteria and adherence to polymer and metal surfaces. Moreover, organization of staphylococci in a biofilm causes enhanced resistance against host defenses and antibiotic treatment and represents an advantage in coping with unfavourable external conditions [220]. The exact molecular details and the conditions of biofilm formation and therefore the bacterial pathogenesis are so far not completely understood [221]. It is in the focus of research interest to acquire a detailed knowledge of the bacterial composition and metabolic characteristics in order to comprehend the mechanisms of bacterial pathogenesis and in order to find better ways for treatment and vaccination.

In the following *Staphylococcus epidermidis* ATCC 35984 is comprehensively characterized. It starts with a brief phenotypic description of the *S. epidermidis* cells and merges to an overall vi-

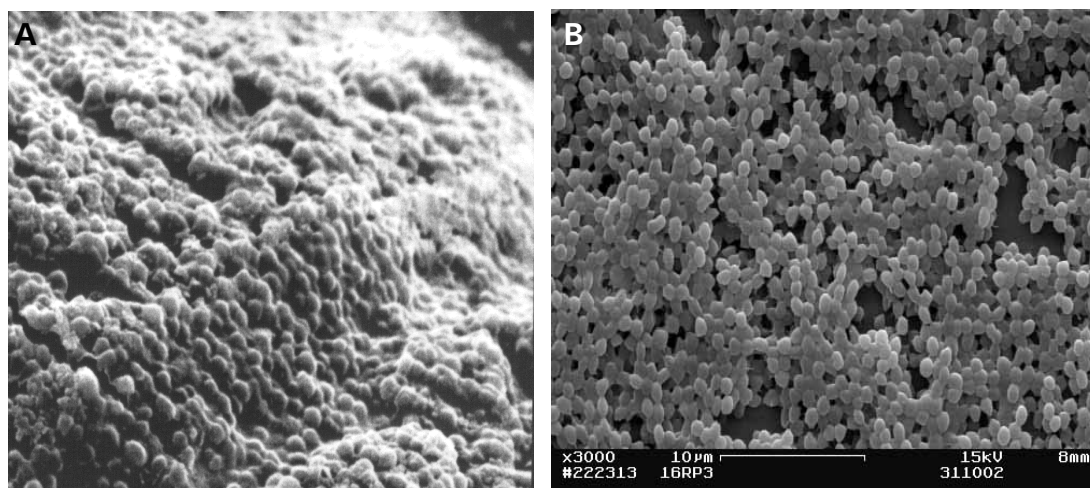


**Figure 4.1:** **A)** Teflon catheter overgrown with a biofilm of *S. epidermidis*, **B)** Scanning electron microscope (SEM) image of the architecture of the biofilm of *S. epidermidis* ATCC 35984 (images taken at the Institut für Infektionsbiologie, Universität Würzburg).

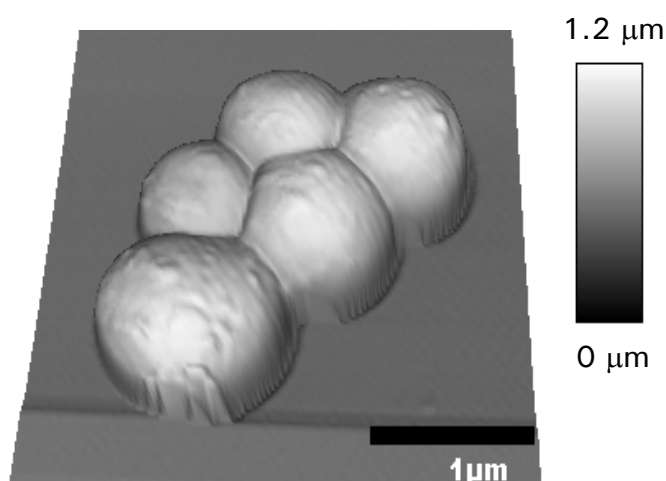


**Figure 4.2:** Pseudo 3D topographic AFM image of a cluster of single *S. epidermidis* cells on a glass surface.

brational spectroscopic characterization of the chemical composition of bacterial bulk material by IR absorption spectroscopy. Less biological material down to a single cell is needed for recording overall chemical information by means of micro-Raman spectroscopy. With UV-resonance Raman spectroscopy the focus is set on selected cell components such as nucleic acid. A vibrational spectroscopic investigation of the growth dependent metabolic changes is presented in the next section (4.3) by means of IR absorption, micro-Raman and UVRR spectroscopy.

*S. epidermidis* are Gram-positive nonsporulating spherical cells of about one micrometer diameter occurring singly, in pairs, short chains and in irregular clusters that are arranged like bunches

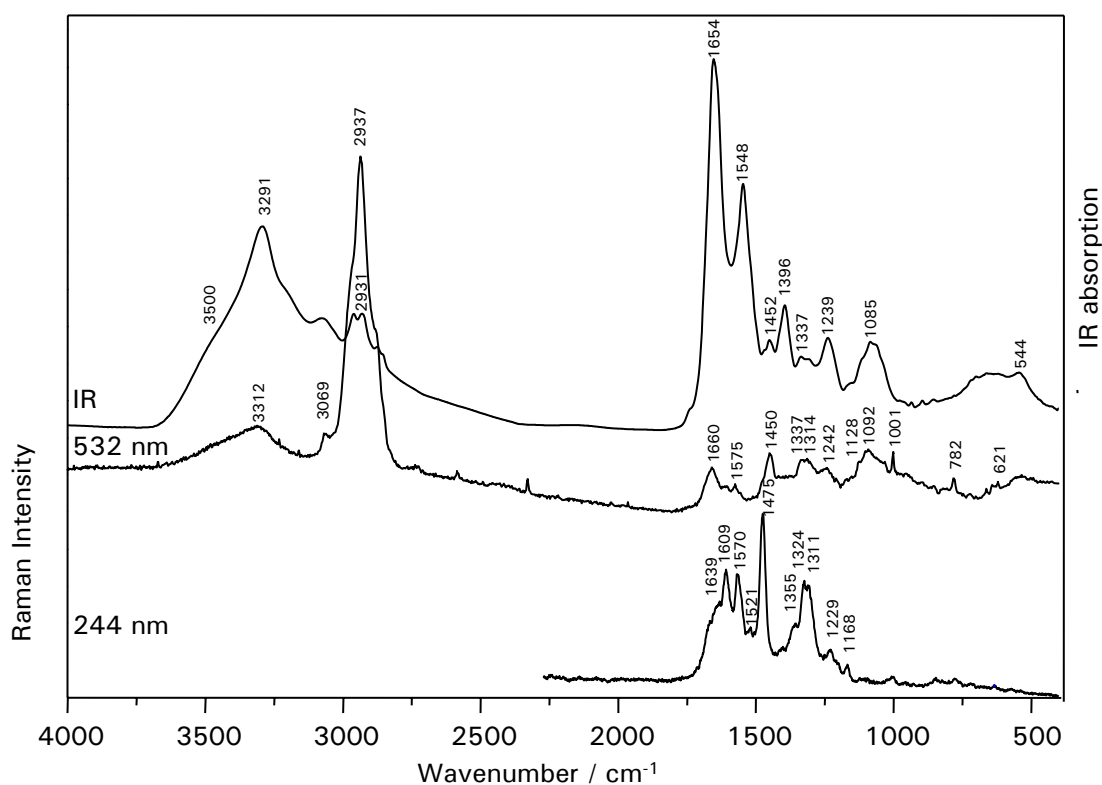


**Figure 4.3:** IR absorption (upper spectrum), micro-Raman (middle spectrum,  $\lambda_{\text{ex}} = 532 \text{ nm}$ ) and UV-resonance Raman spectrum (lowest spectrum,  $\lambda_{\text{ex}} = 244 \text{ nm}$ ) of bulk *S. epidermidis* ATCC 35984.

of grapes (Greek: *staphyle* = bunch of grapes). Figure 4.2 shows an pseudo 3-dimensional AFM image of such a cluster. The colonies of *S. epidermidis* on agar plates are small, circular and white-pigmented.

IR absorption and micro-Raman spectroscopy probe the overall chemical composition of the bacteria with contributions from the genome (DNA, RNA) and phenotypic characteristics (proteome and metabolites). This superposition of the individual components forms a spectral fingerprint of the investigated bacteria. Due to different selection rules, Raman and IR often give complementary information. In figure 4.3 the IR absorption and Raman spectra for *S. epidermidis* are shown. A detailed tentative band assignment is given in table 4.1.

#### 4.1.1.1 IR absorption spectra of *S. epidermidis*

In the IR absorption spectrum of *S. epidermidis* (upper spectrum in figure 4.3) a strong broad band resulting from N-H and O-H stretching vibrations is present around  $3290 \text{ cm}^{-1}$ . C-H stretching vibrations show up between  $2800$  and  $3000 \text{ cm}^{-1}$ . Individual peaks can be spotted for the asymmetric C-H stretch of methyl- and methylene groups ( $2960$  and  $2931 \text{ cm}^{-1}$ , respectively) and for the symmetric C-H stretching vibration ( $2875$  and  $2854 \text{ cm}^{-1}$ , respectively). As in almost all bac-

**Table 4.1:** Tentative assignment of the Raman ( $\lambda_{ex} = 532$  nm) and IR absorption bands of *S. epidermidis* (due to clarity not all vibrational bands are labelled in figure 4.3).

Raman wavenumber in $\text{cm}^{-1}$	tentative assignment	IR absorption band in $\text{cm}^{-1}$	tentative assignment
		3500 sh	O-H str of hydroxyl groups [152]
3312 w,br	bonded N-H str; H-bonded OH groups [152]	3291 s,br	N-H str
3069 w	C=C-H str aromatic, olefinic [152]	3077 m, br	
2955 sh		2960 mw	C-H str (asym) of $-\text{CH}_3$ [152]
2937 s	$\text{CH}_3$ str and $\text{CH}_2$ str	2931 mw	C-H str (asym) of $-\text{CH}_2$ [152]
		2875 w	C-H str (sym) of $-\text{CH}_3$ [152]
		2854 w	C-H str (sym) of $-\text{CH}_2$ [152]
		2705 vw,sh	Hydroxyl bonded phosphoric ester (P-OH)
		1742 w,sh	C=O stretching in saturate esters [152]
		1695, 1685, 1675 sh	amide I (antiparallel pleated sheets and $\beta$ -turns) [152]
1660 m	amide I (C=O stretch, $\text{NH}_2$ bending, C=N stretching) [151][152], C=C str (lipids) [185]	1654 vs	amide I ( $\alpha$ -helix) [152]
1614 vw	tyrosine (tryptophan) (C=C) [152, 185]	1639 sh	amide I ( $\beta$ -pleated sheet) [152]
1607 w	phenylalanine (tyrosine) (C=C) [152, 185]		
1575 m	nucleic acids (G+A ring stretch) [152]		
1450 m	$\text{CH}_2$ scis [276, 283, 151], $\text{CH}_2$ def. [152]	1548 s	amide II [152]
1337 m	CH def [151]	1452 w	C-H def of $\text{C-H}_2$ [152]
1314 m	guanine, CH def (protein) [185]	1396 m	C=O str (sym) of $\text{COO}^-$ [152]
1242 w	amide III [151, 152]	1337 m	
1128 m	C-N and C-C str [151, 152], =C-C= (unsat. fatty acids in lipids) [229]	1300-1240 w,sh	amide III [152]
1130-1030	carbohydrates, mainly -C-C- (skeletal), C-O, C-O-H def [229]	1239 m	P=O str (asym) of $\text{PO}_2^-$ (phosphodiester) [152]
1092 m	CC skeletal, C-O-C asymmetric stretching in aliphatic esters, glycosidic ring [152]	1178-1000 br	C-O, C-C str, C-O-H, C-O-C def of carbohydrates [152]
1001 m	CC str aromatic ring (Phe) [151]	1085 m	P=O str (sym) of $\text{PO}_2^-$ [152], aliphatic esters [72]
899 vw	COC str [152]		
855 w	CC str, COC 1,4 glycosidic ring, "buried" tyrosine [152]		
782 m	CC str ring breathing (cytosine, uracil) [276, 283, 151, 152]		
723 vw	adenine [152]	720	C-H rock of $\text{C-H}_2$ [152]
663 w	guanine [152]		
642 vw	tyrosine (skeletal, C-C twist) [152, 185]		
621 w	phenylalanine (skeletal, C-C twist) [152, 185]		
535 w,br	C-O-C def glycosidic ring [229]	544 w	C-O, P-O-C bonding (phospholipids, RNA)

## 4 Bacteria

terial spectra the most prominent features in the IR absorption spectrum are the amide I band at  $1654\text{ cm}^{-1}$  and the amide II band at  $1548\text{ cm}^{-1}$ . Another protein contribution with less intensity is the amide III band at  $1239\text{ cm}^{-1}$ . This band also has some contributions from the asymmetric P=O stretching vibration of phosphodiesteres. The weak band at  $1452\text{ cm}^{-1}$  is due to the  $\text{CH}_2$  deformation vibration. The symmetric CO stretch of the deprotonated carboxyl group results in a band centered at  $1396\text{ cm}^{-1}$ . The band of medium intensity at  $1085\text{ cm}^{-1}$  can be assigned to the symmetric PO stretching vibration of  $\text{PO}_2^-$  as it is found in nucleic acids, and also to contributions from the asymmetric C-O-C stretching vibration in aliphatic esters and various oligo- and polysaccharides. The spectral region below  $900\text{ cm}^{-1}$  contains only very poor resolved spectral features, so that an assignment is hard to achieve. Contributions to the spectral contour may arise from aromatic ring vibrations of the aromatic amino acids and various nucleotides but also  $\text{CH}_2$  rocking modes of fatty acid side chains. The band at  $544\text{ cm}^{-1}$  was assigned to C-O and P-O-C bending vibration, e.g. as in phospholipids or nucleic acids.

### 4.1.1.2 Micro-Raman spectra

As mentioned above, similar and in part complementary information about the chemical composition of the bacteria can be gained by Raman and IR absorption spectroscopy. Due to the different selection rules the vibrational pattern of the Raman spectrum is quite different from the one of the IR spectrum as can be seen in figure 4.3. The most prominent feature within the Raman spectrum is the broad band centered around  $2937\text{ cm}^{-1}$  which is a superposition of the symmetric and antisymmetric C-H stretching vibrations of the  $\text{CH}_2$  and  $\text{CH}_3$  groups from lipids, proteins and carbohydrates. The scissoring and deformation of the C-H bond is found around  $1450\text{ cm}^{-1}$  and  $1337\text{ cm}^{-1}$ , respectively. Like in the IR spectrum, the amide bands can be found around  $1660\text{ cm}^{-1}$  (amide I) and around  $1242\text{ cm}^{-1}$  (amide III), but with less intensity. Further amino acid contributions can be found at  $1001\text{ cm}^{-1}$  together with the C-C stretching vibration of the aromatic ring of phenylalanine. The band at  $1575\text{ cm}^{-1}$  was assigned to the nucleic acid ring stretches, especially to contributions from guanine and adenine. C-N and C-C stretching vibrations cause the band at  $1128\text{ cm}^{-1}$ . The extended mode assignment of the Raman and IR spectra is summarized in table 4.1.

The IR and Raman spectra of the bulk material result from the averaged signal over several bacteria. The amount of sample cells probed with each scan were estimated to be  $10^6 - 10^8$  for the IR absorption spectroscopy and about 30 cells for micro-Raman investigations [81]. With micro-Raman spectroscopy it is also possible to focus down to only one individual cell, thus allowing to collect full spectral information from minimal sample volume. As expected, the general features at the single cell level are similar as for bulk spectra. The single cell spectra will be discussed in more detail later in this work in connection with the growth curve (section 4.3).



**Table 4.2:** Assignment of the UV-resonance Raman bands of *S. epidermidis*

Raman wavenumber in $\text{cm}^{-1}$	assignment (based on reference [145])
1639	T
1609	Tyr + Trp
1570	G + A
1521	C
1475	G + A
1355	T + A
1324	A + G + Tyr
1311	
1229	G + A + U
1168	Tyr

#### 4.1.1.3 UV-resonance Raman spectra: Nucleic acid and proteins

IR absorption and Raman spectra excited at 532 nm result in spectra representing the overall chemical composition with contributions from all substances (according to their cross sections) as was presented in the last sections. However, for some biological or medical problems only selected components, such as nucleic acids, are in the main focus of interest. Resonance Raman spectroscopy provides this vibrational selection when using the right excitation frequency.

The nucleic acid bases and the aromatic amino acids strongly absorb in the UV range (190 - 280 nm). Therefore, by using UV light for exciting the Raman spectra, it is possible to particularly enhance the Raman signals of those components within the whole bacteria. Figure 4.3 (lowest spectrum) shows an UV-resonance Raman spectrum of the staphylococci using an excitation wavelength of 244 nm, which is clearly dominated by the contributions of the nucleic acids, in particular by the two purine bases (table 4.2). Adenine (A) and guanine (G) contribute with C-N stretching vibrations to the most prominent band at  $1475 \text{ cm}^{-1}$  and with the  $\text{NH}_2$  deformations to the band at  $1570 \text{ cm}^{-1}$ . Besides guanine and adenine also uracil (U) vibrations show up via the band at  $1229 \text{ cm}^{-1}$ , and thymine (T) and adenine vibrations are responsible for the Raman band at  $1355 \text{ cm}^{-1}$ . The band at  $1521 \text{ cm}^{-1}$  was assigned to cytosine (C). The aromatic amino acids tyrosine (Tyr) and tryptophan (Trp) are responsible for the band at  $1609 \text{ cm}^{-1}$ , and in addition tyrosine also contributes to the Raman band at  $1324 \text{ cm}^{-1}$ .

The GC content, which is the percentage of guanine (G) and cytosine (C) in the DNA (and RNA) of the cell, is specific for the species and is used as a distinguishing mark between bacteria of different strains. The GC ratio varies from about 30% for staphylococci up to over 70% for streptomycetes and micrococci. Since the UV-resonance Raman spectra of bacteria are dominated by the nucleic acid components, attempts were made to use the characteristic Raman band intensities to determine the GC content of bacteria [177]. With the simplifying assumption that G and A from both DNA and RNA contribute with equal magnitude to the Raman scattering, the intensity of the band at  $1475 \text{ cm}^{-1}$  (A+G) can be set proportional to the total nucleic acid content. Therefore, the fraction of guanine+cytosine in the bacteria should be proportional to the ratio of the Raman peaks at  $1521 \text{ (C)}$  and  $1475 \text{ cm}^{-1}$ . From the area under the curve of those two Ra-

## 4 Bacteria

man bands, a band ratio of 0.23 was calculated which corresponds to a GC ratio of 31 to 37% when using the calibration plot prepared by Nelson, Manoharan and Spiro [177]. This value is in good agreement with a GC ratio of  $35.2 \pm 0.5$  mol% determined for *S. epidermidis* via biological methods [118].

### 4.1.2 *Bacillus pumilus*

*Bacillus pumilus* is a common bacterium found in soil and water. As a rhizobacteria it can live on plant roots or reside in the rhizosphere, a soil zone spanning a few millimeters around roots, where the bacteria feed on plant juices. In industry *Bacillus pumilus* is used for alkaline protease production, environmental decontamination of dioxins, and in the baking industry. It also finds application as a pesticide active ingredient. However, *Bacillus pumilus* can also cause food poisoning.

Figure 4.4A shows in the top an averaged Raman spectrum of *Bacillus pumilus* DSM 361 excited at 532 nm. It exhibits similar spectral features as discussed in section 4.1.1.2 for *S. epidermidis*: the amide I band around  $1660\text{ cm}^{-1}$ , the nucleic acid ring stretches around  $1580\text{ cm}^{-1}$ , the  $\text{CH}_2$  and CH deformation modes around  $1450\text{ cm}^{-1}$  and  $1336\text{ cm}^{-1}$ , the C-N and C-C stretching modes around  $1128\text{ cm}^{-1}$  and the sharp CC aromatic ring stretch of phenylalanine around  $1001\text{ cm}^{-1}$ . Even though the spectra of the different bacterial strains appears very similar on first sight distinct differences in band position and band intensities can be found due to different molecular composition. This allows the differentiation between different bacterial strains by means of vibrational spectroscopy as will be briefly sketched in section 4.2.

### 4.1.3 *Bacillus subtilis*

Another common soil bacterium is *Bacillus subtilis*. It can be found especially in the upper soil layers and in the rhizosphere of plants and is responsible for the decomposition of organic materials.

This rod-shaped bacteria has a typical size of 2 to 3  $\mu\text{m}$  and a height of 0.6  $\mu\text{m}$ . The Gram-positive cells are flagellated. Under certain conditions (stress) it can form spores. *B. subtilis* is non-pathogenic, but its close phylogenetic relation to pathogens as e.g. staphylococci and mycobacteria make it to an interesting object for the biomolecular and medical research and nowadays it is one of the best-studied Gram-positive bacteria. *B. subtilis* also has industrial importance e.g. as a pharmaceutical product (Utilin<sup>®</sup> or Bactisubtil<sup>®</sup>) against dermatosis or intestinal dysfunctions, as a biological fungicide, for the synthesis of riboflavin (vitamin B12) or for the production of a detergent enzyme (e.g. Subtilisin<sup>®</sup>).

The second spectrum from the top in Figure 4.4A shows an averaged Raman spectrum of *Bacillus subtilis* DSM 10 excited at 532 nm. It shows great similarities to the Raman spectrum of *B. pumilus*, a strain of the same genus, and also to the spectrum of *S. epidermidis*, a strain to which *B. subtilis* is in close phylogenetic relation.

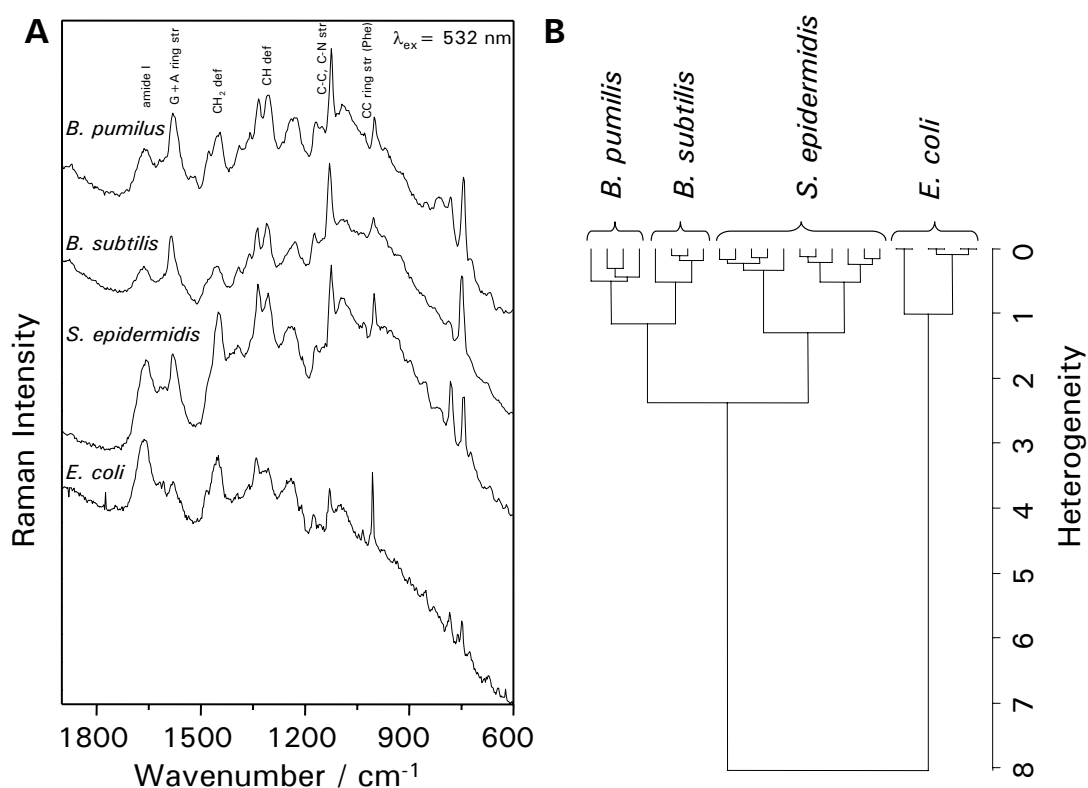


**Figure 4.4:** **A)** Raman spectra of *B. pumilus*, *B. subtilis*, *S. epidermidis* and *E. coli*. **B)** hierarchical cluster analysis of the spectra shown in A (standard method, Ward's algorithm).

#### 4.1.4 *Escherichia coli*

*Escherichia coli* are rod-shaped cells, 1-2  $\mu\text{m}$  in length and 0.1-0.5  $\mu\text{m}$  in diameter as can be seen in the AFM images in figure 4.5. *E. coli* are Gram-negative and flagellated. They are aerobic and facultative anaerobic and non-spore-forming. *E. coli* cells are a natural inhabitant of the gut flora. However, if displaced the bacteria can cause infections of the urinary tract or meningitis. *Escherichia coli* is one of the most often used bacteria in molecular biology and modern biological engineering. Its complete genome has been identified and by transformation it can be modified so that the bacteria can serve as "factories" to synthesize DNA, amino acids or a variety of other compounds such as insulin, for example.

Figure 4.4A shows in the bottom an averaged Raman spectrum of *Escherichia coli* DSM 423 excited at 532 nm.

## 4 Bacteria

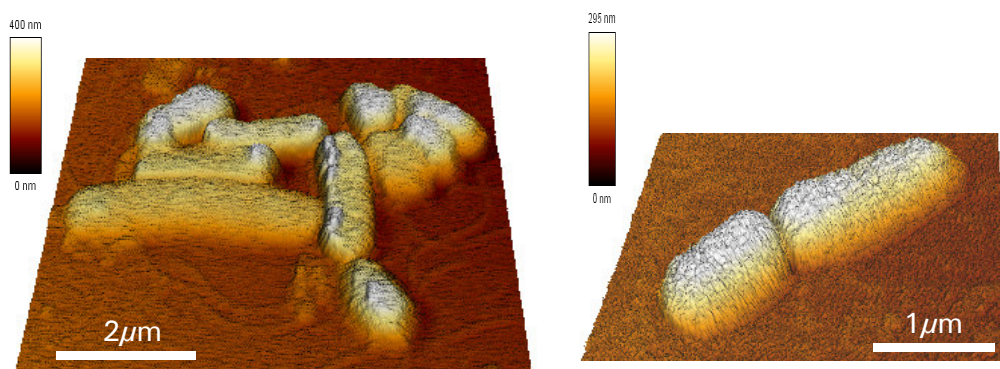


**Figure 4.5:** Pseudo 3D AFM image of *E. coli*.

### 4.2 Vibrational spectroscopic discrimination of bacteria

The degree to which a causative organism requires identification varies but identification is most useful in complex clinical cases; for example to distinguish relapse, to indicate failure of an antibiotic treatment, and to detect reinfection with a different organism in patients with recurrent infections.

Using conventional methods, laboratory examination of potentially infected material is expensive, time-consuming and labor-intensive: approximately 24 h incubation is required to obtain an accurate colony count. An additional  $12 \pm 24$  h is needed for organism identification and susceptibility testing, which may further delay administration of the most appropriate narrow-spectrum antibiotic [86, 192].

Figure 4.4B presents a hierarchical cluster analysis of the bulk Raman spectra of the bacteria shown in figure 4.4A using standard method and Ward's algorithm (see section 2.3.1). Even though the spectra look very similar on the first view it is possible to classify them according to the bacterial strain. Two distinct clusters are formed between the Raman spectra of the Gram-negative escherichia bacteria and the Gram-positive bacilli and staphylococci. Further subclusters are formed between *S. epidermidis* and the two bacillus strains. The two clusters of the closely related *B. pumilus* and *B. subtilis* are separated only by a small heterogeneity. It has been shown that appropriate classification with high recognition rates above 95% on the strain level also for larger data sets using hierarchical cluster analysis and support vector machines [96, 95, 218].

### 4.3 Bacterial metabolism: Vibrational spectroscopic study of bacterial growth

Information about the unperturbed bacterial growth is necessary for judging the influence of drugs on the bacterial metabolism. Also for a reliable identification of bacteria of unknown age precise information about the range of spectral variations within one species are required. In the following the bacterial growth of *S. epidermidis* is monitored by means of IR absorption, micro-Raman and resonance Raman spectroscopy. The subtle changes in the spectra are evaluated by statistical methods. The vibrational spectroscopic characteristics obtained in the previous section help to assign the observed changes in the vibrational spectra to chemical components within the bacterial cell. For *B. pumilus* a similar analysis is shown for the growth dependent UV-resonance Raman spectra.

#### 4.3.1 *Staphylococcus epidermidis* ATCC 35984

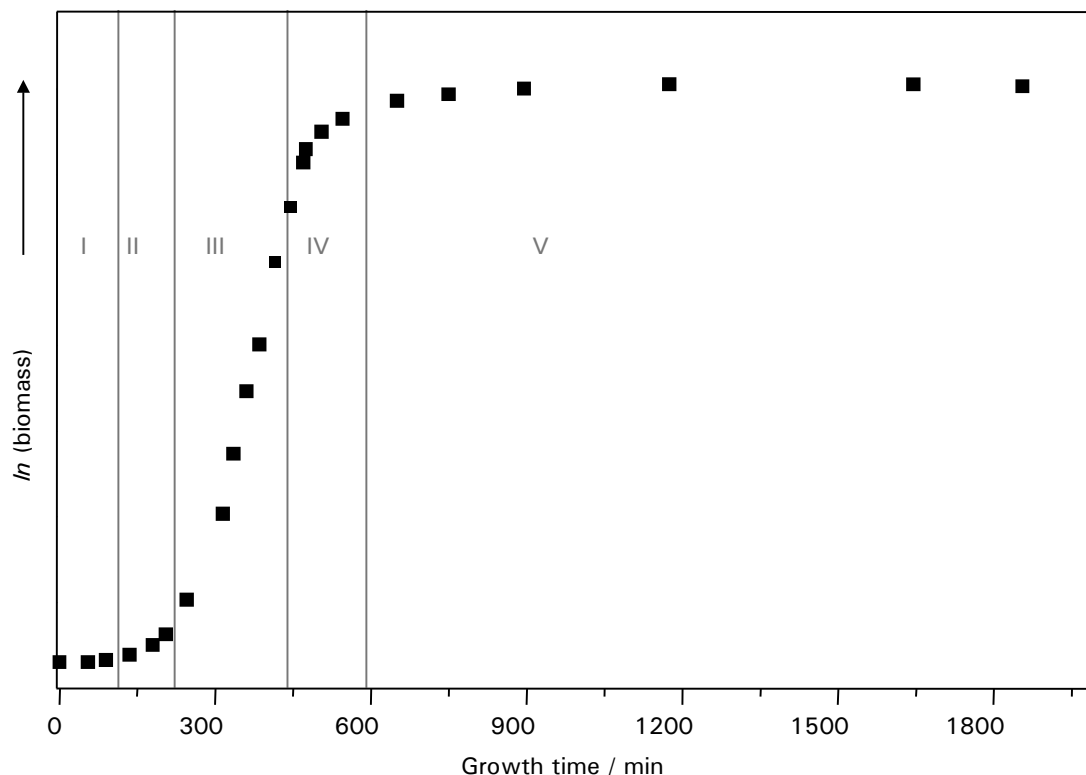
##### 4.3.1.1 Growth curve

Figure 4.6 shows a typical growth curve for *Staphylococcus epidermidis* ATCC 35984 under batch conditions in a semi-logarithmic representation (natural logarithm of the cell mass as a function of growth time). During the lag phase (I) (<100 min) the bacterial cells prepare their metabolism for the upcoming growth phase and no net-increase of the biomass is observed. During the acceleration phase (II) the growth rate  $\mu$  is increasing until it reaches a constant value in the exponential growth phase (III). This value for  $\mu$  is specific for the bacterial strain and the growth conditions. In the exponential growth phase, also called logarithmic phase, the number of bacteria increases following the equation [123]:

$$N = N_0 \exp(\mu t) \quad (4.1)$$

with  $N$  being the number of bacteria at time  $t$  and  $N_0$  the number of bacteria at the beginning of the exponential growth phase. From the slope of the growth curve in the exponential phase the growth rate of *Staphylococcus epidermidis* ATCC 35984 in CASO at 37°C was determined to be  $\mu = 0.789 \text{ h}^{-1}$ , the generation time  $g = \ln 2 / \mu = 0.879 \text{ h}$ , and the dividing rate  $v = 1/g = 1.138 \text{ h}^{-1}$ . These values are in good agreement with the growth rates determined by Pitt and Ross for different growth conditions [199]. When the substrate is used up, or the population density is getting too high, the growth rate decreases and the culture enters the retardation phase (IV). It follows the stationary phase (V) where there is no net increase of biological mass. Finally, as the bacterial cells age, the dying off phase follows (not shown in the diagram) in which lysis of the biomass occurs.

Vibrational spectroscopy is used to further monitor the metabolic changes occurring during bacterial growth. For a systematic investigation of the growth phenomenon IR absorption, micro-Raman and UV-resonance Raman spectra were recorded at the different growth phases, mainly



**Figure 4.6:** Growth curve of *S. epidermidis* under batch conditions in CASO at 37°C. The amount of biomass was determined by measuring the UV/vis absorption of the bacterial culture at 630 nm at different growth times. The different growth phases are marked by Roman numbers: I lag phase, II acceleration phase, III exponential growth phase, IV retardation phase, V stationary phase.

during the exponential growth phase and stationary phase. During the lag phase no spectra were recorded since the bacterial concentration was too low to harvest a sufficient amount of cells. The spectra were subjected to statistical analysis, such as hierarchical cluster analysis (HCA), principal component analysis (PCA) and linear discriminant analysis (LDA) with reverse elimination method tabu search (REM-TS) in order to identify the wavenumber changes and therewith the involved chemical species.

#### 4.3.1.2 Bacterial growth monitored by IR absorption spectroscopy

Figure 4.7A shows representative IR absorption spectra for different growth times in the wavenumber region between 1900 and 500  $\text{cm}^{-1}$ . Metabolic changes within the bacteria with growth time are reflected in slight changes in the intensity of some IR bands. For a rough estimation of the increase of nitrogenous structures during bacterial growth the increase of the ratio of the relative intensities of the amide I absorption band (1654  $\text{cm}^{-1}$ ) and the band at 1085  $\text{cm}^{-1}$  due to aliphatic esters, including phospho-esters as found in the DNA and RNA backbone can be consulted, as

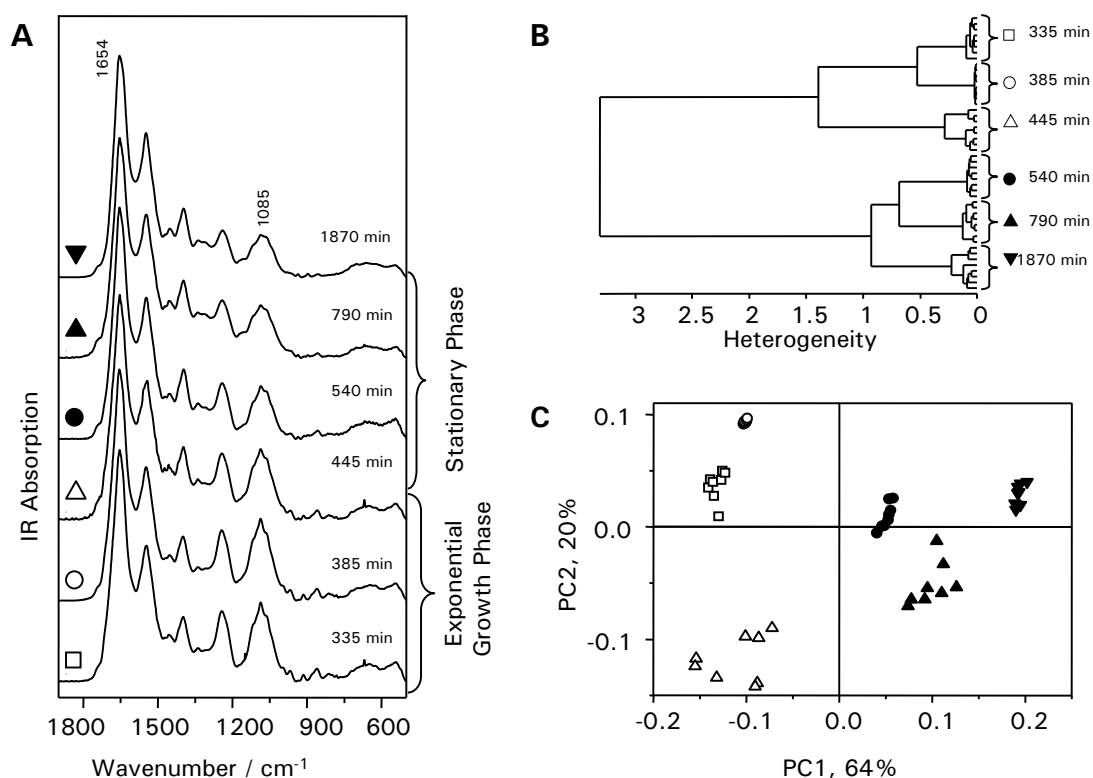


**Figure 4.7:** **A)** IR absorption spectra of *S. epidermidis* at different growth times; **B)** Hierarchical cluster analysis for the IR spectra of *S. epidermidis* at different growth times (first derivative, vector normalization, standard method, Ward's algorithm); **C)** Scores plot of the first two principal components of the PCA of the IR spectra of *S. epidermidis* at different growth times.

was shown previously for *Bacillus subtilis* [72]. Table 4.3 depicts an increase of this ratio for *S. epidermidis* from 2.9 for 335 min (exponential growth phase) to 5.3 for 1870 min (stationary phase). A significant increase is observed between the growth time 445 min and 540 min where the bacterial culture changes from the exponential growth phase to the stationary phase (see figure 4.6).

For a more profound analysis of the subtle changes occurring during bacterial growth the whole spectra between 1900 and 500  $\text{cm}^{-1}$  were subjected to statistical analysis. The hierarchical cluster analysis (HCA) shown in figure 4.7B reveals a clear separation of the spectra of the exponential growth and the stationary phase (including late retardation phase). Within these two clusters a further separation into sub-clusters of the individual growth times is observed, i.e., during bacterial growth significant, systematic changes occur in the bacterial cells and can be visualized by means of IR absorption spectroscopy. While the differences in the spectra for different growth time within the same growth phase are relative small, more pronounced differences are visible between bacterial spectra of different growth phases.

**Table 4.3:** Change of the relative intensities of the amide I absorption band ( $1654\text{ cm}^{-1}$ ) and the band at  $1085\text{ cm}^{-1}$  due to aliphatic esters (including DNA) in the IR absorption spectra of *S. epidermidis* with growth time.

growth phase	growth time in min	intensity ratio $1654\text{ cm}^{-1}/1086\text{ cm}^{-1}$
log phase	335	2.9
(exponential growth)	385	2.8
	445	3.2
	540	4.4
stationary phase	790	4.2
	1870	5.3

The wavenumbers experiencing the highest variation during bacterial growth can be identified by principal component analysis (PCA). The scores plot of the first two principal components which describe together 84% of the data is shown in figure 4.7C. The spectra arrange in well separated clusters along the first principal component (PC1) according to the growth time. IR absorption spectra of bacteria in the exponential growth phase have negative values for PC1 while the PC1-value of the spectra of the bacteria in the stationary growth phase is positive and increasing with increasing growth time. The correlation of PC1 with growth time affirms the expectations since growth time is the only varying external parameter for the individual spectra. The loading plot for PC1 (not shown) identifies the wavenumbers around  $1720$  and  $1669\text{ cm}^{-1}$  to have the most important contributions to this PC, indicating that at those wavenumbers the IR spectra show the largest variance. Further wavenumbers exhibiting noticeable contributions are  $1643$ ,  $1635$ ,  $1543$ ,  $1555$ ,  $1262$ ,  $1079$ ,  $671$  and  $665\text{ cm}^{-1}$ . Those bands can mainly be assigned to protein moieties (amide bands) and to vibrations of esters and carboxyl groups (see table 4.1).

In order to select the wavenumber regions with the highest discrimination power Fisher's linear discriminant analysis (LDA) in combination with the reverse elimination method tabu search (REM-TS) [20] was applied. For the aforementioned IR data, the wavenumbers contributing the most to the classification of the spectra could not be determined unambiguously since a multitude of variable subsets achieve extremely good classification results with LDA. The external predictions showed 98% of correctly classified spectra across the 100 different splits into training and test sets. Thus, almost all spectra could be classified correctly using different subset combinations. One out of the many equally good variable subsets is:  $1685\text{ cm}^{-1}$  (amide I),  $1548\text{ cm}^{-1}$  (amide II) and  $1085\text{ cm}^{-1}$  (P=O str). Using these variables for classification achieved a cross-validated (internal) recognition rate of 98% for LDA as well as a test set performance of 98% correctly classified spectra.

Thus, for the classification of the IR absorption spectra with growth time especially the protein moieties, esters and compounds with carboxylic groups are responsible. This is in good agreement with the ratio of the amide I absorption band ( $1654\text{ cm}^{-1}$ ) and the band at  $1085\text{ cm}^{-1}$  due to aliphatic esters (including the phospho esters in the DNA backbone) which was used by Filip et al. [72] to estimate the progress in bacterial growth.



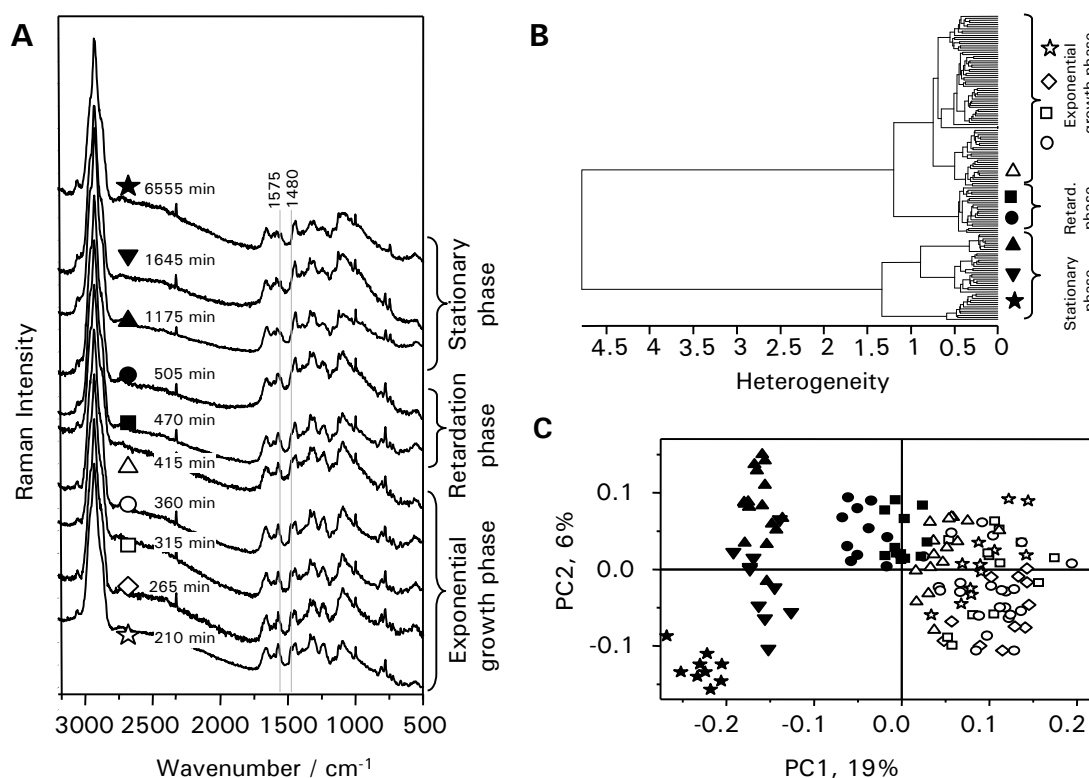


**Figure 4.8:** **A)** Micro-Raman spectra of single *S. epidermidis* cells at different growth times; **B)** Hierarchical cluster analysis for the micro-Raman spectra (first derivative) of single *S. epidermidis* cells at different growth times (vector normalization, standard method, Ward's algorithm); **C)** Scores plot of the first two principal components of the PCA of the micro-Raman spectra of single *S. epidermidis* cells at different growth times.

#### 4.3.1.3 Bacterial growth monitored by micro-Raman spectroscopy

A similar analysis was performed for the data from micro-Raman spectroscopy. Figure 4.8A shows the micro-Raman spectra of single *S. epidermidis* cells at different growth times. As for the IR spectra, the differences between the spectra are quite subtle. Slight intensity variations can be seen around 1575 and 1475  $\text{cm}^{-1}$ . Like for the IR spectra the hierarchical cluster analysis (HCA) shown in figure 4.8B reflects a distinct separation between the spectra of the exponential growth phase (including the retardation phase,  $t < 600$  min) and the stationary growth phase ( $> 600$  min). In contrary to the IR data, the formation of individual sub-clusters for the different growth times is only achieved for the stationary and the retardation phase. The relative poor classification power for the exponential growth phase can be explained with the higher variability due to the sampling of individual bacterial cells. While some of the dividing cells are growing bigger to prepare for the upcoming chromosome division, others already form the new cross wall between the almost

#### 4 Bacteria

divided cells. When recording bulk spectra, as in the IR, an average is acquired and individual variations do not contribute so much to the classification result.

The principal component analysis (PCA) shown in figure 4.8C resembles the same features as the HCA. In the scores plot of the first two principal components a clear separation of the spectra of the exponential growth phase on the positive side of the first PC from the spectra of the stationary phase on the negative side of PC1 is seen with the spectra of the retardation phase being found in between. As for the IR spectra it is again the first PC which correlates to the growth time. From the loading plot of PC1 the wavenumbers 1575 and 1475  $\text{cm}^{-1}$  (nucleic acid [229]) were identified to have the major contribution to the spectral variances. Minor contributions result from the vibrational bands at 2955, 1232  $\text{cm}^{-1}$  (protein random coils) and 782  $\text{cm}^{-1}$  (nucleic acid [230]).

The latter results are further supported by REM-TS and LDA. The wavenumber regions that were selected more than 50 times in 100 runs, and thus having the highest discrimination power were the following: 3069  $\text{cm}^{-1}$ , 2937  $\text{cm}^{-1}$ , 1575  $\text{cm}^{-1}$ , 1475  $\text{cm}^{-1}$ , 1450  $\text{cm}^{-1}$ , 1242  $\text{cm}^{-1}$ , 1128  $\text{cm}^{-1}$ , and 855  $\text{cm}^{-1}$ , with 3069  $\text{cm}^{-1}$  (C=C-H str), 1242  $\text{cm}^{-1}$  (amide III), and 1128  $\text{cm}^{-1}$  (C-N, C-C str) being selected more than 70 times. Although the selection is quite robust with respect to data set composition, the recognition rate was low. The test set recognition rate obtained by major voting was only 67%. Using the eight strongest regions of wavenumbers with an occurrence of more than 50 times out of the 100 runs achieved an internal recognition rate of 66% in LMO-CV for LDA.

These results suggest that in particular changes in the bands due to the nucleic acid ring stretches and due to protein (amide bands) are responsible for the classification during bacterial growth. This confirms what is known from biology and is in good agreement with the results obtained from the IR spectra.

##### 4.3.1.4 Bacterial growth monitored by UV-resonance Raman spectroscopy

The analysis of the IR and micro-Raman spectra revealed that especially the Raman bands due to the nucleic acids and protein change during bacterial growth. Therefore, UV-resonance Raman (UVRR) spectroscopy with excitation at 244 nm should be a well suited method to follow the bacterial growth, since this technique is especially sensitive to the vibrational modes of the DNA and RNA bases as well as of the aromatic amino acids due to resonance enhancement. The bacterial UVRR spectra for different growth times are shown in figure 4.9A. Here the relative increase of the tyrosine and tryptophan band at 1609  $\text{cm}^{-1}$  with respect to a decreasing purine base (guanine and adenine) band at 1475  $\text{cm}^{-1}$  is easily visible, indicating the relative increase of proteins with respect to the DNA/RNA content with growth time. For a first quantitative estimation the spectral region between 1850  $\text{cm}^{-1}$  and 1250  $\text{cm}^{-1}$  was deconvoluted with seven Lorentzian profiles (see experimental section 3.3). The ratio of the area under the curve for the "nucleic acid band" at 1475  $\text{cm}^{-1}$  and the "protein band" at 1609  $\text{cm}^{-1}$  is plotted as a function of growth time in figure

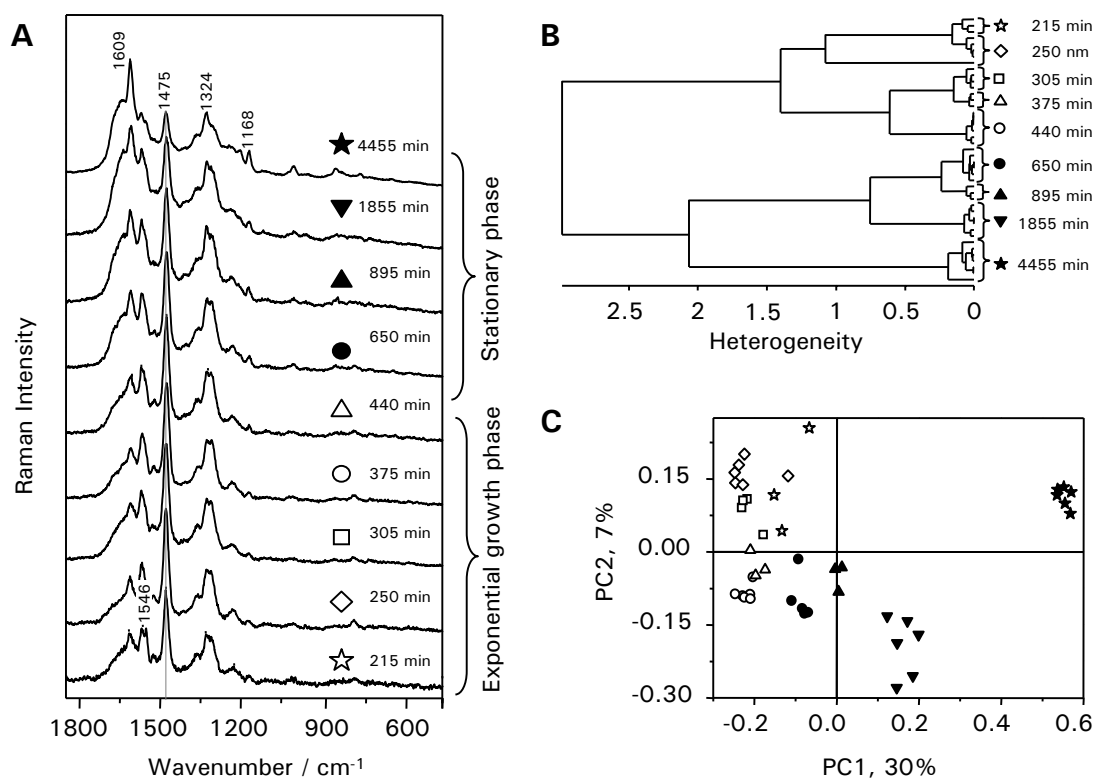


**Figure 4.9:** **A)** UV-resonance Raman spectra of *S. epidermidis* at different growth times; **B)** Hierarchical cluster analysis for the UV-resonance Raman spectra of *S. epidermidis* at different growth times (vector normalization, factorization method using three factors, Ward's algorithm); **C)** Scores plot of the first two principal components of the PCA of the UV-resonance Raman spectra of *S. epidermidis* at different growth times.

4.10 in comparison with the growth curve. The nucleic acid/protein ratio is high at early growth times and falls to an almost constant level in the stationary growth phase. For a detailed quantitative analysis more data are necessary. However, the phenomenon of a relative high RNA content at the beginning of the exponential growth phase and a high protein content in the bacteria in the stationary phase [126] is reflected very well by the data. At the end of the exponential growth phase the reduced nutrient content and the increased quorum sensing force the bacteria to change their metabolism. In the following stationary phase the material and energy intensive protein synthesis is reduced, the number of ribosomes is decreases and other proteins are present. With the simple intensity ratio method the qualitative shift to other types of proteins is not resolved, but rather a constant protein level in the stationary phase is detected.

In order to treat the whole spectral region from  $500$  to  $1850 \text{ cm}^{-1}$  and not only two bands, further unsupervised statistical analysis were performed. The dendrogram generated by hierarchical cluster analysis (figure 4.9B) shows a clear separation between the bacterial spectra of the exponential growth phase (early growth times;  $< 600$  min) and the bacterial spectra of the stationary

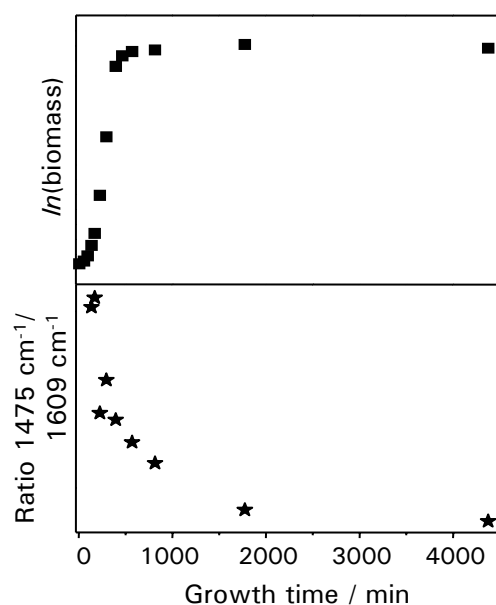


**Figure 4.10: Bottom)** Relative ratio of nucleic acid and protein content of *S. epidermidis* in the different growth phases as determined from UV resonance Raman spectra using the nucleic acid band at  $1475\text{ cm}^{-1}$  and the protein band at  $1609\text{ cm}^{-1}$  in comparison with the growth curve (**Top**).

phase ( $> 600\text{ min}$ ). Within the exponential growth phase the spectral distances between spectra of different growth times are on the same order of magnitude as between repeated measurements of the same growth time. Therefore, the spectra of early growth times do not form individual sub-clusters. This changes when reaching the stationary growth phase and well separated sub-clusters are formed for each growth time. The bacterial spectra after three days (4455 min) are even apart from all other spectra. This can be explained with aging processes, which change the overall composition, especially of the protein manifold.

A similar result is obtained from principal component analysis as can be seen in the scores plot of the first two PCs in figure 4.9C. For a rough classification, the first PC describing 30% of the data contains the information of growth time with the RR spectra of bacteria in the exponential growth phase having negative values for PC1 and increasing growth time resulting in an increased value for the first PC. A separation into individual clusters is recognizable but not very pronounced at early growth times while the spectra of bacteria in the stationary phase clearly form individual groups. From the loading plot for the first PC the Raman wavenumbers containing the largest spectral variances were identified to be  $1609$  and  $1475\text{ cm}^{-1}$ . This is in good agreement with the expected results from the observed changes in the nucleic acid/protein ratio. The Raman bands at  $1546$  and  $1168\text{ cm}^{-1}$  show minor contributions to the first PC.

Subset selection by REM-TS coupled to LDA identified the wavenumbers  $1639\text{ cm}^{-1}$  (T),  $1609\text{ cm}^{-1}$  (Tyr+Trp), and  $1475\text{ cm}^{-1}$  (G+A) with an occurrence of  $> 50$  out of 100 runs to have

the most significant discrimination power. The spectral region at  $1324\text{ cm}^{-1}$  (A+G+Tyr) was selected more than 20 times out of the 100 runs. The external recognition rate by bagging accounted for 80%. A combination of the four strongest regions of wavenumbers with an occurrence of more than 20 times out of the 100 runs achieved an (internal) performance of 77% of correctly classified spectra in LMO-CV and LDA.

With the vibrational techniques discussed so far the bacterial cells have been characterized with their overall chemical composition and more detailed information about the nucleic acids was obtained by UVRR spectroscopy. The statistical analysis of the Raman and IR spectra during the growth process revealed significant changes in protein and nucleic acid moieties. Also the results of the UV-resonance Raman spectroscopic analysis display the same biological facts. The relative intensity change of the hydrogen-bonding Raman marker band of the guanine and adenine stretching modes at  $1477\text{ cm}^{-1}$  in the UVRR spectra suggest changing concentrations of free nucleotides at the end of the exponential growth phase. The reduced free nucleotides initiate a switch in the protein synthesis (e.g. less ribosomes are produced), and a change in the protein and nucleic acid concentration is detected by Raman spectroscopy.

#### 4.3.2 *Bacillus pumilus*

A similar analysis as was just presented for *Staphylococcus epidermidis*, but only with focus on the UV-resonance Raman spectra is shown in this section for *Bacillus pumilus*.

Figure 4.11A, upper panel, shows a typical growth curve for *Bacillus pumilus* DSM 361 under batch conditions in the semi-logarithmic representation. It shows the same characteristics as the growth curve of *S. epidermidis* shown in figure 4.6: during the short lag phase (I) (<50 min) the bacterial cells prepare their metabolism for the upcoming growth phase. No Raman spectra were taken during this period since the bacterial concentration was too low. During the exponential growth phase (II) the number of bacteria increases following equation 4.1. The relative growth rate  $\mu$  which is specific for the bacterial strain and the growing conditions like media and temperature was determined from the slope of the growth curve for *Bacillus pumilus* (30°C, nutrient broth) to be  $\mu = 0.54\text{ h}^{-1}$ . The generation time  $g$  and the dividing rate  $\nu$  were calculated from the constant  $\mu$  to be  $g = \ln 2 / \mu = 1.3\text{ h}$ , and  $\nu = 1/g = 0.8\text{ h}^{-1}$ , respectively. These values are in good agreement with the range of  $g = 60 - 150\text{ min}$  given for soil bacteria [226]. When the substrate is used up, or the population density is getting too high, the growth rate decreases and the culture enters the retardation phase (III). It follows the stationary phase (IV) where there is no net increase of biological mass. Finally, as the bacterial cells age, the dying off phase follows (not shown in the diagram, > 3000 min) in which lysis of the biomass occurs.

Figure 4.11B shows the UV-resonance Raman spectra for three different growth times which are marked in Figure 4.11A with circles. The lower spectrum was taken at the beginning of the exponential phase (II,  $t = 100\text{ min}$ ), the middle one at the end of the log phase in the retardation phase (III,  $t = 450\text{ min}$ ) and the upper spectrum in the stationary phase (IV,  $t = 1700\text{ min}$ ). With

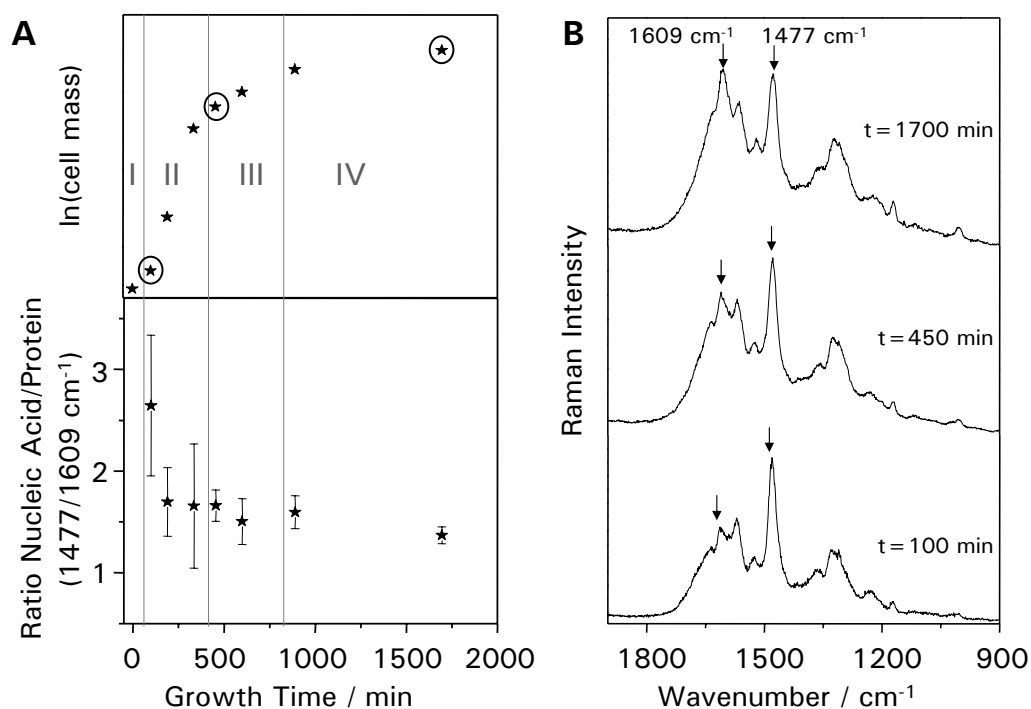


**Figure 4.11:** **A, Top)** Growth curve of *Bacillus pumilus* under batch conditions (natural logarithm of the cell mass as function of growth time), the different growth phases are as follows: I, lag-phase; II, exponential phase; III retardation phase; IV, stationary phase. **A, Bottom)** the relative ratio of nucleic acid and protein content of the bacteria in the different growth phases as determined from UV-resonance Raman spectra using the nucleic acid band at  $1477\text{ cm}^{-1}$  and the protein band at  $1609\text{ cm}^{-1}$ . **B)** UV-resonance Raman spectra ( $\lambda_{ex}=244\text{ nm}$ ) for three different growing times, marked in figure A (Top) with circles. The arrows point on the Raman bands used for the calculation of the nucleic acid/protein ratio in figure A.

excitation at 244 nm, especially the vibrational bands due to the aromatic amino acids and the nucleic acid bases are enhanced, as was discussed in section 4.1. Therefore, this method is especially suitable to monitor changes that involve proteins and DNA. The general features of all spectra are the same but the relative intensities change with time, which is visualized in figure 4.11A, lower panel, for the nucleic acid/protein ratio as an example. The two Raman bands used to calculate this ratio are indicated by the two arrows in figure 4.11B. The band around  $1477\text{ cm}^{-1}$  is mainly due to the N-C stretch of the guanine and adenine residues of the nucleic acids; the Raman band around  $1609\text{ cm}^{-1}$  is mainly caused by the aromatic amino acids tyrosine and tryptophan [145], and therefore can be used as a representative band for protein.

**Table 4.4:** Wavenumbers showing the largest variance and the highest discriminative power for the bacterial spectra (IR absorption, micro-Raman ( $\lambda_{ex}=532$  nm) and UV-resonance Raman ( $\lambda_{ex}=244$  nm)) of *S. epidermidis* at different growth times as determined by means of PCA and REM-TS/LDA, respectively.

IR loadings PC1 in $\text{cm}^{-1}$	IR REM-TS/LDA in $\text{cm}^{-1}$	micro-Raman ( $\lambda_{ex}=532$ nm) loadings PC1 in $\text{cm}^{-1}$	micro-Raman ( $\lambda_{ex}=532$ nm) REM-TS/LDA in $\text{cm}^{-1}$	UVRR ( $\lambda_{ex}=244$ nm) loadings PC1 in $\text{cm}^{-1}$	UVRR ( $\lambda_{ex}=244$ nm) REM-TS/LDA in $\text{cm}^{-1}$	assignment
			3069			C=C-H str (aromatic, olefinic)
1695	1685	2955	2937			CH <sub>3</sub> str, CH <sub>2</sub> str amide I (antiparallel pleated sheets and $\beta$ -turns)
1652						amide I ( $\alpha$ -helix)
				1609	1639 1609	nucleic acid (T) Tyr+Trp
		1571	1575			nucleic acids (G+A ring str)
1549	1548			1546 1475		amide II nucleic acid (G+A)
		1475	1475 1450			CH <sub>2</sub> def
					1324	A+G+Tyr
1236		1232	1242			amide III, P=O str (asym)
			1128	1168		C-C str, C-O
1985	1085		855			P=O str (sym)
						CC str, COC, "buried" tyrosine
668		781				CC str ring breathing (C, U)

#### 4.4 Conclusion

Bacteria of the strain *S. epidermidis* have been extensively characterized by the different types of vibrational spectroscopy, focussing on different aspects of the biochemical composition of the cell. The protein moieties of enzymes and structure elements account for the strong amide I, amide II and amide III vibrational bands especially in the IR absorption spectrum, but can also be found with different intensity ratios in the micro-Raman spectrum. Contributions from the nucleic acids (phosphate backbone) and various oligo- and polysaccharides are present in the spectrum with characteristic vibrational bands. With UV-resonance Raman spectroscopy almost exclusively the nucleic acids (purine and pyrimidine bases) and the aromatic amino acids from proteins can be probed within intact living bacteria which enables e.g. the determination of the GC ratio of the bacteria. This detailed knowledge of the vibrational bands assigned to chemical structures within the cell provides the basis for the investigation of the metabolic changes that go along with growth and aging of bacteria.

The metabolic changes during bacterial growth and aging are monitored by IR absorption and micro-Raman (*S. epidermidis*) and also by UV-resonance Raman spectroscopy (*S. epidermidis* and *B. pumilus*). For the data of *S. epidermidis* a detailed statistical analysis was performed and valuable information about characteristic changes in the bacterial composition are extracted from the

#### 4 Bacteria

fingerprint-like spectra. Principal component analysis (PCA) identifies the wavenumbers showing the largest variance across the different spectra. By means of Fisher's linear discriminant analysis (LDA) in combination with reverse elimination method tabu search the wavenumbers having the highest discriminative power are identified. Table 4.4 summarizes those wavenumbers for the growth curves probed with the different spectroscopic methods. A high similarity of the selected bands is found for the different spectroscopic techniques, variations are mainly due to different selection rules. The spectroscopic data also resemble quite well to what is known from biology: during bacterial growth DNA is translated and new proteins are synthesized, different ones during different growth phases. The bands having the highest discrimination power are mainly due to protein moieties (amide I, II and III bands above  $1600\text{ cm}^{-1}$ , around  $1548\text{ cm}^{-1}$  and around  $1240\text{ cm}^{-1}$ , respectively) and DNA components. While IR absorption spectroscopy visualizes especially the DNA and RNA backbone vibration with the symmetric and asymmetric PO stretches at  $1085$  and  $1239\text{ cm}^{-1}$ , the micro-Raman and in particular the UV-resonance Raman spectroscopy focus on the changes at the nucleic acid bases (guanine and adenine ring stretches around  $1575\text{ cm}^{-1}$  and around  $1475\text{ cm}^{-1}$ , respectively). Therefore, the subtle changes occurring within the bacterial cell during bacterial growth such as the change of the relative amount of RNA and protein with the transition from the exponential growth phase to the stationary phase can be tracked and located by means of vibrational spectroscopy.



## 5 Tip-enhanced Raman spectroscopy (TERS) of complex biological surfaces

Tip-enhanced Raman spectroscopy bears a high potential for the investigation of surfaces because it allows the recording of the topography of the investigated surface with highest spatial resolution below the diffraction limit [247] while at the same time rich chemical information from those surface structures can be obtained via vibrational spectra. Those information are especially useful for studying surface problems as they occur in material science, catalysis or life sciences. Many vital processes that take place at and through the cell membrane are not completely understood so far, as e.g. signal transduction, mass transport, adhesion on surfaces, cell recognition and enzyme reactions. Because an intact cell wall is crucial, many antibiotics, e.g. of the group of the  $\beta$ -lactams, penicillines and glycopeptides interfere with the synthesis of the bacterial cell wall. Sometimes, extracellular substances forming a biofilm around the bacteria may alter the effectiveness of the antibiotics. Therefore, it is of greatest interest to learn more about the chemical composition of the bacterial surface and its spatial arrangement on a molecular level, as well as getting an understanding of the dynamics of the cell membrane.

Up to now tip-enhanced Raman spectroscopy has been successfully applied to small pure substances like CN-ions adsorbed at gold surfaces [196], malachite green isothiocyanate [197, 198], benzenethiol [210], rhodamine 6G [270], single walled carbon nanotubes [94, 93] and DNA components [205]. In this chapter TERS spectra from surfaces of complex biological systems, such as whole bacterial cells are presented and compared to TERS spectra of pure substances. A tentative band assignment is given. Furthermore, dynamics are observed on the cell surface which could be due to surface processes. This marks a big step forward towards the non-invasive investigation of bacterial surfaces without the need of labelling techniques.

### 5.1 Biological fundamentals: Cell wall structure of Gram-positive bacteria

In the previous chapters the focus was set on bacteria as whole cells and their metabolism in the absence and presence of drugs has been studied, as well as selected biological targets (DNA, gyrase). However, the structure and molecular composition of the bacterial surface are of special interest to microbiologist and pharmacologists. As a sample organism *Staphylococcus epidermidis* ATCC 35984 has been chosen for the following experiments. As already introduced in chapter 4

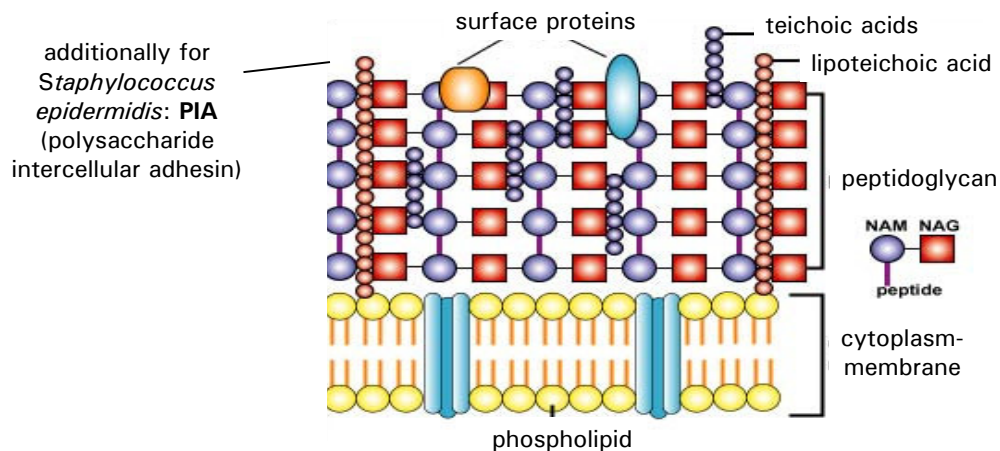


**Figure 5.1:** Scheme of the structure of the cell wall of Gram-positive bacteria (Figure adapted from Ref. [3]).

*S. epidermidis* evolved to a major cause of nosocomial infections, especially associated with the use of implanted medical devices [36]. The pathogenic potential of this strain mainly results from binding to polymer surfaces and biofilm formation. From the biofilms, especially associated with implanted medical devices, the bacteria get into the blood of the patients and cause a septic disease pattern. The biofilm matrix is also responsible for reduced susceptibility of the bacteria for antibiotics. Therefore, it is of greatest interest to learn more about the surface of the bacteria, because those results might lead to a more profound understanding of biofilm formation and help in the fight of *S. epidermidis* as a major cause of infections.

A scheme of the cell wall of Gram-positive bacteria is given in figure 5.1 (adapted from Ref. [3]). As for all Gram-positive bacteria its cytoplasm membrane is surrounded by peptidoglycan, also known as murein, which is made up by linear chains of the two alternating amino sugars N-acetyl glucosamine (NAG) and N-acetyl muramic acid (NAM). The NAM are cross-linked by short (4 to 5 residues) amino acid chains. The peptidoglycan layer which is assumed to be around 50 nm thick is pervaded by other polysaccharides like teichoic acid and a variety of surface proteins [36, 176]. Furthermore, on the cell membrane there are also different catalysis centers of enzymes and anchoring and binding sites for adhesion on surfaces and cell recognition. Depending on the growth conditions, a biofilm consisting mainly of the two polysaccharides teichoic acids (TA) and PIA (polysaccharide intercellular adhesin), surrounds *S. epidermidis* ATCC 35984 to a more or lesser extend. These polymers were found to be a 1,3-Poly(glycerol phosphates) substituted with D-glucose (Glc), D-glucosamine (GlcN), D-Alanine (Ala) and D-Glc6Ala; and a linear beta-(1,6)-linked N-acetylglucosaminoglycan partially substituted with O-succinyl groups and parts of the N-acetylglucosamine units being deacetylated, respectively [220, 221]. In summary, the cell is presenting to the outside a variety of sugar and peptide components.

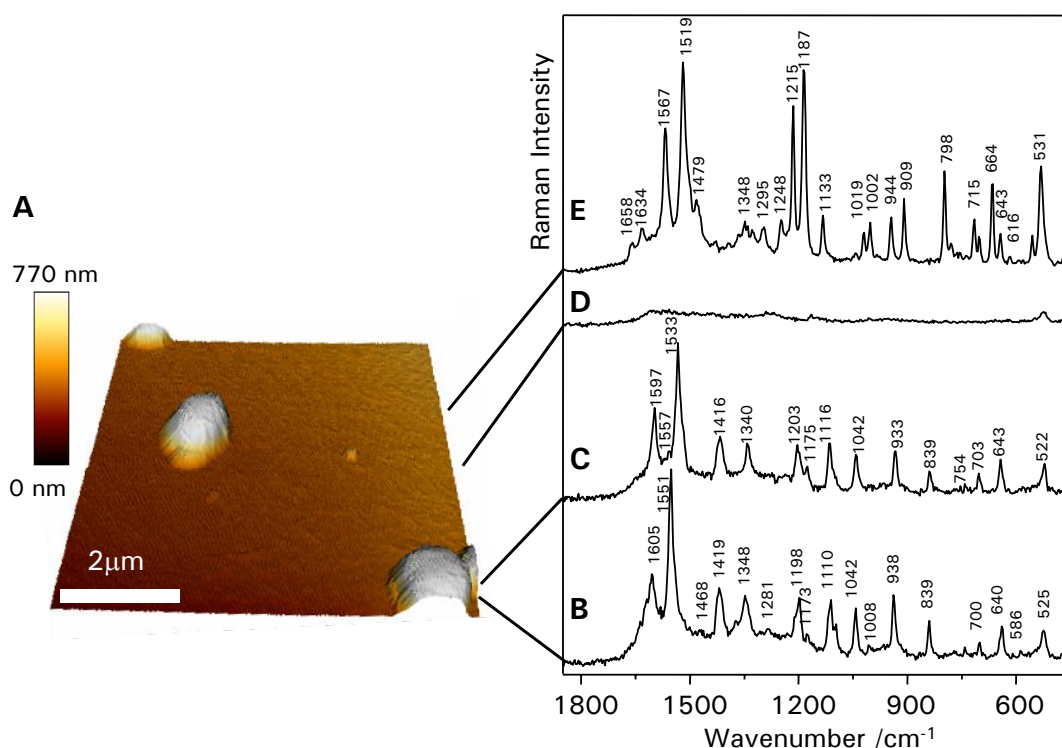


**Figure 5.2:** **A)** Pseudo three-dimensional topographic image ( $7 \times 7 \mu\text{m}$ ) of single *S. epidermidis* cells on a glass surface, **B,C,D,E)** TERS spectra recorded from one line while scanning the sample surface with the AFM. **B,C)** and **E)** show spectra when a cell passed the tip, **D)** the spectrum was recorded when there was no cell within that line scan.

The bacterial surface is not stiff and rigid, however dynamics can be observed. Experimental proof could be given so far by fluorescence correlation spectroscopy [14], fluorescence resonance energy transfer (FRET) [187] and also by video enhanced differential interference contrast microscopy [128, 213]. With the latter technique, proteins were observed to move for 20 to 200 nm in less than 30 ms [128, 213, 4].

## 5.2 TERS while scanning the bacterial surface with AFM

For recording the tip-enhanced Raman spectra and the topography of the bacterial cells, the sample was moved in the stage-scanning mode of the AFM in xy-direction by a piezo, while the enhancing tip was maintained in the laser focus and operated in the intermittent contact mode (for more experimental details see section 3.1.5).

An example of a topographic image of *S. epidermidis* ATCC 35894 on a glass surface is shown in figure 5.2A. The scanned area is  $7 \times 7 \mu\text{m}^2$  and the bacterial cells can be seen as round features on the glass surface with a diameter of 1  $\mu\text{m}$ .

## 5 Tip-enhanced Raman spectroscopy (TERS) of complex biological surfaces

The AFM was scanning the sample surface with a rate of 1 Hz, which means, that it took 1 s to acquire the topography of one line (7  $\mu\text{m}$ ). Simultaneously, tip-enhanced Raman scattering (TERS) spectra were recorded with 1 s acquisition time, so that one TERS spectrum represents the average TERS signal of the substances on one line of the scanned area. Raman signals were only observed when a cell has passed the tip during that line scan. Figure 5.2B and C show such TERS spectra of two adjacent lines on one cell as marked in the figure. Figure 5.2E was recorded while scanning over the second cell as indicated in the figure. When no cell was underneath the tip, no Raman signal was detected as can be seen in figure 5.2D. The good signal-to-noise ratio TERS signals which are only obtained from lines where a bacterial cell is underneath the enhancing tip indicate that the observed Raman signal originates indeed from the cell. The results could be reproduced with two other *S. epidermidis* cells on different days using a different silver coated AFM-tip (results not shown). However, sometimes it was difficult to obtain a good topography and good TERS spectra. The TERS signature slightly varies from line to line suggesting that the chemical composition of the cell surface is not completely homogeneous. However, the spectra present an average Raman signal over the whole line scanned by the AFM in 1 s, which includes the width of the whole cell. It is desirable to make use of the high spatial resolution power of the AFM and record TERS spectra from well defined positions on the cell surface. Results from those experiments are shown in the next section together with a more detailed analysis of the vibrational bands.

### 5.3 TERS on selected points on the sample surface

After recording the topography of the single *S. epidermidis* cells on glass as shown in figure 5.2A several positions were chosen on the cell to record the TERS spectra. For reference purposes spectra were also recorded on spots where no cells were present. Figure 5.3B-D shows exemplarily three tip-enhanced Raman spectra recorded on the cell surface of the cell in the lower right corner of the investigated sample. Figure 5.3E shows a background spectrum from the the glass surface without any cell present. The enhanced Raman signal originates just from a very small area in the vicinity of the tip, corresponding roughly to the tip apex size [63, 184]. In this case the diameter of the tip apex is assumed to be less than 50 nm. Taking this nominal tip radius into account, chemical information from the vibrational spectra of different spots on the cell can be resolved with a spatial resolution down to a few 50 nm. The acquisition time for every spectrum was 30 seconds and the Raman intensity axes are scaled in the same way. While pronounced Raman spectra were obtained on the cell, no signal was recorded from the background. The ever present Raman band around  $519\text{ cm}^{-1}$  is due to Raman signals from the silicon of the silver coated AFM tip. As can be seen in figure 5.3, the relative intensities of the Raman scattering bands from the bacterial cell are changing, as well as some of the Raman bands are disappearing and some new are appearing in different spectra when recording spectra on one spot. This suggests some kind of surface dynamics and that issue will be addressed in more detail in the next section (5.4). No

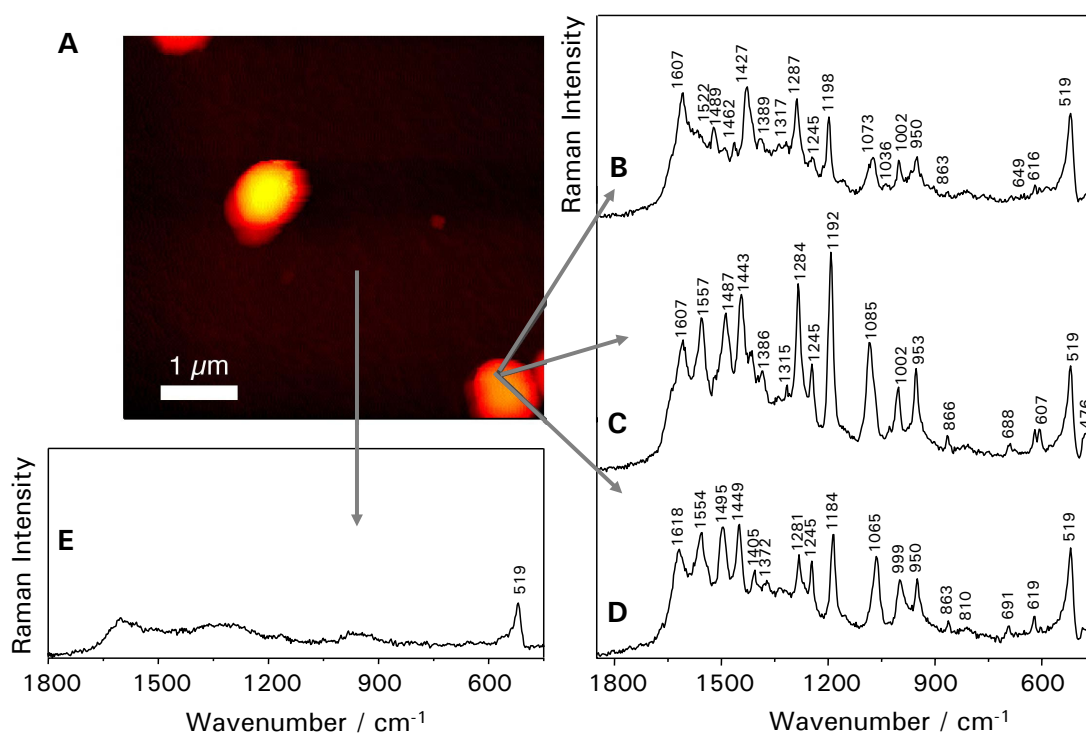


**Figure 5.3:** **A)** Topographic image of *S. epidermidis* cells with marked locations of the corresponding TERS measurements. **B, C, D)** denote TERS spectra measured with a silver coated AFM cantilever on top of a bacterium whereas **E)** corresponds to a reference TERS experiment on the glass surface. The always present band around  $519\text{ cm}^{-1}$  is attributed to Raman scattering of the silicon tip.

detailed spectral features are visible and no fluctuation of the Raman signal is observed from a spot where no cell is present (figure 5.3E).

Another way of verifying that the observed Raman signals are indeed due to the signal enhancement of the silver coated tip over the cell surface is by performing a tip retraction experiment. Figure 5.4A shows a spectrum recorded on the surface of *S. epidermidis* with the tip being in the laser focus and in feedback with the sample surface. Figure 5.4B shows a spectrum recorded at the same position with the same sampling conditions but the tip being retracted for about 100 nm from the sample surface. There is no Raman signal obtained in that case. This is true for both cases: when the laser focus is kept at the cell surface and when the laser focus is moved up together with the tip (controlled via a piezo feedback loop). Therefore, it can be excluded that observed Raman signals are just normal Raman bands and also that the enhanced signal results from a contamination of the probing tip.

Further experiments have been performed with other (staphylococcal) cells, also on different days using a different enhancing tip. Figure 5.5 shows five TERS spectra recorded on various positions on different individual *Staphylococcus epidermidis* cells (cell 1-5). Again slight fluctua-

## 5 Tip-enhanced Raman spectroscopy (TERS) of complex biological surfaces

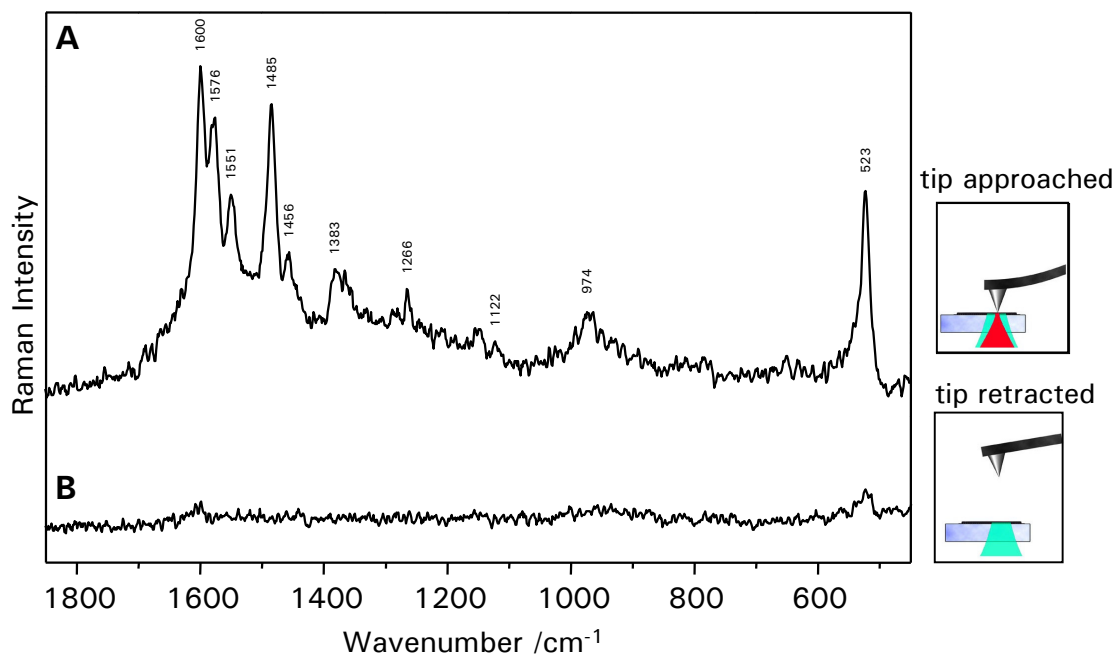


**Figure 5.4:** TERS spectra of *S. epidermidis* **A**) the enhancing tip is approached to the sample surface and a SERS spectrum with good signal-to-noise ratio is obtained, **B**) the enhancing tip is retracted. No TERS signal from the bacterial surface is recorded anymore.

tions in the Raman signal intensity have been observed when recording successive TERS spectra on one spot of the bacterial surface. Fluctuating signals have also been reported by Kudelski and Pettinger [126] when probing carbon chain segments. They assigned the variation of the scattered signal to surface chemistry processes producing a variety of carbon chain configurations. Summing up several of the individual spectra obtained by Kudelski and coworker resulted in a typical carbon spectrum with just two broad bands centred at  $1380$  and  $1590\text{ cm}^{-1}$ . The TERS spectra of the bacterial cells shown in figure 5.5 are the calculated average from 15 individual 1 s-spectra recorded on one spot on the cell surface. As the summation of the spectra does not result in a typical carbon spectrum as found by Kudelski and Pettinger [126] carbonaceous contaminations can be excluded and more complex processes have to account for the dynamics (see section 5.4).

It was not possible to record completely identical spectra on two different spots on a cell surface, but characteristic bands of the different chemical species present on the surface occurred repeatedly in different spectra. The spectral variations are explained by the heterogeneity of the cell surface on a nanometer scale. As explained in a previous section (5.1) the bacterial surface consists of a variety of sugar moieties from the murein layer and the polysaccharides PIA and TA and various peptide moieties from the numerous surface proteins that pervade the sugar layer.

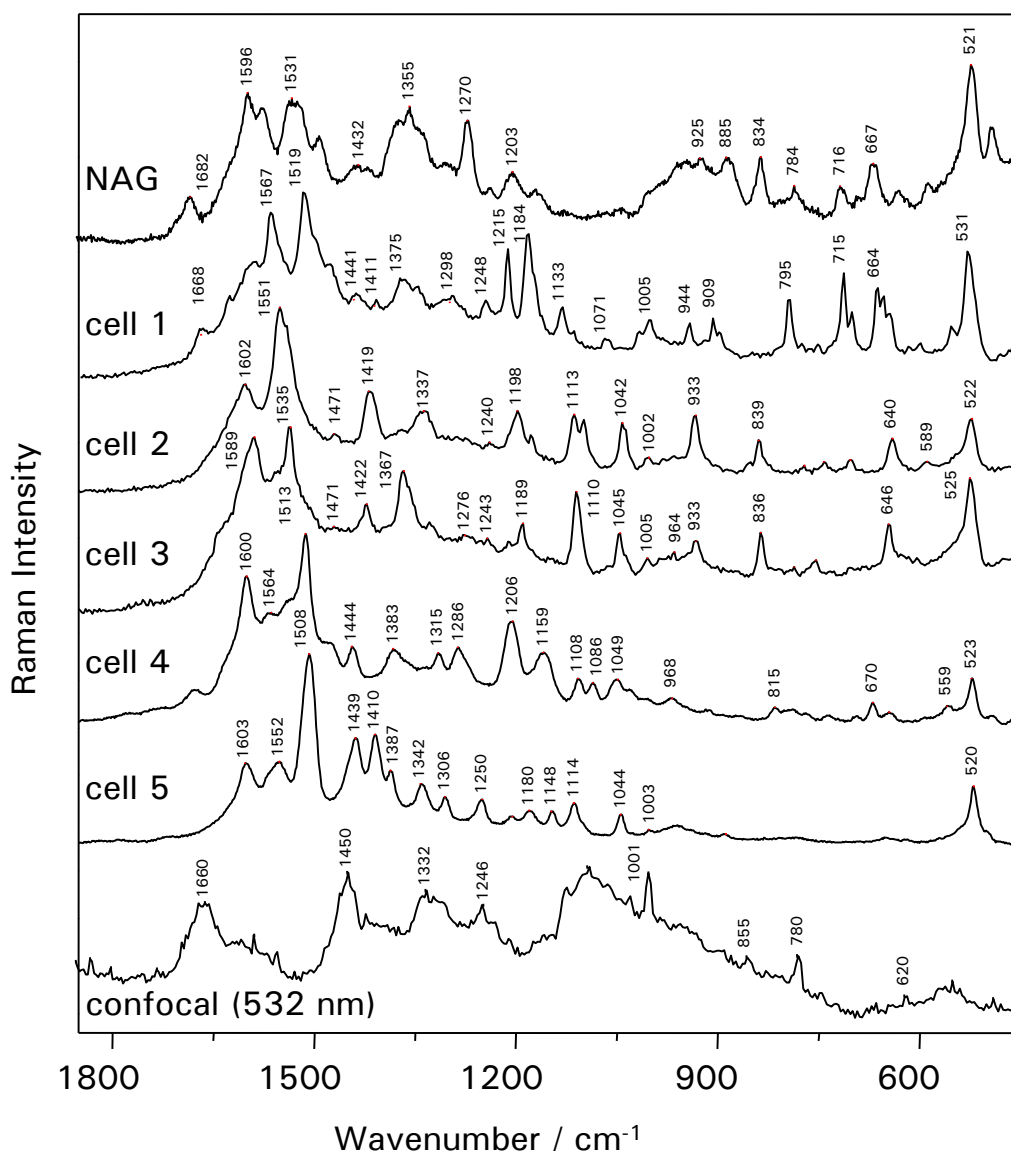


**Figure 5.5:** Tip-enhanced Raman spectra ( $\lambda_{ex} = 568$  nm) of *S. epidermidis* from different individual cells (cell 1-5). For comparison a TERS spectrum of the cell wall building block N-acetylglucosamine (NAG) is shown in the top and a confocal Raman spectrum ( $\lambda_{ex} = 532$  nm) of a single *S. epidermidis* cell at the bottom.

Varying intensity ratios of the TERS signals are expected for a different chemical composition in the very small sample volume underneath the tip apex experiencing the signal enhancement, as well as for a different orientation of the individual components.

At the bottom of figure 5.5, a confocal micro-Raman spectrum of a single *S. epidermidis* cell excited with 532 nm is shown for comparison. Distinct differences to the TERS spectra are observed. With the confocal micro-Raman spectrum a volume element of circa  $0.8 \times 0.8 \times 3 \mu\text{m}^3$  is probed. In contrast, the TERS signal results only from an area of less than  $50 \times 50 \text{ nm}^2$ , with a penetration

## 5 Tip-enhanced Raman spectroscopy (TERS) of complex biological surfaces

depth of a few nm. Due to the much higher spatial resolution, the chemical information contained in the TERS spectra results from much less chemical species and is confined to the outer most surface layer. In standard (confocal) Raman spectroscopy a much larger volume element is probed and the Raman bands are broader compared to the TERS bands. Similar discrepancies in band positions and intensities were observed by Zeiri and Efrima [288] when comparing the normal Raman spectra of *E. coli* with the corresponding SERS spectra.

### 5.3.1 Tentative band assignment

#### 5.3.1.1 TERS of *S. epidermidis*

A tentative band assignment of the TERS spectra of the bacterial surface of *S. epidermidis* shown in the previous sections is summarized in table 5.1. The assignment is based on typical SERS assignments for biological samples from the literature. Most of the Raman bands are due to contributions from peptides and polysaccharides. Protein contributions are present with the amide I band above  $1650\text{ cm}^{-1}$ , and N-acetyl-related bands (amide II) around  $1535\text{-}1564\text{ cm}^{-1}$  and  $1514\text{ cm}^{-1}$  [61]. For the amide III band a wide spectral range is given in the literature, so that the bands around  $1340$ ,  $1280$ ,  $1240$ ,  $1206$  and  $1198\text{ cm}^{-1}$  might have contributions of the amide III band from different amino acids [243]. The latter two wavenumbers are reported to contain major contributions from tyrosine and phenylalanine [243]. Further peptide Raman bands are present with the  $\text{NH}_2$  twist (alanine) at  $1144\text{ cm}^{-1}$  [250], the C-C and C-H modes of phenylalanine at  $1004$  and  $1030\text{ cm}^{-1}$  [243], the C-C skeletal modes in proteins between  $930$  and  $938\text{ cm}^{-1}$  [243, 287], the NCO deformation of tyrosine at  $646\text{ cm}^{-1}$  [243] and the NCO deformation of phenylalanine at  $623\text{ cm}^{-1}$  [243]. The  $\text{CH}_2$  scissoring vibration around  $1432\text{-}69\text{ cm}^{-1}$  and the  $\text{CH}_2$  bending vibrations around  $1419\text{ cm}^{-1}$  have contributions from the amino acid side chains as well as from the carbohydrates. Further Raman bands of different carbohydrate moieties are found with the CH bending of the  $\text{CH}_2\text{OH}$  group at  $1319\text{-}22$  and  $1209\text{-}1205\text{ cm}^{-1}$  [61], and the COH and OH deformation vibration at  $1265\text{-}72$  and  $1338\text{-}39\text{ cm}^{-1}$  up to  $1360\text{ cm}^{-1}$  in oligo- and polysaccharides [61], as well as the CC backbone vibration at  $474\text{ cm}^{-1}$  [243, 61].

The observed dominance of vibrational bands due to protein and sugar moieties is in good agreement with what is known about the chemical composition of the staphylococcus surface: sugar derivatives dominate with the peptidoglycan layer which is pervaded by TA and covered with PIA, and in between different proteins are present.

#### 5.3.1.2 TERS of pure substances: N-acetylglucosamine (NAG)

As explained in a previous section (5.1) the biofilm of *S. epidermidis* is assumed to consist mainly of the polysaccharides PIA and extracellular teichoic acids (TAs) [220, 221]. PIA is a poly- $\beta$ -(1-6)-N-acetylglucosamine and TA is a (1-3)-linked poly(glycerol phosphate) which is substituted at the 2-position of the glycerol residues with glucose, N-acetylglucosamine (NAG), and alanine. Furthermore, a variety of peptide moieties from the numerous surface proteins that pervade the



Table 5.1: Tentative band assignment of the TERS bands of *S. epidermidis*

Fig. 5.2		Fig. 5.3		Fig. 5.4		Fig. 5.5			Fig. 5.6			Fig. 5.7		Lit.-bands	Assignment				
B	C	E	B	C	D	A	cell 1	cell 2	cell 3	cell 4	cell 5	6s	14s			31s	51s	TERS	NAG
1605	1597	1634	1607	1600	1618	1600	1668	1602	1603	1600	1603	1777	1629	1601	1604	1595	1682	1593	V <sub>CO</sub> ester V <sub>C=O</sub> amide I; V <sub>C=C</sub> cis of fatty acids [61] V <sub>C=C</sub> olefinic V <sub>C=C</sub> aromatic, olefinic; Phe, Tyr [65, 243]
1551	1533	1567	1565	1576	1554	1551	1567	1551	1552	1564	1552	1560	1541	1555	1555	1576	1576	1576	$\delta_{NH}$ and $\nu_{CN}$ amide II [65]
		1519	1522	1485			1441	1471	1508	1444	1439	1514	1505	1514	1512	1531	1531	1490	N-acetyl-related bands (amide I) amide II [243] $\delta_{CH_2}$ [65]
1419	1416	1427	1489	1485	1495	1485	1411	1471	1513	1444	1439	1443	1445	1440	1444	1458	1432	1436	CH <sub>2</sub> scissoring [106]; CH <sub>3</sub> , C(6)-H <sub>2</sub> , COH (mono-, oligosaccharides) [61] $\delta_{CH_2}$ scissoring (fatty acid chains, phospholipids, amino side-chains of proteins, mono-, oligosaccharides) [243, 61] $\delta_{CH_2}$ V <sub>CO2</sub> $\alpha$ -amino acids [106, 287]
		1479	1462	1456			1375	1337	1387	1383	1387	1387	1373	1379	1337	1372	1355	1301	V <sub>CON</sub> -symm., $\delta_{CH_2}$ [65] $\delta_{CH_2}$ , $\delta_{OH}$ [65] $\delta_{OH}$ (polysaccharide) [61]; amide III, Trp [243] $\delta_{CH_2}$ , in-plane $\delta_{OH}$ [65] $\rho_{CH_2}$ [65]
1348	1342	1348	1337	1340	1372	1383	1298	1245	1286	1286	1286	1286	1261	1307	1307	1300	1270	1242	amide III [106], $\delta_{CH_2}$ , COH (mono-, oligosaccharides) [61] amide III [243] $\rho_{CH}$ , CH <sub>2</sub> OH group (polysaccharide) [61]; Tyr, Phe, T, amide III [243]
		1329	1317	1315			1248	1240	1243	1206	1206	1201	1213	1208	1208	1235	1203	1173	Tyr, Phe, amide III [243] NH <sub>2</sub> twist (alanine) [250] V <sub>CC</sub> (n-alkanes) [106]
1198		1187	1198	1184	1184	1122	1184	1198	1189	1180	1180	1166	1163	1179	1179	1168	1127	1147	V <sub>CC</sub> sym. glycosidic ring; ring breathing [65] C-O-C asymmetric stretching in aliphatic esters V <sub>CC</sub> aromatic ring [65] V <sub>CC</sub> aromatic ring [65] $\delta_{CH}$ in plane, Phe, V <sub>CC</sub> aromatic ring [243]; CC ring breathing (polysaccharides) [61] $\rho_{CH_2}$ [65], lipid layer components of the cell wall and membranes [202]
		1295	1287	1284	1281		1184	1198	1276	1286	1286	1286	1261	1307	1307	1270	1270	1242	carboxylate stretch, CC-skeletal modes in protein ( $\alpha$ -helix), $\rho_{CH_2}$ terminal [243, 287] V <sub>CC</sub> [65]
1110	1116	1133	1158				1133	1113	1110	1159	1148	1107	1122	1114	1147	1127	1114	1114	symm. stretch (CON-) V <sub>PO2</sub> , V <sub>CC</sub> ring breathing (RNA/DNA) [243] $\rho_{CH_2}$ [106]
1042	1042	1042	1073	1085	1065	1122	1071	1113	1110	1108	1114	1107	1083	1097	1047	1085	1086	1086	
		1019	1039	1065	1065		1005	1042	1045	1049	1044	1054	1054	1047	1047	1054	1054	1003	
938	933	944	1002	1002	999		944	1002	1005	1003	1003	974	958	958	958	944	944	970	
		909	950	953	950		944	933	933	968	968	917	958	920	958	944	944	970	
839	839	798	863	866	863		909	839	836	815	815	874	874	874	874	885	885	862	
		715	863	866	863		795	772	786	815	815	815	803	803	803	834	834	662	
700	703	703	688	691	691		754	742	754	670	670	671	696	670	670	749	749	584	
640	643	664	649	643	619		715	703	703	670	670	671	696	670	670	716	716	524	
640	643	664	649	643	619		664	640	646	670	670	671	696	670	670	692	692	524	
616	619	616	619	619	519		601	589	559	523	523	521	523	523	523	646	646	584	
525	522	531	519	519	519		537	522	525	523	520	521	523	523	523	525	525	492	
			476				491	491	491	483	483	491	483	483	483	474	474	492	

## 5 Tip-enhanced Raman spectroscopy (TERS) of complex biological surfaces

sugar layer is present on the outside of the bacterial cell. As was shown in the previous sections, indeed characteristic vibrational bands that could be assigned to the functional groups of those sugar and protein moieties dominate the tip-enhanced Raman spectra of the bacterial surface. For reference purposes the monomer N-acetylglucosamine (NAG) which is an abundant building block of the two surface polymers PIA and TA and also of the cell wall itself has been investigated by means of tip-enhanced Raman spectroscopy.

A TERS spectrum of the pure substance is shown at the top in figure 5.5 and the assignment of the vibrational bands is included in table 5.1. Several bands show a very good agreement with the Raman bands of the staphylococcus cell-surface, confirming the rich abundance of this sugar on the cell surface.

### 5.4 Dynamics on the bacterial cell surface probed by TERS

As was already mentioned in section 5.3 and shown in figure 5.3 some of the Raman bands from the bacterial surface show variations in intensity and peak position. Therefore, further experiments were performed and without changing the position of the sample successive spectra were taken on one spot on the bacterial surface. As observed before, the Raman bands exhibit variations in intensity and position with time. Figure 5.6 depicts in a false-color plot the evolution of the TERS signal with time on one spot on a cell. The ordinate axis represents the wavenumbers of the spectra and the abscissa shows the progress of time. The intensities of the TERS signal are color coded (high intensities in red and white, low intensities in black and blue). Four spectra recorded at different times (6 s, 14 s, 31 s, and 51 s) are shown on the right panel in figure 5.6B. It can be seen that certain bands experience changes in intensity, disappear and reappear again on a time scale of a few seconds, e.g. the vibrational band at  $1541\text{ cm}^{-1}$  in figure 5.6B, which is most likely an amide II vibration or a coupled ring vibration. This band at  $1541\text{ cm}^{-1}$  is the most prominent feature in the spectrum after 6 s, it hardly visible in the spectrum after 14 s anymore, reappears again in the spectrum after 31 s and is also very prominent in the spectrum after 51 s. This behavior suggests some dynamics taking place on a molecular level. Since the probed volume with TERS is only very small (on the order of  $50 \times 50 \times 10\text{ nm}^3$ ) and the bacterial surface is known to be dynamic it is very likely that a glimpse of the molecular motions on the bacterial surface is caught. Thus some molecules experiencing the strong enhanced field, give rise to a strong TERS signal. Once they move out of the excitation volume these molecules do not contribute to the TERS spectrum anymore causing the TERS signal to decay or disappear. Besides a movement of the molecule of interest out of the range of the evanescent field enhancement, a change in Raman signal can also be caused by a change of orientation. The TERS signal can reappear when the same molecule or a chemical similar fragment moves again into the sample volume. It is not completely clear whether those probed dynamics are some intrinsic properties of the cell surface as Kusumi and coworkers observed them by video enhanced differential interference contrast microscopy

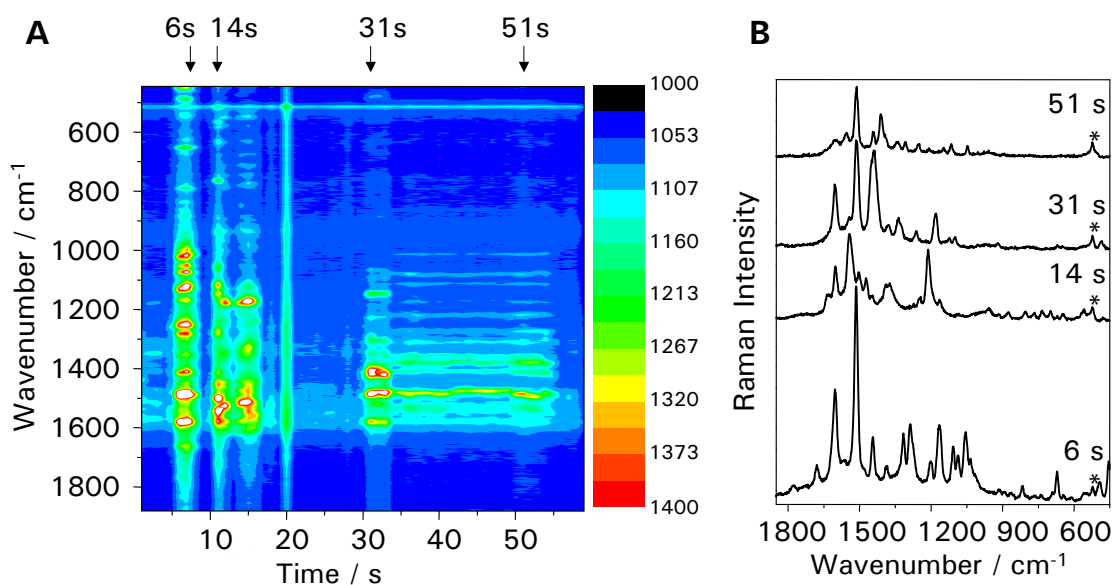


**Figure 5.6:** Evolution of the TERS signal on one spot of the bacterial surface with time **A)** False color plot, **B)** Four different individual TERS spectra from the false color plot in **A)** at four different times.

of labelled proteins within membranes [128, 213, 4], or whether they are induced by the strong localized electromagnetic field of the evanescent field in the proximity of the illuminated tip.

Kudelski and Pettinger reported remarkably fluctuating Raman bands with rather narrow halfwidth due to carbon deposition on SERS substrates [126]. Here, those fluctuating Raman signals are only observed when the tip was placed above a bacterial cell. Therefore, it is very unlikely that the signal variations are due to a carbon-contaminated tip.

## 5.5 TERS of bacteria under special conditions: Cells under argon

Fluctuating signals have also been reported for certain SERS experiments. As a possible explanation hot spot reactions of the metal surface with oxygen were given. In order to rule out this side reaction on the metal tip the cells were purged with pure argon gas while performing the experiment.

The dry argon atmosphere caused the bacterial cells to collapse due to dehydration as can be seen in the pseudo three dimensional image in figure 5.7A, and therefore, the experiment was not carried on. Nevertheless, tip-enhanced Raman spectra could be recorded from the sample surface which also showed slight signal fluctuations in intensity and position. In figure 5.7B an averaged spectrum from one point on the sample surface is shown. The vibrational bands are similar to those reported earlier in this chapter for *S. epidermidis* under ambient conditions (see table 5.1). A more detailed analysis of surface processes associated with the dehydration of the cells is beyond

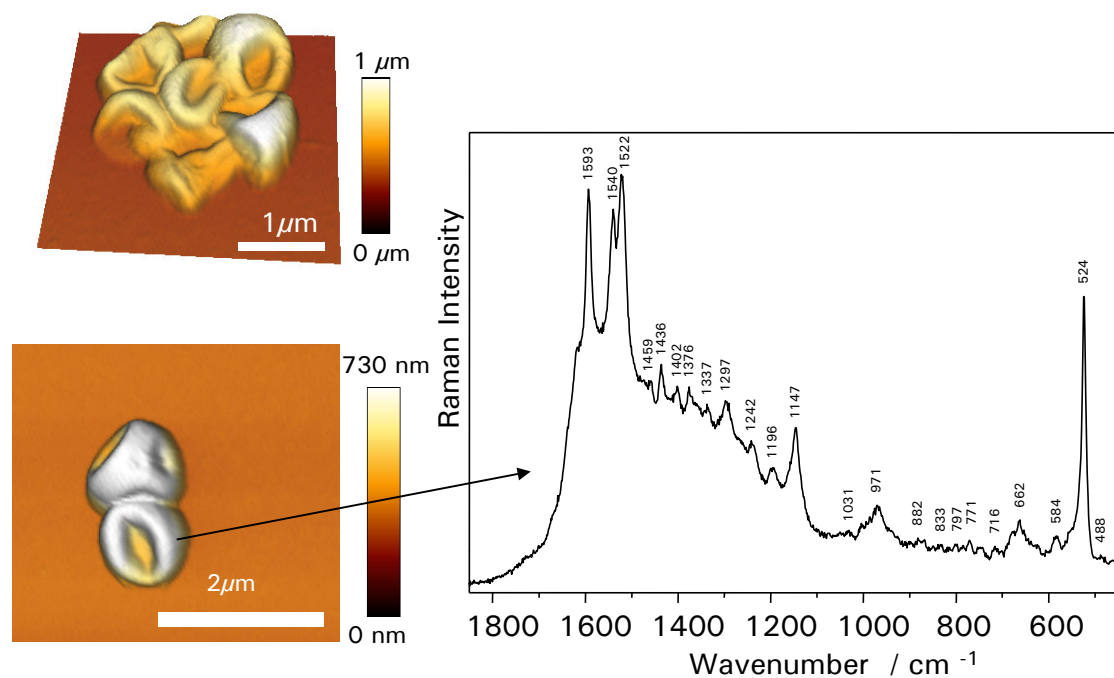


**Figure 5.7:** Pseudo-3D-image **A)** and TERS spectra **B)** of *S.epidermidis* under an argon atmosphere. The dry argon gas caused the cells to collapse.

the scope of this work and more experiments have to be performed to provide trusted results. In future experiments under argon the noble gas should be saturated with water to provide a friendly atmosphere for the bacteria.

## 5.6 Estimation of the enhancement factor

To judge the intensity of the tip-enhancing effect the enhancement factor for the experiments has been estimated from the signal-to-noise ratio (SNR) and the probed sample area and volume to be around  $10^4$ - $10^5$ . It was not possible to directly compare the Raman intensity with and without the tip since in the absence of the enhancing metal tip no Raman spectrum of the bacteria could be recorded under the chosen experimental condition.

An exemplarily estimation of the enhancement factor is given in the following using the TERS spectrum in figure 5.3C. The standard deviation of the signal base line was determined in a reasonably flat section of the spectrum above  $1800\text{ cm}^{-1}$  to be 15 units. For further evaluations three times of that standard deviation was used. The maximum signal of the sample was around  $1190\text{ cm}^{-1}$  with an intensity of 1500 units above the lowest signal level. Using these values gave a signal-to-noise ratio of around 35. No signal could be observed under same experimental con-

ditions (same acquisition time of one second) when the probe was removed. Assuming that the non-enhanced Raman signal could just be not detected leads to a relative enhancement of 35. To estimate the absolute value also the different excitation areas have to be taken into account. The spot diameter of the laser is around 1  $\mu\text{m}$ , as can be estimated from figure 3.6 in section 3.1.5. The active area of the tip should be in the order of magnitude of the apex diameter which is between 20 and 50 nm as estimated from SEM pictures (figure 3.3 in section 3.1.5). This means the enhanced area in the TERS experiment is a factor of 2500 smaller than the actual laser spot resulting in an area corrected enhancement factor of  $1.5 \cdot 10^5$ , or of  $2.4 \cdot 10^4$  when using a tip diameter of 50 nm. The measurements were performed in the intermittent-contact mode of the AFM, meaning that the tip is not in permanent contact with the sample, but rather oscillating up and down with a specific amplitude. The TERS enhancement is strongly distance dependent as discussed in more detail in, for instance, Richards et al. [211] or Nothinger and Elfick [184]. A distance of 5-10 nm away from the sample results in a signal loss between 10-1000 depending on the theoretical models used. Assuming an oscillation amplitude of 6 nm (as selected with the set point) and a linear approximation of the enhancement between the highest and lowest tip position means that half of the time the sample experiences full enhancement and the other half 10-1000 times less. According to this assumption, the net enhancement factor of the probe (if it is closest to the sample surface) is between  $10^6 - 10^8$ . These estimations do not take any chemical enhancement nor the sample thickness into account. The far-field Raman experiment collects signal from the whole cell depth, whereas the TERS is restricted to a very small depth of a few tens of a nanometer. The estimated enhancement factors are roughly in the same order of magnitude as the ones obtained by Stöckle et al. [247] and Pettinger et al. [197].

### 5.7 Possible problems

**Preparation of the enhancing tips** Essential for a high enhancement is the small SERS active metal particle at the tip apex of the AFM tip. In these experiments this was obtained by silver deposition on commercial AFM tips. Even though the silver evaporation procedure is quite controlled the silver coating is not always identical. Therefore, there are always tips which do not give a good enhancement, maybe because they do not have an enhancing silver particle at the tip apex, or because the size and shape of that particle shifts the plasmon resonance to other frequencies so that they could not be excited with the applied laser. A first estimation could be done by characterizing the plasmon resonant frequency of the silver coated tips *by near-field absorption* prior to the experiment. The technique was not available when the experiments have been performed but should be operable soon in the future.

**Pushing of the sample by the tip** All the shown topographies and TERS spectra have been recorded in the intermittent contact mode of the AFM. When using the AFM in the contact mode the staphylococcus cells have been moved by the tip on the glass surface. Figure 5.8 shows the

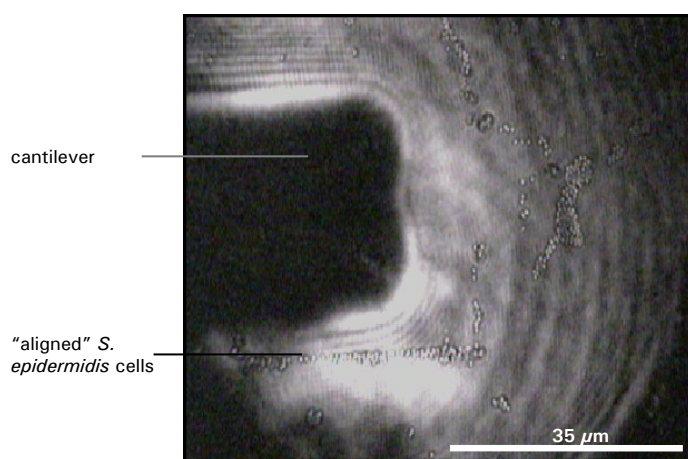


**Figure 5.8:** *S.epidermidis* moved on the glass plate by the AFM tip.

"aligned" bacterial cells (seen as small circles) on the support after the tip has pushed them just outside the scanned region. The black rectangular on the left side of the picture represents the cantilever underneath which the tip is located. This pushing problem has not been observed when investigating *Escherichia coli* cells or using the intermittent contact mode.

**Contamination of the tip** When investigating soft biological material such as bacterial cell surfaces special care has to be taken to avoid a contamination of the probing tip. Figure 5.9 shows a scanning electron microscope (SEM) image of an AFM tip that has picked up parts of the cell material. As the consequence artefacts in the AFM topography image as well as TERS spectra irrespective of the probed sample area have been obtained. One of the easiest ways to confirm a clean tip is to simply detect a TERS signal (or just the background signal) from the clean substrate after it was in contact with the sample. Additional information can be obtained from SEM images of the tip after the experiment. Furthermore AFM images after the TERS measurement can verify intact cells.

## 5.8 Summary and outlook

Tip-enhanced Raman spectroscopy provides valuable chemical information of the bacterial surface with a high spatial resolution below the diffraction limit in a non-invasive manner as was shown for *S. epidermidis* in this chapter. The spectra of the intact surface of the whole cell contain mainly contributions from protein and peptide moieties which is in good agreement with the biological known composition of the outer bacterial layer. Characteristic vibrational bands from N-actylglucosamine, the main building block of the cell wall and of the surface polymers PIA and TA, could be identified in the TERS spectra of the bacteria confirming the rich abundance of this

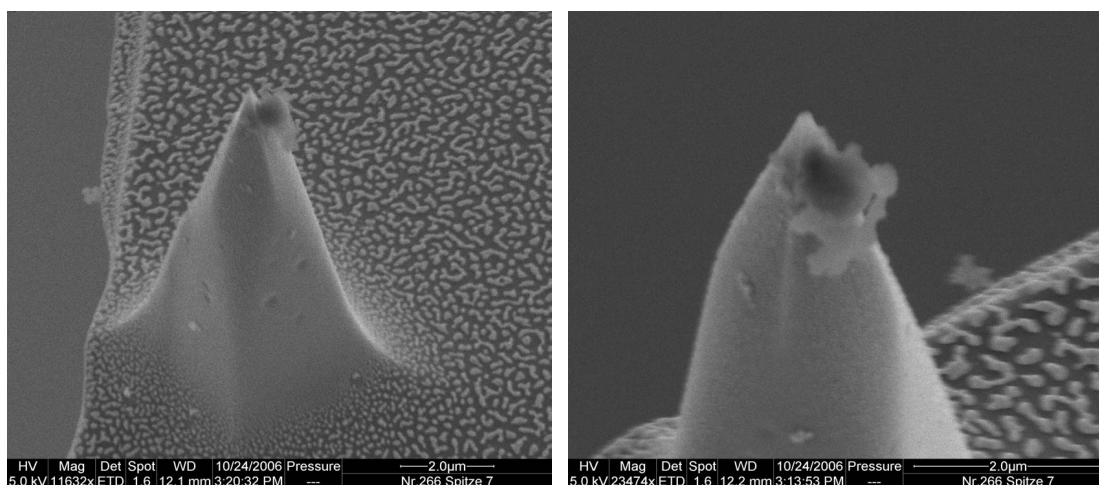


**Figure 5.9:** REM image of contaminated AFM tips after the experiment with attached sample.

compound at the outer layer of the cell. Due to the signal enhancement only short integration times are required to record tip-enhanced Raman spectra with good signal-to-noise ratio. A rough estimation of the enhancement factor from the signal-to-noise ratio (SNR) and the probe sample area and volume results in an overall enhancement on the order of  $10^5 - 10^8$  which is in good agreement with the electric field enhancement estimated by Notinger and Elfrick [184]. The spectra recorded on specified spots on the bacterial surface change on a time scale of a few seconds and might provide a glimpse on the surface dynamics of the cell. However, the influence of the high local electromagnetic field on the surface dynamics has not yet been investigated.

These first experiments using TERS to investigate biological cells raise a lot of further experiments to study a variety of biological and biomedical problems. First of all, other bacterial surfaces such as of Gram-negative bacteria such as for example *Escherichia coli* could be investigated and their spectra compared with those from Gram-positive bacteria. It is also desirable to move to a more natural environment for the bacteria and perform the experiments in solution. The addition of drugs such as  $\beta$ -lactams and glycopeptides should alter the surface of bacteria and when the tip is chemically modified specific drug-target interactions or specific "communication" between different cells might be sensed. Further research effort should also be invested in the production and characterization of reproducible well-defined enhancing tips.

The great potential of tip-enhanced Raman spectroscopy is provided by the rich chemical information with a high spatial resolution while the sample preparation is very easy. It doesn't require any pretreatment and therefore allows the investigation in the natural biological environment. The application of this technique to complex biological systems marks a big step forward towards the investigation of bacterial surfaces without the need of labelling techniques. With the high spatial resolution down to a few 10 nm and the rich structural information of the vibrational spectra obtained by TERS provide new insights into structure details, composition and arrange-

## *5 Tip-enhanced Raman spectroscopy (TERS) of complex biological surfaces*

ment of the individual components on the cell surface can be gained. Such information is crucial for understanding many biological processes and mechanisms, for example, cell recognition, bacterial adhesion, formation of biofilms and bacterial pathogenesis. Furthermore it can be helpful on the way to a detailed elucidation of the mode of action of cell-wall-attacking antibiotics such as  $\beta$ -lactams and glycopeptides, and it might open new perspectives for the design of new drugs.



## 6 Fluoroquinolones – important antibiotics

In the previous two chapters bacteria have been characterized extensively using vibrational spectroscopy and insights have been gained in the metabolic changes during bacterial growth. As bacteria are often the cause of infections, effective methods are desired to fight them. Different types of antibiotics exist which interfere with various vital metabolic processes within the bacteria. This chapter focusses on drugs of the fluoroquinolone type which attack the bacterial enzyme gyrase. A variety of gyrase inhibitors (nalidixic acid, oxolinic acid, cinoxacin, flumequine, norfloxacin, ciprofloxacin, lomefloxacin, ofloxacin, enoxacin, sarafloxacin and moxifloxacin) are investigated by means of micro-Raman spectroscopy excited with various excitation wavelengths, both in the off-resonance region (532, 633, 830 and 1064 nm) and in the resonance region (resonance Raman spectroscopy at 244, 257 and 275 nm). Furthermore DFT calculations are performed to assign the vibrational modes, as well as for an identification of intramolecular hydrogen bonding motifs. The effect of small changes in the drug environment was studied by adding successively small amounts of water until physiological low concentrations of the drugs in aqueous solution were obtained. At these low concentrations resonance Raman spectroscopy proved to be a useful and sensitive technique. Supplementary information was obtained from IR and UV/vis spectroscopy.

### 6.1 Background and history

Quinolones are important and effective agents for the treatment of bacterial infections [15, 102]. Since the discovery of nalidixic acid for the treatment of Gram-negative urinary tract infections in 1962, much effort was invested in the development and improvement of these drugs. New groups were introduced in order to increase the potency of the drugs for a broader class of pathogens and to obtain better pharmacodynamics and pharmacokinetics. Nowadays they are potent antibiotics against Gram-negative and Gram-positive bacteria as well as against problematic germs like chlamydia or anaerobes [194]. Recently they are also used against mycobacteria [254, 253]. In 1994 fluoroquinolone made up 25% of all prescribed antibiotics against bacterial infections.

The development of the quinolones within little more than four decades can be divided into three generations. The first-generation agents derived directly from nalidixic acid and include cinoxacin, oxolinic acid and also the progenitor fluorinated agent, flumequine (the structures are depicted in figure 6.1). They were predominantly used for the treatment of urinary tract infections. The second-generation drugs show an enhanced activity, mainly against Gram-negative pathogens, but also a balanced broad spectrum of activity with increased potency against pneumococci. The

## 6 Fluoroquinolones – important antibiotics

most popular representative of the second-generation agents is ciprofloxacin, which remains the most potent fluoroquinolone against Gram-negative bacterial pathogens, including *Pseudomonas aeruginosa* [16]. In a period of 15 years it has been prescribed more than 340 million times [16, 17, 234]. However, many of the second-generation drugs caused adverse drug reactions in the patients and had to be withdrawn again from the market. The third-generation agents are characterized by markedly increased potency against Gram-positive pathogens yielding minimal inhibition concentrations in the range of 0.06-0.25 mg/L. Moxifloxacin is a popular representative of this generation.

The quinolones inhibit the action of the bacterial enzyme gyrase and thereby causing cell death (for a more detailed description of gyrase and its action see chapter 8). Even though the fluoroquinolones are used as active agents in many antibiotics, the detailed mechanism of action on a molecular level is so far not known. It is of greatest interest to shed light on this drug-target interaction to provide useful information in the fight against growing resistances and obtain new insights for the development of new powerful drugs. To reach this goal, on a first step it is essential to understand the structural characteristics of the drugs and the effects that are caused by the environment in detail.

### 6.2 Structural characteristics of the fluoroquinolones

The common structural element of the fluoroquinolone drugs is the central quinolone unit. It is depicted with the atom numbering in the bottom right corner of figure 6.1. In a few cases, as in nalidixic acid and enoxacin, substitution of the carbon atom at 8-position by a nitrogen atom leads to a naphthyridone skeleton. Figure 6.1 shows the chemical structure of a variety of those drugs from different stages of development. All of them have been investigated within the frame of this work.

Furthermore, the five precursors of the fluoroquinolone moxifloxacin have been included in the study. Their structures are shown in figure 6.2. The precursor structures A, B and C do not have a free carboxyl group in position 3. They did not show any antibacterial activity as was found in antibiotic susceptibility tests (see section 3.2.1). In contrast, the structures D and E, which are the free acids of the esters A and B were highly active against bacteria with minimal inhibition concentrations of less than 0.05 µg/ml, as determined in antibiotic susceptibility tests. It can therefore be concluded that the carboxyl group in position 3 is pivotal in the mechanism of action.

Several modifications were done to the structure of the first quinolone drug nalidixic acid discovered in 1961. Piperazine substitution at the 7-position led to compounds with increased activity, also against *Pseudomonas aeruginosa*, fluorination in 6-position resulted in the fluoroquinolones and gave together with the modification of other side chains enhanced activity against Gram-positive bacteria, improved potency against pneumococcus, improved pharmacokinetic profiles and longer serum half-lives [15].

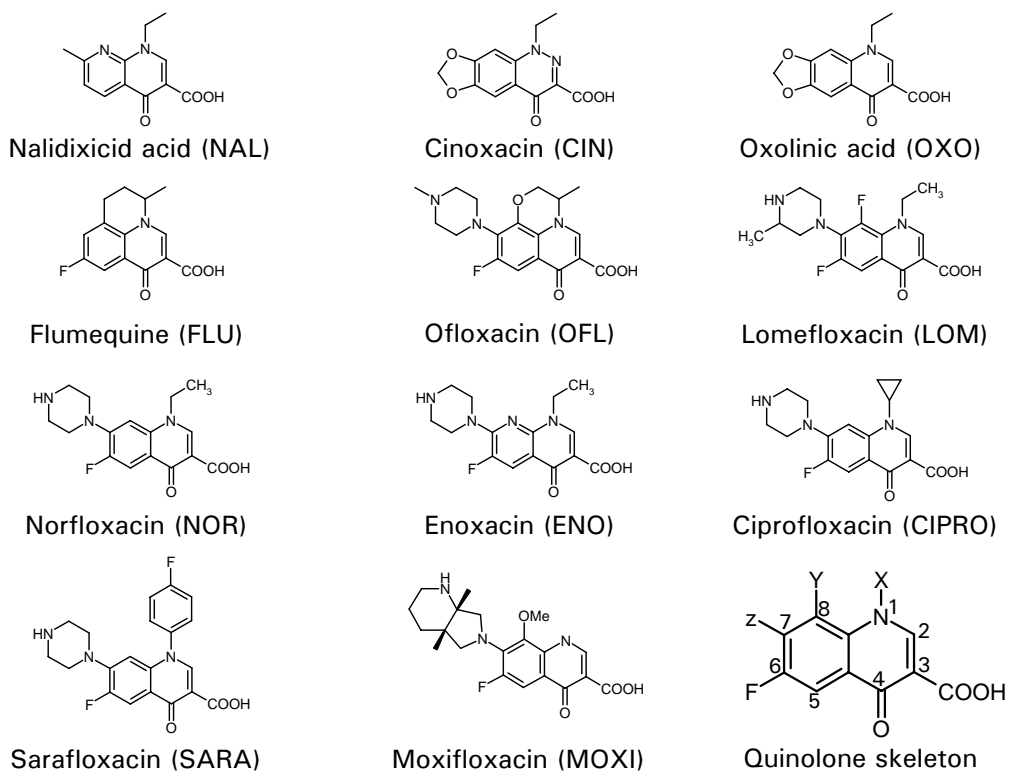


**Figure 6.1:** Chemical structure of the investigated quinolones (yellow: carbon, blue: nitrogen, red: oxygen, white: hydrogen).

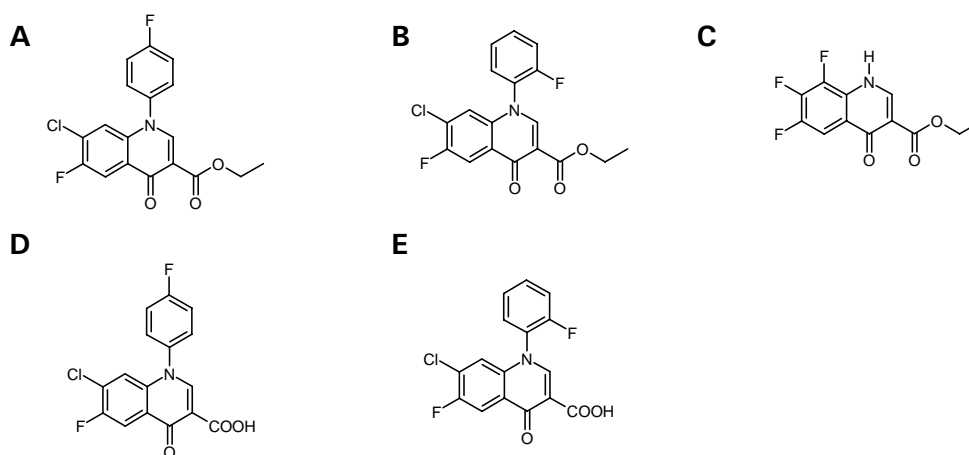


**Figure 6.2:** Chemical structure of five precursors for moxifloxacin.

## 6 Fluoroquinolones – important antibiotics

Moxifloxacin is one of the newer fluoroquinolone drugs which reached the UK market in 2000 as a powerful respiratory agent. The addition of an azabicyclo group in position 7 improves the activity against Gram-positive bacteria, and brings also a marked lipophilicity and half-lives of more than 10 hours [9]. Moxifloxacin retains activity against many staphylococcal isolates that developed resistance to the older fluoroquinolone drug ciprofloxacin [142]. This testifies the recognized fact in pharmaceutical and medical research that the only solution to overcome the threat of growing resistances is to continuously develop new drugs [138]. In order to facilitate target-oriented research new techniques that provide a fast and reliable insight into the molecular mode of action of antibiotics are in high demand.

### 6.3 Proposed mode of action of the fluoroquinolones

Despite many microbiological, chemical and spectroscopic investigations the exact impact mechanism against infectious diseases of the 4-quinolones is not yet fully understood. It is known that the gyrase inhibitors of the quinolone type attack the bacterial gyrase-DNA-complex [88]. This gyrase-DNA-complex is responsible for the supercoiling of bacterial DNA and necessary during bacteria replication (see also chapter 8). The double-stranded DNA is bound to the enzyme, which is formed by two of each subunits GyrA and GyrB. The DNA is cut and both strands are moved against each other so that supercoils are inserted. The disturbance of this process by the quinolones is bactericidal. It was shown that the 4-quinolones neither bind specifically to the enzyme gyrase itself nor to the DNA itself but only to the gyrase-DNA-complex. Models by Shen et al. [238, 239] and Heddle et al. [98] therefore assume the inclusion of the quinolones into the sliced double-stranded DNA. As was found by mutation and resistance experiments the ternary complex with the quinolone is essentially stabilized by the amino acids Ser83 and Asp87, and also Ala67, Gly81 and Gln106 of the GyrA-subunit of the gyrase [18]. These amino acids and Tyr122 are supposed to be part of the binding pocket for the 4-quinolones. Supported by mutational experiments and X-ray structural analysis of the enzyme without DNA [29, 45], it is assumed that there are two binding pockets, one for the intercalation of the 4-quinolone into the DNA, the other for interaction of the drug with Ser83 and Asp87 of the GyrA-subunit of the enzyme [98]. However, the way the quinolones interact with the amino groups is still unclear. They might interact through hydrogen bonding with the 4-oxo-3-carboxyl-group, but this is not yet proved. Even though X-ray crystallography is a powerful tool, it is really problematic to apply it for the elucidation of structure-activity relationships, since this technique shows only a snapshot of the very dynamical process which is accompanied with huge conformational changes of the enzyme during the supercoiling of the DNA. Therefore other techniques like Raman spectroscopy or NMR, for instance, are necessary to gain insight in the mechanism. Lecomte and Baron [130] and Lecomte et al. [131] did some first NMR and surface enhanced Raman (SER) spectroscopic investigations of the system 4-quinolone pefloxacin,  $Mg^{2+}$  and single and double-stranded DNA. These studies showed that pefloxacin-DNA-interactions are enhanced in the presence of  $Mg^{2+}$ , and that a better binding of

pefloxacin to DNA is achieved with double-stranded DNA than with single stranded DNA. In the work of Lecomte et al. [131], only pefloxacin was used as a quinolone and no drug-amino acid interactions were considered. The interaction of quinolone antibacterial agents with metal ions was also reviewed by Turel [260], focussing on thermal analysis, potentiometric measurements, IR-, UV/vis and NMR spectroscopy. Vibrational spectroscopic techniques like Raman spectroscopy represent one of the most useful tools for obtaining information about structure and properties of molecules [195]. However, the assignment of the Raman bands of polyatomic molecules is rather complicated. Theoretical calculations, first of all DFT calculations, are therefore the appropriate tools to obtain a deeper insight into the microscopic atomic displacements of complicated molecules.

In this chapter vibrational spectroscopical and theoretical (DFT calculations) investigations are performed on different quinolones, including quinolones of the first generation (nalidixic acid, cinoxacin), second generation, that are used as standard quinolones nowadays (norfloxacin, ciprofloxacin, ofloxacin, enoxacin) and of the third generation (moxifloxacin, sarafloxacin) (figure 6.1). The understanding of the spectral properties of the quinolones could help to further optimize already existing active agents, and also assist a specific search for new effective structures. Furthermore, the spectroscopic characterization of the quinolones should provide important information towards the identification of the exact target structure on a molecular level and providing the tool to observe the cooperative effects more closely. The ultimate goal is the understanding of the exact mechanism of action of the fluoroquinolones which is so far unknown, but of greatest interest in order to fight growing resistances [98, 101]. In order to accomplish this ambitious goal one has to start with a detailed vibrational spectroscopical characterization of the pure reactive agent (fluoroquinolones) (and also of the isolated biological targets DNA (chapter 7) and gyrase (chapter 8)), since the biological functionality of an agent critically depends on its structure. But not only the pure substance itself, but also its interaction with the environment needs to be understood in detail in order to describe the action of the antibiotics in the real biological environment. Therefore, the artificial environment should be successively changed into a real biological system. In this chapter, in a first step water was added in a well defined manner to the pure substances until biological relevant concentrations were obtained. Furthermore, the influence of different pH values was studied. Raman spectroscopy proved to be a very sensitive tool to monitor even weak inter- and intramolecular interactions of the active agents, e.g. hydrogen bonding. The problem that arises from the really low concentrations of the active agents in solution was overcome by the use of the highly sensitive resonance Raman spectroscopy technique. With the help of DFT calculations vibrational bands could be assigned and the observed spectral changes interpreted. That way it was possible to identify the structure as well as weak interactions between the molecules, e.g. intramolecular H-bonding which once again proved the high potency of vibrational spectroscopy to study the complex interaction phenomena.

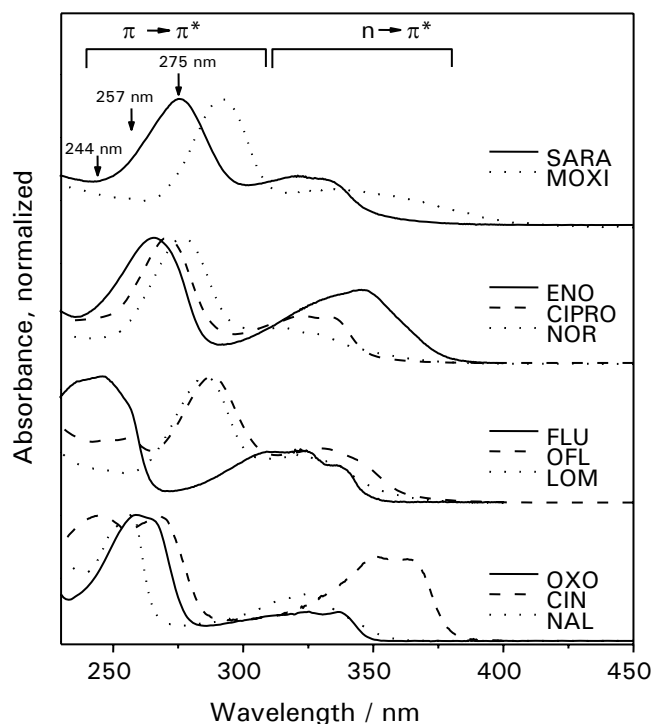


**Figure 6.3:** UV/vis absorption spectra of the quinolones in water.

#### 6.4 UV/vis absorption spectra

All UV/vis spectra of the investigated substances (solutions in water) show a characteristic absorption band between 300 and 380 nm (figure 6.3). A second maximum is observed between 240 and 300 nm which is mainly due to the aromatic ring absorption ( $\pi \rightarrow \pi^*$ -transition). The longest wavelength maximum is due to an  $n \rightarrow \pi^*$  (HOMO-LUMO) electronic transition [244] and consists of two subpeaks which are caused by an equilibrium of the quinolones forming an intermolecular hydrogen bond with the solvent molecule water and quinolones forming an intramolecular hydrogen bond of the 4-keto and the 3-carboxylic acid group.

CIN is the only observed quinolone with a nitrogen atom at 2-position (see figure 6.1) influencing the chromophoric system and resulting in an absorption maximum that is bathochromically shifted compared to the other quinolones.

NAL has the fewest electron-pushing and pulling groups (no F, no piperazyl) of all investigated substances, i.e. its absorption maximum is found blueshifted compared to all other substances.

The quinolones contain one acidic (COOH) and a basic functional group (lone pair at nitrogen) which can be involved into protonation and deprotonation reactions. The  $pK_a$  values associated with the carboxylic acid function range from 5.3 to 6.9 for the observed substances (table 6.1, last column) which is slightly higher than the usual values observed for aromatic carboxylic acids, such as benzoic acid having a  $pK_a$  of 4.2. This decrease in acidity can be attributed to an intramolecular

**Table 6.1:** Absorption maxima (nm) of the quinolones in aqueous solutions at different pH values.

Substance	Acidic pH 2	Neutral pH 7	Basic pH 12	pK <sub>a</sub> (COOH)/pK <sub>a</sub> (N)
nalidixic acid	315	325	335	6.04 <sup>a</sup>
oxolinic acid	335	337	339	6.92 <sup>a</sup>
cinoxacin	354	361	361	5.32 <sup>a</sup>
lomefloxacin	320	320	329	5.82/9.3 <sup>b</sup>
ofloxacin	330	332	332	6.05/8.22 <sup>b</sup>
flumequine	336	336	342	6.30 <sup>a</sup>
norfloxacin	330	334	334	6.3/8.38 <sup>b</sup>
ciprofloxacin	329	334	334	6.09/8.74 <sup>b</sup>
enoxacin	338	345	345	6.31/8.69 <sup>b</sup>

<sup>a</sup> Values reported by Jimenez-Lonzano et al. determined by UV spectra [111]

<sup>b</sup> Values reported by Ross and Riley [219]

H-bond formation of the acidic group with the neighboring keto function resulting in a stabilization of the protonated species. For a physiological pH value (pH~7.4) the molecules exist as a mixture of the neutral and the zwitterionic form [219].

Especially the long wavelength absorption band is sensitive to pH changes. Upon increasing the pH value of the solution a bathochromic shift of the absorption maximum is observed (see Table 6.1). This can be explained by a change of the state of protonation. For low pH values a protonated cationic form is formed, while for intermediate pH values the neutral form and for high pH values the deprotonated anionic form exists. As an example the UV/vis absorption spectra of NOR for different pH values are shown in figure 6.4A.

## 6.5 DFT calculations

Figure 6.4B presents the optimized molecular structure of NOR (top) and its anion (bottom) with the corresponding atom numbering as obtained by DFT calculations. The rigid quinolone ring system is planar; the ethyl group at N1 is sticking out of the plane. The piperazine ring is in the usual chair conformation. As can be seen in figure 6.4B (top), NOR in the solid state forms really strong intramolecular hydrogen bonds between the hydrogen atom of the carboxylic acid and the carbonyl oxygen O4 which causes a lengthening of the C(4) O bond (calc. 1.25 pm). In the anionic form (figure 6.4B (bottom)) the carboxylic group is deprotonated and since hydrogen bonding is not possible anymore, the carboxylic group is rotated along the C3- C11 axis, so that electrostatic repulsions between the two oxygen atoms O1 and O3 are minimized. The plane through the atoms C11, O1 and O2 is rotated by about 36° against the plane through the quinolone rings. The calculated structures resemble the bond distances and angles obtained from X-ray crystallography for several NOR derivatives by Turel et al. [262] and Florence et al. [74]. The analysis of some metal complexes of NOR indicated the presence of two non-equivalent protonated NOR molecules [262]. One of the NOR molecules presents an intramolecular hydrogen bond between the carboxyl and carbonyl groups. The C4=O bond length in a copper complex is 126.6 pm while

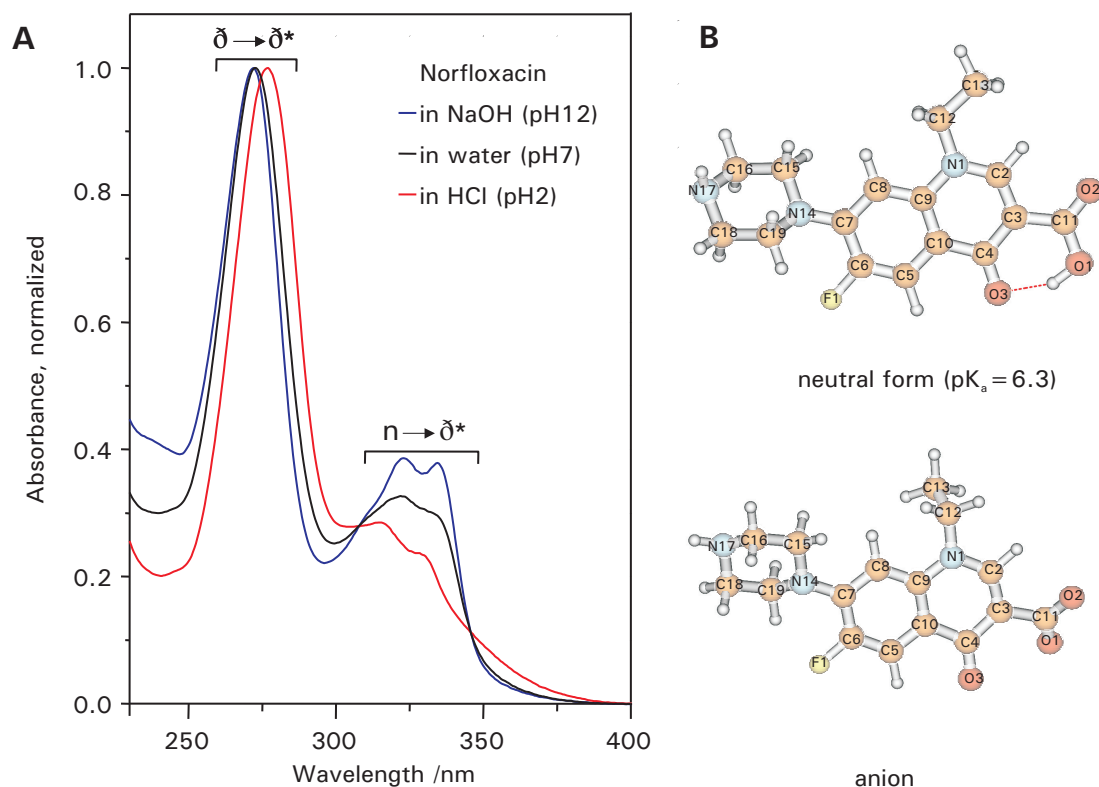


**Figure 6.4:** A) UV/vis absorption spectra of NOR at different pH values (dashed line: NOR in NaOH, pH12; full line: NOR in water, pH 7; dotted line: NOR in HCl, pH 2); B) Optimized structure (B3PW91/6-31+G(p,d)) of NOR (top) and its anion (bottom).

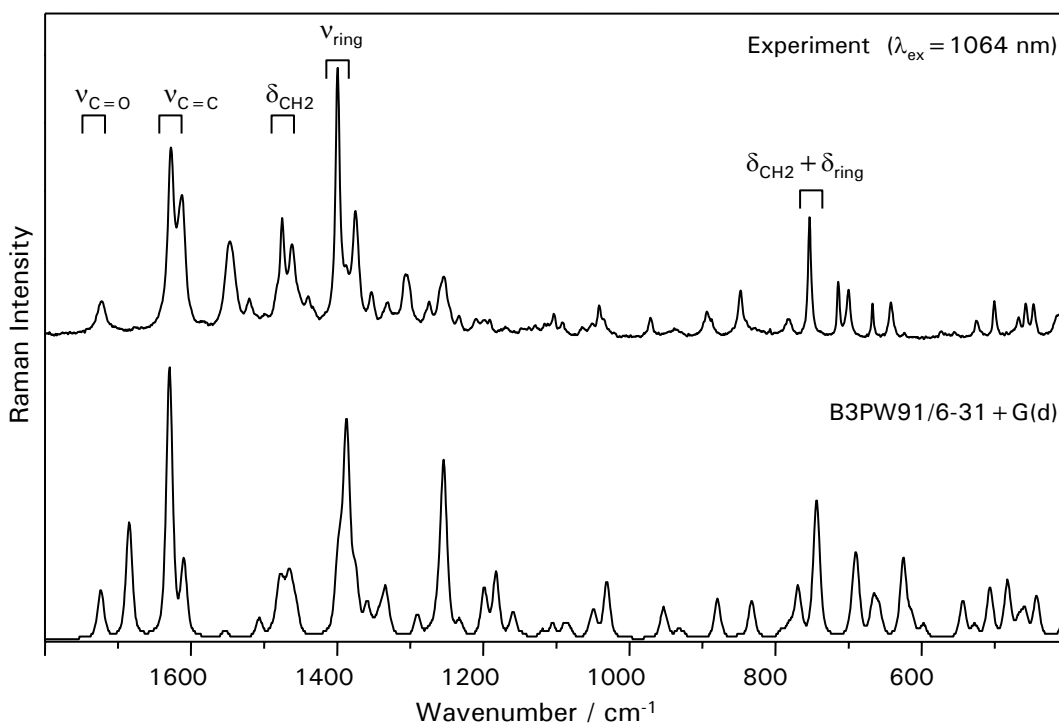
the carboxylic C=O bond is 120.8 pm and the C-O bond is 135.4 pm indicating the very strong intramolecular hydrogen bonding.

## 6.6 Raman spectra of the bulk substances

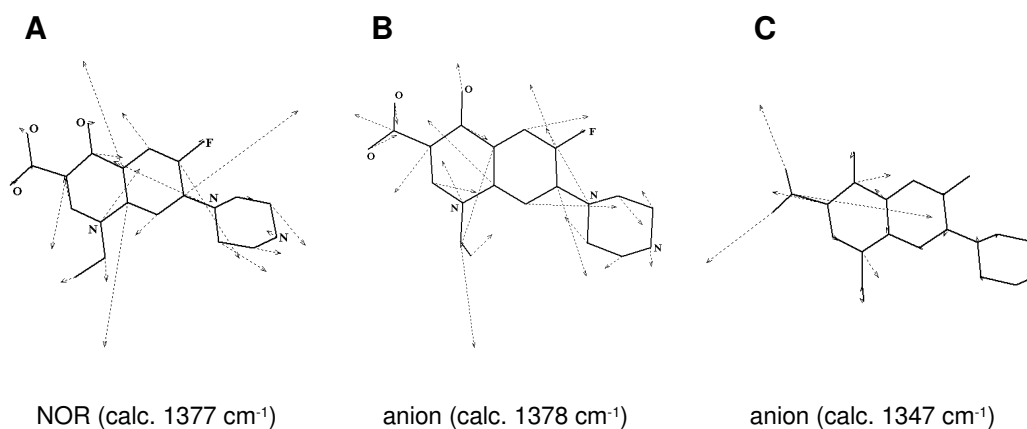
### 6.6.1 Micro-Raman spectra of norfloxacin

Figure 6.5 shows the calculated (DFT) and experimental Raman spectra ( $\lambda_{ex}= 1064$  nm) of NOR being a representative example for the investigation of the quinolones. The calculations resemble well the experimentally observed Raman wavenumbers and intensities. Therefore, the calculations allow for a detailed mode assignment as it can be seen in table 6.2 for NOR. The vibrations of the most intense band at  $1400\text{ cm}^{-1}$  (calc.  $1377\text{ cm}^{-1}$ ) are visualized with a picture of the vibrating molecule in figure 6.6A where the length of the arrows is proportional to the intensity of the vibration.





**Figure 6.5:** Calculated and experimental Raman spectrum ( $\lambda_{ex} = 1064 \text{ nm}$ ) of NOR.



**Figure 6.6:** Some characteristic vibrations of norfloxacin (A) and its anion (B and C), hydrogen atoms are omitted for clarity.

6 Fluoroquinolones – important antibiotics

**Table 6.2:** Detailed vibrational analysis of NOR (some experimental vibrational wavenumbers of CIPRO are also included),  $\lambda_{ex}=1064$  nm, calc. BPW91/6-311+G(d).

Raman CIPRO (cm <sup>-1</sup> )	Raman NOR (cm <sup>-1</sup> )	Raman NOR/ H <sub>2</sub> O (cm <sup>-1</sup> )	calc. (cm <sup>-1</sup> )	vibrational assignment
—	1722w	—	1737	vC11=O2(66) - δCO1-H(9) - δCC3-C11(7)
sh	1627s	1629sh	1615	δ <sup>im</sup> R1,R2(30) - vC5-C6(20) - vC8-C9(10) + vC5-C10(6) - δN1C12C13(5)
1617vs	1612ms	1616vs	1606	vC2-C3(23) - vN1-C2(9) - δ <sup>im</sup> R1(9) - δivN1C12C13(9) + vC4=O(6) v <sup>asym</sup> COO- in CIPRO and hydrated NOR
1591vs	1547m	1584br	1558	vC4=O(39) + δ <sup>im</sup> N1C12C13(15) - δ <sup>im</sup> R1(10) + vN1-C2(7) - vC3-C4(6)
1542vw	1520w		1527	vC6-C7(20) - vC5-C10(19) + vC9-C10(13) + δ <sup>im</sup> R2(8)
1499vw	sh		1491	δ <sup>scis</sup> C12H <sub>2</sub> (40) + δ <sup>im</sup> N1C12C13(36)
			1489	δ <sup>im</sup> N1C12C13(45) + δ <sup>scis</sup> C12H <sub>2</sub> (32)
	1475m		1482	δ <sup>asym</sup> CH <sub>3</sub> (22) + δ <sup>scis</sup> C12H <sub>2</sub> (16) + δ <sup>im</sup> R1(10) + δ <sup>im</sup> CN1-C11(9) + δCO1-H(8) + δ <sup>asym</sup> CH <sub>3</sub> (8)
			1477	δ <sup>asym</sup> CH <sub>3</sub> (66) - δ <sup>asym</sup> CH <sub>3</sub> (21) - δ <sup>rock</sup> CH <sub>3</sub> (7)
			1474	δ <sup>scis</sup> C12H <sub>2</sub> (65) + δN1C12C13(22)
1455w	1462	1459	1467	δCN17H(54) + δ <sup>scis</sup> C15H <sub>2</sub> (13) + δ <sup>scis</sup> C19H <sub>2</sub> (6)
			1458	δ <sup>scis</sup> C15H <sub>2</sub> (42) + δ <sup>scis</sup> C19H <sub>2</sub> (29) - δ <sup>scis</sup> C12H <sub>2</sub> (7)
			1452	δ <sup>im</sup> CO1-H(21) - δ <sup>im</sup> R1(15) - δ <sup>scis</sup> CH <sub>2</sub> (9) - δ <sup>im</sup> CN1-C11(8) + δN1C12C13(6)
1448w			1448	δ <sup>scis</sup> C18H <sub>2</sub> (54) + δ <sup>scis</sup> C16H <sub>2</sub> (25) - δ <sup>scis</sup> C15H <sub>2</sub> (12)
	1440		1445	δ <sup>scis</sup> C19H <sub>2</sub> (39) - δ <sup>scis</sup> C15H <sub>2</sub> (14) + δ <sup>scis</sup> C16H <sub>2</sub> (7) - δ <sup>im</sup> CN1-C11(6)
			1440	δ <sup>scis</sup> C16H <sub>2</sub> (55) + δ <sup>scis</sup> C18H <sub>2</sub> (35)
			1398	δ <sup>im</sup> CN1-C11(47) + δ <sup>wag</sup> C12H <sub>2</sub> (10) + δ <sup>sym</sup> CH <sub>3</sub> (9) + δ <sup>scis</sup> C12H <sub>2</sub> (5)
			1389	δ <sup>sym</sup> CH <sub>3</sub> (31) - δ <sup>im</sup> CN1-C11(18) + δ <sup>im</sup> R1(8) - nC8-C9(6)
1382vs	1400vs	1392	1377	vC9-C10(15) - vN1-C9(8) + vC7-C8(8) - vC7-N14(7) - vC5-C6-C7(10) - δ <sup>im</sup> CN1-C11(5)
	1388sh		1371	δ <sup>wag</sup> C19H <sub>2</sub> (27) + δ <sup>wag</sup> C15H <sub>2</sub> (13) + δ <sup>im</sup> CN1-C11(5)
1364m	1375m	1381sh	1367	δ <sup>wag</sup> C16H <sub>2</sub> (9) + δ <sup>wag</sup> C12H <sub>2</sub> (9) - vC6-C7(8) + vC7-C8(8) + vC9-C10(7) - δ <sup>sym</sup> CH <sub>3</sub> (7)
			1361	δ <sup>wag</sup> C16H <sub>2</sub> (15) + δ <sup>wag</sup> C18H <sub>2</sub> (15) + δ <sup>wag</sup> C19H <sub>2</sub> (7) + vC3-C4(5)
	1353w		1345	δ <sup>wag</sup> C18H <sub>2</sub> (17) + δ <sup>wag</sup> C15H <sub>2</sub> (12) - vC5-C10(8) + δ <sup>wag</sup> C19H <sub>2</sub> (8) + δ <sup>twist</sup> C16H <sub>2</sub> (8) + vC7-N14(5)
	1331vw		1335	δ <sup>wag</sup> C16H <sub>2</sub> (27) + δ <sup>twist</sup> C19H <sub>2</sub> (10) + δ <sup>wag</sup> C18H <sub>2</sub> (8) - vC7-C8(6) + vC5-C10(6)
			1323	δ <sup>wag</sup> C15H <sub>2</sub> (29) + δ <sup>wag</sup> C18H <sub>2</sub> (19) + δ <sup>wag</sup> C19H <sub>2</sub> (17) + δ <sup>wag</sup> C16H <sub>2</sub> (9)
			1322	δ <sup>twist</sup> C16H <sub>2</sub> (23) + δ <sup>twist</sup> C18H <sub>2</sub> (20) + δ <sup>wag</sup> C19H <sub>2</sub> (12) + δ <sup>wag</sup> C15H <sub>2</sub> (9)
	1306br		1307	δN1C12C13(55) - δ <sup>im</sup> CN1-C11(11) + vN1-C2(6) - vN1-C9(6) + δ <sup>wag</sup> C12H <sub>2</sub> (5)
			1301	δ <sup>twist</sup> C12H <sub>2</sub> (82) - δ <sup>rock</sup> CH <sub>3</sub> (7)
1264	1274vw	1269	1288	vC3-C11(9) + vN1-C12(9) - vC3-C4(8) + vC4-C10(7) - δ <sup>im</sup> CC2H(7) + δ <sup>im</sup> R1(7) + vC5-C10(6) - vN1-C9(5)
			1256	δ <sup>twist</sup> C19H <sub>2</sub> (19) + δ <sup>twist</sup> C18H <sub>2</sub> (12) + δ <sup>twist</sup> C16H <sub>2</sub> (11) + vC5-C10(5)
	1254w		1250	δ <sup>twist</sup> C15H <sub>2</sub> (27) - δ <sup>im</sup> CN1-C11(10) + nC7-N14(7) + δN1C12C13(5) - nC7-C8(5) - δ <sup>im</sup> CC2H(5) + δ <sup>wag</sup> C16H <sub>2</sub> (5)
	1233vw		1235	δ <sup>im</sup> CC8H(21) + δ <sup>im</sup> N1C12C13(12) - δ <sup>im</sup> CC5H(11) - δ <sup>im</sup> CN1-C11(10) + δ <sup>im</sup> R1(7) - nC8-C9(7)
			1192	δN1C12C13(10) + δ <sup>twist</sup> C19H <sub>2</sub> (9) - δ <sup>im</sup> R2(13) - vC4-C10(7) - vC6-F(7) - vC11-O1(6) - vN14-C15(5)
			1187	δ <sup>twist</sup> C15H <sub>2</sub> (23) δ <sup>twist</sup> C18H <sub>2</sub> (14) + δ <sup>twist</sup> C19H <sub>2</sub> (10)
			1179	vC11-O1(13) - vN1-C9(13) + vN1-C12(10) + δ <sup>im</sup> CC2H(10) - δN1C12C13(7) + δ <sup>im</sup> R2(6)
			1153	δN1C12C13(31) - δ <sup>im</sup> CN1-C11(11) - vC11-O1(8) + vN14-C15(7) - vN14-C19(5)
			1145	δN1C12C13(25) - δ <sup>im</sup> CN1-C11(16) + vN14-C19(6) + vC6-F(5)
			1130	δ <sup>rock</sup> C12H <sub>2</sub> (43) + δ <sup>rock</sup> CH <sub>3</sub> (31) - δ <sup>out</sup> CN1C11(7) + δ <sup>twist</sup> C12H <sub>2</sub> (6)
			1121	δ <sup>out</sup> R3(13) - δ <sup>rock</sup> C15H <sub>2</sub> (11) + δ <sup>rock</sup> C16H <sub>2</sub> (10) + δ <sup>rock</sup> C18H <sub>2</sub> (10)
1104vw			1111	vN17-C18(26) - vC16-N17(22) + vC15-C16(10) + vN14-C19(9) - vN14-C15(8) - vC18-C19(7)
1092vw			1091	δN1C12C13(52) - δ <sup>im</sup> CN1-C11(25) + δ <sup>im</sup> CC12-C13(10)
			1082	δN1C12C13(40) - δ <sup>im</sup> CN1-C11(24) + δ <sup>im</sup> CC12-C13(11)
	1041w		1045	δN1C12C13(40) + δ <sup>im</sup> CC12-C13(35) + δ <sup>rock</sup> CH <sub>3</sub> (5)
			1018	δ <sup>im</sup> R3(21) + δ <sup>rock</sup> C16H <sub>2</sub> (12) - δ <sup>rock</sup> C15H <sub>2</sub> (12) + δ <sup>im</sup> R2(7)
			1006	δ <sup>rock</sup> C19H <sub>2</sub> (22) + δ <sup>rock</sup> C16H <sub>2</sub> (17) - δ <sup>rock</sup> C15H <sub>2</sub> (12) + δ <sup>rock</sup> C18H <sub>2</sub> (8) + δCN14H(7) - δ <sup>out</sup> R3(6)
			1002	vC18-C19(20) + vC15-C16(18) - vN14-C19(10) - vN14-C15(8) - δ <sup>im</sup> R3(15)
	971w		968	δ <sup>im</sup> CN1-C11(30) + nC12-C13(23) + δ <sup>im</sup> R1(9) + δ <sup>im</sup> CC12-C13(7) + δ <sup>rock</sup> CH <sub>3</sub> (6)
			927	vC16-N17(10) + δ <sup>im</sup> R1,2(17) - vN14-C19(8) + vN17-C18(7) - vN14-C15(7) - vC12-C13(6)
			915	δ <sup>out</sup> CC2H(64) - δ <sup>out</sup> CC3-C11(16) + δ <sup>out</sup> R1(13)
			909	vC15-C16(28) - vC18-C19(19) - δ <sup>out</sup> CC7-N14(9)
	894w		888	δ <sup>out</sup> CC5-H(65) - δ <sup>out</sup> R2(24)
			875	δ <sup>im</sup> R1(16) - δN1C12C13(11) - δ <sup>rock</sup> C15H <sub>2</sub> (6)
	848w		849	δ <sup>out</sup> CO1-H(94)
			838	δN1C12C13(24) - δ <sup>im</sup> CN1-C11(24) + δ <sup>im</sup> R1,2(12)
			819	δ <sup>rock</sup> C16H <sub>2</sub> (14) - δ <sup>rock</sup> C12H <sub>2</sub> (11) + δ <sup>rock</sup> CH <sub>3</sub> (10) + δ <sup>rock</sup> C19H <sub>2</sub> (8) - δ <sup>out</sup> CC8H(6)
			816	δ <sup>rock</sup> C12H <sub>2</sub> (20) - δ <sup>rock</sup> CH <sub>3</sub> (18) - δ <sup>out</sup> CC7-N14(7) + δ <sup>rock</sup> C16H <sub>2</sub> (6) + δ <sup>out</sup> CC8H(5)
	783vw		781	δ <sup>out</sup> CC7-N14(33) + δ <sup>out</sup> R2(19) - δ <sup>out</sup> CC8H(12)
			776	δ <sup>out</sup> CN17H(24) + δ <sup>out</sup> CC7-N14(14) - δ <sup>out</sup> CC8H(9) + δCN17H(9) + δ <sup>out</sup> R2(8) - vN17-C18(7) - vC16-N17(7)
			769	δ <sup>out</sup> CC7-N14(13) + δ <sup>out</sup> R2(9) - δ <sup>out</sup> CC8H(8) - δN1C12C13(8) + δ <sup>im</sup> R1(13)
			746	δN1C12C13(40) - δ <sup>im</sup> CN1-C11(26) - δ <sup>im</sup> R1(9)
			741	δ <sup>out</sup> R1,2(33) - δ <sup>out</sup> CC3-C11(22) + δ <sup>out</sup> CC11=O(12) + δ <sup>out</sup> CC11-O(12) - δ <sup>out</sup> CC4=O(8)
	714w		705	δ <sup>out</sup> R1,2(69) - δ <sup>out</sup> CC4=O(7)
	700w		696	δN1C12C13(53) - δ <sup>im</sup> CN1-C11(18) - δ <sup>im</sup> R2(5)
			687	δ <sup>out</sup> CC7-N14(37) + δ <sup>out</sup> R2(30) - δ <sup>out</sup> CC6-F(7)
	667w		682	δ <sup>out</sup> R2(24) + δ <sup>out</sup> CC7-N14(22) - δ <sup>im</sup> CC12-C13(10) - δ <sup>out</sup> CC6-F(6) + δ <sup>im</sup> CC11=O(5) - δ <sup>im</sup> CC11-O(5)
	642w		631	δ <sup>out</sup> R1,2(68) - δ <sup>out</sup> CN1C11(8)
	624		617	δ <sup>im</sup> CN1-C11(19) - δ <sup>out</sup> R1,2(37) - δN1C12C13(13) + δ <sup>out</sup> R2(8)
			606	δ <sup>im</sup> R1(33) + δ <sup>im</sup> CC7-C14(5)
	525		554	δN1C12C13(33) - δ <sup>im</sup> CN1-C11(20) - δ <sup>im</sup> R3(7)
			539	δN1C12C13(57) - δ <sup>im</sup> CN1-C11(36)
	500w		490	δ <sup>out</sup> R1,2(64) + δ <sup>out</sup> CC3-C11(14) + δ <sup>out</sup> CN1C11(12)
			474	δN1C12C13(53) + δ <sup>im</sup> CC12-C13(30) - δ <sup>im</sup> CN1-C11(11)
	467vw		470	δ <sup>im</sup> R3(31) + δN1C12C13(26) + δ <sup>im</sup> CC12-C13(15) - δ <sup>im</sup> CN1-C11(5)
	457w		454	δ <sup>out</sup> CC7-N14(59) - δ <sup>out</sup> R2(14)
	447w		451	δ <sup>im</sup> CC12-C13(44) + δ <sup>im</sup> CN1-C11(19) - δ <sup>im</sup> R1(6)
	401vw		426	δ <sup>im</sup> CC12-C13(40) + δN1C12C13(17) + δ <sup>im</sup> CC4=O(8)
	394vw		389	δ <sup>out</sup> R3(46) + *** (10) - δ <sup>out</sup> R2(6) + δN1C12C13(5) + δ <sup>im</sup> CC7-C14(5)
	377vw		376	δ <sup>out</sup> R1,2(44) - δ <sup>out</sup> CC3-C11(15) - δN1C12C13(8) + δR2,3(6)
			359	δN1C12C13(42) - δ <sup>im</sup> R1(18) - δ <sup>im</sup> CC4=O(8) + δ <sup>im</sup> CC12-C13(6)
			348	δN1C12C13(47) - δ <sup>im</sup> CN1-C11(24)
			334	τR1,2(22) - δN1C12C13(22) + δ <sup>out</sup> CN1C11(22) - δ <sup>out</sup> CC3-C11(7) + δ <sup>im</sup> CN1-C11(6)
	316w		317	δN1C12C13(59) + δ <sup>im</sup> CC12-C13(30) - δ <sup>im</sup> CN1-C11(5)
			297	δ <sup>im</sup> CC12-C13(44) + δN1C12C13(26)
			289	δ <sup>out</sup> R1,2(42) - δ <sup>out</sup> CC3-C11(13) + δ <sup>im</sup> CC12-C13(12)
			266	τR1,2(29) - δ <sup>out</sup> CC3-C11(20) - δ <sup>im</sup> CC12-C13(11) - δ <sup>out</sup> R3(11) + δ <sup>out</sup> CN1C11(5)
			250	δ <sup>im</sup> CC12-C13(30) + δ <sup>out</sup> R3(13) - δ <sup>out</sup> CC3-C11(10) + δN1C12C13(7) + δ <sup>im</sup> CN1-C11(6)
	242w		233	δ <sup>out</sup> CC3-C11(15) + δ <sup>out</sup> R1,2(31) + δ <sup>im</sup> CC12-C13(10) - δ <sup>out</sup> CN1C11(6)
	217w		207	δ <sup>im</sup> CC12-C13(66) + δ <sup>im</sup> CN1-C11(19) + δN1C12C13(10)

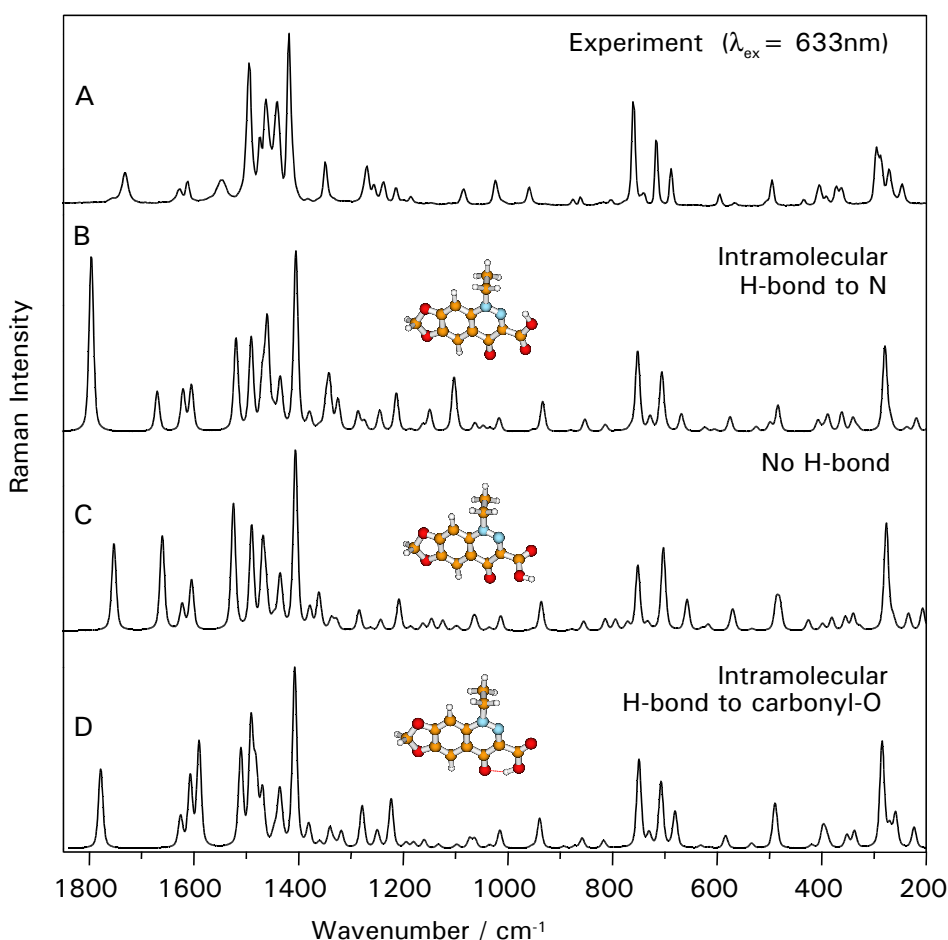


**Figure 6.7:** Calculated Raman spectra of different conformation of CIN in comparison with measured Raman spectra of the solid sample: **A**) experimental spectrum of CIN ( $\lambda_{ex} = 633$  nm); **B**) calculated for CIN with intramolecular H-bond to N2; **C**) CIN without H-bond; **D**) CIN with intramolecular H-bond to the carbonyl-O.

Very rarely a vibrational band is only due to two vibrating atoms. Most of the time it involves a larger number of internal coordinates (many atoms). An exception are the C=O stretching vibration around  $1700\text{ cm}^{-1}$ , the CH vibrations above  $2900\text{ cm}^{-1}$  and a few CH vibrations around  $900\text{ cm}^{-1}$ .

### 6.6.2 Assignment of hydrogen bonding in the fluoroquinolones

DFT calculation can also be useful for an assignment of intermolecular hydrogen bonding. As an example the calculations for CIN are shown in figure 6.7. Besides the hydrogen bond between the carboxylic group and the adjacent keto group (figure 6.7D), which is possible in all observed quinolones, in CIN also hydrogen bonding to the nitrogen in position 2 of the quinolone ring is conceivable (figure 6.7B). Comparison with the measured Raman spectrum of solid CIN (figure

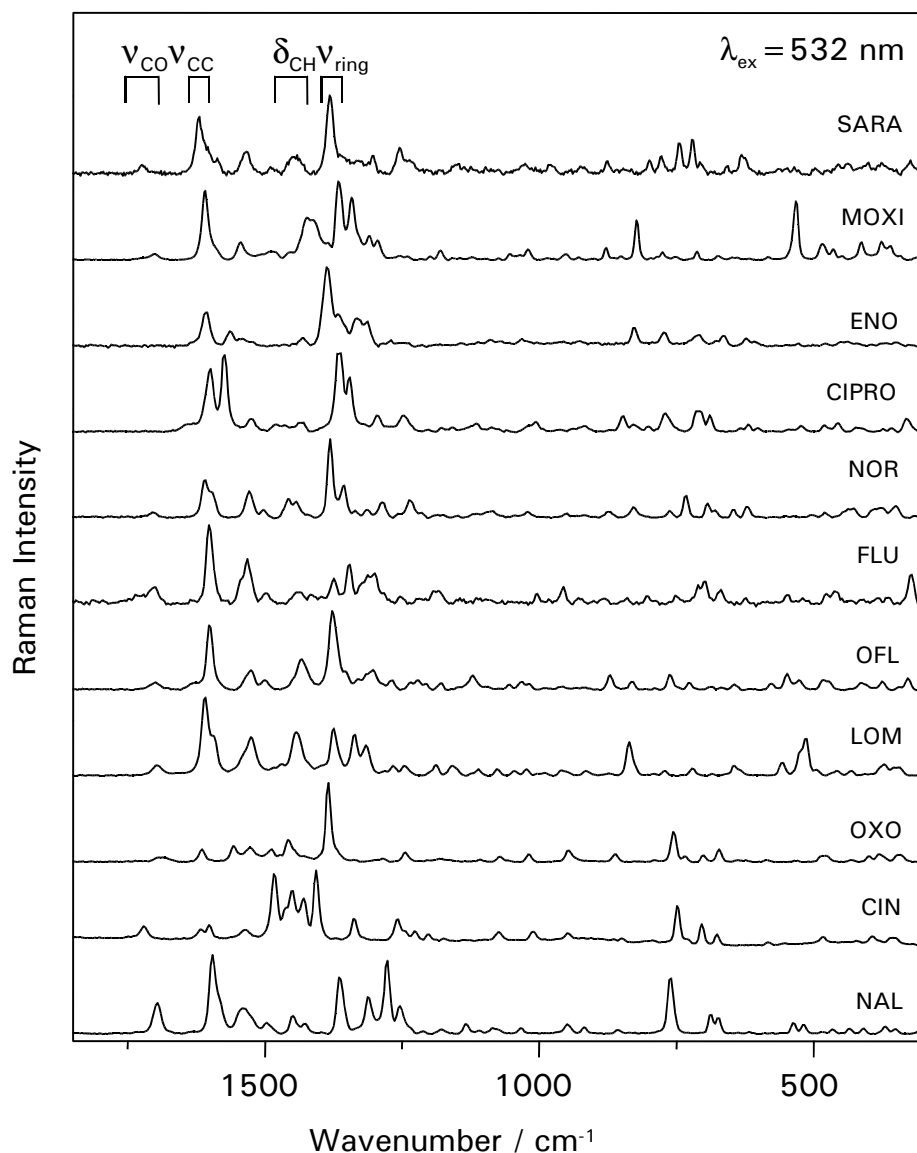


**Figure 6.8:** Raman spectra of different quinolone derivatives ( $\lambda_{\text{ex}} = 532 \text{ nm}$ ).

6.7A) shows best agreement with the calculated spectrum of CIN forming an intramolecular hydrogen bond to the adjacent keto group indicating that in bulk substance CIN mainly exists with an intramolecular hydrogen bond to the keto oxygen. This is in good agreement with the observed decrease of acidity of the carboxylic group. Similar calculations were performed for the other quinolones showing that the formation of an intramolecular hydrogen bond is favorable, because a stable 6-membered ring is formed, which leads to the geometric structure with the lowest energy (energetically favored species).

**Table 6.3:** Some characteristic Raman wavenumbers of the quinolone in the solid state.

Substance		$\nu_{CO}$ ( $\text{cm}^{-1}$ )	$\nu_{CC}$ ( $\text{cm}^{-1}$ )	$\nu_{CO}$ ( $\text{cm}^{-1}$ )	$\delta_{CH_2}$ ( $\text{cm}^{-1}$ )	$\nu_{ring,ip}$ ( $\text{cm}^{-1}$ )	$\delta_{out}$ ( $\text{cm}^{-1}$ )
Nalidixic acid	NAL	1714	1614	1560	1465	1380	779
Oxolinic acid	OXO	1710	1632	1575	1476	1403	773
Cinoxacin	CIN	1741	1621	1555	1503	1424	768
Lomefloxacin	LOM	1714	1625	1542	1549	1392	788
Ofloxacin	OFL	1717	1619	1543	1452	1395	779
Flumequine	FLU	1718	1619	1549	1473	1390	767
Norfloxacin	NOR	1722	1612	1547	1475	1400	777
Ciprofloxacin	CIPRO	–	1617	1591	1448	1382	786
Enoxacin	ENO	–	1621	1579	1446	1402	787
Moxifloxacin	MOXI	1702	1611	1544	1422	1367	823
Sarafloxacin	SARA	1724	1622	1533	1448	1382	721

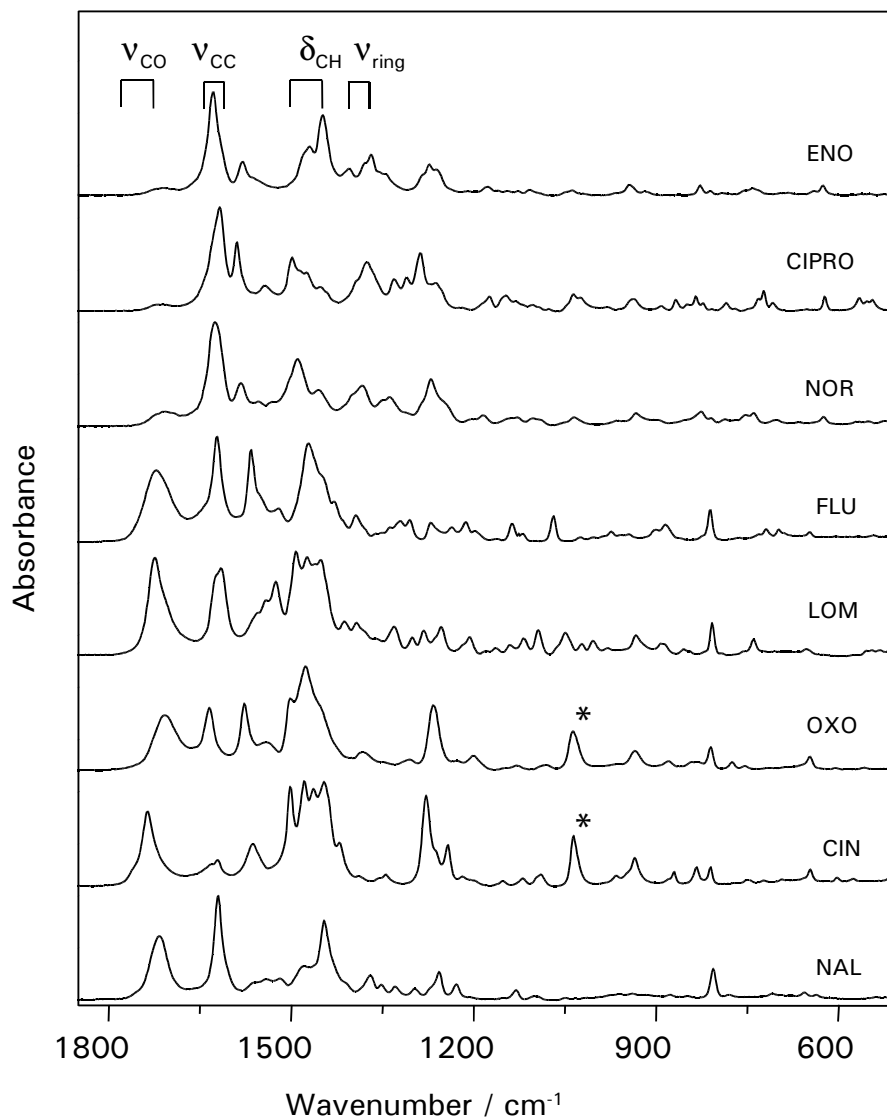
### 6.6.3 Raman spectra of the other fluoroquinolones

Figure 6.6.3 presents the bulk Raman spectra of different quinolone derivatives. A typical feature found in the spectra of all investigated quinolones is the strong band around  $1400 \text{ cm}^{-1}$ . This band was assigned to the stretching vibration of the quinolone ring system ( $\nu_{ring}$ ). Depending on the substituents the wavenumber is shifted slightly ranging from  $1380 \text{ cm}^{-1}$  in NAL to  $1424 \text{ cm}^{-1}$  in CIN (Table 6.3). The weak C=O stretching vibration of the carboxyl group ( $\nu_{CO}$ ) is found between  $1700$  and  $1725 \text{ cm}^{-1}$  for almost all quinolones. In CIN an unusual high wavenumber value was found for this vibration ( $1741 \text{ cm}^{-1}$ ) which might be due to the nitrogen in the 2- position of the ring system which has an influence on the distribution of the electrons in the molecule and due to a weaker intramolecular hydrogen bonding. For CIPRO and ENO the C=O vibration around  $1700 \text{ cm}^{-1}$  could not be observed at all indicating that these two compounds exist as zwitterions in the crystalline state. X-ray analysis of water complexes of CIPRO proved the preference of the zwitterions in the polycrystalline state. The carboxylic proton is here found at the terminal piperazine nitrogen atom. For zwitterionic CIPRO the corresponding C=O bond lengths are 125.1, 125.1 and 125.4 pm, for the C4=O bond, the carboxylic C=O and the C-O bond, respectively [261]. Other characteristic vibrational bands that can be found in the Raman spectra of the investigated quinolones are the C=C stretching vibration of the aromatic rings ( $\nu_{CC}$ ) around  $1620 \text{ cm}^{-1}$ , and the CH-bending vibrations ( $\delta_{CH}$ ) in the region between  $1440$  and  $1500 \text{ cm}^{-1}$ . Since all the investigated quinolones possess a similar molecular frame (figure 6.1) they show similar characteristic features in the Raman spectra. Nevertheless, each of the active agents can be distinguished by its own spectral fingerprint and individual features.

### 6.7 IR absorption spectra of the bulk substances

Complementing the Raman spectroscopic investigations, IR spectroscopy was employed as another vibrational spectroscopic technique to record spectra of the solid quinolones in KBr (figure 6.9). Since the investigated molecules possess C1-symmetry, the vibrations of the molecules are

## 6 Fluoroquinolones – important antibiotics



**Figure 6.9:** IR absorption spectra of the quinolones (\* denotes the C-O vibration of the cyclic ether).

both, IR and Raman active. However, different selection rules result in different intensities with respect to the Raman spectra, but nevertheless, the same characteristic features of the quinolones can be observed: the C=O stretching vibration of the carboxyl group ( $\nu_{CO}$ ) around 1715 cm<sup>-1</sup>, the C=C stretching vibration of the aromatic rings ( $\nu_{CC}$ ) around 1620 cm<sup>-1</sup>, the CH-bending vibrations ( $\delta_{CH_2}$ ) in the region between 1440 and 1500 cm<sup>-1</sup> and the stretching vibration of the quinolone ring system ( $\nu_{ring}$ ) around 1400 cm<sup>-1</sup>, just to name a few of them.

Nevertheless, vibrational spectroscopy is also very well suited to point out the characteristic structural differences of the observed quinolones. As an example the C-O vibration of the cyclic ether at 1037 cm<sup>-1</sup> in OXO and CIN is pointed out (asterisk near the vibrational band in figure

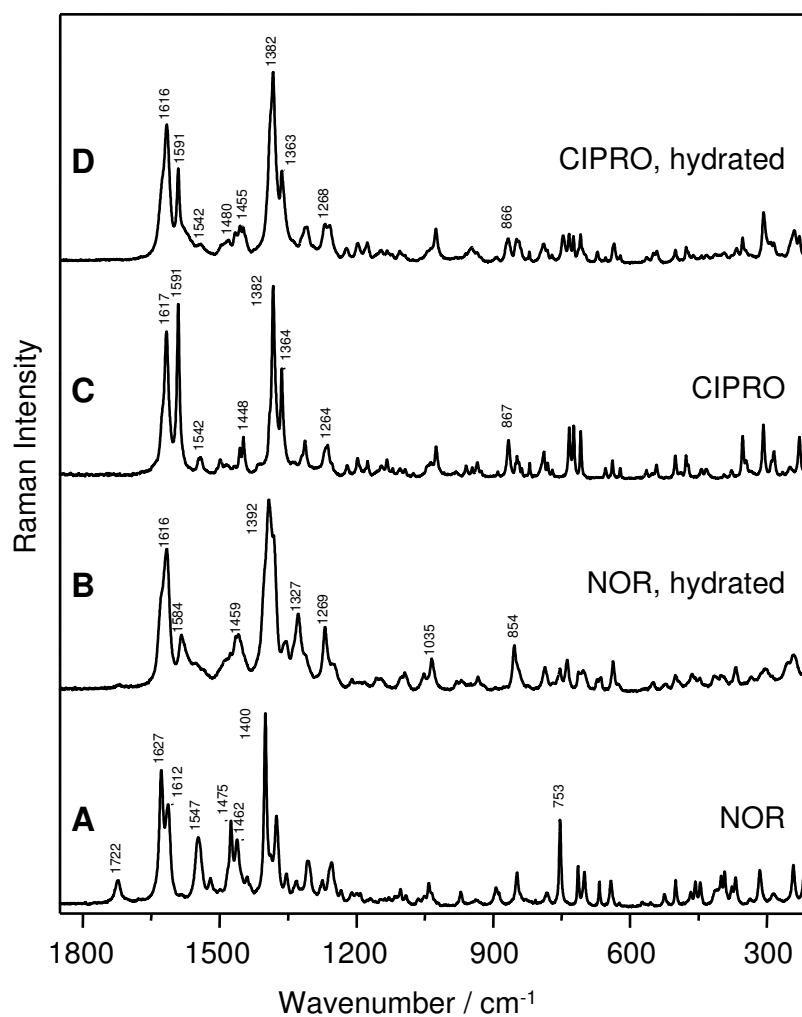


**Figure 6.10:** FT-Raman spectra of anhydrous and hydrated norfloxacin and ciprofloxacin ( $\lambda_{ex} = 1064$  nm).

6.9). Only in these two quinolones this cyclic ether is present and only here this vibrational band is observed.

## 6.8 Raman spectra of the quinolones in hydrated environment

Since the ultimate goal of this work is to elucidate the detailed interaction of the quinolones with their biological targets, it is very crucial to understand the effects that are caused by small changes of the drug environment. In the cell environment water plays an important role as a solvent. Therefore, the first step in successively getting from the pure crystal phase (artificial environment) towards the biological environment is to add water molecules to the bulk substances in a well defined manner. This can be achieved by the addition of crystal water. Raman spectroscopy as a vibrational spectroscopic technique is very sensitive for such slight changes in the environment and

## 6 Fluoroquinolones – important antibiotics

with the help of DFT calculations the observed spectral changes of band positions and intensities will shed light on the specific drug-solvent interactions on a molecular level.

Figure 6.10 presents the FT-Raman spectra of anhydrous and hydrated NOR (figure 6.10A and B) and CIPRO (figure 6.10C and D). In the spectra of the hydrated species (figure 6.10B and D) a broadening of the vibrational bands occurs, while the spectra of the crystalline compounds are characterized by sharp bands.

Significant changes in the Raman spectra can be observed for NOR upon hydration. The most striking difference between the Raman spectrum of anhydrous NOR and the hydrated species is the disappearance of the band at  $1722\text{ cm}^{-1}$  upon solvation (figure 6.10A and B). This band corresponds to the C=O stretching mode of the carboxyl unit (table 6.2). Nevertheless, carboxylic C=O stretching modes usually arise around  $1750\text{ cm}^{-1}$ . The relatively low wavenumber observed for the carboxylic vibration in the Raman spectrum for NOR indicates a strong intramolecular hydrogen bonding with the neighbouring pyridone C=O group. The absence of this band in the spectrum of the hydrated species indicates the deprotonation of the carboxylic group when water molecules are added and the formation of an anionic or zwitterionic species.

CIPRO already exists in the anhydrous state as a zwitterion. Therefore, the structural changes upon addition of crystalwater are not very significant which is reflected in the great similarity of the spectra of anhydrous and hydrated CIPRO. Here, the carboxylic group is deprotonated from the beginning and therefore, this vibrational band is not observed in CIPRO at all. In Table 6.2 some of the experimental vibrational bands of CIPRO are added.

Interestingly, the DFT calculations for NOR predict the C=O stretching mode of the pyridone group at very low wavenumbers ( $1558\text{ cm}^{-1}$ , see table 6.2) because of the very strong intramolecular hydrogen bonding. Support for this assignment is found in the experiment, where the band at  $1547\text{ cm}^{-1}$  is shifted to  $1584\text{ cm}^{-1}$  (see figure 6.10) upon solvation, when the intramolecular hydrogen bond is destroyed. Moreover, in the Raman spectrum of NOR hydrated with  $\text{D}_2\text{O}$  (spectra not shown) this band arises at  $1576\text{ cm}^{-1}$ , indicating a high sensitivity of this band to the mass effect.

The strong bands at  $1627$  and  $1612\text{ cm}^{-1}$  in the spectrum of anhydrous NOR (figure 6.10A) can be assigned to the stretching modes of the aromatic quinoline ring. These C=C and N=C stretching modes are predicted around  $1600\text{ cm}^{-1}$  by DFT calculations (table 6.2). For NOR· $\text{H}_2\text{O}$  only a small band shift of this mode at  $1612\text{ cm}^{-1}$  in NOR to  $1616\text{ cm}^{-1}$  is observed (figure 6.10B), since this band has probably only small contributions from the carbonyl stretching mode as proved by DFT calculations (see table 6.2).

Nonetheless, there are probably also contributions of the antisymmetrical  $\text{COO}^-$  stretching mode to the very strong band at  $1616\text{ cm}^{-1}$  in the Raman spectra of hydrated NOR, since theoretical calculations for the anionic species predicted the antisymmetrical  $\text{COO}^-$  stretching mode at higher wavenumbers than the carbonyl C=O mode.

The Raman spectrum of CIPRO presents also a broad band at  $1617\text{ cm}^{-1}$  with a shoulder, which can be assigned to the ring stretching modes, but might also get contributions from the antisym-



metrical  $\text{COO}^-$  stretching mode which should be already present in anhydrous CIPRO due to the zwitterionic structure. This is expected from the similar chemical structure of NOR and CIPRO (figure 6.1).

In contrast to NOR, the band of very weak intensity observed at  $1542\text{ cm}^{-1}$  in the Raman spectrum of solid CIPRO (see figure 6.10C) is probably due to the components of the ring stretching modes predicted at  $1558$  and  $1527\text{ cm}^{-1}$ . For CIPRO the strong band at  $1591\text{ cm}^{-1}$  shows changes in intensity upon solvation. Therefore, this band seems to correspond to the carbonyl stretching vibration, but probably also involves the antisymmetrical  $\text{COO}^-$  stretching mode.

As already mentioned in the Raman section for the bulk substances, the most prominent band in the Raman spectra of anhydrous NOR arises at  $1400\text{ cm}^{-1}$ . In the spectrum of hydrated NOR this band is shifted to  $1392\text{ cm}^{-1}$ . Even though, the theoretical calculations predicted several deformation modes of the ethyl and piperazyl group in this spectral region (see table 6.2), this band can be assigned to the ring stretching mode of the quinolone unit calculated at  $1377\text{ cm}^{-1}$  (figure 6.6A). This assignment is in good agreement with the characteristic and very strong band around  $1380\text{ cm}^{-1}$  found in quinoline derivatives [35]. Theoretical calculations performed for the anionic species predicted for the aromatic ring stretching mode a coupling with the symmetrical  $\text{COO}^-$  stretching mode as depicted in figure 6.6B. As CIPRO already exists in the anhydrous state as a zwitterion, coupling of the aromatic ring stretching mode with the symmetrical  $\text{COO}^-$  stretching mode is possible in the anhydrous and the hydrated species as well. Therefore, the corresponding vibrational band experiences no changes upon hydration and is found at  $1382\text{ cm}^{-1}$  in both species (figure 6.10C and D).

Moreover, in the spectrum of hydrated NOR a medium intense band arises at  $1327\text{ cm}^{-1}$  upon solvation which probably corresponds to the symmetrical  $\text{COO}^-$  stretching vibration calculated at  $1347\text{ cm}^{-1}$  for the anionic NOR (figure 6.6C).

Another band which seems to be characteristic to the zwitterionic species is the one at  $1269\text{ cm}^{-1}$  in the spectrum of hydrated NOR (figure 6.10B) as this band is also found in the spectra of anhydrous and hydrated CIPRO at  $1264$  and  $1268\text{ cm}^{-1}$ , respectively (figure 6.10C and D). This mode possibly involves piperazyl stretching modes and for NOR additionally the N1-C12 stretching. Nevertheless, the piperazyl ring stretching modes are predicted at lower wavenumbers, that is in the  $1200\text{-}900\text{ cm}^{-1}$  region. A few very weak and broad bands can be observed in this spectral region in the Raman spectra of NOR and CIPRO. The bands at  $1155$  and  $1035\text{ cm}^{-1}$  observed in the spectra of hydrated NOR (figure 6.10B) being sensitive to the exchange of  $\text{H}_2\text{O}$  for  $\text{D}_2\text{O}$  exhibiting shifts by about  $10\text{ cm}^{-1}$  upon deuteration (spectra not shown here) can be assigned to the piperazyl stretching modes.

The medium intense band at  $1475\text{ cm}^{-1}$  in the spectrum of anhydrous NOR (figure 6.10A) was assigned to the antisymmetrical  $\text{CH}_3$  deformation mode. Such a band is absent in the spectrum of CIPRO (figure 6.10C and D), but the cyclopropyl ring stretching mode probably gives rise to the band at  $866/867\text{ cm}^{-1}$ . Both molecules, CIPRO and NOR, present  $\text{CH}_2$  deformation modes of the piperazyl ring around  $1460\text{-}1440\text{ cm}^{-1}$ . Below  $1000\text{ cm}^{-1}$  several in-plane and out-of-plane

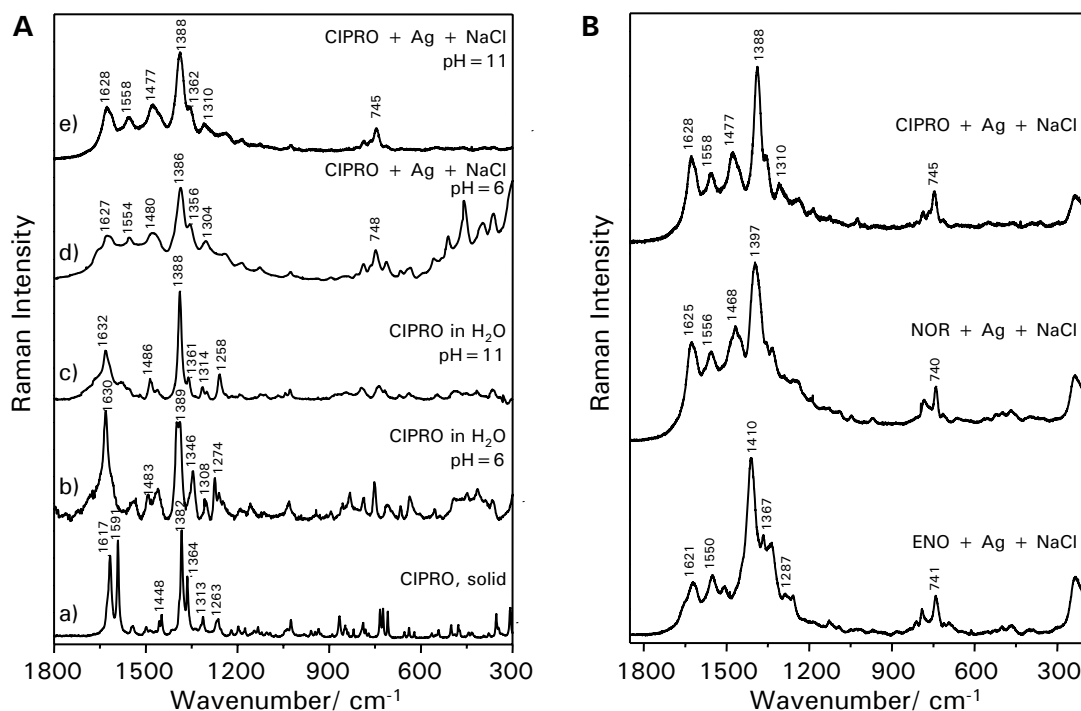


**Figure 6.11:** **A)** Comparison of Raman spectra in the bulk (a) and solution (b and c) at different pH, and in the presence of silver colloid (SERS; d,e) for ciprofloxacin (CIPRO) **B)** Surface enhance Raman spectra (SERS) of enoxacin (ENO, bottom), norfloxacin (NOR, middle) and ciprofloxacin (CIPRO, top).

deformation modes of weak intensity can be observed. Nevertheless, the out-of-plane carbonyl deformation mode is usually quite intense in the Raman spectrum of the solid state and probably gives rise to the bands around 700-750  $\text{cm}^{-1}$  in the Raman spectra of NOR and CIPRO. The band at 854  $\text{cm}^{-1}$  in the spectra of hydrated NOR possibly also involves carboxyl and carbonyl in-plane deformation modes.

## 6.9 Raman spectra in solution, pH-dependence

In the last section only a few water molecules have been added to the substances. However, in a biological relevant environment the antibiotics act in rather dilute aqueous solutions. Therefore, to better resemble the actual conditions in living organism Raman spectra of dilute aqueous solutions of the active substances are investigated in this section. Furthermore, the pH-dependence of the substances is of great interest since all organisms including bacteria are very sensitive to the pH-value of the environment. Low pH-values are found, for example within the human body (gastric acid in the stomach), high pH-values can be reached in the environment of some bacteria (alkaliphiles).

The Raman spectra of an aqueous solution of CIPRO at pH 6 and at pH 11 are shown in comparison with the bulk substance in figure 6.11A Graph b, a and c. At pH 11 only the anionic form should exist, while at pH 6 a mixture of the neutral and the deprotonated species should be in equilibrium. As already seen in figure 6.10, the addition of water causes a solvent induced band broadening. However, it is furthermore possible to detect spectral variations caused by the change of the state of protonation. As an example the vibrational band around  $1590\text{ cm}^{-1}$  in the bulk spectrum (figure 6.11Aa) which gets its main intensity from the carbonyl stretching vibration and the antisymmetric  $\text{COO}^-$  stretching mode should be mentioned. In acidic aqueous solution at pH 6 (figure 6.11Ab) where this group should be at least partially protonated this band is almost vanished, while it is quite intense in basic solution (figure 6.11Ac, pH 11), though slightly shifted in wavenumber values (from  $1591$  to  $1581\text{ cm}^{-1}$ ).

Other bands that experience solvent dependent changes are the vibrational band around  $1617\text{ cm}^{-1}$ , which shows an enhancement upon protonation (at pH 6), and the band around  $1360\text{ cm}^{-1}$ . Also the hydrogen deformation modes of the piperazyl ring hydrogens in the wavenumber range  $1480\text{--}1440\text{ cm}^{-1}$  change with pH due to changed state of protonation of the terminal nitrogen atom of the piperazyl ring. In the solid state (zwitterions) and at pH 6 this nitrogen atom bears two hydrogen atoms while it should be deprotonated at pH 11. Even though only a poor signal-to-noise ratio could be obtained in aqueous solutions due to the low solubility of the quinolones in water it was possible to detect small changes occurring upon changing the environment of the quinolones.

## 6.10 Surface-enhanced Raman spectra

Since quinolones are used as drugs their usual active concentration is quite low (peak concentration in the tissue  $c \sim 2\text{ }\mu\text{g/ml}$ ). For these concentrations the application of conventional micro-Raman spectroscopy for excitation wavelengths in the visible or near infrared region is difficult. To be able to detect the quinolones at physiological concentrations highly sensitive Raman methods are required. One possibility is surface-enhanced Raman spectroscopy (SERS) in which the interaction of the substance of interest with colloidal silver surfaces results in a signal enhancement and makes the detection of smallest amounts of substances possible. In these experiments silver colloidal surfaces were used and due to the signal enhancement it was possible to detect the quinolones at much lower (up to 100 fold) concentrations as in pure solution. At concentrations as low as  $0.2\text{ }\mu\text{g/ml}$  ( $10^{-7}\text{ mol/L}$ ) still Raman spectra with good signal to noise ratio (figure 6.11Ad, Ae) could be recorded.

Furthermore, the SERS studies were also performed to investigate the structure and the orientation of the quinolones upon adsorbing onto surfaces. This could serve as a first model for the quinolones binding to larger particles, like the DNA-gyrase-complex, and give important insight in the characteristic binding sides of the quinolones. The comparison of SERS spectra with Raman spectra in the bulk and in solution at different pH is shown for CIPRO in figure 6.11A. It can be seen, that upon going from the bulk spectrum to the spectrum in solution and to the SERS spectrum

## 6 Fluoroquinolones – important antibiotics

only minor changes of the spectral position of the stretching mode of the aromatic quinolone ring around  $1625\text{ cm}^{-1}$  and of the strong vibrational band around  $1400\text{ cm}^{-1}$  (stretching vibrations of the aromatic quinolone ring system) are observed (the solvent effect was already discussed in the previous section), indicating that CIPRO is not bound chemically to the silver surface, but only via physical interaction. Since these modes are electromagnetically enhanced they should have components perpendicular to the silver surface. This fact is met if the interaction of the quinolones with the silver surface is thought to occur via their carbonyl groups. Upon changing the pH of the Ag solution (figure 6.11Ad, Ae), slight changes of the orientation of the quinolone on the surface are observed. At pH 6 the angle of the molecular plane of the quinolone ring system and the Ag surface is relatively small and therefore a strong enhancement of the out-of-plane vibrations in the low frequency range below  $800\text{ cm}^{-1}$  is observed (figure 6.11Ad). At pH 11 the quinolone exists as an anion. Due to the negative charge the physical binding to the silver surface via the carbonyl groups is improved and the angle formed between the quinolone ring system and the Ag surface is bigger resulting in the out-of-plane vibrations being not any more perpendicular to the Ag surface and therefore experiencing less enhancement (figure 6.11Ae).

Figure 6.11B displays the SERS spectra for CIPRO, NOR and ENO. It can be seen that almost the same modes as in the case of CIPRO (figure 6.11A) are enhanced for these quinolones, indicating that the same adsorption mechanism can be assumed for all quinolones. As already seen in the case of CIPRO, the stretching vibrations of the aromatic ring system around  $1400\text{ cm}^{-1}$  is strongly enhanced and arises to the most intense band in the SERS spectrum. The vibrational band around  $1625\text{ cm}^{-1}$  is assigned to the stretching vibrations of the aromatic ring and the carbonyl vibration. In ENO with a nitrogen atom at position 8, the frequency of the ring vibrations is slightly shifted compared to the other quinolones and an additional shoulder at the high frequency side is observed. The band around  $1555\text{ cm}^{-1}$  is also thought to have strong contributions from the pyridine ring vibration. Due to the tilted adsorption geometry of the quinolones also the  $\text{CH}_2$  bending vibrations of the piperazyl ring contain components perpendicular to the silver surface and are therefore enhanced. This vibration is found around  $1475\text{ cm}^{-1}$  for NOR and CIPRO. Characteristic for all the spectra are also the enhanced CO out of plane vibrations around  $740\text{ cm}^{-1}$ . The enormous enhancement of the Raman intensity in SERS can be explained with the electromagnetic and the chemical model (see also section 2.1.3.2). Upon approaching the silver surface the attaching molecule experiences an additional electromagnetic field with different intensities of parallel and perpendicular components which might cause a profile change of the spectrum, the distance dependence of the Raman signal and the appearance of forbidden modes when the adsorbate is under the influence of a strong electromagnetic field. If a chemical interaction with the metal surface occurs, structural and eventually symmetry changes are induced in the adsorbate molecule which results in a frequency shifts and profile change of the Raman spectrum. Since no spectral changes are observed upon addition of the fluoroquinolones to the silver surface only electromagnetic enhancement should be present in this case.

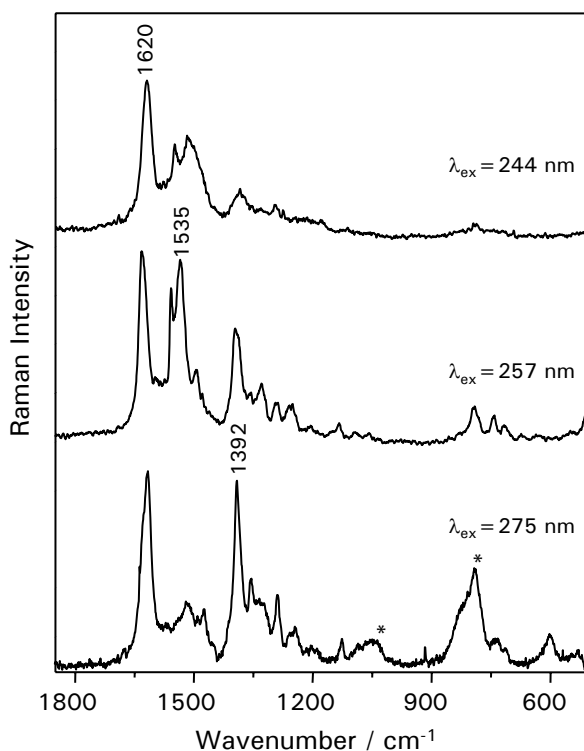


**Figure 6.12:** Resonance Raman spectra of norfloxacin (NOR) at different excitation wavelength.

### 6.11 Resonance Raman spectra

Another possibility to obtain high quality Raman spectra in solution at low concentration of the substance of interest is to apply resonance Raman spectroscopy (see also section 2.1.3.1). Due to the coupling of the Raman signal to the electronic absorption high selectivity and sensitivity is obtained and it is possible to record Raman spectra at physiological low concentrations with a good signal-to-noise ratio. Furthermore, the use of silver which is normally toxic to many organisms including bacteria, can be circumvented.

Resonance Raman spectra for NOR are shown in figure 6.12 for the three different excitation wavelengths 244, 257 and 275 nm. As can be seen in the UV/vis absorption spectra (figure 6.3) excitation with 257 nm and with 275 nm hits the aromatic ring absorption band and a very good signal-to-noise ratio can be obtained. At 244 nm the molar extinction coefficient of NOR is relatively low, therefore the coupling of the Raman and the electronic transition is quite low, which results in a smaller enhancement and in a poorer signal-to-noise ratio.

Due to the selective enhancement of the vibrations coupled to the electronic transition (in this case the vibrations of the aromatic ring) changes of the relative intensities of several bands are observed in the resonance Raman spectrum (figure 6.12). The vibrational mode most enhanced is the C=C stretching vibration and the ring deformation vibration around 1620 cm<sup>-1</sup>. When

## 6 Fluoroquinolones – important antibiotics

exciting with laser light of a wavelength of 257 nm the vibrational modes around  $1535\text{ cm}^{-1}$  (C-C stretch) experience also a strong enhancement. Enhancement with a wavelength of 275 nm causes significant enhancement of the vibrational mode around  $1392\text{ cm}^{-1}$  (C-C stretching vibration).

The resonance enhancement makes it possible to record good Raman spectra of the quinolones at physiological low concentration in aqueous solution. Therefore this technique could be used in future experiments to locate the quinolones within the bacteria.

### 6.12 Conclusion

In this chapter it was shown that the investigated antibiotics can be characterized very well by means of vibrational spectroscopy. DFT calculations show very good agreement with the experimental results and can therefore be helpful in assigning the characteristic vibrational bands. Common characteristic features of this class of substances like the stretching vibration of the aromatic ring system could be summarized, as well as typical individual structural differences pointed out. Cinoxacin (CIN), for example, shows various unique features due to the nitrogen substitution in the 2-position of the quinolone ring system. The application of the highly sensitive resonance Raman method allows one to detect the drugs in aqueous solution at physiological low concentrations. This understanding of the spectral properties of the quinolones is useful for the elucidation of specific interaction of these antibiotics with their biological targets, the bacterial DNA and the enzyme DNA gyrase. Locating the drugs in their biological environment could eventually lead to a determination of cooperative effects and finally to an elucidation of the exact mechanism of the gyrase inhibitors on a molecular level which is so far unknown but is of greatest interest.

In the next two chapters the biological targets of these fluoroquinolone drugs (DNA and gyrase) will be investigated and in chapter 9 the direct effect of the drugs on the bacterial cells will be studied.

## 7 The biological target: DNA

The bacterial DNA is one of the target molecules of the fluoroquinolone drugs. In order to understand the complex drug-target interactions it is crucial to understand the vibrational spectra of pure DNA. DNA is a large molecule which is assembled from the individual nucleotides which constitute of a nucleic acid base, a deoxyribose moiety and a phosphate moiety. In the first section the focus will be set on those small building blocks to provide a sound basis for the understanding of the polymer (DNA) spectra in the later sections.

### 7.1 The DNA building blocks: nucleic acid bases, nucleoside and nucleotides

The DNA building blocks are the nucleotides which consist of a purine or pyrimidine base, a deoxyribose sugar and a phosphate residue. Due to their importance the nucleic acid building blocks gained a lot of research interests in the past years [84, 85, 212, 203, 47, 30]. However, since an understanding of the structural and spectroscopic properties of the small components provides the basis for further investigations of DNA a vibrational spectroscopic characterization of the individual bases, nucleosides (base + sugar) and nucleotides (base + sugar + phosphate) will be given in this section. Micro-Raman and IR absorption spectroscopy has been employed to probe the molecular vibrations of the pure substances, as well as the influence of base pairing on the geometric parameters and the vibrational signature. The assignment of the vibrational bands is based on DFT calculations. In order to assess vibrational spectra of the poorly soluble DNA building blocks resonance Raman spectroscopy with excitation in the UV (244 nm and 257 nm) has been employed.

#### 7.1.1 The nucleic acid bases

##### 7.1.1.1 Structural parameters of the nucleic acid bases

The DNA building blocks are the nucleotides which consist of a purine or pyrimidine base, a deoxyribose sugar and a phosphate residue. In DNA adenine (A), guanine (G), thymine (T) and cytosine (C) are found as nucleic acid bases. In RNA thymine is substituted by uracil, which can be derived from cytosine by oxidation with nitrous acid. In the following the focus is set on the four DNA bases. Figure 7.1 shows the fully optimized structures of those four bases as obtained from DFT calculations (B3PW91/6-31+G(d,p)).

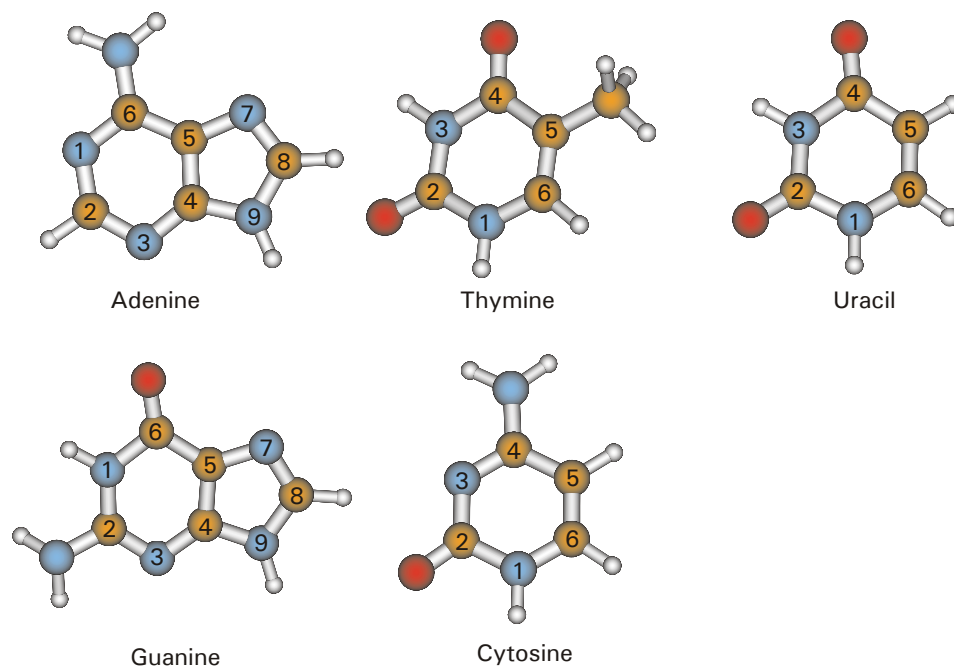


**Figure 7.1:** Structures of the nucleic acid bases and their atom numbering convention. First column: the purine bases adenine and guanine, second and third column: the pyrimidine bases thymine, cytosine and uracil.

The purine and pyrimidine ring system is planar for all bases as indicated by the average of the torsion angles being either  $0^\circ$  or  $180^\circ$ . Remarkable deviation from the all planar structure is observed for the amino group in guanine, where the hydrogen atoms form a dihedral angle of about  $30^\circ$  with the plane of the purine ring. For the amino groups in cytosine and adenine this effect was not observed to this extent. The notably non-planarity of the guanine amino group was reported previously by other groups using *ab initio* calculations [84] and was explained by strong hydrogen-hydrogen repulsion between the amino-hydrogen and the hydrogen bound to N1 which cause the amino-hydrogen to bend out of the plane.

The calculated structural parameters (bond length and angles) of the four DNA bases are compared in table 7.1 with experimental values from the literature obtained from high-resolution X-ray crystallography and neutron scattering. The experimental values are the median bond length and angles from 21 (guanine), 28 (cytosine), 48 (adenine) and 50 (thymine) different crystal structure measurements and therefore should be free of singularities [53]. The measurements were performed with the methylated (N9 for the purines, N1 for the pyrimidines) bases, while the DFT calculations were performed for the pure bases. However, that has only a minor affect on the other bond lengths and angles and therefore the data can be used for comparison with the calculation. The geometric structures obtained by theory are in good agreement with the experimental



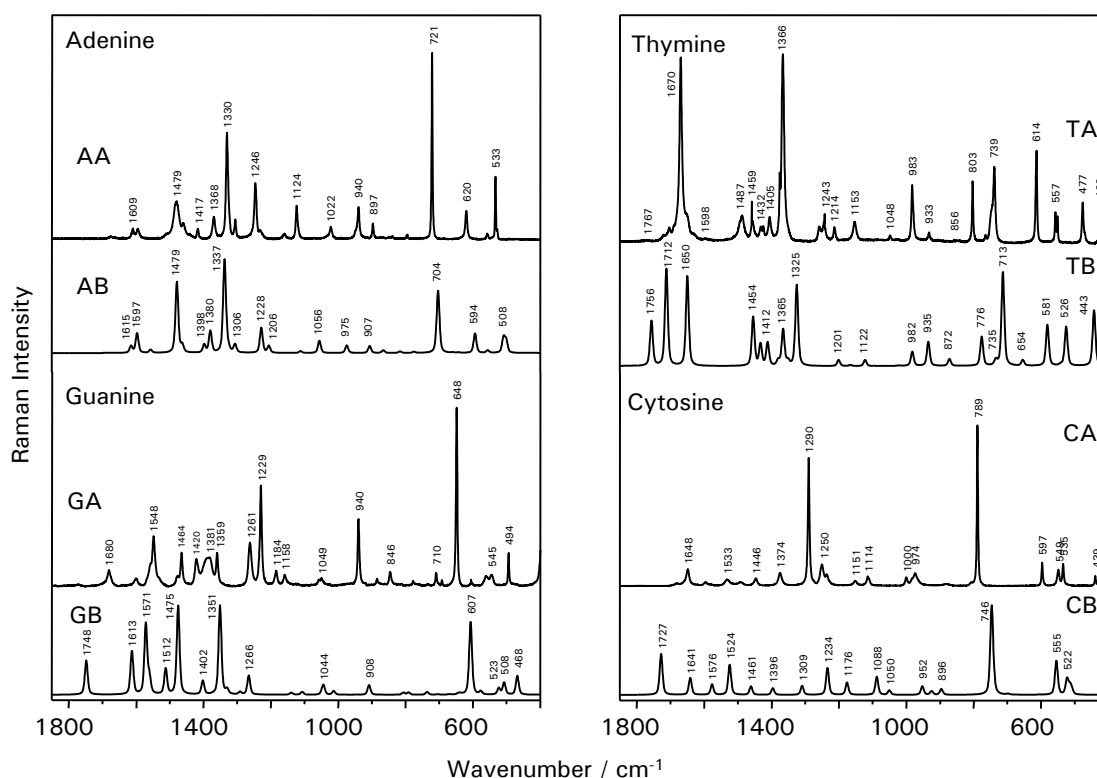


**Figure 7.2:** Micro-Raman spectra of the nucleic acid bases, **XA** experimental spectrum ( $\lambda_{ex}=532$  nm) of the solid bases, **XB** DFT calculation (B3PW91/6-31+G(d,p)) for gas phase.

ones. The maximum relative deviation are for all bonds and angles always below 3%. For adenine the C4C5 bond and the C6N6 bond are calculated too long while the enclosed angles (N6C6C5, C6C5C4 and C5C4N9) were calculated too small. However average relative deviation of the calculation from the experiment is around 0.5%. Only slightly larger deviation were calculated for thymine (deviation 7%) where the N3C4, C4C5 and C5C6 bond were modelled too long. In guanine the double bond character of the C6=O bond, the C4C5 and C2N3 bond has been slightly overestimated in the calculations, while the N1C6 and the C2N2 bond were calculated to be too long. The largest deviations arise for cytosine (average 1.5% deviation). It is assumed that intermolecular hydrogen bonding in the crystal causes those structural modifications in comparison to the calculated gas phase structure. The slight lengthening of the C=O bond (C6=O in guanine and C2=O in cytosine) in the experiment compared to the calculation supports this assumption.

#### 7.1.1.2 Micro-Raman spectra of the nucleic acid bases

The micro-Raman spectra excited at 532 nm of the individual pure nucleic acid bases in the solid state are shown in figure 7.2. On the left side the spectra of the purine bases adenine (top, AA) and guanine (bottom, GA) are shown, on the right side the Raman spectra of the pyrimidine bases thymine (top, TA) and cytosine (bottom, CA). Underneath the experimental spectra the calculated

**Table 7.1:** Comparison of the geometry parameters of the nucleic acid bases obtained by DFT calculations (B3PW91/6-31+G(d,p)) with experimental values from X-ray crystallography. The experimental values are taken from Clowney et al. [53]

adenine			guanine			cytosine			thymine			uracil		
bond length	exp.	calc.	bond length	exp.	calc.	bond length	exp.	calc.	bond length	exp.	calc.	bond length	exp.	calc.
N1-C2	1.340	1.341	N1-C2	1.371	1.368	N1-C2	1.397	1.422	N1-C2	1.376	1.384	N1-C2	1.381	1.403
C2-N3	1.332	1.334	C2-N3	1.324	1.311	C2-N3	1.355	1.367	C2-N3	1.373	1.381	C2-N3	1.374	1.391
N3-C4	1.344	1.337	N3-C4	1.351	1.355	N3-C4	1.335	1.319	N3-C4	1.381	1.402	N3-C4	1.382	1.422
C4-C5	1.385	1.397	C4-C5	1.378	1.394	C4-C5	1.424	1.439	C4-C5	1.446	1.465	C4-C5	1.430	1.462
C5-C6	1.406	1.410	C5-C6	1.418	1.438	C5-C6	1.340	1.359	C5-C6	1.339	1.353	C5-C6	1.338	1.362
C6-N1	1.351	1.343	C6-N1	1.391	1.431	C6-N1	1.365	1.352	C6-N1	1.379	1.376	C6-N1	1.375	1.3803
C5-N7	1.387	1.381	C5-N7	1.388	1.377	C2-O2	1.242	1.222	C2-O2	1.218	1.219	C2-O2	1.219	1.230
N7-C8	1.311	1.310	N7-C8	1.304	1.307	C4-N4	1.334	1.356	C4-O4	1.228	1.222	C4-O4	1.232	1.233
C8-N9	1.372	1.376	C8-N9	1.373	1.380	N1-C(H)1*	1.470*	1.01049*	N1-C(H)1*	1.497	1.496	N1-C(H)1*	1.465*	1.017*
N9-C4	1.374	1.374	N9-C4	1.374	1.366				C5-M5	1.470*	1.496			
C6-N6	1.336	1.350	C2-N2	1.337	1.372				N1-C(H)1*					
N9-C(H)1*	1.464*	1.009	C6-O6	1.238	1.219									
			N9-C(H)1*	1.461*	1.009*									
bond angle			bond angle			bond angle			bond angle			bond angle		
C6-N1-C2	118.5	118.6	C6-N1-C2	125.1	126.6	C6-N1-C2	120.3	123.4	C6-N1-C2	121.2	123.8	C6-N1-C2	121.2	123.8
N1-C2-N3	129.2	128.7	N1-C2-N3	123.7	123.5	N1-C2-N3	119.1	116.4	N1-C2-N3	114.4	112.8	N1-C2-N3	114.9	112.7
C2-N3-C4	110.6	111.2	C2-N3-C4	112.0	112.5	C2-N3-C4	120.0	120.3	C2-N3-C4	127.1	128.0	C2-N3-C4	126.9	128.3
N3-C4-C5	126.7	127.0	N3-C4-C5	128.7	129.3	N3-C4-C5	121.9	124.0	N3-C4-C5	115.3	114.8	N3-C4-C5	114.6	113.4
C4-C5-C6	117.0	115.8	C4-C5-C6	118.8	118.5	C4-C5-C6	117.4	120.0	C4-C5-C6	118.0	117.9	C4-C5-C6	119.6	120.0
C5-C6-N1	117.6	118.7	C5-C6-N1	111.4	109.6	C5-C6-N1	121.0	123.4	C5-C6-N1	123.6	122.7	C5-C6-N1	122.6	121.8
C4-C5-N7	110.6	111.4	C4-C5-N7	110.8	111.0	N1-C2-O2	118.9	118.1	N1-C2-O2	123.1	123.1	N1-C2-O2	122.8	122.7
C5-N7-C8	103.9	104.0	C5-N7-C8	104.4	104.5	N3-C2-O2	121.9	125.5	N3-C2-O2	122.3	124.1	N3-C2-O2	122.3	124.6
N7-C8-N9	113.8	113.4	N7-C8-N9	113.1	112.8	N3-C4-N4	118.1	116.9	N3-C4-O4	119.9	120.2	N3-C4-O4	119.6	120.2
C8-N9-C4	105.8	106.8	C8-N9-C4	106.4	106.8	C5-C4-N4	120.2	119.1	C5-C4-O4	124.9	125.0	C5-C4-O4	125.9	126.4
N9-C4-C5	105.8	104.4	N9-C4-C5	105.4	104.9	C6-N1-C(H)1*	121.0*	121.5*	C4-C5-M5	119.0	118.1	C6-N1-C(H)1*	121.2*	121.3*
N3-C4-N9	127.3	128.6	N3-C4-N9	125.9	125.9	C2-N1-C(H)1*	118.5*	115.1*	C6-C5-M5	122.9	124.0	C2-N1-C(H)1*	117.7*	114.9*
C6-C5-N7	132.5	132.8	C6-C5-N7	130.5	130.5				C6-N1-C(H)1*	120.2*	121.067*			
N1-C6-N6	118.5	118.9	N1-C2-N2	116.4	117.0				C2-N1-C(H)1*	118.3*	115.138*			
C5-C6-N6	123.6	122.4	N3-C2-N2	119.8	119.5									
C8-N9-C(H)1*	127.6*	127.4*	N1-C6-O6	120.0	119.1									
C4-N9-C(H)1*	125.9*	125.8*	C5-C6-O6	128.7	131.3									
			C8-N9-C(H)1*	127.4*	127.597*									
			C4-N9-C(H)1*	126.3*	125.619*									

\* while the experimental values result from base structures with a methyl group attached to N9 (purins) or N1 (pyrimidines) a hydrogen atom was used in the calculations instead.

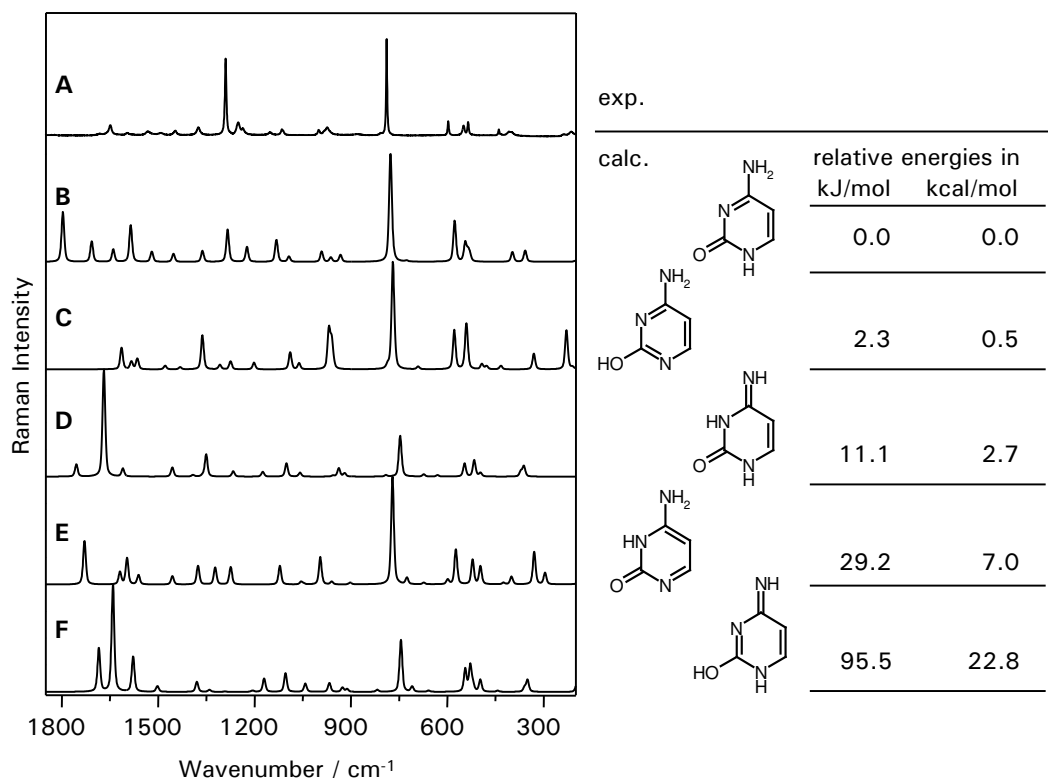


**Figure 7.3:** Five possible cytosine tautomers, **A**) micro-Raman spectra as obtained from DFT calculations (B3PW91/6-31+G(d,p), Graph a shows an experimental spectrum ( $\lambda_{ex}=532$  nm) for comparison; **B**) geometric structure; **C**) relative energy of the different tautomers.

Raman spectra as obtained from ab initio DFT calculations (B3PW91/6-32+G(d,p)) and band folding are shown for comparison (AB, GB, TB, CB). The general features of the experimental data are well reproduced by the calculation, especially for adenine.

Variations in the intensity pattern and wavenumber position between the experimental and calculated spectra are due to the fact that the calculation is based on gas phase molecules while the measurement was performed in the crystalline state of the bases. All the bases possess several hydrogen donor and acceptor sides and therefore, strong intermolecular interactions in the solid phase due to hydrogen bonding will change the force constants within the molecule and thereby the vibrational frequency. Coupling of the vibrations of two or four molecules in the crystal that are in the same unit cell might increase the number of normal modes as has been reported for deoxycytidine and cytosine, respectively [139].

One way to brake the specific crystal interactions would be the investigation of the substances in solution. However, the solubility of the pure nucleic acid bases (especially guanine) is so poor, that no normal Raman spectra with good signal-to-noise ratio of those substances in solution are difficult to record.

**Tautomers** Furthermore, a large variety of nucleic acid base structures is possible for the individual bases when adopting different tautomers such as amino  $\longleftrightarrow$  imino, N7H  $\longleftrightarrow$  N9H (A,G), oxo  $\longleftrightarrow$  hydroxy (G,T,C) and for T and G additionally N1H  $\longleftrightarrow$  N3H. Figure 7.3 shows the calculated Raman spectra of four of the different tautomers of cytosine. For comparison an experimental spectrum of crystalline cytosine is shown in the upper lane on the left side. The tautomer that is second lowest in energy is the one shown in figure 7.3C and is 3.8 kJ/mol (0.9 kcal/mol) higher in energy than tautomer B. Assuming a Boltzmann distribution:

$$\frac{N_{taut}}{N_{total}} = e^{-\frac{\Delta G_{taut}}{RT}} \quad (7.1)$$

results in about 17.6% of tautomer C at room temperature  $T = 298\text{K}$ . For tautomer D which is 12.5 kJ/mol (3.0 kcal/mol) higher in energy than tautomer B the same calculation yields 0.5%, for tautomer E only 0.0004%. Therefore, higher energy tautomers need not to be considered.

Those results are valid for the gas phase. In the crystalline state hydrogen bonding interaction can change the distribution of the different tautomers. From the crystal structure of anhydrous cytosine it was deduced that the amino groups form hydrogen bonds between the carbonyl groups of the neighboring molecules while the N1H forms an H-bond to N3 of the adjacent molecule [76]. Also in cytosine monohydrate extensive intermolecular hydrogen bonding is present and the hydrogen bonded cytosine molecules form parallel ribbons that are cross-linked by water molecules.

The largest deviation between the calculated Raman spectrum and the experimental one is observed for guanine, even though the DFT-optimized geometric parameter match quite well the experimental values (table 7.1). Such discrepancy between the calculated (gas phase) and experimental (solid state) spectra (especially for guanine), has previously been reported in the literature [84] and caused controversial assignment of the vibrational bands by Giese and McNaughton [84, 85], Nowak [186], Florian [75] and Santamaria [223]. However, it has to be noted that the latter two did not use polarization functions for their DFT calculations which is necessary for a correct prediction of the spectra [286].

**Assignment of the vibrational modes with the help of DFT calculations** In this work ab-initio calculations have been performed using the split valence basis set 6-31G which was augmented by d polarization function on heavy atoms (d) and p polarization functions on hydrogen atoms (p). In order to describe the lone pairs accurately diffuse functions were added on heavy atoms (+). Geometry optimization and frequency calculations were performed on the same level of theory and the calculated wavenumbers were used for an assignment of the vibrational modes. Table 7.2 shows the theoretical and experimental wavenumber values together with the assignment of the individual vibrational modes based on the potential energy distribution (PED) for adenine, thymine and cytosine. The PED gives the percentage of potential energy localized in a particular bond for a given mode (number in brackets behind the vibrational assignment). The detailed band

assignment for guanine is presented together with the corresponding nucleoside and nucleotide in table B.1.

Most of the vibrations of the nucleic acid bases are complex and involve strongly coupled motions as can be seen from table 7.2. At high wavenumbers ( $>2900\text{ cm}^{-1}$ ) CH and NH stretching vibrations are found (not shown in the figure). The spectral region around  $1700\text{ cm}^{-1}$  is dominated by  $\text{NH}_2$  scissoring (adenine, guanine, cytosine) and C=O stretching (thymine, cytosine, guanine) motions. Also skeletal vibrations of the unsaturated rings become important. Between  $1450$  and  $1000\text{ cm}^{-1}$ , bending of the external NH and CH angles are found, often coupled to stretching and deformation motions of the pyrimidine (pyr) and imidazole (im) rings. The low wavenumber region between  $1000$  and  $200\text{ cm}^{-1}$  consists of both in-plane and out-of-plane vibrations, torsion and bending modes with relatively weak intensity. The most dominant feature in this wavenumber range is the very intense ring breathing mode (between  $600$  and  $750\text{ cm}^{-1}$  for the different bases). Below  $200\text{ cm}^{-1}$  (not shown in the figure) lattice modes are found.

The nucleic acid bases are only poorly soluble in the common solvents, so it was not possible to prepare a solution with high enough concentrations to give good and well resolved Raman spectra. However, it is possible to record Raman spectra in solution when using resonance Raman spectroscopy (see section 7.1.3).

**Table 7.2** : Assignment of the experimental and theoretical (B3PW91/6-31+G(d,p)) Raman bands of adenine, thymine and cytosine. The numbers in brackets behind the mode assignment gives the percentage of potential energy localized in that particular involved bond. Only contributions over 5% are shown.

mode	DFT in $\text{cm}^{-1}$	DFT scaled in $\text{cm}^{-1}$	Exp. ( $\lambda_{\text{ex}}=532\text{ nm}$ ) in $\text{cm}^{-1}$	Assignment (PED)
<b>Adenine</b>				
1	83	79		$\text{NH}_2$ out (98)
2	165	159		pyr ring tors (69) - $\text{NH}_2$ out (21)
3	219	211		$\text{NH}_2$ out (53) - pyr ring tors2 (13) - C6N out (9) + N9H out (7) - pyr ring tors (6) - $\text{NH}_2$ tors (5)
4	276	265		N6H bend (58) - C6N bend (19) + im ring bend (8) - N9H bend (6) + im ring bend2 (5)
5	300	289		im ring tors2 (44) - pyr ring tors2 (31) - N9H out (17)
6	521	501		N6H bend (54) + N9H bend (25) - C6N bend (9)
7	527	507	527	N9H out (55) + $\text{NH}_2$ tors (17) - im ring tors2 (9) + pyr ring tors (8) - im ring tors (6)
8	530	510	533	pyr ring bend2 (88) + N6H bend (5)
9	545	524		$\text{NH}_2$ tors (93)
10	578	556	558	pyr ring tors (57) - N9H out (17) - im ring tors2 (8) - pyr ring tors3 (6) + $\text{NH}_2$ tors (5)
11	618	594	620	im ring bend (48) + im ring bend2 (20) - N6H bend (18)
12	669	643		im ring tors (67) + $\text{NH}_2$ tors (10) + pyr ring tors (7) + C8H out (5)
13	687	660		im ring tors2 (35) + C6N out (34) + pyr ring tors (14) + pyr ring tors2 (12)
14	732	704	721	im ring bend (38) + N6H bend (23) - N9H bend (19) - im ring bend2 (10)
15	806	775		pyr ring tors3 (31) + C8H out (23) - im ring tors2 (20) + C6N out (14)
16	849	817		C8H out (94)
17	901	866	897	pyr ring bend2 (29) - C8H bend (27) - im ring bend (20) - 17 (9) + im ring bend2 (7)
18	943	907	940	im ring bend2 (79) - N9H bend (14)
19	976	938		C2H out (88) + pyr ring tors (9)
20	1014	975	1022	N6H bend (96)
21	1098	1056	1124	N9H bend (71) - C8H bend (28)
22	1156	1112		C8H bend (69) + N9H bend (12) + N6H bend (7) + im ring bend (7)
23	1254	1206	1232	C8H bend (49) - N6H bend (43)
24	1278	1228	1246	C8H bend (75) + N9H bend (21)
25	1359	1306	1305	C2H bend (53) - C8H bend (32) + N9H bend (12)
26	1380	1326		C2H bend (43) + $\text{NH}_2$ bend (32) + N9H bend (12) - N6H bend (6)
27	1391	1337	1330	C8H bend (57) - N9H bend (30) - im ring bend2 (8)
28	1435	1380	1368	N9H bend (69) - C2H bend (30)
29	1454	1398	1417	$\text{NH}_2$ bend (38) + im ring bend2 (21) + C2H bend (20) + N6H bend (10)

## 7 The biological target: DNA

Table 7.2: continued

mode	DFT in $\text{cm}^{-1}$	DFT scaled in $\text{cm}^{-1}$	Exp. ( $\lambda_{\text{ex}}=532 \text{ nm}$ ) in $\text{cm}^{-1}$	Assignment (PED)
30	1522	1463	1460	NH <sub>2</sub> bend (55) - C2H bend (28) - N9H bend (11)
31	1539	1479	1479	C8H bend (82) + NH <sub>2</sub> bend (12)
32	1620	1557		NH <sub>2</sub> bend (94)
33	1661	1597	1595	N9H bend (54) + C8H bend (22) + im ring bend (9) - N6H bend (9)
34	1680	1615	1609	NH <sub>2</sub> bend (91)
35	3198	3074	3038	C2H str (82) + pyr ring bend2 (16)
36	3273	3146	3115	C8H str (50) - im ring bend2 (39) - N9H bend (8)
37	3640	3499	3294	NH <sub>2</sub> bend (42) - N6H str (31) - N6Hb str (27)
38	3685	3543	3358	N9H str (72) - im ring bend (11) + im ring bend2 (10) + C8H bend (7)
39	3784	3638		N6H str (39) - N6H bend (32) - N6Hb str (28)
<b>Thymine</b>				
1	110	106		ring def1 (53) + N1H out (23) - ring def2 (14)
2	138	133		C5Me tors (65) + ring def2 (13) - N1H out (8) - ring def1 (5)
3	153	147		ring def2 (39) - N3H out (30) - ring def3 (27)
4	273	262		C5Me bend (68) - C4O bend (11) + ring bend1 (7)
5	295	284		C5Me out (47) - ring def1 (17) - N1H out (16) + ring def2 (10)
6	387	373		C2O bend (38) - C4O bend (26) + ring bend1 (12) - N3C4 str (8) - C2N3 str (6)
7	396	380		ring def3 (42) + ring def2 (17) - N1H out (17) - C5Me out (15) - C4O out (6)
8	460	443	477	ring bend2 (69) + C5C str (7) - C2O bend (6) + N3C4 str (6)
9	547	526	551	ring bend1 (52) + C4O bend (9) + C2N3 str (9) + C2O bend (8) + N3C4 str (6)
10	563	542	557	N1H out (89) - N3H out (6)
11	605	581	614	C4O bend (27) + C2O bend (27) + C5Me bend (13) - ring bend1 (8)
12	680	654		N3H out (85) + ring def2 (6)
13	742	713	739	C4C5 str (39) + C5C str (15) - ring bend1 (9) + N3C4 str (5)
14	744	716	749	C2O out (44) + ring def2 (31) - N3H out (12)
15	764	734	764	C4O out (47) + ring def2 (17) - C5Me out (12) + ring def1 (10)
16	807	776	803	ring bend3 (49) + C5C str (17) - N1C2 (10)
17	907	872	933	C6H out (85) + ring def3 (5)
18	972	935	983	N1C2 (26) - CH3 def1 (16) - C4C5 str (9) + C2N3 str (8) + N3H def (7) - C2O bend (5) + CH3 rock (5)
19	1022	982	1048	CH <sub>3</sub> def1 (36) + ring bend3 (17) - CH <sub>3</sub> rock (12) + N1C2 (7) - C5C6 str (6)
20	1062	1021	1153	CH <sub>3</sub> rock (54) + CH <sub>3</sub> def1 (18) + C5Me out (8) - C6H out (7) + CH <sub>3</sub> def (5)
21	1167	1122		N3C4 str (29) - C6N1 str (14) + ring bend3 (9) - C4O bend (8) - N1H def (8) - C5C str (8) - CH3 def1 (6) - C5Me bend (5)
22	1213	1166	1214	N3C4 str (18) - C6H def (18) - C2N3 str (17) + N1H def (15) + C6N1 str (10) - N3H def (6)
23	1249	1201	1243	C5C str (23) - C6N1 str (19) - C4C5 str (11) + N1C2 (10) - C2N3 str (10) - ring bend3 (8) - C6H def (7)
24	1378	1325	1366	C6H def (37) + C5C6 str (12) - C2N3 str (9) + N1C2 (9) - C4C5 str (8)
25	1405	1351	1375	N3H def (62) + N3C4 str (8) + C4O str (6) + N1H def (5) - C6H def (5)
26	1420	1366	1405	CH <sub>3</sub> scis (87) + C5C str (8)
27	1436	1380	1424	N1H def (19) + C2N3 str (19) - C4C5 str (10) + C2O bend (10) - N1C2 (9) - C4O bend (6) - ring bend1 (5) + C5C str (5)
28	1468	1412	1432	CH <sub>3</sub> def (68) + CH <sub>3</sub> wag (23) - CH <sub>3</sub> rock (7)
29	1490	1433	1459	CH <sub>3</sub> wag (60) - CH <sub>3</sub> def (20) + CH <sub>3</sub> def1 (5)
30	1513	1454	1487	N1H def (27) - C6N1 str (21) + C4C5 str (9) + N1C2 (9) + C2O str (6) - N3C4 str (5) + ring bend1 (5)
31	1716	1650	1651	C5C6 str (60) - C6H def (12) - C6N1 str (9) - C5C str (5)
32	1781	1712	1670	C4O str (72) - C4C5 str (7)
33	1827	1756	1705	C2O str (68) - C2N3 str (7) - N1C2 (7)
34	3056	2938	2931	CH str (Me1) (35) + CH str (Me2) (35) + CH str (Me3) (29)
35	3126	3005	2966	CH str (Me1) (50) - CH str (Me2) (50)
36	3147	3026	2990	CH str (Me3) (70) - CH str (Me2) (15) - CH str (Me1) (15)
37	3222	3098	3062	C6H (99)
38	3631	3491		N3H str (100)
39	3674	3532		N1H str (100)
<b>Cytosine</b>				
1	133	128	118	ring def (49) - N1H out (25) + ring def2 (22)
2	139	134	165	NH <sub>2</sub> out (56) - NH <sub>2</sub> twist (24) + C4N out (11)
3	201	193	214	ring def2+(48) - ring def3 (37) - ring def (5)
4	358	344	409	C4N bend (57) - C2=O bend (12) + ring bend (12) + NH <sub>2</sub> bend (8) - C2N3 str (5)
5	397	382	439	ring def3 (40) - N1H out (23) - C5H out (14) + ring def2 (12) - C4N out (7)
6	529	509		C2=O bend (37) + NH <sub>2</sub> twist (25) + C4N bend (13)
7	535	514		NH <sub>2</sub> twist (48) - C2=O bend (11) - ring bend2 (11) - C4N bend (6) + N1H out (5)
8	544	523	535	ring bend2 (52) + ring bend (15) + NH <sub>2</sub> twist (7) - C2=O bend (6)
9	577	555	549	ring bend (57) - ring bend2 (22)
10	630	606	597	N1H out (78) - C4N out (10)
11	726	698		C4N out (29) + ring def2 (21) + C6H out (20) + C5H out (18)
12	767	737		C2O out (49) + C5H out (15) + ring def (9) + ring def2 (9) - N1H out (7) - C4N out (6) + C6H out (5)
13	773	743		ring def2 (33) + C4N out (25) - C5H out (23) + C2O out (13)
14	777	747	789	N1C2 str (23) + C4C5 str (12) - ring bend3 (12) + C4N str (8) + C2N3 str (7) - ring bend (6) + N3C4 str (6) - C5H out (5) + C4N out (5) + ring def2 (5)
15	932	896		N1C2 str (27) - C4C5 str (16) + NH <sub>2</sub> bend (15) + ring bend3 (13) + C2=O bend (5)
16	962	925		C6H out (79) - C5H out (13)

Table 7.2: continued

mode	DFT in $\text{cm}^{-1}$	DFT scaled in $\text{cm}^{-1}$	Exp. ( $\lambda_{\text{ex}}=532 \text{ nm}$ ) in $\text{cm}^{-1}$	Assignment (PED)
17	991	952	974	ring bend3 (50) + C4C5 str (26) - NH <sub>2</sub> bend (7)
18	1092	1050	1000	NH <sub>2</sub> bend (40) - N1C2 str (18) - C2=O bend (16) + C2N3 str (7)
19	1131	1088	1114	C5H bend (44) + N1C6 str (23) + C5C6 str (17) - N1H bend (8)
20	1223	1176	1151	C6H bend (30) - N1H bend (25) + N1C6 str (18) - C5H bend (13) - N1C2 str (5)
21	1283	1234	1250	C2N3 str (45) - N1C2 str (13) - C4N str (10) - C2=O bend (6) - N3C4 str (5)
22	1362	1309	1290	C6H bend (26) + C5H bend (19) + C4N str (17) - C5C6 str (11) + N1H bend (9)
23	1452	1396	1374	N1H bend (35) + N1C6 str (16) + C4C5 str (13) - N3C4 str (7) - C4N str (5)
24	1520	1461	1446	N3C4 str (20) - C4N str (19) + C6H bend (14) - N1C6 str (13) + C5H bend (11) + NH <sub>2</sub> bend (11)
25	1585	1524	1533	N3C4 str (28) - C4C5 str (23) + C5C6 str (10) + N1H bend (8) + N1C6 str (6) - ring bend (6) - C5H bend (5)
26	1640	1576		NH <sub>2</sub> scis (73) + C4N str (15) - C5C6 str (5)
27	1707	1641	1648	C5C6 str (39) - N3C4 str (14) - N1C6 str (10) + C6H bend (10) - ring bend2 (7) + C4N str (6)
28	1797	1727		C2=O str (72) - C2N3 str (10)
29	3223	3098	3096	C6H str (88) - C5H str (11)
30	3249	3124	3114	C5H str (88) + C6H str (11)
31	3634	3494	3189	N4Ha str (61) + N4Hb str (38)
32	3652	3511	3366	N1H str (99)
33	3780	3634	3445	N4Hb str (62) - N4Ha str (38)

### 7.1.1.3 Hydrogen bonding between complementary base pairs

The DNA adopts its typical double helical structure due to the strong hydrogen bonds between the complementary base pairs of both DNA strands. In the classical Watson-Crick binding model guanine forms three hydrogen bonds with cytosine, and adenine forms two hydrogen bonds with thymine (figure 7.4). This specific base pairing is essential for the transfer and expression of genetic information. Base pairing is also detectable by vibrational spectroscopy since the force constants of the involved bonds are changed due to the hydrogen bonding.

**Adenine-thymine Watson-Crick base pair** Figure 7.4A shows the optimized geometric structure of the adenine-thymine Watson-Crick base pair as obtained from DFT calculations (B3PW91/6-31+G(d,p)). Due to the hydrogen bonding interactions between the amino hydrogen of N6H<sub>2</sub> of adenine and the carboxyl oxygen C4=O of thymine and between the hydrogen at N3 of thymine and the nitrogen N1 of adenine the bond length of the C6N6 bond in adenine and the N3C4 bond in thymine are reduced while the C4O bond in thymine and the N1C6 bond in adenine loose double bond character and are longer in the base pair than in the free base (see table 7.3).

These geometric changes affect also the force constants and changes in the vibrational spectra can be detected. The simulated Raman spectrum of the adenine-thymine base pair (middle spectrum) is shown in figure 7.4B in comparison with the simulated spectra of the free bases adenine (upper spectrum) and thymine (lower spectrum). The most obvious changes are seen in the wavenumber region above  $2800 \text{ cm}^{-1}$  where the NH-, NH<sub>2</sub> and CH stretching vibrations occur. Due to the hydrogen bonding interaction force constants between the hydrogen and nitrogen N6 of adenine are weakened and therefore the vibration is found at lower wavenumbers (for a first approximation compare with Equation 2.1). The adenine N6H stretching vibration in the base pair (the H vibrates towards the O4 of thymine) is found at  $3279 \text{ cm}^{-1}$  while the unperturbed N6H<sub>2</sub> stretching vibration in free adenine is found at  $3499 \text{ cm}^{-1}$ . A similar behavior shows the N3H

## 7 The biological target: DNA

**Table 7.3:** Geometry changes in the nucleic acid bases upon base pairing.

adenine-thymine base pair				guanine-cytosine base pair			
parameter	adenine			parameter	guanine		
bond length	free base	in base pair	diff (pair-free) in %	free base	in base pair	diff (pair-free) in %	
N1-C2	1.341	1.345	0.33	N1-C2	1.368	1.372	0.28
C2-N3	1.334	1.330	-0.32	C2-N3	1.311	1.324	1.03
N3-C4	1.337	1.339	0.21	N3-C4	1.355	1.346	-0.69
C4-C5	1.397	1.396	-0.10	C4-C5	1.394	1.399	0.29
C5-C6	1.410	1.413	0.23	C5-C6	1.438	1.428	-0.69
C6-N1	1.343	1.351	0.64	C6-N1	1.431	1.402	-2.03
C5-N7	1.381	1.380	-0.08	C5-N7	1.377	1.380	0.25
N7-C8	1.310	1.310	0.01	N7-C8	1.307	1.305	-0.11
C8-N9	1.376	1.376	0.01	C8-N9	1.380	1.383	0.17
N9-C4	1.374	1.373	-0.07	N9-C4	1.366	1.368	0.13
C6-N6	1.350	1.340	-0.77	C2-N2	1.372	1.347	-1.80
				C6-O6	1.219	1.241	1.78
bond angle				bond angle			
C6-N1-C2	118.6	119.7	0.95	C6-N1-C2	126.6	125.9	-0.56
N1-C2-N3	128.7	128.2	-0.44	N1-C2-N3	123.5	123.3	-0.15
C2-N3-C4	111.2	111.2	0.03	C2-N3-C4	112.5	112.4	-0.11
N3-C4-C5	127.0	127.2	0.20	N3-C4-C5	129.3	129.3	0.00
C4-C5-C6	115.8	116.3	0.46	C4-C5-C6	118.5	117.7	-0.69
C5-C6-N1	118.7	117.3	-1.16	C5-C6-N1	109.6	111.5	1.69
C4-C5-N7	111.4	111.5	0.02	C4-C5-N7	111.0	111.1	0.08
C5-N7-C8	104.0	104.0	0.03	C5-N7-C8	104.5	104.5	-0.07
N7-C8-N9	113.4	113.3	-0.08	N7-C8-N9	112.8	112.9	0.10
C8-N9-C4	106.8	106.8	0.01	C8-N9-C4	106.8	106.9	0.11
N9-C4-C5	104.4	104.5	0.03	N9-C4-C5	104.9	104.6	-0.23
N3-C4-N9	128.6	128.3	-0.22	N3-C4-N9	125.9	126.1	0.20
C6-C5-N7	132.8	132.2	-0.42	C6-C5-N7	130.5	131.3	0.56
N1-C6-N6	118.9	119.5	0.55	N1-C2-N2	117.0	116.7	-0.24
C5-C6-N6	122.4	123.1	0.59	N3-C2-N2	119.5	120.0	0.43
				N1-C6-O6	119.1	119.7	0.54
				C5-C6-O6	131.3	128.8	-1.91
parameter				parameter			
bond length	thymine			free base	cytosine		
free base	in base pair	diff (pair-free) in %	free base	in base pair	diff (pair-free) in %		
N1-C2	1.384	1.388	0.28	N1-C2	1.422	1.404	-1.25
C2-N3	1.381	1.376	-0.31	C2-N3	1.367	1.354	-0.94
N3-C4	1.402	1.386	-1.16	N3-C4	1.319	1.338	1.44
C4-C5	1.465	1.462	-0.22	C4-C5	1.439	1.442	0.21
C5-C6	1.353	1.354	0.08	C5-C6	1.359	1.356	-0.23
C6-N1	1.376	1.372	-0.29	C6-N1	1.352	1.358	0.43
C2-O2	1.219	1.222	0.20	C2-O2	1.222	1.236	1.16
C4-O4	1.222	1.236	1.07	C4-N4	1.356	1.333	-1.71
C5-M5	1.496	1.496	0.00				
bond angle				bond angle			
C6-N1-C2	123.8	123.6	-0.16	C6-N1-C2	123.4	122.5	-0.69
N1-C2-N3	112.8	113.6	0.73	N1-C2-N3	116.4	117.5	0.94
C2-N3-C4	128.0	126.7	-1.02	C2-N3-C4	120.3	121.2	0.72
N3-C4-C5	114.8	116.3	1.32	N3-C4-C5	124.0	121.6	-1.90
C4-C5-C6	117.9	117.5	-0.37	C4-C5-C6	120.0	117.0	-2.53
C5-C6-N1	122.7	122.3	-0.32	C5-C6-N1	123.4	120.3	-2.51
N1-C2-O2	123.1	122.2	-0.78	N1-C2-O2	118.1	118.3	0.12
N3-C2-O2	124.1	124.2	0.12	N3-C2-O2	125.5	124.3	-0.99
N3-C4-O4	120.2	120.5	0.29	N3-C4-N4	116.9	117.7	0.67
C5-C4-O4	125.0	123.2	-1.49	C5-C4-N4	119.1	120.7	1.32
C4-C5-M5	118.1	118.6	0.44				
C6-C5-M5	124.0	123.9	-0.07				



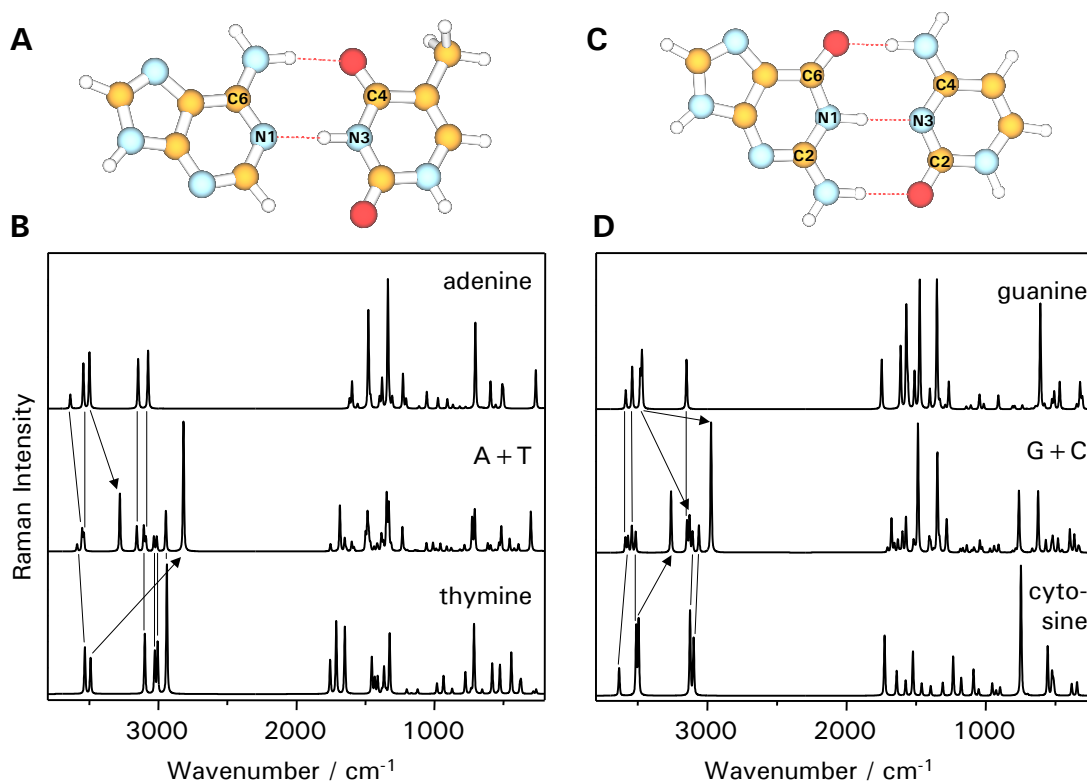


**Figure 7.4:** The Watson-Crick DNA base pairs. **A)** and **C)** show the optimized structure of the adenine-thymine and guanine-cytosine base pair, respectively. **B)** and **D)** show the corresponding calculated Raman spectra (B3PW91/6-31+G(d,p)).

stretching vibration of thymine. In the free base this vibration occurs at  $3491\text{ cm}^{-1}$  and due to the hydrogen bonding interaction with N1 of adenine it is lowered to  $2922\text{ cm}^{-1}$ .

In the wavenumber region below  $1900\text{ cm}^{-1}$  the normal modes are not located at only a small part of the molecule (such as just one bond), but rather involve larger parts of the molecule as was discussed together with table 7.2. Nevertheless, the wavenumbers associated with the C4=O carbonyl group shift to lower wavenumbers, since the C=O double bond loses electron density and therewith double bond character (see also table 7.3). The N1H bending vibration of thymine was found to move to higher wavenumbers by about 40 wavenumbers. Also the ring breathing modes (around  $730$  and  $710\text{ cm}^{-1}$ ) were found to shift slightly to higher wavenumbers. This effect is less pronounced for the larger purine ring system of adenine ( $+4\text{ cm}^{-1}$ ) than for the smaller pyrimidine ring ( $+14\text{ cm}^{-1}$ ).

**Guanine-cytosine Watson-Crick base pair** The same analysis as for the adenine-thymine base pair was also performed for the guanine-cytosine Watson-Crick base pair. Figure 7.4C shows the optimized geometric structure as obtained from DFT calculations (B3PW91/6-31+G(d,p)). Changes in bond length (in the order of magnitude of 1%) are observed due to hydrogen bonding for the bonds in close proximity to the hydrogen bonding interaction sites. The bonds close to

## 7 The biological target: DNA

the electron donors are lengthened due to the reduced electron density. In guanine this affects the C6=O and the C2N3 bond, and in cytosine the C2=O and the N3C4 bond. The bonds adjacent to the hydrogen donors are shortened. Those are the C6N1 and the C2N2 bond in guanine and the C4N4 bond plus the N1C2 bond in cytosine (see table 7.3).

The calculated Raman spectra of guanine (upper spectrum), cytosine (lower spectrum) and of the Watson-Crick base pair (middle spectrum) are presented in figure 7.4. As for the adenine-thymine base pair major changes occur in the wavenumber region of the NH- and CH stretching vibrations (above  $2800\text{ cm}^{-1}$ ). The hydrogen bonding interaction between C2NH<sub>2</sub> of guanine and C2=O of cytosine causes a shift of the NH stretching vibration from  $3494\text{ cm}^{-1}$  in the free guanine to  $3260\text{ cm}^{-1}$  in the Watson-Crick base pair. The N1H vibration of guanine shifts from  $3481\text{ cm}^{-1}$  in the free base to  $3106\text{ cm}^{-1}$  in the hydrogen bonded state, and finally, the symmetric N6H<sub>2</sub> vibration in free guanine is found at  $3469\text{ cm}^{-1}$  while in the H-bonded state the N6H stretching vibration is found at  $2973\text{ cm}^{-1}$ .

As for adenine and thymine the wavenumber region below  $1900\text{ cm}^{-1}$  shows a rather complex origin of the involved parts of the molecule (see table 7.2). However, the shift of the C=O stretching vibrations to lower wavenumbers in the hydrogen bonded base pair can clearly be seen in figure 7.4. Due to the loss of electron density in the C=O double bond the double bond character reduces (see also table 7.3) and the vibrations are shifted about 20 to  $40\text{ cm}^{-1}$  to lower wavenumbers. All the vibrations in the wavenumber region down to around  $1350\text{ cm}^{-1}$  contain contributions from NH deformation modes that are involved in hydrogen bonding. The ring breathing modes of guanine ( $607\text{ cm}^{-1}$  in the free base) and of cytosine ( $646\text{ cm}^{-1}$  in the free base) are found at higher wavenumbers in the base pair (shift by about  $16\text{ cm}^{-1}$ ) which can be explained by an increased stability of the ring due to van der Waals interactions.

The base pairing will be discussed later in this chapter when discussing the DNA spectra.

To determine the hydrogen bonding energy of the Watson-Crick base pair a single point calculation with the perturbation theory method MP/6-31++G(d,p) has been performed. The basis set superposition error (BSSE) could be avoided by performing the single point calculation of guanine within the ghost basis of the optimized cytosine structure of the Watson-Crick base pair and vice versa. The stabilization enthalpy of the guanine-cytosine pair was determined to be  $24\text{ kcal mol}^{-1}$  ( $100\text{ kJ mol}^{-1}$ ) and the Gibbs free energy to be  $13\text{ kcal mol}^{-1}$  ( $53\text{ kJ mol}^{-1}$ ). Since guanine and cytosine form three hydrogen bonds this gives a bonding enthalpy of  $8\text{ kcal mol}^{-1}$  for each hydrogen bond. Santamaria et al. [223] reported a value of  $34\text{ kcal mol}^{-1}$  ( $142\text{ kJ mol}^{-1}$ ) for the stabilization energy of the guanine-cytosine Watson-Crick base pair. The discrepancy to the literature value can be explained by the fact that Santamaria et al. used a basis set which was not augmented by polarization function. The calculated value is still higher than the experimental value which was obtained from temperature dependent IR absorption measurements performed by Carmona et al. [47]. They determined the cytosine-guanine Watson-Crick base pair association enthalpy to be  $6.8 \pm 0.6\text{ kcal mol}^{-1}$  ( $28.5\text{ kJ mol}^{-1}$ ).

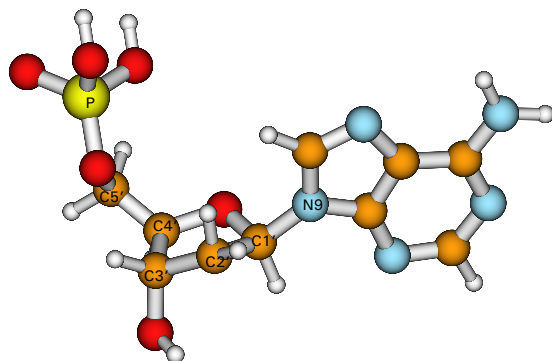


**Figure 7.5:** Optimized structure of deoxyadenosine-5'-monophosphate as obtained from DFT calculations (B3PW91/6-31+G(d,p)).

Further hydrogen bonding interactions between the base pairs are possible, such as inverse Watson-Crick, Hoogsteen or inverse Hoogsteen base pairs, or even triple or quadruple interactions. Some of them were found in naturally occurring RNA. However, since their importance in the biological interactions of DNA is rather low, they have not been studied in detail within this work.

## 7.1.2 The nucleosides and nucleotides

So far, only the nucleic acid bases have been discussed. However, in the DNA the bases are bound to a deoxyribosyl moiety (via a glycosidic linkage to N9 in adenine and guanine, and N1 in thymine and cytosine) to form a nucleoside. The individual nucleosides are connected via a phosphate bridge which forms an ether bond with the hydroxyl groups on C3' and C5' of the sugar ring. Those nucleotides composed from a nucleic acid base, a sugar moiety and a phosphate form the building blocks of the nucleic acid.

### 7.1.2.1 Structural parameters

Figure 7.1.2.1 shows the fully optimized structure deoxyadenosine and deoxyadenosine-5'-monophosphate as obtained from the DFT calculations (B3PW91/6-31+G(d,p)). The nucleoside and nucleotide of the other nucleic acid bases can be obtained from the pure base by addition of the sugar moiety and the phosphate in the same manner. In DNA the sugar deoxyribose is implemented while in RNA ribose is used. The two pentoses differ only in an OH-group at C2' which is present in ribose and absent in deoxyribose as depicted in figure 7.1.2.1.

The sugar moiety is connected to the base via a glycosidic linkage to N9 (for the pyrimidine bases it would be N1) with a torsion angle  $\chi$  (O4'-C1'-N9-C4 or O4'-C1'-N1-C2). If the value of  $\chi$  ranges from  $-110^\circ$  to  $-180^\circ$  the conformation is called anti [34]. This is the most common orientation found in nucleotides and within the double helix of DNA and RNA (see also section

## 7 The biological target: DNA

7.2). The example in figure 7.1.2.1 adopts an angle of  $\chi = -124^\circ$ . Upon addition of the sugar moiety to the base the purine and pyrimidine ring systems stay planar. The most common sugar conformation is the twist conformation where three atoms are in one plane (for ribofuranose the C1'-O4'-C4' plane is fixed) and two atoms (C2' and C3') are sticking out of plane. The sugar pucker will also affect the shape of the  $\alpha$ -helix of the DNA double strand as will be discussed in section 7.2. In figure 7.1.2.1 C2' is sticking out of the plane of the molecule on the same side as the carbon atom C5' (endo) and C3' on the opposite side (exo). This is also the conformation found in the common B-DNA. However, in single nucleoside and nucleotides the energy barrier between the different conformations is quite low and therefore different sugar conformations are present via a rapid equilibrium. Another important angle is the torsional angle  $\gamma$  around the C5'C4' bond. In figure 7.1.2.1 it adopts  $\gamma_{(O5'-C5'-C4'-C3')} = 52^\circ$  which corresponds to a gauche (g+) orientation. This orientation ( $\gamma = 30 - 90^\circ$ ) is also common in helical nucleotides. To minimize steric interactions the torsion angle  $\beta_{(P-O5'-C5'-C4')}$  is found to be periplanar ( $\beta \sim -170^\circ$ ). The bond length and bond angles of the nucleic acid base change only slightly upon N-linkage with the sugar moiety. However, coupling of the vibrational modes occurs which affects the vibrational spectra as will be discussed in the next section.

The sugar and the phosphate can also be attached in a different orientation to the nucleic acid base. For example, the glycosidic linkage could be in syn conformation or the deoxyribose ring could adopt another conformation (twist with other atoms out of the plane, or higher energy envelope conformations). Also the torsional angle along the C4'-C5' or C5'-O5' could vary. The structure shown above is an energy minimum structure for nucleotides and also the configuration adopted in the Z-DNA (see also section 7.2).

### 7.1.2.2 Raman spectra

The addition of the ribosyl and the phosphate moiety alters also the Raman spectra. Exemplarily, the Raman spectra of guanine, guanosine and guanosine-5'-monophosphate (GMP) are shown in figure 7.6. The Raman spectra of the other DNA bases in comparison with their nucleosides and nucleotides are presented in the appendix (section B).

As was mentioned previously, most of the Raman bands arise from vibrations that are not localized at only one bond, but rather involve many atoms. Upon addition of the sugar moiety coupling across the furanose ring and phosphate side chain occurs as can be seen in table B.1 in the appendix where a vibrational band assignment is given for guanine, guanosine and guanosine-5'-monophosphate. The broadening of the Raman lines in the nucleosides and nucleotides is most likely due to overlapping bands of different sugar configurations that vary only slightly in energy.

The vibrational bands due to the furanose occur in the spectral region below  $1500 \text{ cm}^{-1}$  (see also table B.1). Furthermore the Raman bands of the nucleic acid base ring system experience slight changes in vibrational frequency and intensity due to the vibrational coupling. For example the triene vibrational mode of the purine ring in guanine shifts from  $1464 \text{ cm}^{-1}$  to  $1481 \text{ cm}^{-1}$  in

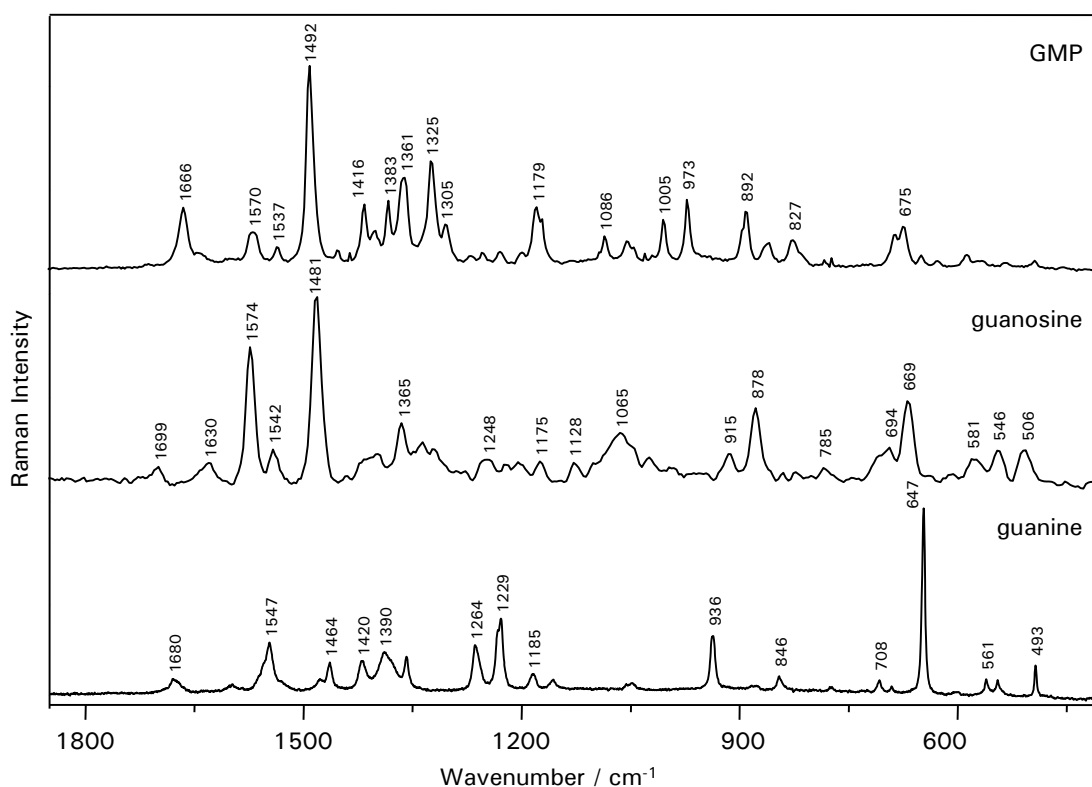


**Figure 7.6:** Raman spectra of guanine, guanosine and guanosine-5'-monophosphate.

guanosine and to  $1492\text{ cm}^{-1}$  in GMP. Additionally, it gains markedly intensity due to the coupling to the sugar vibrations. Due to the coupling the vibrational bands in the region between  $1100$  and  $600\text{ cm}^{-1}$  are sensitive to the DNA conformation and can be used as marker bands [139, 70]. The characteristic  $\text{PO}_3$  stretching vibrations are found at higher wavenumbers in the nucleotides than in the DNA because the ester bond to the 3'-hydroxyl group of the sugar of the next nucleotide is missing.

### 7.1.2.3 IR absorption spectra

IR absorption spectra have been recorded of the individual bases, the nucleosides and the nucleotides. IR absorption spectra of adenine, adenosine and adenosine-5'-monophosphate are shown exemplarily in figure B.4 in the appendix (section B).

Due to the different selection rules of Raman and infrared spectroscopy the IR absorption spectra look slightly different than the Raman spectra. High intensity is observed for those vibrational bands in the IR spectrum with a strong change in the dipole moment. However, since the crystals of the nucleic acid bases, nucleosides and nucleotides were found to have a non-centrosymmetric symmetry group [133, 134, 136] all modes should be Raman and IR active. Therefore, tables 7.2 and B.1 can be used for band assignment. Additional bands arise in the IR spectrum from over-

## 7 The biological target: DNA

tones and combination tones, especially in the wavenumber region above  $1000\text{ cm}^{-1}$ , as was also reported earlier by Florian [75] and Giese and McNaughton [84].

### 7.1.2.4 UV/vis absorption spectroscopy of the DNA building blocks

The nucleic acid bases (especially guanine) are only poorly soluble in the common solvents, so it is difficult to prepare solutions with high enough concentrations to give a good Raman signal. However, the scattering cross section can be increased by about 6 orders of magnitude when performing resonance Raman spectroscopy and using an excitation wavelength within an absorption band of the molecule of interest (see section 2.1.3.1 in the theoretical fundamentals). To select the appropriate excitation wavelength it is necessary to know and understand the UV/vis absorption spectra of the substances. The nucleic acid bases, nucleosides and nucleotides are white substances and therefore they absorb only in the UV. The UV absorption spectra have been recorded of the aqueous solutions and the spectra of the deoxynucleotides are shown in figure 7.7. In the spectral region above 200 nm the absorption is almost exclusively due to electronic transitions located at the heterocyclic rings of the nucleic acid bases. Therefore, the absorption spectra of the pure base, the nucleosides and the nucleotides show the same features and only the absorption spectra of the deoxy-nucleotides are depicted in figure 7.7. Major achievements in the assignment of the electronic transitions have been performed by Callis [46] and Fodor et al. [77] and will be summarized briefly in the following.

The long-wavelength absorption maximum of deoxy-guanosine-triphosphate (dGTP) is composed of two electronic transitions, one centered around 275 nm and one around 253 nm. The electronic transition at 253 nm is centered at N7=C8 and shows a long axis polarization. The longest wavelengths transition was assigned to the lowest energy  $\pi - \pi^*$  transition of the triene C2=N3-C4=C5-N7=C8 with a polarization along the short axis. A second weak triene transition is found at 218 nm. The strong absorption bands around 205 nm and 190 nm are due to a  $\pi - \pi^*$  transition involving both rings and an  $n - \pi^*$  transition localized at the C6=O bond.

The second purine based nucleotide, deoxy-adenosine-triphosphate (dATP), shows similar electronic transitions, however the energy ordering of the first two lowest energy transitions is reversed with respect to guanine: the  $\pi - \pi^*$  transition localized at N7=C8 occurs at 260 nm, and the (weak) triene transition at 245 nm. A second (very weak) triene transition can be found at 230 nm. The absorption band at low wavelength is composed of a  $\pi - \pi^*$  transition at 213 nm of the ring system with long axis polarization and an  $n - \pi^*$  transition at 200 nm with strong contributions from NH<sub>2</sub>.

The nucleotide of the pyrimidine base thymine (deoxy-thymidine-triphosphate, dTTP) shows only two electronic transitions in the investigated spectral region: one at 265 nm associated with the  $\pi - \pi^*$  transition of the enone system (C6=C5-C4=O) and a second (perpendicular) transition at 209 nm centered at the C2=O bond.

Deoxy-cytidine-triphosphate (dCTP) shows a more complex absorption spectrum with four electronic transitions in the region of interest: around 270 nm an enamine  $\pi - \pi^*$  transition (C6=C5-

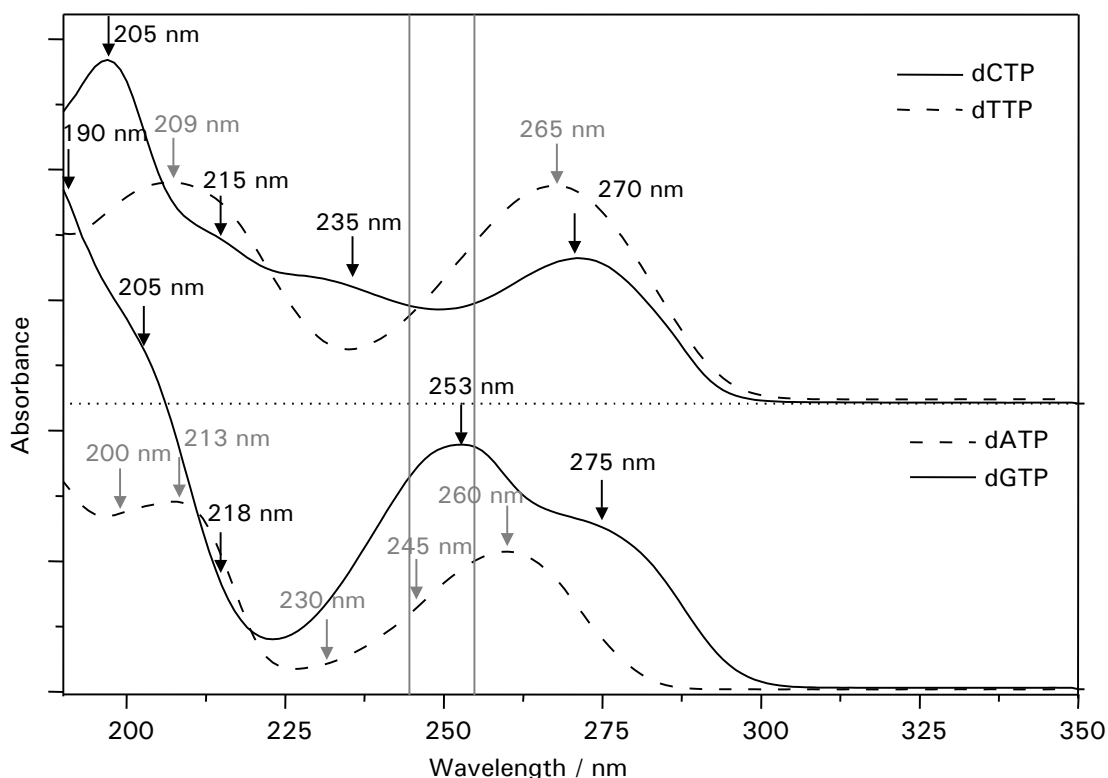


**Figure 7.7:** UV absorption spectra of the deoxy-nucleotides: **in the top** the UV absorption spectra of the pyrimidine based deoxy-thymidine-triphosphate (dTTP, dashed line) and deoxy-cytidine-triphosphate (dCTP, solid line), **in the bottom** the two purine based deoxy-adenosine-triphosphate (dATP, dashed line) and deoxy-guanosine-triphosphate (dGTP, solid line) are shown.

The arrows above the spectra indicate the electronic transitions. The thin grey vertical lines denote the two UV excitation wavelength 244 nm and 257 nm used for the UV-resonance Raman experiments.

C4=N3), at 235 nm another enamine  $\pi - \pi^*$  transition (C6=C5-C4=N3) with major contributions of the exocyclic C4-NH<sub>2</sub> bond. The transition at 215 nm involves also the enamine  $\pi - \pi^*$  transition (C6=C5-C4=N3) with major contributions from the C2=O bond, and finally, the electronic transition around 205 nm is due to an  $n - \pi^*$  transition located at NH<sub>2</sub>.

The wavelength chosen for recording the resonance Raman spectra of the nucleotides will have a great influence on the enhancement pattern, due to the vibrational modes coupling to the chosen electronic transition dominating the spectrum. In the following experiments 244 and 257 nm are used for excitation as marked in the UV absorption spectra of the bases in figure 7.7. For completeness the UV absorption spectra of aqueous solutions of all four nucleic acid bases, nucleosides and nucleotides are shown in the appendix (figure B.6- B.9).

## 7 The biological target: DNA

**Molar extinction coefficient** The molar extinction coefficient of the nucleotides was determined to be  $11800 \text{ L mol}^{-1} \text{ cm}^{-1}$  for AMP,  $10000 \text{ L mol}^{-1} \text{ cm}^{-1}$  for GMP, and  $7100 \text{ L mol}^{-1} \text{ cm}^{-1}$  for CMP.

### 7.1.3 UV-resonance Raman spectroscopy of the DNA building blocks

To assess also structural information of the DNA building blocks in solution resonance Raman spectroscopy as a special Raman techniques was applied to overcome the low scattering efficiency of normal Raman spectroscopy. As excitation wavelength the frequency doubled argon ion laser lines at 244 nm and 257 nm were used. Both wavelengths lie within an electronic  $\pi - \pi^*$  transition of the heterocyclic rings of the nucleic acid bases (see figure 7.7). The sugar and phosphate moieties do not absorb in this spectral region (spectra not shown).

The UV-resonance Raman spectra of the aqueous solutions of the nucleic acid bases (A), the nucleosides (B), the nucleotides (C) and the deoxy-triphosphate-nucleotides (D) with excitation at 244 nm are shown in figure 7.8. In the resonance Raman spectra only those vibrations that couple to the excited electronic transition are enhanced. Therefore, only Raman bands of the nucleic acid bases (the purine and the pyrimidine ring system) are detected and the spectra of all four different substituted DNA building blocks (the base, the nucleoside, the nucleotide and the deoxy-triphosphate) look quite similar (especially for adenine and thymine). Raman bands associated with vibrations of the sugar or phosphate moiety do not show up in the spectra. However, they exhibit a slight influence on the ring vibrations of the bases via vibrational coupling. Most of the bands present in the UV-resonance Raman spectra have already been observed for visible Raman excitation. However, the spectral intensities differ greatly from the ones of the off-resonance Raman spectra excited with 532 nm (figure 7.6 and figure B.1-B.3 in the appendix). Nevertheless, the vibrational assignment of the off-resonance Raman spectra can be used for an assignment of the resonance Raman bands together with the knowledge of the involved electronic transitions discussed in the previous section 7.1.2.4. A comparison of the experimental resonance Raman bands and the assignment from the visible spectra together with several assignments from the literature are given in table 7.4 for guanine and adenine. For some bands the different references show slight discrepancies.

When using 244 nm to excite the resonance Raman spectra, the triene and N7=C8  $\pi - \pi^*$  transitions of the purines and the enone C6=C5-C4=O  $\pi - \pi^*$  transition of thymine as well as the enamine C6=C5-C4=N3  $\pi - \pi^*$  transition of cytosine are involved (see figure 7.7 and figures B.1-B.3 in the appendix). Therefore, the band assignment taking those vibrations located at those groups into account should be most reliable.

The visible Raman spectra appear much more crowded due to overlapping bands of the sugar moieties. Selective enhancement with the UV light can simplify the spectra and overlapping bands can be resolved. When changing the excitation wavelength so that different electronic transitions are enhanced different vibrations can selectively be probed. However, when changing the exci-



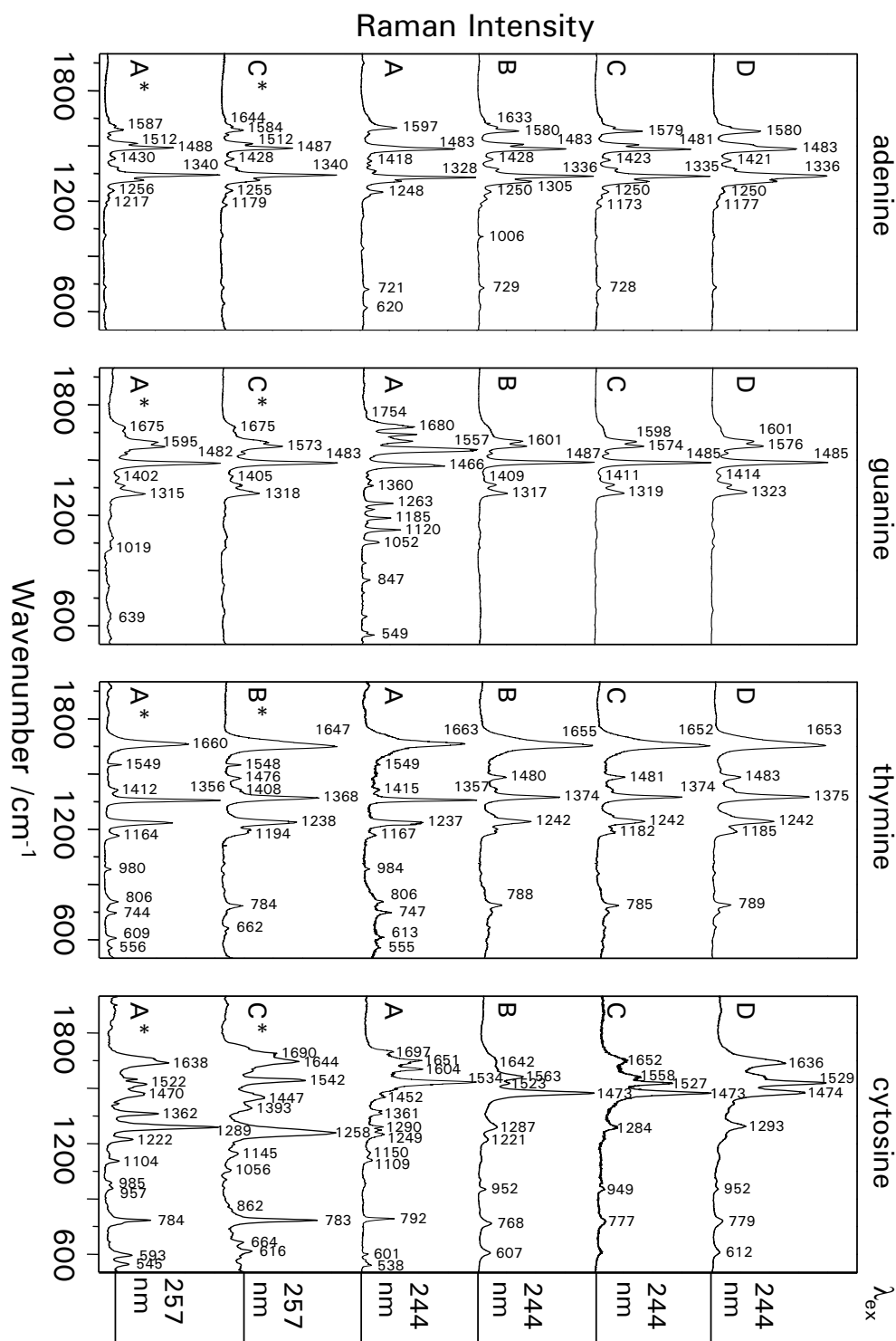


**Figure 7.8:** UV-resonance Raman spectra of the aqueous solutions of the nucleic acid bases (A, A\*), the nucleosides (B, B\*), the nucleotides (C, C\*) and the deoxy-triphosphate-nucleotides (D) with excitation at 244 nm (A-D) and at 257 nm (A\*,B\*,C\*). The nucleic acid base is named above the spectral array (from left to right): adenine, guanine, thymine and cytosine.

**Table 7.4:** Vibrational band assignment of the UV-resonance Raman spectra of the DNA building blocks based on guanine and adenine. Wavenumbers are given in  $\text{cm}^{-1}$ .

G	$\lambda_{\text{exc}}=244 \text{ nm}$			$\lambda_{\text{exc}}=257 \text{ nm}$			$\lambda_{\text{exc}}=257 \text{ nm}$			$\lambda_{\text{exc}}=257 \text{ nm}$			$\lambda_{\text{exc}}=532 \text{ nm}$			$\lambda_{\text{exc}}=633 \text{ nm}$			
	G <sub>S</sub>	GMP	dGTP	G	GMP	dATP	G	GMP	dATP	G <sub>S</sub>	dGs	dGs	G (calc.)	G (exp)	assignment	G (calc.)	G	assignment	
1680	1680	1680	1680	1675	1675	1644	1685	1685	1685	1685	1685	1685	1818	1680	C6O str, NIC6, CSC6, NIH	1797	1675	str C6O-C5C6, bend NIH	
1639	1639	1639	1639	1595	1594	1604	1643	1643	1643	1643	1643	1643	1677	1609	N2H <sub>2</sub> sciss, C2N3 str, C2N1 str, NIH def	1667	1602	sciss NH <sub>2</sub> , str C2N2-C2N3	
1557	1574	1574	1576	1572	1573	1577	1577	1577	1577	1577	1577	1577	1635	1547	N2H <sub>2</sub> sciss, N9H, ring (C4)	1621	1551	str C2N3-N3C4, sciss NH <sub>2</sub> , bend NIH	
1466	1487	1485	1485	1482	1483	1489	1489	1489	1489	1489	1489	1489	1623	1464	N2H <sub>2</sub> sciss, ring str, N9H ring str, NIH, C2NH <sub>2</sub>	1610	1551	str N3C4-C4C5+C2N3, sciss NH <sub>2</sub> str	
1420	1409	1411	1414	1402	1405	1413	1413	1413	1413	1413	1413	1405	1420	N9H, C5N7 str, rim	1441	1421	str N7C8-N3C4-N1C2, bend C8H, NIH		
1388	1364	1364	1363	1359	1361	1367	1367	1367	1367	1367	1367	1383	1390	C5N7 str, C4N9 str, N9H def, C8H def	1390	1390	str N1C2-N7C8+C4N9, bend NIH, rock NH <sub>2</sub> , bend N9H, str C8N9-C5N7		
1360	1317	1319	1323	1315	1318	1319	1319	1319	1319	1319	1319	1322	1322	N7C8 str, C8H bend	1365	1361	str C5N7-C4N9-C5C6-N3C4, bend C8H, N9H		
1263													1343	1264	NIH def, N2H def, N3C4 str, C8H	1337	1265	bend NIH, N2H <sub>2</sub> (str C5N7-C2N2-N3C4)	
1232													1316	1229	NIH def, C8H def, N9H	1310	1234	bend NIH, N9H, C8H, str C2N2-N7C8	
1185													1185	1185	C8H def, N9H def, ring	1176	1186	bend C8H, str C5N7, def R6 (sqz N3C4C5)	
1120													1151	1090	N2H <sub>2</sub> def, N1C6 str, ring	1141	1159	rock NH <sub>2</sub> , str N1C6	
1052													839	846	C8N9 str, N1C2 str, N9H def, NH2 def	1074	1048	str C8N9-N1C6, bend N9H, C8H	
847													545	561	pur ring def	835	848	def R5 (sqz C4N9C8, str C5N7), R6 (sqz N1C2N3)	
549														561	N9H out, N2H <sub>2</sub> wag	536	562	wag N9H	
A	$\lambda_{\text{exc}}=244 \text{ nm}$	A <sub>S</sub>	AMP	dATP	$\lambda_{\text{exc}}=257 \text{ nm}$	A	AMP	dAs	Ref. [273], $\lambda_{\text{exc}}=257 \text{ nm}$ assignment	9-EIA	Ref. [257], $\lambda_{\text{exc}}=266 \text{ nm}$ assignment	A (calc.)	B3PW91/6-31+G(d,p) and $\lambda_{\text{exc}}=532 \text{ nm}$ assignment	A (exp)	assignment	A (calc.)	Ref. [85], B3LYP/6-31+G(d,p) and $\lambda_{\text{exc}}=633 \text{ nm}$ assignment	A (exp)	assignment
1633	1600	1599	1580	1607	1604	1603	1603	1603	NH <sub>2</sub> bend, CSC6, C6N str	1648	NH <sub>2</sub>	1680	1609	NH2 bend + C8H bend + im ring bend -N6H bend	1665	1674	sciss NH <sub>2</sub> , str C6-N6, C5-C6		
1597	1580	1579	1580	1587	1584	1580	1580	1580	C4C5, N3C4 str	1605	NH2	1620	1595	NH <sub>2</sub> bend	1643	1613	str N3-C4, N1-C6, C5-N7, N7-C8, bend N9-H		
1565	1508	1505	1505	1512	1512	1506	1506	1506	C4N9 str, C8H bend	1518	acceptor sites	1539	1479	C8H bend + NH2 bend	1613	1597	sciss NH <sub>2</sub>		
1483	1483	1481	1483	1488	1487	1482	1482	1482		1487	acceptor sites, Zlow v/ Zhigh v) correlates with the H-bond strength at NH	1522	1479	NH <sub>2</sub> bend (55) - C2H bend (28) - N9H bend (11)	1524	1483	str N7-C8, bend C8-H, sciss NH <sub>2</sub>		
1418	1428	1423	1421	1430	1428	1424	1424	1424	N1C6, C6N str	1420	acceptor sites	1435	1417	N9H bend - C2H bend	1441	1419	str C4-N9, C4-C5, C6-N6, N7-C8, bend C2-H		
1393	1373	1373	1372	1372	1379	1375	1375	1375		1368	NH <sub>2</sub> and acceptor sites	1391	1368	C8H bend - N9H bend - im ring bend <sup>2</sup>	1423	1372	bend C2-H, N9-H, str C8-N9, C4-N9		
1364	1336	1335	1336	1340	1340	1336	1336	1336	C5N7, N7C8 str	1334	acceptor sites	1380	1330	C2H bend + NH <sub>2</sub> bend + N9H bend -N6H bend	1365	1333	str C5-N7, N1-C2, bend C2-H, C8-H,		
1306	1305	1306	1307	1311	1312	1310	1310	1310	C8N9, C2N3 str, C8H bend	1311	acceptor sites and NH <sub>2</sub>	1278	1305	C8H bend + N9H bend	1341	1308	str C2-N3, N1-C2, C5-C6, C5-N7		
1248	1250	1250	1250	1256	1255	1250	1250	1250	N1C2, C8N9 str, C2H bend	1254	NH <sub>2</sub> and acceptor sites	1254	1247	C8H bend -N6H bend	1272	1248	bend C8-H, N9-H, str N7-C8		
	1210	1220		1217		1208	1208	1208	C8H, N7C8 str	1156	acceptor sites	1156	1232	C8H bend + N9H bend + N6H bend + im ring bend	1246	1234	rock NH <sub>2</sub> , str C5-N7, N1-C2, C2-N3		
				1179		1173	1173	1173	C7N8, C1C2 str, C6NH bend	1197	acceptor sites	1098	1022	C2H out + pyr ring tors	1148	1162	bend C8H, N10-H11, str C4-N9, N3-C4, C6-N10		
721	729	728				730	730	730	ring breath			976	721	im ring tors <sup>2</sup> + C6N out + pyr ring tors + pyr ring tors <sup>2</sup>	1012	1025	rock NH <sub>2</sub>		
620												618	620	im ring bend + im ring bend <sup>2</sup> - N6H bend	726	723	ring breath whole molecule (distorted)		
																618	623	def R6 (sqz group C4C5-C6, N1-C6-N10), R5 (sqz group C5-N7-C8)	

tation wavelength from 244 nm to 257 nm rather minor changes occur in the spectra as can be seen in figure 7.8 when comparing the upper four spectra ( $\lambda_{ex}=244$  nm) with the lower two ( $\lambda_{ex}=257$  nm). This similarity is also expected from the UV absorption spectra shown in figures 7.7 and B.1-B.3. For adenine, guanine and thymine both lines, 244 nm and 257 nm, excite the same electronic transition. For cytosine (and the related compounds) two different enamine transitions are involved, one centered around 240 nm and the other one centered around 270 nm (for CMP). This is also reflected in the UV-resonance Raman spectra as can be seen in figure 7.8 far right panel.

The excitation at 257 nm is close to the absorption maximum of DNA (see section 7.4.2). At this wavelength the adenine band at  $1336\text{ cm}^{-1}$  will dominate the spectrum of a mixture of equally concentrated nucleotides.

When exciting at 244 nm the vibrational band at  $1485\text{ cm}^{-1}$  resulting from guanine will have the highest intensity. Furthermore, the adenine band at  $1336\text{ cm}^{-1}$  and  $1483\text{ cm}^{-1}$  can be used as marker bands. For thymine the vibrational bands at  $1653\text{ cm}^{-1}$  and  $1357\text{ cm}^{-1}$  are ideally suited when exciting at 244 nm as well as when exciting at 257 nm. For cytosine the vibrational bands at  $1289\text{ cm}^{-1}$  and  $784\text{ cm}^{-1}$  are important when 257 nm is used as excitation wavelength and around  $1530\text{ cm}^{-1}$  when exciting at 244 nm. Cross section of prominent resonance Raman bands have been determined before and are reported in the literature [273]

#### 7.1.4 Summary

This section made familiar with the characteristic features (structure and spectroscopy) of the individual nucleic acid bases nucleosides and nucleotides. Raman, IR absorption and resonance Raman spectra have been used to comprehensively characterize the bases. DFT calculations assisted in the assignment of the vibrational bands. The Raman and IR absorption spectra of the polynucleotides (and also of the nucleic acids, as will be seen later) are complex due to the overlap of many vibrational bands. Nevertheless it is possible to identify special marker bands for the different nucleotides. The most prominent Raman bands of the solid nucleic acids are around  $1330\text{ cm}^{-1}$  and  $720\text{ cm}^{-1}$  in adenine, around  $1230\text{ cm}^{-1}$  and  $648\text{ cm}^{-1}$  for guanine, around  $1670\text{ cm}^{-1}$  and  $1366\text{ cm}^{-1}$  for thymine and  $1290\text{ cm}^{-1}$  and  $790\text{ cm}^{-1}$  for cytosine.

The vibrational signature can be simplified when using resonance Raman spectroscopy. Only those vibrational bands will be enhanced in the Raman spectrum that couple to the excited electronic transition. UV absorption spectroscopy can be used to identify the electronic transitions and explain the wavelength dependence of the UV-resonance Raman spectra. In these experiments the lines 244 or 257 nm of an frequency doubled argon ion laser were used as excitation wavelength. These two wavelength excite the vibrations of the purine and pyrimidine ring system of the nucleic acid bases and the vibrational bands associated with these transitions will dominate the spectrum. The most prominent Raman bands of the four nucleotides are the triene vibration around  $1485\text{ cm}^{-1}$  for guanine with a high Raman cross section, the CN stretching vibration

## 7 The biological target: DNA

around  $1483\text{ cm}^{-1}$  of adenine, also with a quite high Raman cross section. For the two pyrimidine bases cytosine and thymine the CN stretching vibration around  $1530\text{ cm}^{-1}$  (C) and the CC and CN stretching vibrations around  $1660\text{ cm}^{-1}$  (T) and  $1370\text{ cm}^{-1}$  (T) will dominate the spectrum, however, with a smaller Raman scattering cross section than for the Raman bands of the purine bases.

Furthermore, it was shown that Raman spectroscopy can be applied to assess information about the environment of the nucleic acid bases, such as hydrogen bonding interactions. Also the configuration of the molecules such as the orientation of the sugar moiety showed influence on the vibrational signature. This fact will be used in later sections when studying DNA configurations.

### 7.2 Primary and secondary structure of DNA

The DNA is a double stranded polymer made of the nucleotides of the four nucleic bases adenine (A), guanine (G), thymine (T) and cytosine (C), that were investigated in detail in the previous section. The primary structure, which is the sequence of the bases, encodes the genetic information. The two strands which run in opposite directions are connected via hydrogen bonds between the complementary purine and pyrimidine bases: A pairs with T via two hydrogen bonds, and G pairs with C via three hydrogen bonds (see the Watson-Crick base pairs in figure 7.4 in section 7.1.1). This hydrogen-bonded double helical structure is called the secondary structure of the DNA. According to the geometric parameters, such as helix diameter, rise per base pair, screw sense and orientation of the glycosidic bond, the Watson-Crick double helix is classified into A-, B- and Z-DNA (and further modifications of minor importance which should not be discussed here). A-DNA with a helix diameter of  $25.5\text{ \AA}$  is the broadest of the three types, and 11 base pairs are necessary to complete a turn in the right-handed double helix. A-DNA has a narrow and very deep major groove and a very broad and shallow minor groove. B-DNA is also right-handed, with 10.4 base pairs per turn of the helix. It possesses wide and quite deep major grooves and narrow, but quite deep minor grooves. The helix diameter is about  $23.7\text{ \AA}$ . Unlike A- and B-DNA, Z-DNA is a left-handed helix with a diameter of only  $18.4\text{ \AA}$  and 12 base pairs are necessary to complete one turn. The major groove is flat, the minor groove very narrow and deep. The geometric parameters (torsion angles) of the DNA-molecule are summarized in table 7.5 for A-, B- and Z-DNA. For A-DNA the sugar pucker is C3'-endo, and in B-DNA it adopts C2'-endo configuration. A more detailed discussion of the DNA structure and modifications of the ideal forms is provided by Saenger [222]. Since B-DNA is the lowest energy configuration, it is the most common structure encountered *in vivo*. Also the extracted plasmid pBR322 exists in this form as proved later in this work.

The primary sequence of the DNA was also found to affect the flexibility of the DNA chain. A:T sequences are more flexible than G:C sequences. This fact is called the secondary genetic code because some proteins seem to bind based on structure and flexibility to DNA and not by contacting DNA in sequence specific manner.

**Table 7.5:** Torsional angles for A-, B- and Z-DNA [34]

structure type	torsion angles and atoms involved						
	$\alpha$ O3'-(n-1)-P-O5'-C5'	$\beta$ P-O5'-C5'-C4'	$\gamma$ O5'-C5'-C4'-C3'	$\delta$ C5'-C4'-C3'-O3'	$\epsilon$ C4'-C3'-O3'-P	$\zeta$ C3'-O3'-P-O5'-(n+1)	$\chi$ O4'-C1'-N1-C2 (pur) O4'-C1'-N9-C4 (pyr)
A-DNA	-50	172	41	79	-146	-78	-154
B-DNA	-41	136	38	139	-133	-157	-102
Z-DNA (C-res.)	-137	-139	56	138	-95	80	-159
Z-DNA (G-res.)	47	179	-169	99	-104	-69	68

### 7.3 The plasmid-DNA pBR322

Most of the experiments within this work were exemplarily performed with the plasmid pBR322. The name pBR322 derives from p for plasmid, the letters B and R acknowledge the discoverer of the plasmid F. Bolivar and R.L. Rodrigues, and 322 is just a laboratory number. The molecular weight was determined to be 2.9 MDa. This plasmid is the first widely used cloning vector from *E. coli*. With a length of 4361 base pairs (bp) it is still small enough to separate the different topoisomers (relaxed, superhelical und open circle) in an electrophoretic gel, which is of special interest when investigating the action of the enzyme gyrase. At the same time it is also large enough to provide a sufficient working surface for the gyrase and therefore act as a target for the enzyme.

Its complete nucleotide sequence is known and shown in table 7.6. Within the first 1300 bp and within the last 1000 bp, when starting the base pair count at the EcoRI site as done in table 7.6, the plasmid pBR322 carries the resistance genes to the antibiotics tetracycline and ampicillin, respectively. This fact was used when cultivating *E.coli* for the extraction of the plasmid pBR322. Tetracycline and ampicilline were added to the culture during bacterial growth in order to select only those bacteria that carry the plasmid (see section 3.2.2). Of special interest for further binding experiments to the enzyme gyrase is the nucleotide sequence around the T<sub>990</sub>-site: 5' – AGGCTGGATTGGCCTTCCCAT – 3'. Lockshon and Morris identified this region to preferentially bind to the GyrA subunit [144]. The ester formation with the tyrosine moiety of the GyrA involves the phosphate group of the central tyrosine marked with underline. For further details about the gyrase-DNA interactions see section 8.1.2 and section 8.4.1.

## 7.4 Spectroscopic characterization of DNA

### 7.4.1 Micro-Raman spectroscopy

Figure 7.9 shows a micro-Raman spectrum of native plasmid DNA pBR322 in the solid state (precipitate after the phenol-chloroform purification (see experimental section 3.2.2)). The spectrum contains contributions from the purine and pyrimidine bases, the sugar and the phosphate moieties. Comparison with the micro-Raman spectra of the individual nucleotides discussed in the previous section (section 7.1) can help assigning the vibrational bands. Slight changes in the position and

7 The biological target: DNA

**Table 7.6:** Complete nucleotide sequence of the *Escherichia coli* plasmid pBR322 [251] (Origin of the base count at the EcoRI site).

base count	sequence					
1	ttctcatggt	tgacagctta	tcacgataa	gcttfaatc	ggtagtttat	cacagttaaa
61	ttgctaacc	agtccaggcac	cggtgatgaa	atctaacaat	gcgctcatcg	tcacctcgg
121	caccgtcacc	ctgagctgct	taggcataagg	ctfgtttatg	ccggtactgc	cgggcctctt
181	gcgggatac	gtccatcccg	acagcaccge	cagtcactat	ggcgtgctgc	tagcgtctata
241	tgcgttgatg	caatttctat	gcgcaccctg	tctcggagca	ctgtccgacc	gctttggccg
301	ccgccaccgc	ctgctgcctt	cgctactggg	agccactatc	gactaccgca	tcacgagcac
361	cacaccgtc	ctgtggatcc	tctacgccgg	acgcatcgtg	gccggcatca	ccggcgccac
421	aggtgcggtt	gctgcgcctt	atatgccgga	catcaccgat	ggggaagatc	ggcctgccca
481	ctcgggctc	atgagcgtt	gtttcggcgt	gggtatggtg	gcagcccccg	tgccgggggg
541	actgttgggc	gccatctcct	tgcatgcacc	atctctgctg	gcggcgggtg	tcacggcctt
601	caactacta	ctgggctgct	tctaatagca	ggaagtcgat	aaggagagac	gtcgaccgat
661	gcccttgaga	gccctcaacc	cagtcagctc	cttccggtgg	gcgcggggca	tgactatcgt
721	cgccgcactt	atgactgtct	tctttatcat	gcaactcgtg	ggacaggtgc	cgcgacgctt
781	ctgggtcatt	ttcggcgagg	accgcttctg	ctggagcgcg	acgatgatcg	ggcttgcctt
841	tgcgttatic	ggaatcttgc	acgcctctgc	tcaagccttc	gtcactgttc	ccgcaccaaa
901	acgtttcggc	gagaagcagg	ccattatcgc	cggcatggcg	gccgagcgcg	ttggctactg
961	ctgtctggcg	ttcgcgacgc	gaggctggat	ggcctcccc	attatgattc	ttctcgtctt
1021	cggcgccatc	gggatgcccg	cgftgcaggc	catgctgccc	aggcaggtag	atgacgacca
1081	tcaggggacag	ctcaaggat	cgctcggcgc	tcttaccagc	ctaactcga	tcactagacc
1141	gctgatgctc	acggcgattt	atgcgccttc	ggcgagcaca	tgaacgggtt	tgcatggatg
1201	tgtaggcgcc	gccctatacc	ttgtctgctt	cccccgttgg	cgfcgctgtg	catggagccg
1261	ggccacctcg	acctgaatgg	aagccggcgg	cacctcgcct	acggattcac	cactcaaga
1321	attggagcca	atcaattctt	gcggagaact	gtgatgcgc	aaaccaacc	ttggcagaac
1381	ataccatcgc	cgctcggcat	ctccagcagc	cgcacgcggc	gcactcgggg	cagcgttggg
1441	tcctggccac	gggtgcgcct	gatcgtcttc	ctgtcttga	ggaccggcct	agctgcggcg
1501	ggttgcctta	ctgcttagca	gaatgaatca	ccgatacgcg	agcgaacgtg	aagcgactgc
1561	tgtcacaana	cgctcgcgac	ctgagcaaca	acatgaatgg	tcttcgtttt	ccgtgtttcg
1621	taaaactctg	aaacgcggaa	gtcagcggcc	tgcaacttga	tgctccgatg	ctgcatcgca
1681	ggatgctgct	ggctaccctg	tggaacctct	acatctgtat	taacgaagcg	ctgcatgta
1741	ccctgagtga	ttttctctg	gtcccggcgc	atccataacc	ccagttgttt	acctcaaca
1801	cgcttcagta	accggcatg	ttcatcatca	gtaaccgcta	tcgtgagcat	ccctctctgt
1861	ttcactgcta	tcattacccc	catgaacaga	aatccccctt	acacggagcg	atcagtgacc
1921	aaacagga	aaacgcctct	taacatggcc	cgctttatca	gaagccagac	attaacgctt
1981	ctggagaaac	tcaacagctc	ggacgcggat	gaacaggcag	acatctgtga	atcgtctaac
2041	gaccacgctg	atgacttfta	ccgcagctgc	ctcgcgcgtt	tcggtgatga	cggtgaaaac
2101	ctctgacaca	tgcaagctcc	ggagacggtc	acagctgttc	tgtaaagcga	tgcccgggag
2161	agacaagccc	gtcagggcgc	gtcagcgggt	gttggcgggt	gtcggggcgc	agccatgacc
2221	cagtcacgta	gcgatacggg	agtgtatact	ggcttaacta	tgcgcatca	gacgagattg
2281	tactgagagt	gcacatattg	cggtgtgaaa	taccgcacag	atcgtaaggg	agaaaatacc
2341	gcatcaggcg	ctctccgctt	tcctcgtca	ctgactcgtc	gcgctcgttc	gttcgctcgc
2401	ggcgagcggg	atcagctcac	tcaaaggcgg	taatacgggt	atccacagaa	tcaggggata
2461	acgcagaaaa	gaacatgtga	gcaaaagccc	agcaaaagcg	caggaacctg	aaaaaggccg
2521	cggtctggcg	gtttttccat	aggctccgcc	ccccgacga	gcatacaaaa	aatcgactct
2581	caagtccagag	gtgcgcaaac	ccgacagagc	tataagata	ccagcgtttt	ccccctgaaa
2641	gctccctcgt	gcctctcctt	gttcgacccc	tgccccttac	cggtatacctg	ccgccttttc
2701	tcctctcggg	aagcgtggcg	ctttctcata	gctcacgctc	tagttatctc	agttcgtgtg
2761	aggtctgttcg	ctccaagctg	ggctgtgtgc	acgaaccctc	cgctcagccc	gaccctgtcg
2821	ctttatccgg	taactatcgt	cttgatcca	acccggtaag	acacgactta	tcgccactgg
2881	cagcagccac	tgtaaacagg	attagcagag	cgaggtatgt	aggcgtgtct	acagatgtct
2941	tgaagtggtg	gcctaactac	ggctacacta	gaaggacagt	atttggatc	tcgctcttgc
3001	tgaagccagt	tactctcgga	aaaagagttg	gtagctcttg	atccggcaaa	caaacaccgg
3061	ctgtagcggg	tggttttttt	gtttgcaagc	agcagattac	gcgcagaaaa	aaagatcttc
3121	aagaagatcc	tttgalcttt	tctacggcgt	ctgacgtcca	gtggaaagaa	aactcacgtt
3181	aaggatgttt	ggctatgaga	ttatcaaaaa	ggatcttacc	ctagatcctt	ttaaattaaa
3241	aatgaagttt	taaataaact	taaagtatat	atgagtaaac	ttgtctgac	agttaccaat
3301	gctaatcag	tgaggcacct	atcagcaga	tctgttactt	tcgtctacc	atagttcctt
3361	gactccccgt	cggttagata	actacgatac	gggagggcct	accatctggc	cccagtgctg
3421	caatgatacc	gcgagaccga	cgctcaccgg	ctccagattt	atcagcaata	aaccagccag
3481	ccggaaggcg	cgagcgcaga	agtggtcctg	caactttatc	cgctctcacc	cagttcttta
3541	attgttcccg	ggaagctaga	gtaagtgtt	cgccagttaa	tagtttgcgc	aacgttgttg
3601	ccattctcgc	agcactcgtg	gtgtcacgct	cgctggttgg	tatgcttca	ttcagctccg
3661	gttcccaacg	atcaaggcga	gttacatgat	ccccatggtt	gtgcaaaaa	gcggttagct
3721	ctctcggctc	tccgatctct	gtcagaagta	agttggccgc	agttttatca	ctcatgttta
3781	tgcgagcact	gcataattct	cttactgtca	tgccatccgt	aaagatcctt	tctgtgactg
3841	gtgagtactc	aaccaagtca	ttctgagaa	agttgatgctg	gcgaccgagt	tgcttctggc
3901	cgcgctcaac	acgggataat	accgcgccac	atagcagaac	tttaaagtg	ctcatcattg
3961	gaaaacgttc	ttcggggcga	aaactctcaa	ggactttacc	gctgttgaga	tcagtttcca
4021	tftaacccac	tcgtgcaccc	aaactgatct	cagcatcttt	tactttcacc	agcgtttctg
4081	ggtgagcaaa	aacaggaagg	caaaatcccg	caaaaaaggg	aaataaggcg	accgggaaat
4141	gttgaatact	catactcttc	cttttcaat	attatgaag	catttatcag	ggttattgtc
4201	tcatgacggg	atacatattt	gaaatatttt	agaaaaataa	acaaataggg	gttcggcgca
4261	cafttcccg	aaaagtgcga	cctgactctt	agaaacat	tattatcatg	acattaacct
4321	ataaaaatag	gcgtatcacg	aggccctttc	gtctcaaga	a	

a., adenosine (983), c., cytosine (1210), g., guanosine (1134), t., thymidine (1034)

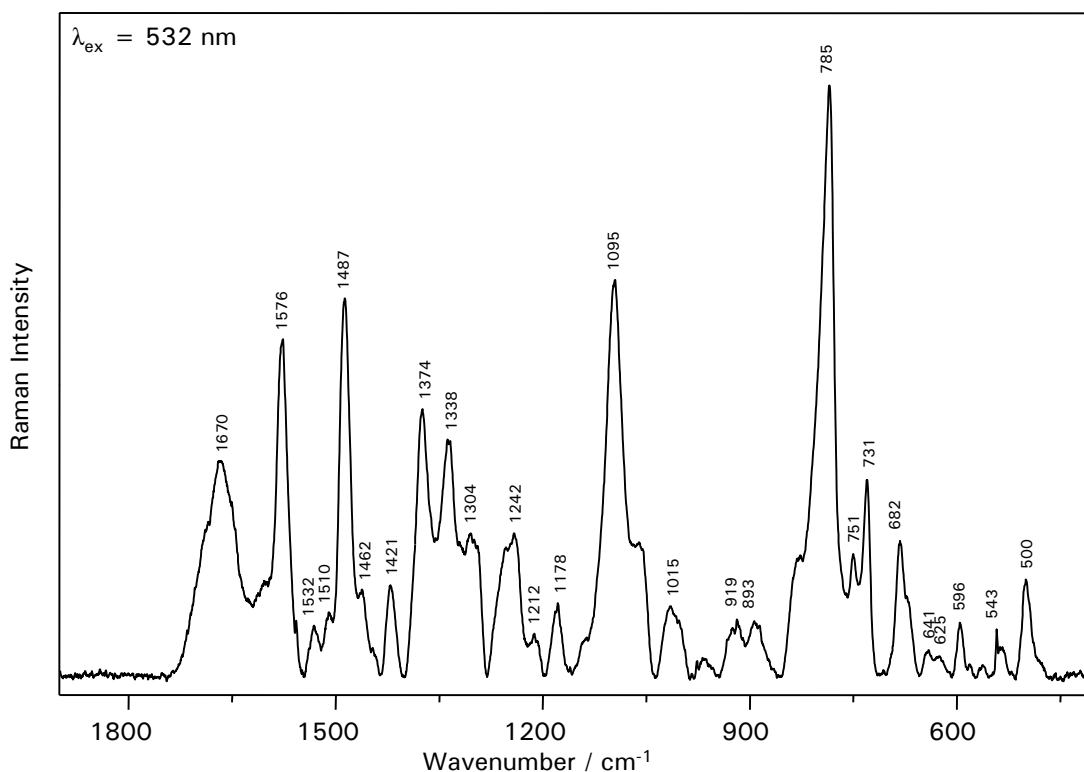


**Figure 7.9:** Raman spectrum of the plasmid DNA pBR322 ( $\lambda_{ex} = 532$  nm).

intensity can be attributed to base stacking interactions and different bonding angles due to the formation of the double helix.

In the spectral region  $1600\text{--}1750\text{ cm}^{-1}$  the carbonyl stretching modes of thymine ( $\text{C}2=\text{O}$  and  $\text{C}4=\text{O}$  at  $1672\text{ cm}^{-1}$  and  $1652\text{ cm}^{-1}$ ), guanine ( $\text{C}6=\text{O}$  str at  $1713\text{ cm}^{-1}$ ), and cytosine ( $\text{C}2=\text{O}$  around  $1680\text{ cm}^{-1}$ ) are found and form together the broad band around  $1670\text{ cm}^{-1}$ .

The in-plane ring vibrations of the bases can be seen in the vibrational region  $1600\text{--}1150\text{ cm}^{-1}$  and the vibrational bands due to the sugar residues show up between  $1050$  and  $600\text{ cm}^{-1}$ . The Raman bands between  $900\text{--}600\text{ cm}^{-1}$  can be used to assign the deoxyribose (and phosphate) conformation and to draw conclusions about the secondary DNA structure. The spectrum of pBR322 shown in figure 7.9 presents the plasmid in the popular B-Form. All the B-form marker bands can be identified in the Raman spectrum: the O-P-O vibrations at  $795 \pm 5$  and  $835 \pm 7\text{ cm}^{-1}$ . The latter one is typically only found in B-DNA [25]. The A-DNA marker band of the C-O vibration at  $706\text{ cm}^{-1}$  and the Z-DNA marker band at  $745\text{ cm}^{-1}$  are both absent in the spectrum.

Another prominent vibrational band is the symmetric stretching vibration of the  $\text{PO}_2^-$  moiety at  $1092\text{ cm}^{-1}$ . It shows up in all DNA spectra and is sometimes used for normalization.

A more detailed vibrational band assignment is given in table 7.7.

The DNA investigated by micro-Raman spectroscopy was in the solid state as it was precipitated (and washed) after the phenol-chloroform purification (see experimental section 3.2.2). Recording

## 7 The biological target: DNA

**Table 7.7:** Vibrational band assignment of the Raman spectrum ( $\lambda_{ex}=532$  nm) of pBR322.

pBR322 cm <sup>-1</sup>	ref cm <sup>-1</sup>	assignment
500	499	dG+dT [269]
596	596	dG and/or dC [269]
682	681	dG with C2'-endo sugar pucker and anti glycosyl torsion [62], O4'-endo-anti [183]
	682	G in B-form [264]
731	728	dA with C2'-endo sugar pucker and anti glycosyl torsion [62]
751	750	dT ring breathing [62, 23]
	780/790	cytosine/thymine [62]
785	783	dC with C2'-endo sugar pucker and anti glycosyl torsion [62]
830	835±5	deoxyribose-linked phosphodiester network (5'C-O-P-O-C3) [62], (C2'-endo) [264]
893	895	deoxyribose moieties [62]
919	922	deoxyribose moieties [62]
1015	1015	C-O str [264]
1061	1053	deoxyribose moieties (C-O str) [62, 264]
1095	1092	sym str of O=P=O. [62, 264]
	1094	B-conformation [264]
1178	1178	in-plane vib. of C-residues [62]
1212	1214 (H <sub>2</sub> O)	T [264]
1242	1237-1239	dT
1304	1293	C [62]
1338	1339	ring mode (A, G), nucleoside conformation marker: dA in C2'-endo/anti [23]
1374	1376	dT [62]
1421	1420	deoxyribose (backbone) [62]
1446	1444	deoxyribose moieties
1462	1460	deoxyribose (backbone) [62]
1487	1489	in-plane ring vib. of G-residues [62]
	1482	in-plane vib. of A-residues [62]
1510	1511	in-plane vib. of A-residues [62, 269]
1532	1531	in-plane vib. of C-residues [62]
1576	1578	in-plane vib. of G/A-residues [62]
1670	1672	T (C=O str) [62]
	1672	hydrogen-bonded (base-paired) C=O of T [264]

spectra in solution with a reasonable signal-to-noise ratio would require high DNA concentrations around 10 mg/ml, which are much higher concentrations than found within biological systems. Therefore, the signal enhancement of resonance Raman spectroscopy was used and UV-resonance Raman spectra were recorded from the aqueous DNA solutions and will be discussed in section 7.4.3.

### 7.4.2 UV absorption spectroscopy

The main advantage of resonance Raman spectroscopy is the enhanced scattering efficiency of selected chromophores which allows the investigation of native DNA in (dilute) solution. The vibrational modes gain their enhancement by the coupling to an allowed electronic transition which is in resonance with the excitation wavelength. In order to obtain the largest enhancement, the excitation wavelength should be near an absorption maximum of the chromophore. Figure 7.10 shows the UV absorption spectrum of plasmid DNA pBR322 (solid line). It exhibits an absorption maximum at 259 nm, which results from a superposition of the  $\pi - \pi^*$  transitions of the purine and the pyrimidine ring systems of the nucleic acid bases. The absorption spectra of the individual nucleotides are shown for comparison in figure 7.10 with dashed and pointed lines. Their absorption spectra have been discussed in detail in section 7.1.2.4. The plasmid pBR322 contains in each strand 983 adenosine, 1210 cytosine, 1134 guanosine, and 1034 thymidine, which makes 4361 basepairs (bp) in total. The vertical line marks the Raman excitation wavelength of 244 nm. It hits the edges of the  $\pi - \pi^*$  absorption band of the two purine bases guanosine and adenosine. The two pyrimidine bases thymidine and cytidine show only weaker extinction coefficients in this



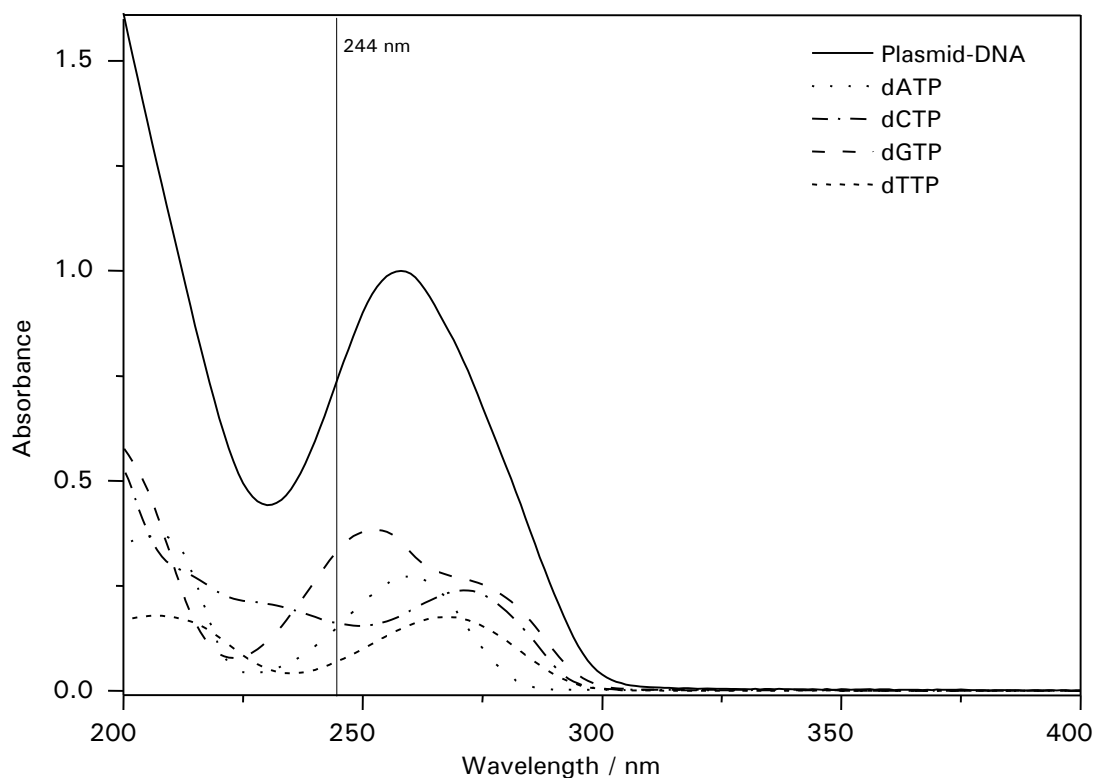


**Figure 7.10:** UV absorption spectra of plasmid DNA and the individual nucleotides. The concentration of the nucleotide is chosen corresponding to their concentration within the plasmid. The vertical line marks the 244 nm excitation wavelength of the resonance Raman spectra.

spectral region. Therefore, the UV-resonance Raman spectrum with excitation at 244 nm will be dominated by contributions from the vibrations of the purine bases. The phosphodiester conformation marker bands of the DNA backbone will not show up, since those vibrations couple to higher lying electronic transitions.

### 7.4.3 UV-resonance Raman spectroscopy

The UV-resonance Raman spectrum of the (native, superhelical) plasmid pBR322 is depicted as solid line in figure 7.11. The UV RR spectra of the individual nucleotides scaled in the intensity ratio, which correlates to the composition of pBR322, are shown for comparison in the same figure. The dominant feature in the DNA spectrum is the strong vibrational band at  $1487\text{ cm}^{-1}$  resulting from a rarefaction along the long axis of the purines guanine (G) and adenine (A) [209] with special involvement of the coupled vibration of the N7=C8 and C8-N9 stretching modes as well as from C6=O in dG [256]. This vibrational band is associated with the electronic transition around 255 nm in guanine and around 260 nm in adenosine [77]. Guanine and adenine stretching motions are also responsible for the weak band at  $1419\text{ cm}^{-1}$  as well as for the band at  $1577\text{ cm}^{-1}$  which is

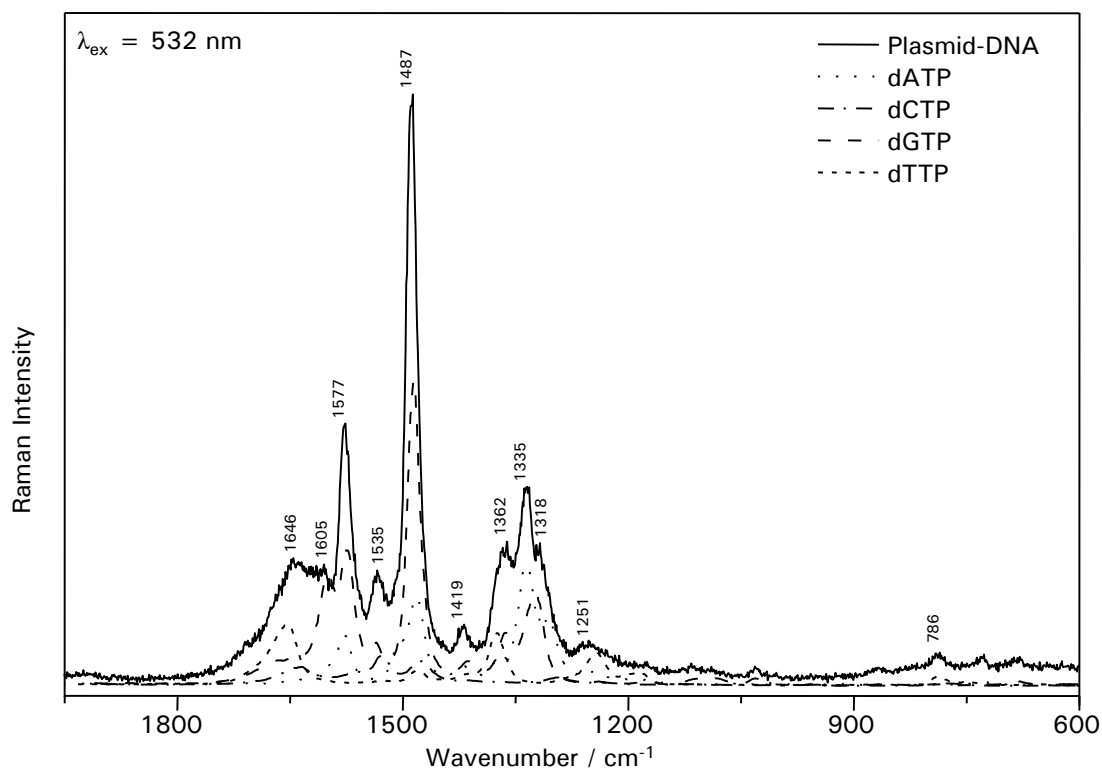


**Figure 7.11:** UV-resonance Raman spectra of plasmid pBR322 and the individual nucleotides.

due to adenosine C4C5 and C4N3 and guanosine C4N3+C5C4-N7C5 triene stretching vibrations [209] with strong localization at N3 [256]. Due to the delocalized mode, also the hydrogen bonding sites of the exocyclic amino group N6H<sub>2</sub> and the in-plane bending of the C2-N1-H contribute to this vibration [167, 124]. The band at 1535 cm<sup>-1</sup> was assigned mainly to cytosine and also partly to thymine moieties [78] like the weak band at 1253 cm<sup>-1</sup> [78]. C=O stretching vibrations of the carbonyl group show up at 1646 cm<sup>-1</sup> which was assigned to the C2=O stretching vibration in cytosine with minor contributions of the C4=O-C4C5 vibration in thymidine [209, 78]. The band at 1605 cm<sup>-1</sup> is due to NH bending vibrations, notably from adenine [78] and from the N1H interbase H-bond in guanine [256, 124]. The bands around 1362 cm<sup>-1</sup> and 1335 cm<sup>-1</sup> result from imidazol ring stretches of the adenine moiety, the latter also with contributions from the guanine moiety [209, 256, 77, 78]. The band around 1320 cm<sup>-1</sup> was assigned to the imidazol ring vibration localized at N7 in guanosine which is coupled to the ribose ring puckering and therefore sensitive to the orientation of the glycosidic bond [256, 124]. When investigating polynucleotides of the type poly(dC-dG)-poly(dG-dC) the two bands centered at 1335 and 1319 cm<sup>-1</sup> have been assigned to a split band of the 1326 cm<sup>-1</sup> band of dGMP [78]. Tsuboi and co-workers attribute a similar effect seen in visible-excitation Raman spectra to sugar conformational variation, on the basis of an analysis of ribose-sensitive modes of guanine [183]. A summary of the band assignment of the plasmid DNA is given in table 7.8.

**Table 7.8:** Assignment of the UV-resonance Raman bands of DNA ( $\lambda_{ex}= 244$  nm)

Wavenumber in $\text{cm}^{-1}$	Assignment	Reference
1708	C6=O str (G)	[78, 256]
1646	C2=O str (C), C4=O-C4C5 (T)	[78, 209]
	N2H <sub>2</sub> scissors (G)	[256]
1605	N2H <sub>2</sub> def (A)	[78]
	dG: N1H interbase H-bond; dG: C2, N1-H	[124, 256]
1577	adenosine C4C5 and C4N3 str and guanosine C4N3+C5C4-N7C5	[209]
	dG (pyrimidine ring vibration localized at N3)	[256]
	guanine ring vibration involving in-plane bending of the C2-N1-H linkages	[124]
1535	N3=C4 (C), T	[77, 78]
1487	rarefaction along the long axis of the purines (A, G)	[209]
	coupled vibration of the N7=C8 and C8-N9 stretching modes (G, A)	[77]
1419	G, A (C4N9, C8H def)	[78, 77]
1362	A	[78]
1335	adenosine out-of-phase stretch (C5N7, C8N7)	[77, 209]
1320	dG (C2'-endo/syn)	[124]
1253	C (C6H def, C4N4), T	[78, 77]
1237	dT	[124]
785	C, dT, backbone OPO (g-/g-)	[78, 124]

## 7.5 Tertiary structure of DNA: supercoiling

DNA supercoiling plays a fundamental role for many biological cell processes. It is the slightly underwound tertiary structure of native DNA that enables the proper function of vital processes such as replication, recombination and transcription. Also the high potential utility of plasmid DNA for gene replacement therapy, therapeutic applications, and vaccines raise the demand of a profound and detailed knowledge of the varieties of DNA structures [160, 259].

Supercoiling may be introduced into linear DNA when both ends are fixed so that the DNA strands cannot rotate with respect to another. This is always the case in closed circular DNA because of the topological linkage of the two complementary strands. When the DNA double strand of a covalently closed domain is twisted around itself it imposes strain. To accommodate this strain the DNA adopts a more compact tertiary structure which is called supercoiled. Depending on the direction of the twist with respect to the sense of the Watson-Crick-helix the DNA is either under- or overwound. All naturally occurring DNA is underwound, i.e. the DNA is negatively supercoiled. The degree of supercoiling is determined by the linking number  $Lk$ , which is the number of times that one DNA strand crosses about the other when the DNA is made to lie flat on a plane. In relaxed B-form DNA a turn of the double helix contains around 10.4 base pairs (bp), i.e. there is a link each 10.4 bp. The linking number ( $Lk$ ) is a topological invariant and can only be changed by cutting and resealing one or both strands of the DNA. The deviation from the helical chain of the relaxed double helix is expressed by the linking number difference,  $\Delta Lk$ , between superhelical and relaxed form. In order to compare the superhelicity of DNAs of different size the superhelical density parameter was introduced. It is the ratio of the differences in linking number of supercoiled and relaxed DNA and the total linking number. For native DNA the superhelical

## 7 The biological target: DNA

density is between -0.05 and -0.07 (5-7% underwinding). The native supercoiled form of the plasmid pBR322 used in this experiment was found to have a superhelical density parameter of  $\sigma = -0.069$  [236], corresponding to 29 negative superhelical turns [264]. The number of helical turns in the DNA is called twist. It is a local phenomenon and may be altered by deformation. However, in relaxed DNA the twist is equal to the linking number. The global contortion of circular DNA, so to speak the supercoiling of the helix in space, is specified by the writhe. According to White's formula the abstract mathematical property "supercoiling" is represented as the sum of twist and writhe [274]. That implies that a minimization of the writhe can be achieved by alteration of the twist. This can be facilitated by a loss of base pairing [140]. The enzyme that introduces the negative coils into bacterial DNA is called gyrase, a topoisomerase II, and will be discussed in chapter 8.

### 7.5.1 Differentiation by gel electrophoresis

Superhelical and relaxed DNA fulfil different functions within the cell. The supercoiled topoisomer is also the storage form of the DNA. Due to the supercoiling the DNA is compact and fits into the cell. The easiest way to differentiate between the two forms of the DNA tertiary structure is by gel electrophoresis using the different electrophoretic mobilities of the compact supercoiled form and the more elongated relaxed form. Figure 7.12 shows the stained agarose gel after electrophoresis of the two different topoisomers of the plasmid DNA pBR322. The supercoiled (S) topoisomer in the left lane migrates farther in the same time than its relaxed (R) counterpart which is due to the significantly greater electrophoretic mobility of the compact supercoiled form. The very slow fractions present in both lanes (in the top of figure 7.12) were assigned to aggregated plasmids. Again the aggregates of the supercoiled topoisomers show a higher mobility than their relaxed analogs. It was also inevitable to have small amounts of open circle form of the plasmid which migrates as fast as the relaxed DNA topoisomer.

### 7.5.2 Differentiation by UV-resonance Raman spectroscopy

**Results** The UV-resonance Raman spectra of supercoiled and relaxed DNA exhibit the same spectral features as is expected from the identical primary structure of both topoisomers. However, the change in topology is reflected in the resonance Raman spectrum by slight intensity changes and wavenumber shifts of some vibrational bands as can be seen in figure 7.13. The difference spectrum (bottom of figure 7.13) was calculated by subtracting the spectrum of the supercoiled form from the spectrum of the relaxed form in order to visualize the differences between both topoisomers. For a detailed spectral analysis curve fitting would be necessary, but for a first estimate of the observed changes spectral subtraction seemed to be sufficient.

Changes are visible in the region of the exocyclic vibrations, i.e. for the C=O stretching and NH<sub>2</sub> scissoring modes between 1600 and 1700 cm<sup>-1</sup>. The C=O stretching vibration around 1650 cm<sup>-1</sup> is slightly more intense in the superhelical form than in the relaxed counterpart, while the band

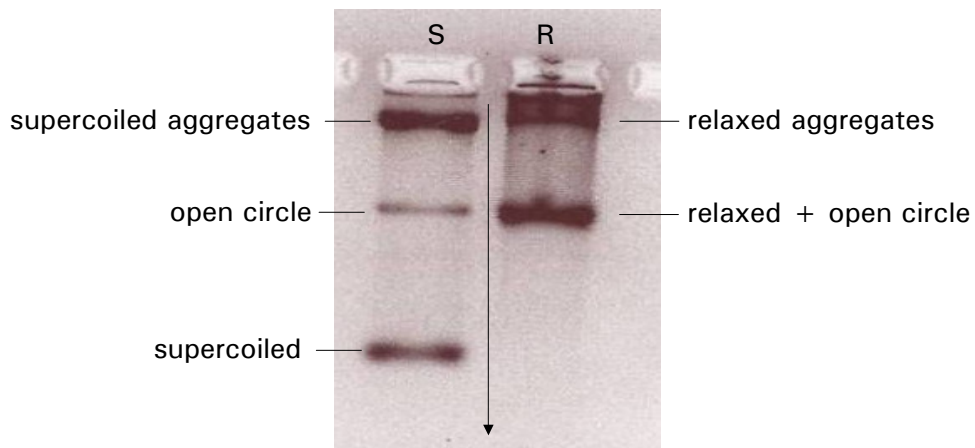


**Figure 7.12:** Agarose gel of supercoiled (S, left lane) and relaxed (R, right lane) plasmid pBR322. The compact supercoiled topoisomer migrates faster than the relaxed one.

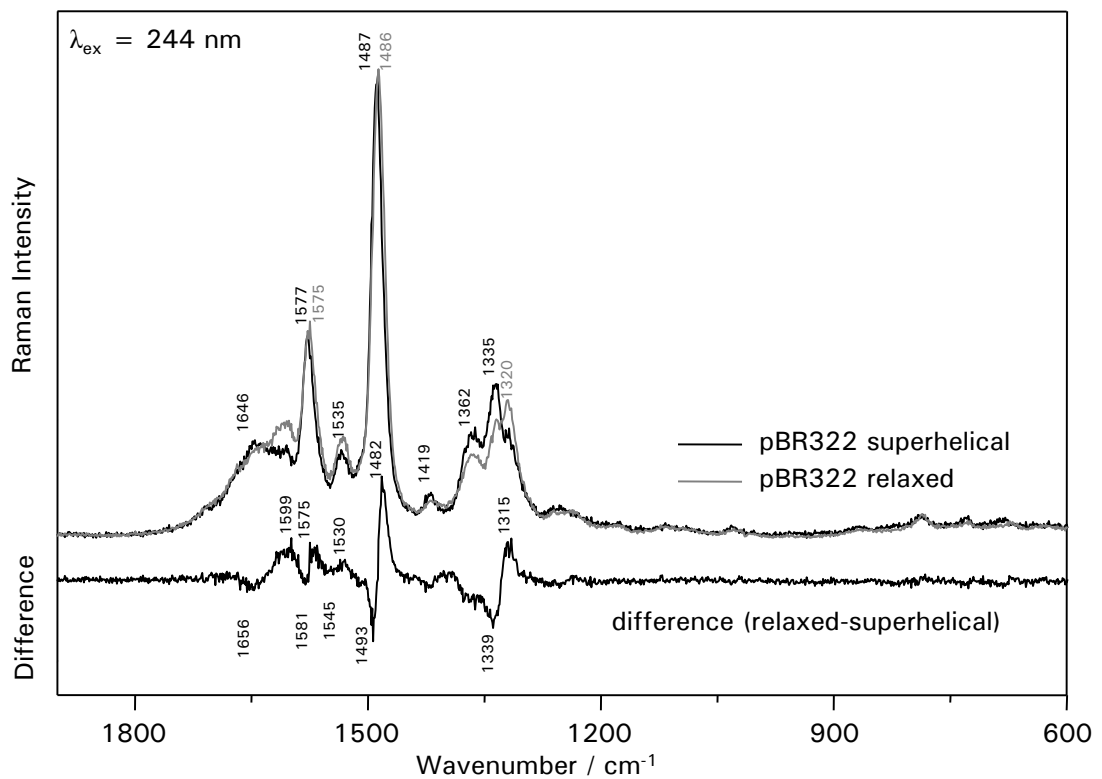


**Figure 7.13:** UV-resonance Raman spectra of plasmid pBR322 in the superhelical (black) and relaxed (grey) form, and the calculated difference spectrum (relaxed-superhelical, lower spectrum).

## 7 The biological target: DNA

around  $1600\text{ cm}^{-1}$  exhibits a reduced intensity in the superhelical form. A slight, but reproducible shift to higher wavenumbers in the spectrum of the superhelical plasmid DNA is observed for the ring modes of adenine and guanine at  $1578\text{ cm}^{-1}$  as well as for the strong triene stretching vibration at  $1486\text{ cm}^{-1}$ . Both vibrations contain contributions from hydrogen bonding sites.

Further variations in the resonance Raman spectra due to the different tertiary structure of the plasmid are observed in the wavenumber region between  $1320\text{ cm}^{-1}$  and  $1370\text{ cm}^{-1}$  where the stretching vibrations of the pyrimidine and imidazole rings coupled to the ribose vibrations occur. While in the supercoiled form the vibrational bands at  $1362\text{ cm}^{-1}$  and  $1335\text{ cm}^{-1}$  are more intense than in the relaxed form, the opposite is true for the vibrational band at  $1320\text{ cm}^{-1}$ .

**Discussion** The resonance Raman spectra of superhelical and relaxed plasmid DNA reflect small but clear differences between the two topoisomers. Especially the vibrational bands involving hydrogen bonding sites ( $1700\text{-}1450\text{ cm}^{-1}$ ) and coupled sugar vibrations ( $1400\text{-}1200\text{ cm}^{-1}$ ) are affected. In the high wavenumber region between  $1600$  and  $1700\text{ cm}^{-1}$  the vibrational bands of the exocyclic vibrations (C=O stretching and  $\text{NH}_2$  scissoring) are found. Changes in this spectral region indicate changes in the hydrogen bonding between the DNA strands. Vasmel [264] used the intensity of the thymine band around  $1650\text{ cm}^{-1}$  to determine the amount of free (non hydrogen-bonded) C=O groups in the DNA double strand. The increased intensity of this band in the superhelical form suggests a local denaturation of the DNA in the superhelical state. This assumption is supported by the more intense band of the interbase hydrogen bond of the N1H of guanine at  $1605\text{ cm}^{-1}$ . Locally melted states for superhelical plasmids were reported previously in the literature and occur as a natural consequence of supercoiling. For a twist density of  $-0.069$  as found in pBR322 [236] about 3.5 % of the base pairs are assumed to appear in the locally melted state [27].

Hydrogen bonding between the base pairs also affects the vibrational bands at  $1578\text{ cm}^{-1}$  and  $1486\text{ cm}^{-1}$  [166, 256]. A slight shift to higher wavenumbers in the superhelical DNA compared to the relaxed plasmid is observed for the ring mode of adenine and guanine at  $1578\text{ cm}^{-1}$  which contains contributions from the exocyclic amino group ( $\text{N6H}_2$ ) and the ring nitrogen (N1H). Also the position of the strong triene stretching vibration at  $1486\text{ cm}^{-1}$  is slightly shifted to higher wavenumbers in the superhelical form compared to the relaxed form indicating a change of the hydrogen bonding at C6=O in dG. These effects are only small, but reproducible for various measurements on different days with samples from different extraction series. A shift to higher wavenumbers indicates tighter hydrogen bonds of the involved groups. The sensitivity of those Raman bands for the hydrogen bonding state was shown by Fujimoto et al. [79] and Toyama et al. [256] using isotope-edited Raman spectroscopy in several solvents with different hydrogen bonding properties. Further support of the hydrogen bonding sensitivity of those two bands comes from thermal DNA melting experiments and from quantum chemical calculations (DFT) of the vibrational bands of the single bases and the interbase complexes (data not shown). The observation of stronger hydrogen bonds in the superhelical form is in contrast to the intensity variation of

the C=O stretching and NH<sub>2</sub> scissoring vibrations discussed before and also to the locally melted states in supercoiled DNA. However, previous studies by Serban, Benevides and Thomas, Jr. using Raman spectroscopy with excitation in the visible revealed also tighter hydrogen bonding at the N7 acceptor site in small subsets of guanine from wavenumber shifts of the vibrational band at 1488 cm<sup>-1</sup> [236].

Further variations in the resonance Raman spectra due to the different tertiary structure of the plasmid are observed in the wavenumber region between 1320 cm<sup>-1</sup> and 1370 cm<sup>-1</sup> where the stretching vibrations of the pyrimidine and imidazole rings coupled to the ribose vibrations occur. While in the supercoiled form of the plasmid DNA the vibrational bands at 1362 cm<sup>-1</sup> and 1335 cm<sup>-1</sup> are more intense than in the relaxed form, the opposite is true for the vibrational band at 1320 cm<sup>-1</sup>. These changes in the ribose-sensitive modes of guanine and adenine indicate variations in the sugar conformation due to the twist. In order to accommodate the increased strain in the superhelical coil slight alterations in the ribose C2'-endo pucker occur. In earlier studies Brahms et al. report also changes in the sugar pucker vibrations when investigating pBR322 by non-resonant Raman spectroscopy with excitation at 514 nm [38]. Those findings could not be confirmed in the Raman study (532 nm excitation) of pUC19 by Serban et al. [236]. However, it should be noted that all the previous vibrational spectroscopic results were obtained by using excitation wavelength in the visible. Therefore, new results might be assessable when profiting from the UV-resonance enhancement of Raman spectroscopy which especially focuses on the purine and pyrimidine bases of the nucleic acid.

## 7.6 Intercalation of ethidium bromide

The superhelical stress within negative supercoiled DNA can also be reduced by the addition of intercalators such as ethidium bromide [222, 129]. A consequence of the phenanthridinium intercalation is the lengthening of the DNA helix and a concomitant unwinding of the phosphodiester backbone to accommodate a molecule of the intercalator. This changes  $\Delta Lk$  and  $\sigma$  to become less negative [23, 289, 201, 59]. Intercalation is a phenomenon of widespread biological importance, because those structural modifications can lead to functional changes, often to the inhibition of transcription and replication processes, which make intercalators potent mutagens. Raman spectroscopy with its information rich vibrational signatures has great potential for probing structural details of solution complexes. However, ethidium bromide and ethidium bromide-DNA complexes show a very strong fluorescence in the spectral region between 400-600 nm and make the use of excitation wavelength in the NIR [23, 25] or UV necessary.

Understanding DNA drug interactions is of greatest interest because it can provide useful insights into mechanisms of inhibition of translation and transcription which is important for the design of chemotherapy. It might further be extended to protein-DNA recognition processes. In the following the focus is set on the changes in the DNA structure caused by the intercalation of

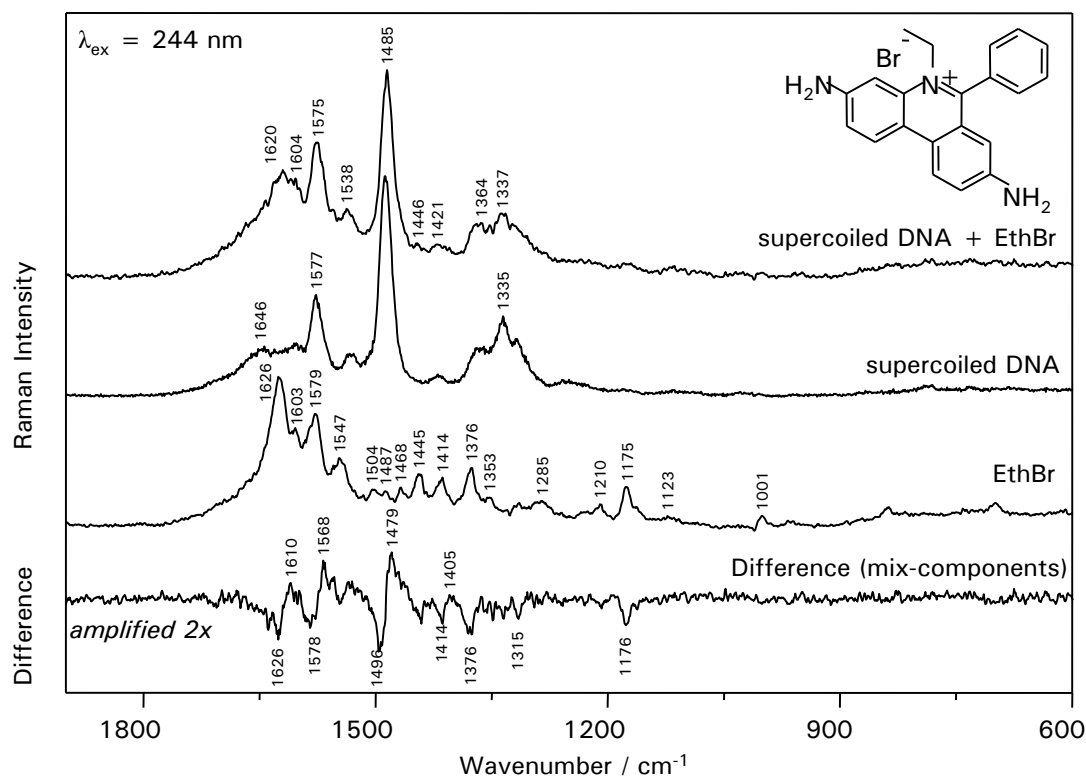


**Figure 7.14:** UV-resonance Raman spectra of ethidium bromide (EthBr, c), supercoiled DNA (b) and a mixture of both (a, 1 drug molecule per 30 bp). The bottom spectrum (d) shows the calculated difference spectrum obtained by subtracting the spectral sum of ethidium bromide + DNA from the complex spectrum. The inset shows the chemical structure of the phenanthridinium drug ethidium bromide.

the phenanthridinium drug ethidium bromide. The structure of the drug is shown in the inset in figure 7.14.

**Results** The superhelical form of DNA is treated with ethidium bromide (EthBr) and the observed changes in the vibrational bands are compared with the differences in the spectra of the supercoiled and the relaxed form of the plasmid (recall from previous section 7.5). Difficulties arise because ethidium bromide itself shows also Raman bands in the spectral region of interest as can be seen in figure 7.14c. An assignment of the vibrational bands of ethidium bromide is given in table 7.9, based on the assignment of the vibrational bands from the NIR Raman spectrum ( $\lambda_{\text{ex}} = 752 \text{ nm}$ ) by Benevides and Thomas [23]. The 2<sup>nd</sup> spectrum in figure 7.14 (b) shows again the resonance Raman spectrum of supercoiled DNA and the upper spectrum (a) the mixture of DNA and ethidium bromide with a DNA:ethidium bromide ratio of 30 base pairs per drug molecule. At this ethidium bromide concentration almost all of the ethidium is bound to the DNA [59]. Due to the overlapping vibrational bands of the individual components, a simple analysis



**Table 7.9:** Assignment of the UV-resonance Raman bands of ethidium bromide ( $\lambda_{ex}=244$  nm).

wavenumber in $\text{cm}^{-1}$	assignment [25]
1626	NH <sub>2</sub> scissor, phenanthridinium ring
1603	phenyl ring
1579	phenanthridinium ring
1547	
1504	
1487	phenanthridinium ring
1468	CH <sub>3</sub> def
1445	CH <sub>2</sub> def
1414	phenanthridinium ring
1376	phenanthridinium ring/ CH <sub>3</sub> def
1353	phenanthridinium ring
1285	CH def
1210	phenyl ring
1175	phenyl ring
1123	C-C, C-N str
1001	phenyl ring
837	phenanthridinium ring
699	phenanthridinium ring

of the spectra is not easily possible. For a first qualitative investigation the difference spectrum was computed by subtracting the spectral sum of the two individual components supercoiled DNA and ethidium bromide from the spectrum of the mixture. The (amplified) difference spectrum shown in figure 7.14d displays contributions from ethidium bromide (1629, 1581, 1417, 1379 and 1179  $\text{cm}^{-1}$ ) and DNA (peak and trough feature at 1499 and 1482  $\text{cm}^{-1}$ , 1581 and 1318  $\text{cm}^{-1}$ ) indicating that complex formation leads to perturbation of the vibrational modes of both interacting species. A large perturbation is found around 1490  $\text{cm}^{-1}$  where the purine stretching vibrations occur. Other prominent features in the difference spectrum are located around 1575  $\text{cm}^{-1}$  where both DNA (purine ring vibration) and drug (phenanthridinium ring) exhibit vibrational bands. The vibrational bands that were identified to change with the topology of the plasmid DNA are also affected by ethidium bromide intercalation (mainly the bands around 1486, 1578 and 1318  $\text{cm}^{-1}$ ). However, they are superimposed by contributions from the ethidium bromide moiety. Therefore, it would be desirable to separate the two contributions. An attempt was done by applying principal component analysis on the orthogonalized spectra.

**Discussion** In order to separate the contributions of ethidium bromide interactions and changes in the supercoiling in the DNA, principal component analysis was performed with the UV-resonance Raman spectra of supercoiled DNA, relaxed DNA, and complexes of ethidium bromide and superhelical DNA with three different ethidium bromide concentrations. Since ethidium bromide gives rise to a Raman spectrum itself, the spectral contributions of the drug were removed by orthogonalization before analyzing the data. Figure 7.15 shows the amount (portion) of ethidium bromide subtracted from the spectra according to  $\hat{w}$  mentioned in the Material and Method section 3.4.5. It

7 The biological target: DNA

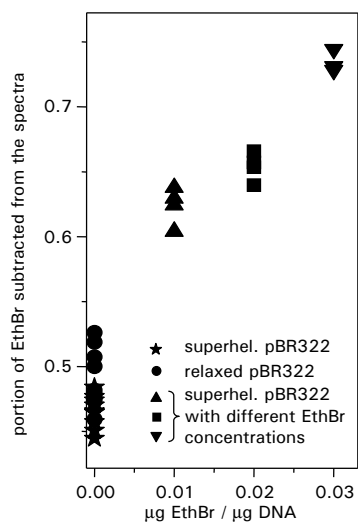


**Figure 7.15:** Amount (portion) of ethidium bromide (EthBr) subtracted by orthogonalization from the UV-resonance spectra of pure relaxed and superhelical DNA and of a DNA-EthBr complex with varying ethidium bromide concentrations. The higher the ethidium bromide concentration the larger the subtracted portion of ethidium bromide.

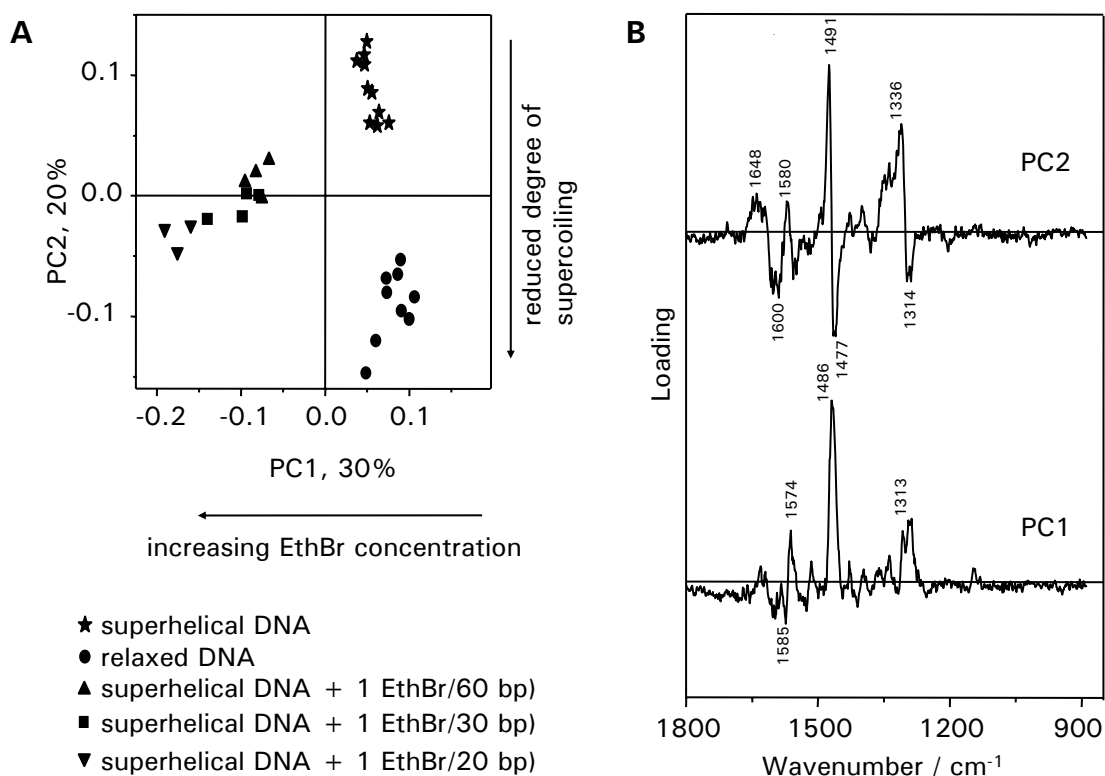


**Figure 7.16:** **A)** 2D scores plot of the first two principal components of the UV-resonance Raman spectra of relaxed DNA, supercoiled DNA and the DNA-ethidium bromide complex with three different ethidium bromide concentrations **B)** Loading plot for the first (lower graph) and second (upper graph) principal component.

can be seen that the amount of the subtracted features correlates well with the increasing ethidium bromide concentration. The spectra of supercoiled DNA and relaxed DNA, to which no ethidium bromide was added, also show some accidental correlations with the ethidium bromide spectrum, which are assumed to be negligible. After eliminating the spectral information of pure ethidium bromide by orthogonalization, the PCA was performed on the basis of the orthogonalized matrix of the UV-resonance Raman spectra. Figure 7.16A shows the 2D scores plot of the first two principal components. The Raman spectra of the different topoisomers and the DNA-ethidium bromide complex form three well separated clusters. The first principal component which describes 30% of the spectral variations was found to correlate negatively with the ethidium bromide concentration. The spectra of the mere plasmid DNA cluster at positive values of PC1, while the spectra of supercoiled DNA + ethidium bromide are found at negative values of PC1. The higher the ethidium bromide concentration in the DNA-EthBr complex the more negative are the PC1-values of those spectra. The second principal component which describes 20% of the spectral variances correlates in a first approximation to the degree of supercoiling of the plasmid DNA. At positive values of PC2 the spectra of the supercoiled topoisomer are found, at negative values of PC2 the spectra of the relaxed form arrange. The spectra of supercoiled DNA + EthBr are found in between the mere topoisomers at PC2 values around 0. Increasing ethidium bromide concentrations (still below saturation of the DNA double strand with the intercalating drug) result in a reduced degree of supercoiling. For the chosen ethidium bromide concentrations (60, 30 and 20 bp per drug molecule) the change in supercoiling is relatively small, but detectable. Such results are in good agreement with sedimentation experiments of plasmid DNA and intercalating ethidium bromide [289].

To identify the spectral bands that contribute the most to the spectral variances of PC1 and PC2 the loading plots of the two principal components were investigated and are shown in figure 7.16B. The first principal component (lower spectrum in figure 7.16B) which correlates with the ethidium bromide concentration gets its major contributions from the wavenumber around  $1486\text{ cm}^{-1}$  and minor contributions from the wavenumbers around  $1585$ ,  $1574$  and  $1313\text{ cm}^{-1}$ . Since the contributions from pure ethidium bromide have been subtracted prior to calculating the PCA the loadings do not reflect wavenumbers directly related to the pure EthBr molecule as would be the case when the PCA is performed with the spectra as measured without removing the contributions of EthBr by orthogonalization (not shown). The high loadings around  $1486\text{ cm}^{-1}$  most likely represent the changes in base stacking in the DNA upon ethidium bromide intercalation, as well as changes in the phenanthridinium ring vibration of the drug upon interaction with the DNA.

The second principal component (PC2, upper spectrum in figure 7.16B) which was found to account for the spectral variations due to the different tertiary structure of the plasmid DNA obtains its major contributions from the CN stretching mode of guanine and adenine at  $1487\text{ cm}^{-1}$  (high loadings around  $1491$  and  $1477\text{ cm}^{-1}$ ) and the adenosine out-of-phase stretch (C5N7, C8N7) around  $1339\text{ cm}^{-1}$  as well as the conformation sensitive ribose-coupled mode of guanosine around  $1320\text{ cm}^{-1}$ . Those wavenumbers describing the largest spectral variations along PC2 are in good agreement with the vibrational bands that were found to be affected by the change in topology be-

tween superhelical and relaxed DNA. Therefore, UV-resonance Raman spectroscopy can indeed be used to investigate the perturbations of localized vibrational modes due to complex formation of the interacting drug and the DNA molecules.

## 7.7 Summary and outlook

In this chapter DNA has been characterized by means of vibrational spectroscopy. The band assignment was supported by extensive studies of the DNA building blocks. Rich vibrational fingerprints of the DNA molecule give insights into the composition and the conformation of the DNA double strand. With the help of resonance Raman spectroscopy it is possible to investigate DNA in aqueous solutions at biological low concentrations. Especially the vibrational modes associated with the purines and pyrimidine ring systems are enhanced when using 244 and 257 nm excitation wavelength. Structural differences between different DNA topoisomers (supercoiled and relaxed) can be assessed by resonance Raman spectroscopy. This marks an important step on the way to monitor the gyrase activity because "educt" and "product" of the enzyme gyrase can be distinguished. This suggests that this easy and non-destructive technique can further be used for the investigation of the mode of action of the fluoroquinolone drugs in dilute aqueous solutions. Even though no information can be attained about the DNA backbone, insight can be gained into changes at the hydrogen bonding sites of the purine and pyrimidine bases of the nucleic acids as well as on sugar orientations.

The technique holds also high power for the investigation of DNA-drug interactions in solution as was shown for the example of ethidium bromide intercalation into superhelical DNA. The interpretation of the UV-resonance Raman spectra of the DNA - ethidium bromide - intercalation complex is not straightforward because vibrational contributions from ethidium bromide overlap with DNA vibrational signatures. However, statistical methods such as principal component analysis help to identify the vibrational bands that experience the largest variations which can be correlated with the ethidium bromide concentration and also with the change in topology of the DNA.

## 8 The biological target: DNA-gyrase

### 8.1 Structure and biological function of the enzyme gyrase

As discussed in the previous chapter (DNA, chapter 7) the topological state of the DNA is crucial for many vital cell processes such as transcription, recombination and replication. The transformation between the different topological states of the DNA is catalyzed by the action of special enzymes called topoisomerases [48, 268, 55]. According to the mechanism of action the topoisomerases are divided into two types. Topoisomerases of type I which are monomers, cut a single DNA strand and cause a change in linking number (see section 7.5) by  $\Delta LK=1$ . Topoisomerases of type II are dimers, cut both of the DNA double strands and change the linking number by  $\Delta LK=2$ .

Supercoiling is required for the DNA to reach the compact state in order to fit into the bacterium. Furthermore, the correct function of the DNA replication process depends on the effective function of the topoisomerases. Due to their essential function topoisomerases evolved to important targets of many drugs, such as chemotherapeutics against cancer or antibiotics [55, 69, 90, 156, 200]. Many of those drugs attack the enzyme-DNA complex and cause cell death. An important group of those drugs, the fluoroquinolones, have already been discussed in chapter 6.

A popular type II topoisomerase is the enzyme gyrase. It is a vital enzyme in all bacteria, but does not exist in the same structure in eucaryotes. Therefore, it is a very popular target for antibiotics. Nowadays there are two important groups of gyrase inhibitors, first the coumarins (e.g. novobiocin) which attack the ATP binding site on GyrB, and second, the quinolones which interfere with the action of the GyrA subunit when resealing the DNA double strand [168]. The latter are of special interest for this work and have been characterized spectroscopically in chapter 6.

#### 8.1.1 Structure of the bacterial enzyme gyrase

The enzyme gyrase consists of two subunits GyrA and GyrB that form together a heterotetramer  $A_2B_2$  the active enzyme. The GyrB-subunit which is for *E.coli* 90 kDa in size can be divided into two domains: the N-terminal domain (NTD, 47 kDa) with the ATP binding site and the carboxyl terminal domain which forms the connection to the GyrA subunit and binds the DNA. The GyrA subunit (97 kDa for *E. coli*) is also composed by two domains: the 59 kDa N-terminal domain (NTD, GyrA59) and the 38 kDa carboxyl terminal domain. The GyrA59 domains of both GyrA subunits form together a saddle like structure with a positively charged surface. The electrostatic surface potential of the GyrA59 domain is depicted in figure 8.1 and discussed in more detail by

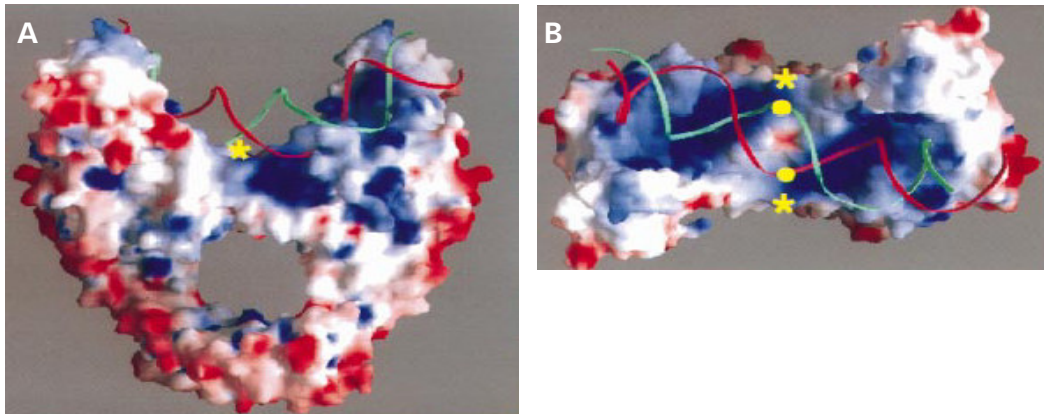


**Figure 8.1:** Graphical representation of the electrostatic surface potential of the GyrA59 dimer (DNA breakage reunion domain) calculated with GRASP [181]. **A)** side view, **B)** topview; Negatively charged surfaces are depicted in red, positively charged surfaces in blue. The DNA backbone is shown as a green and red ribbon; the active site tyrosines in the binding region are indicated as yellow stars, and the target phosphoryl groups as yellow dots. (reproduced from Morais Cabral et al. [45]).

Morais Cabral et al. [45]. Figure 8.1 nicely indicates the active site tyrosines by yellow stars. They are responsible for opening and resealing the DNA double strand by transesterification between the tyrosine moiety and a phosphate moiety of the DNA. The C terminal domain (CTD) of the GyrA subunit binds the DNA double strand and wraps it around itself so that one end of the DNA strand can be moved through the opened double strand at the GyrA59 domain under introduction of negative supercoils [54, 55, 99, 112].

The gyrase holoenzyme is quite large and so far it was impossible to assess the complete structure by X-ray crystallography. However, individual parts of the GyrB or GyrA subunit have successfully been crystallized and characterized [275, 45, 55]. Also homologous structures are available for structure elucidation [55].

### 8.1.2 Mode of action of the bacterial enzyme gyrase

The function of the bacterial enzyme DNA-gyrase is to introduce negative supercoils into the closed circular DNA. This involves hydrolysis of ATP. The mechanism is presented in figure 8.2.

The DNA strand (the "line" in the top of figure 8.2) is bound with the gate segment (G, in red) by the DNA cleavage domain of GyrA59 (depicted in blue) by the positively charged surface extending over about 30 base pairs (bp). Preferential binding occurs at the nucleotide sequence 5'RNNNRNNRTGRYCTYNYNGNY-3', with R being a purine base, N a nucleotide, Y a pyrimidine base and T thymine [144]. In the plasmid pBR322 which was used in these experiments such

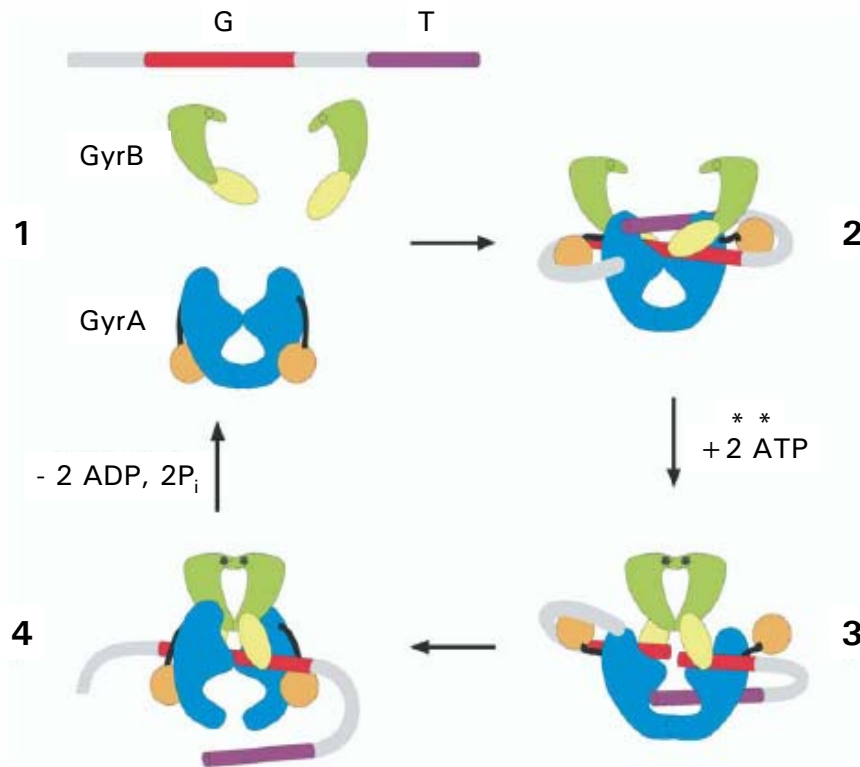


**Figure 8.2:** Schematic view of supercoiling by DNA gyrase (reproduced from Costenaro et al. [55].) Explanation is given in the text.

a sequence is found around the T<sub>990</sub>-site: 5' – AGGCTGGATTGGCCTTCCCCAT – 3' (see section 7.3). Formation of an ester bond between the hydroxyl group of a tyrosine moiety and a phosphate group of the DNA backbone facilitates opening of the DNA double strand. The other ends of the DNA, which have to be at least 130 bp in length, get wrapped around the enzyme (stage 2 in figure 8.2) in a right handed manner [143, 188, 55] by interacting with the carbonyl-terminated domain (CTD) of GyrA (depicted in orange) [54, 208]. This forces the GyrA to obtain an extend conformation, the flexible linkers (black lines in figure 8.2) between the cleavage domain GyrA59 and the CTD are outstretched so that one of the DNA strands, the transported segment (T, in purple), is presented above the G segment in the DNA cleavage domain. The gate segment is transiently opened by the reversible formation of a covalent linkage between its 5'P and the Tyr-122 residue of GyrA. The T segment is moved through this opening in the DNA double stand introducing two negative supercoils into the DNA (stage 3) [42, 99]. The energy needed for the T segment to slide through the opening is gained by consumption of ATP (black stars in figure 8.2) by the GyrB subunit (ATPase domain in green, and the CTD of GyrB is depicted in yellow in figure 8.2). ATP-binding to the GyrB subunit promotes the closure of the GyrB N-terminal side and this structural

transition allows the T segment to move [41]. The energy used for religation of the G segment of the DNA is gained from the hydrolysis of the tyrosine-phosphate-ester (stage 4) [168].

The quinolones interfere with this supercoiling mechanism by attacking the gyrase-DNA complex. The detailed mechanism on a molecular level is not yet completely elucidated but of greatest interest in order to fight growing resistances and to advance in the development of new drugs. However, it seems difficult to assess because of the high complexity and the large size of the enzyme-DNA complex. Most of the high-resolution structural methods such as NMR or X-ray crystallography are difficult to apply. Up to now, there is no complete X-ray structure of the full length enzyme. Also *ab initio* modelling reaches its limits when it comes to the gyrase holoenzyme, not to speak about the complex with DNA or even the drug. Raman spectroscopy and its variations are not limited by the size of the investigated particle and therefore, could provide a way to access useful information. However, before investigation the ternary gyrase-DNA-drug complex, the vibrational spectra of the individual components need to be understood. The results for the active agents, the fluoroquinolones, and the DNA have already been discussed in the previous chapters (chapters 6 and 7). This section now deals with the enzyme gyrase.

## 8.2 The protein building blocks: the amino acids

As was done for the DNA in the previous chapter, the protein building blocks, the amino acids, should be investigated briefly before discussing the spectral signature of the whole enzyme gyrase.

### 8.2.1 UV absorption spectra of the amino acids

According to their structure the amino acids can be divided into aliphatic amino acids, aromatic amino acids and heterocyclic amino acids. Exemplary the UV absorption spectrum of one representative of each group is shown in figure 8.3. The aliphatic amino acids do not show any significant absorption at longer wavelength than 240 nm. As an example lysine is shown which is present with 23 molecules in the GyrA subunit of the enzyme gyrase. The aromatic and the heterocyclic amino acids possess low energy  $\pi - \pi^*$  and  $n - \pi^*$  transitions and therefore, absorb light of longer wavelength. As an example the UV absorption spectra of tyrosine and tryptophane are shown in figure 8.3. In total there are 15 tyrosine molecules present in the GyrA subunit. Two of them are found close to the DNA breakage-reunion region and are involved in the DNA binding by forming an ester bridge to the phosphate of the DNA backbone (see section 8.1).

### 8.2.2 Raman spectroscopic characterization of the amino acids

From biological experiments it is known that the amino acid tyrosine exerts a special function within the DNA binding process. Therefore, the Raman spectroscopic characterization of the amino acids will be exemplarily shown for tyrosine. Further Raman and resonance Raman spectra of other amino acids will be presented in the appendix (section B).



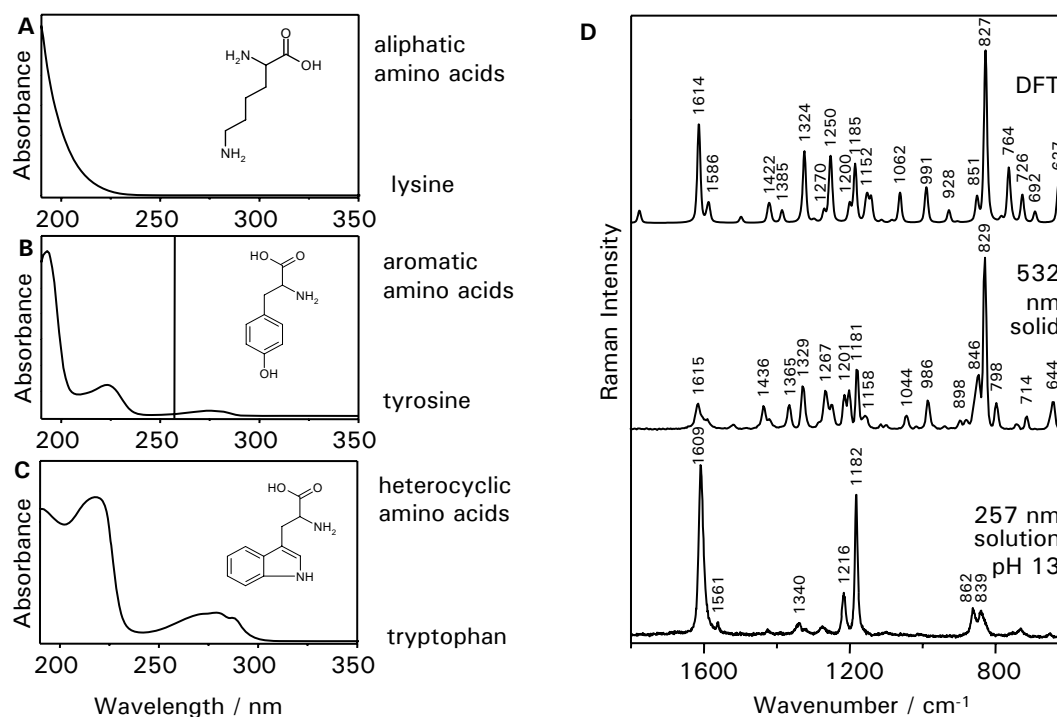


**Figure 8.3:** Left panel: UV absorption spectra of amino acids, **A)** the aliphatic amino acid lysine, **B)** the aromatic amino acid tyrosine, **C)** the heterocyclic amino acid tryptophan. The inset above the spectrum shows the structure of the amino acid.

**Right panel: top)** simulated Raman spectrum of the aromatic amino acid tyrosine from DFT calculations (B3PW91/6-31+G(d,p)), **middle)** Raman spectrum of tyrosine in the crystalline state; **bottom)** UV-resonance Raman spectrum of tyrosine in aqueous solutions, pH 13.

The middle spectrum in the right panel of figure 8.3 shows the Raman spectrum of tyrosine excited with visible light (532 nm) in comparison with the calculated Raman spectrum as obtained from DFT calculations (top spectrum). Even though the calculations were performed for molecules in the gas phase and the experiment was performed in the crystalline state, the simulated Raman spectrum using DFT calculations (B3PW91/6-31+G(d,p)) resembles the experimental spectrum quite well and can be used for an assignment of the vibrational bands (see table 8.1).

The Raman spectrum excited with visible light is dominated by a vibrational band around 830 cm<sup>-1</sup>. When just referring to the DFT calculations the intense band around 830 cm<sup>-1</sup> would be assigned to a combination vibration of a NH<sub>2</sub> out-of-plane vibration and ring breathing. The band around 850 cm<sup>-1</sup> would be due to an NH<sub>2</sub> out-of-plane vibration, together with CH<sub>2</sub> rocking and ring breathing vibrations. However, this vibrational region (850 and 830 cm<sup>-1</sup>) has already been investigated carefully by Siamwaza et al. [241]. Protonation and polarization experiments as well as symmetry considerations for several para-substituted benzenes including tyrosine resulted

**Table 8.1:** Assignment of the vibrational Raman bands of tyrosine. (Calculations were performed by DFT-calculations (B3PW91/6-31+G(d,p)),  $\lambda_{ex} = 532$  nm, the numbers in brackets behind the mode assignment denote the percentage of potential energy localized in that particular involved bond. Only contributions over 5% are shown)

calc. cm <sup>-1</sup>	calc. scal. cm <sup>-1</sup>	exp. cm <sup>-1</sup>	assignment
32	31		CC tors (39) + CC tors2 (30) - CC tors3 (19)
41	40		CC tors3 (55) + CC tors2 (15) - CN tors (5) - CH <sub>2</sub> bend (5)
74	71		CC tors (27) + CC tors3 (26) - CC tors2 (17) + ring tors (10)
78	75		CC tors (23) - CC out (15) - CH <sub>2</sub> bend (14) - CC tors3 (13) - ring tors (10) - CN bend1 (6)
160	154		ring tors (32) - CCC bend aliph (22) - CH <sub>2</sub> bend (12) - CN bend1 (7) + CC bend (5)
224	216		CCC bend aliph (24) + CCOO bend (16) + ring tors (16) - CC bend (9) - CH <sub>2</sub> bend (7) + CCO bend (6) - CC out (6)
264	254		CN tors (78) - CN bend1 (6)
275	264		CHN bend3 (31) - CHN bend2 (15) - COOH out (13) - CC bend (8) - CN bend1 (6)
328	316		CC bend (23) + CCC bend aliph (11) - CC tors (9) + CO bend (ring)(9) + CN bend1 (7) + ring def (6)
330	317		COH tors (ring)(57) + CN bend1 (8) - CCOO bend (6)
334	321	335	COH tors (ring)(37) - CN bend1 (13) + CCOO bend (6) + CC bend (6) - COOH out (5)
353	340		ring tors2 (20) + CC out (11) + CO out (ring)(9) + ring def (9) + CCO bend (7) - CC str (6)
422	406	379	ring out (63) + CO bend (ring)(13)
426	409	429	ring out (39) - CO bend (ring)(28) - ring def2 (10) + CC bend (8)
493	474		CO out (ring)(23) + ring tors (20) - CCO bend (17) + ring tors2 (9) + CCC bend aliph (5)
525	504	526	ring def (31) - CCO bend (12) + CC out (8) - CO out (ring)(8) - ring tors (7) - CHN bend3 (7)
562	541		CO out (ring)(22) + ring tors (17) - CC out (11) + ring def (9) + CH <sub>2</sub> bend (9) + CCO bend (5)
584	562		CCOO bend (28) - CCC bend aliph (15) + COH tors (11) + CC(OOH)str (7) - CH <sub>2</sub> rock (7)
623	599		COH tors (66) - COO bend (8) + CCO bend (5)
653	627	644	ring def2 (78) - CO bend (ring)(6)
719	692		ring tors2 (64) - CO out (ring)(13) - CC out (10)
756	726	714	COOH out (36) - COH tors (11) + CC(OOH)str (8) + CCO bend (6) - ring tors2 (6) + CN str (5)
787	756		NH <sub>2</sub> out (18) - ring def3 (12) - ring tors2 (10) + CringC str (6) - CN str (6) - CO str (ring)(6) - CH <sub>2</sub> bend (5)
794	764		CC(OOH)str (23) - CH <sub>2</sub> rock (9) + ring def3 (9) + NH <sub>2</sub> out (8) + CO str (8) + CCO bend (6) + CC str (5)
816	784		CH out (ring) (56) + CH out (ring2)(21)
850	817	798	CH out (ring3) (45) + CH out (ring4) (21) - CO out (ring)(9) - ring tors (8)
861	827	829	NH <sub>2</sub> out (17) + ring breath (13) + CO str (ring)(10) + CC str (ring)(8) + CC str (ring2)(8) + CC str (ring3)(8) + CringC str (6) + CH <sub>2</sub> rock (6)
885	851	846	NH <sub>2</sub> out (33) + CH <sub>2</sub> rock (18) - CC str (ring4, breath)(6)
940	904		CH out (ring2) ((53) - CH out (ring)(22) - ring tors2 (14)
965	928		CH <sub>2</sub> rock (30) + CC(OOH)str (12) - CC str (9) + NH <sub>2</sub> twist (8) - NH <sub>2</sub> out (6)
979	942		CH out (ring4)(54) - CH out (ring3) (27) + ring tors3 (6)
1028	988	986	CC str (19) + ring def3 (19) + CN str (9) - NH <sub>2</sub> twist (7) - CH <sub>2</sub> bend (6) + CN bend1 (6)
1031	991		ring def3 (26) - CC str (14) + CC str (ring4)(7) - CC str (ring)(7) - CN str (7)
1104	1062	1044	CN str (54) - CC str (8) + CCC bend aliph (6) - CH <sub>2</sub> twist (6)
1128	1084		CH bend (ring3)(14) - CH bend (ring4)(11) + CC str (ring5)(9) + CH bend (ring)(9) - CH bend (ring2)(9) - CH str (ring)(9) - CN str (6)
1157	1112	1181	CO str (37) - COH bend (27) + CH <sub>2</sub> twist (7)
1187	1141	1201	CO bend (ring)(55) - CC str (ring2)(10) + CH bend (ring)(8) + CC str (ring)(6) + CH bend (ring3)(6)
1197	1151		CH bend (ring2)(21) - CH bend (ring3)(18) + CH bend (ring4)(17) - CH bend (ring2)(16)
1202	1155		CH <sub>2</sub> twist (24) + CHN bend3 (13) + NH <sub>2</sub> twist (12) - CHN bend2 (12) - CH bend (ring2)(6) - CO str (5)
1232	1185		CringC str (33) + ring def3 (12) + CH <sub>2</sub> wag (8) - CH bend (ring4)(7) - CC str (ring3)(5) - CC str (ring4)(5)
1248	1200		NH <sub>2</sub> twist (27) - CH <sub>2</sub> twist (22) + CHN bend3 (10) + CC str (9)
1301	1250	1247	CO str (ring)(38) - CHN bend (10) - COH bend (7) - ring def3 (6) - CH bend (ring)(5)
1304	1253		CHN bend (26) + CO str (ring)(17) + COH bend (13) + CO str (5)
1321	1270	1267	CH <sub>2</sub> wag (24) - CHN bend (21) + COH bend (15) - NH <sub>2</sub> twist (7) + CO str (7)
1349	1297		CH bend (ring4)(25) + CH bend (ring2)(19) + CH bend (ring)14) + CH bend (ring3)(14) + CH <sub>2</sub> twist (8) - CO bend (ring)(6)
1377	1324		CH <sub>2</sub> wag (39)+CHN bend (22)+CC str (8) -CN bend1 (8) -CringC str (7)
1387	1333	1329	CC str (ring4)(16) -CC str (ring3)(15) -CC str (ring)(13)+CH str (ring)(13)+CC str (ring2)(12) -CC str (ring5)(11)+CO bend (ring)(7)
1441	1385	1365	CHN bend2 (34) + CC(OOH)str (16) - NH <sub>2</sub> twist (11) + CHN bend3 (8) - CO str (7)
1475	1418		CH <sub>2</sub> scis (36) + CC str (ring5)(13) - CH str (ring)(11) - CH bend (ring3)(8) - CH bend (ring)(6)
1479	1422		CH <sub>2</sub> scis (60) - CC str (ring5)(6) + CH str (ring)(5)
1558	1498	1436	CH bend (ring)(13) - CH bend (ring4)(12) + CH bend (ring2)(12) + CC str (ring3)(11) - CC str (ring)(11) + CO str (ring)(10) - CC str (ring2)(9)
			- CH bend (ring3)(9) + CC str (ring4)(7) - CringC str (6)
			CC str (ring)(21) + CC str (ring4)(17) - CC str (ring2)(17) - CC str (ring3)(9) + NH <sub>2</sub> scis (8) - ring def2 (8)
			NH <sub>2</sub> scis (86)
1650	1586	1615	CC str (ring5)(20) + CH str (ring)(20) + ring def (11) - CC str (ring2)(10) - CC str (ring3)(9) - CH bend (ring2)(6)
1656	1592		C=O str (80) - CCO bend (6) - CC(OOH)str (5)
1678	1614		CH str aliph (99)
1848	1777		CH str (CH <sub>2</sub> )(86) + CH str2 (CH <sub>2</sub> )(14)
2979	2864		CH str2 (CH <sub>2</sub> )(85) - CH str (CH <sub>2</sub> )(14)
3055	2937		CH str (ring)(58) - CH str (ring3)(41)
3129	3008		CH str (ring3)(58) + CH str (ring)(41)
3171	3048		CH str (ring5)(53) - CH str (ring2)(47)
3188	3065		CH str (ring2)(53) + CH str (ring5)(46)
3213	3089		NH str (51) + NH str2 (49)
3227	3102		NH str2 (51) - NH str (48)
3531	3395		OH str (100)
3627	3487		OH str (ring)(97)
3783	3637		
3862	3713		

in an convincing assignment of those two bands to a Fermi doublet arising from Fermi resonance involving a ring breathing mode (expected near  $840\text{ cm}^{-1}$ ) and the first overtone of an out-of-plane ring bending vibration near  $420\text{ cm}^{-1}$  [241, 155]. Using the results of the DFT-calculations could correlate the vibrations of the Fermi doublet to the ring breathing vibration calculated at  $861\text{ cm}^{-1}$  (scaled  $827\text{ cm}^{-1}$ ) and the out-of-plane vibration calculated to occur at  $422\text{ cm}^{-1}$  and  $426\text{ cm}^{-1}$  (scaled  $406$  and  $409\text{ cm}^{-1}$ , respectively). Siamwiza et al. report an intensity ratio of 3:10 for the Fermi doublet ( $845\text{ cm}^{-1}$  :  $803\text{ cm}^{-1}$ ) of tyrosine in the solid state [241]. This is in good agreement with an ratio of 0.26 (area under the curve) determined from the experimental spectra recorded within the frame of this work.

When using laser light with a wavelength of 257 nm to record the (resonance) Raman spectra especially the vibrational bands coupling to the  $L_b$  electronic transition with polarization perpendicular to the twofold axis of the phenolic ring [155] are enhanced. Due to the selective enhancement the spectrum simplifies and the vibrational bands around  $1610\text{ cm}^{-1}$  (Y8a, [92]) and at  $1182\text{ cm}^{-1}$  (Y9a, [92]) exhibit the highest intensities. The vibrational bands at  $1216\text{ cm}^{-1}$  (Y7a, [92]) and around  $850\text{ cm}^{-1}$  show up with medium intensity. The doublet around  $850\text{ cm}^{-1}$  appears with different intensity with ultraviolet excitation than with visible excitation. Rava and Spiro attributed this effect to the selective enhancement of the polarizability associated with the ring-breathing mode [207].

### 8.2.3 Peptide structure

Proteins, as e.g. the enzyme gyrase, are linear polymers which are condensation products of amino acids. The monomers (the amino acids) are linked via a peptide bond ( $-\text{C}=\text{ONH}-\text{R}$ ). The linear sequence, that is the order of the amino acids determines the primary structure of the peptide or protein. The local arrangement in space which is determined by the torsion and dihedral angles of the peptide bond is described by the secondary structure. The most popular are  $\alpha$ -helix,  $\beta$ -sheet and random coil. Within a protein several regions of a different secondary structure may be present. The overall three dimensional structure of the protein is called tertiary structure. The arrangement of several proteins to an active complex is referred to as quaternary structure.

**Characteristic vibrational bands** A peptide bond gives rise to several vibrational modes. The in-plane amide I, amide II and amide III vibrational modes are depicted in figure 8.4.

The amide I is found in the Raman spectrum (and very prominent in the IR spectrum) around  $1650\text{ cm}^{-1}$ . It arises mainly from the peptide carbonyl stretching vibration with small contributions from the N-H in-plane bending and CN stretching vibration. The amide II (around  $1550\text{ cm}^{-1}$ ) is due to the out of phase combination of CN stretching and NH bending vibrations. The amide III band originates mainly from the NH vibration and is found in the spectral region between  $1200$  and  $1300\text{ cm}^{-1}$ . The vibrational frequency of this band was found to correlate with the Ramachandran angle of the single peptide bonds and therefore the amide III band can be used as peptide conformation marker. Also the vibrational frequencies of the other amide bonds are dependent on the

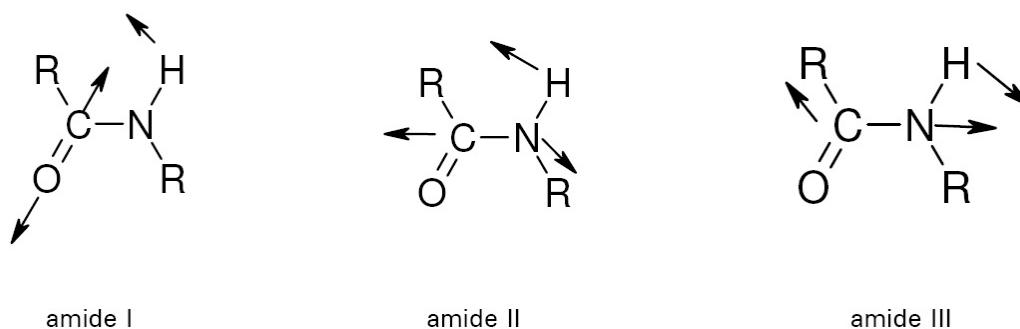


**Figure 8.4:** In plane vibrational modes of the peptide bond (figure adopted from Tu [258]).

**Table 8.2:** Structure dependence of the amide vibration [50].

secondary structure vibration	$\alpha$ -helix in $\text{cm}^{-1}$	$\beta$ -sheet in $\text{cm}^{-1}$	unordered in $\text{cm}^{-1}$
amide I	1648	1654	1665
amide II	1545	1551	1560
amide III	1299	1235	1267

secondary structure of the peptide, even though their effect is not as strong as can be seen in table 8.2.

## 8.3 Spectroscopic characterization of the enzyme

### 8.3.1 Micro-Raman spectroscopy

The obtained aqueous solutions of the enzyme were too dilute to record valuable micro-Raman spectra. Therefore the enzyme was investigated in the lyophilized state for an excitation of 532 nm.

The Raman spectrum shown in figure 8.5A exhibits characteristic protein features, such as the amide I band around  $1655 \text{ cm}^{-1}$ , the amide II band around  $1551 \text{ cm}^{-1}$  and the amide III band around  $1250 \text{ cm}^{-1}$ . From the position of the amide vibrational bands it can be concluded that a significant portion of the protein adopts  $\beta$ -sheet structure. The sharp band around  $1004 \text{ cm}^{-1}$  can be assigned to the CC aromatic ring stretches of phenylalanine and tryptophan [151, 152, 283]. The CH stretching band around  $2930 \text{ cm}^{-1}$  is the dominating Raman band in the spectrum. The contributions of the aromatic CH stretching vibrations around  $3055 \text{ cm}^{-1}$  are smaller, but still significant (in the GyrA subunit the aromatic amino acids represent slightly more than 8% of the total number of amino acids). Other resolved features are the  $\text{CH}_2$  deformation vibration around  $1446 \text{ cm}^{-1}$  and the C-O stretching vibration around  $1085 \text{ cm}^{-1}$  [152].

However, the structures in the spectrum are broad, many bands overlap and are only poorly resolved. It would be very hard or impossible to distinguish very small changes in the vibra-

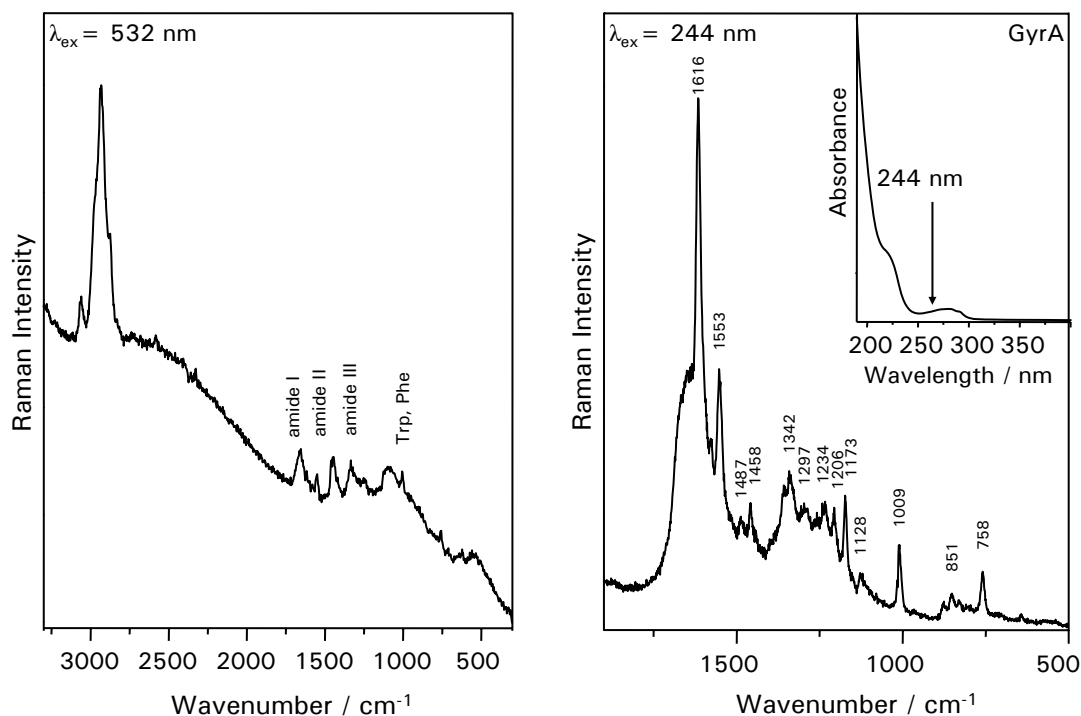


**Figure 8.5:** **A)** Raman spectrum of the enzyme gyrase ( $\lambda_{ex}=532$  nm); **B)** resonance Raman spectrum of the GyrA subunit ( $\lambda_{ex}=244$  nm). The inset shows the UV absorption spectrum of the protein in aqueous solution.

tional signature due to the interaction with DNA and/or the drug. Therefore, resonance Raman spectroscopy was applied.

### 8.3.2 UV-resonance Raman spectroscopy

**Fresh extract** Figure 8.5B shows the resonance Raman spectrum of the fresh extract (aqueous solution) of the GyrA subunit of gyrase excited at 244 nm. The UV absorption spectrum of the protein is shown as an inset in the right corner and the arrow indicates where the excitation wavelength hits the electronic transitions. In the Raman spectrum in particular the vibrational modes of the aromatic amino acids that absorb in this spectral region are enhanced with high selectivity and high specificity. The most prominent band at  $1616\text{ cm}^{-1}$  contains contributions from tyrosine (Y8a) and tryptophan. Tryptophan also accounts for the vibrational bands at  $1576\text{ cm}^{-1}$ ,  $1009\text{ cm}^{-1}$  (W16) and  $757\text{ cm}^{-1}$  and contributes to the bands around  $1555\text{ cm}^{-1}$  (W3),  $1458\text{ cm}^{-1}$  as well as the two bands around  $1357$  (W7) and  $1340\text{ cm}^{-1}$  (for comparison see the resonance Raman spectrum of tryptophan in the appendix B figure B.11). The tyrosine Fermi doublet is only weak in the spectrum of the gyrase subunit GyrA. The vibrational band around  $850\text{ cm}^{-1}$  is slightly higher in intensity than the band around  $830\text{ cm}^{-1}$ . This intensity ratio is in good agreement with

## 8 The biological target: DNA-gyrase

"exposed" tyrosines [241] as they are expected on the surface of the DNA-breakage-reunion region (see figure 8.1) when the phenolic OH is simultaneous acceptor and donor of moderately to weak hydrogen bonds from and to the solvent.

**Redissolved lyophilisate** The tertiary structure of proteins can be disrupted very easily and as a consequence the protein will lose its biological activity. Therefore, the experiments with the gyrase have been performed shortly after the extraction of the protein and all handling of the protein was done at 4°C. However, it is desirable to keep the protein over a longer period of time. Several ways to do that are known from biology. Most of them involve the addition of adequate stabilizers, such as glycerol before freezing. These methods are inappropriate since in most cases the added substance shows a strong Raman spectrum which will complicate the spectral analysis. Freeze-drying (lyophilisation) seems to be the method of choice. Care must be exercised especially during the freezing process, it should be very rapid to shock-freeze the protein in its native structure, so that it will survive the extreme pH and salt concentrations arising during the freezing process. Furthermore the salts present in the solution and buffer can become important for conservation of the structure. In this experiment the GyrA extract was lyophilized after removing the imidazole by dialysis against KCl (see section 3.2.3).

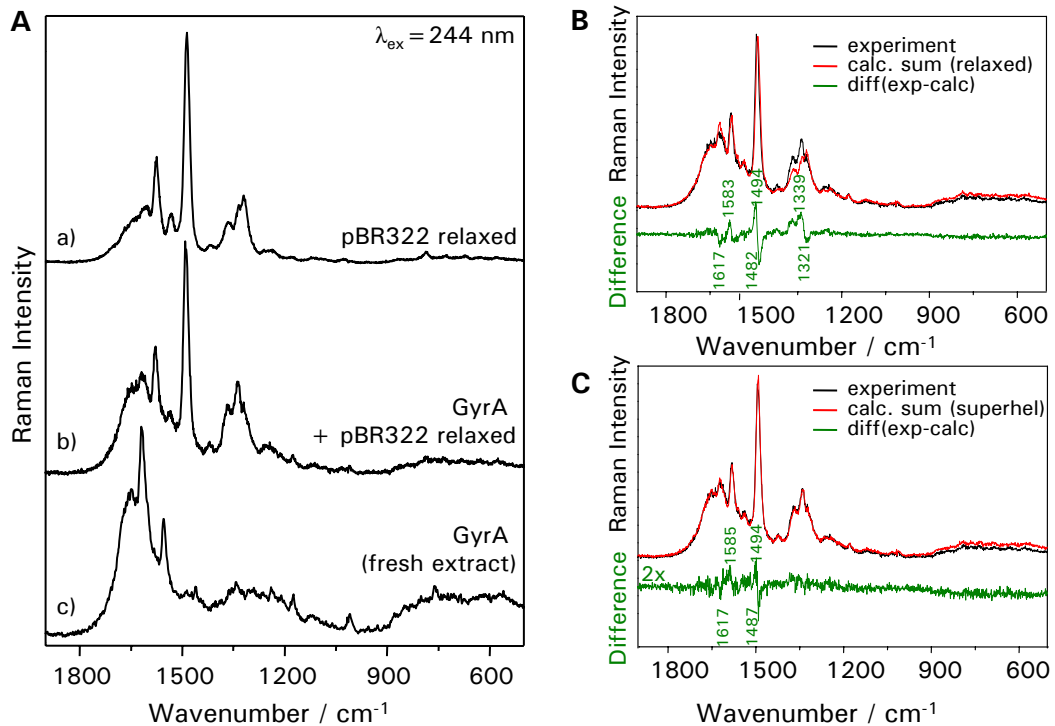
The resonance Raman spectrum of the redissolved lyophilisate of GyrA looks very similar to the resonance Raman spectrum of the fresh extract (see the GyrA spectra in figure 8.7), however slight differences are detected in the spectra. The most significant difference is the higher intensity of the vibrational band around  $1630\text{ cm}^{-1}$  (long wavelength shoulder of the Tyr/Trp band at  $1616\text{ cm}^{-1}$ ). Minor (unstructured) deviations arise in the spectral region between  $800$  and  $570\text{ cm}^{-1}$ . The tryptophan W16 band occurs also with slightly higher intensity in the spectrum of the redissolved lyophilisate. Experiments assessing the biological activity of the redissolved lyophilisate and the fresh extract will be performed in the next section.

## 8.4 Interactions with DNA and the drug

### 8.4.1 Interactions with DNA

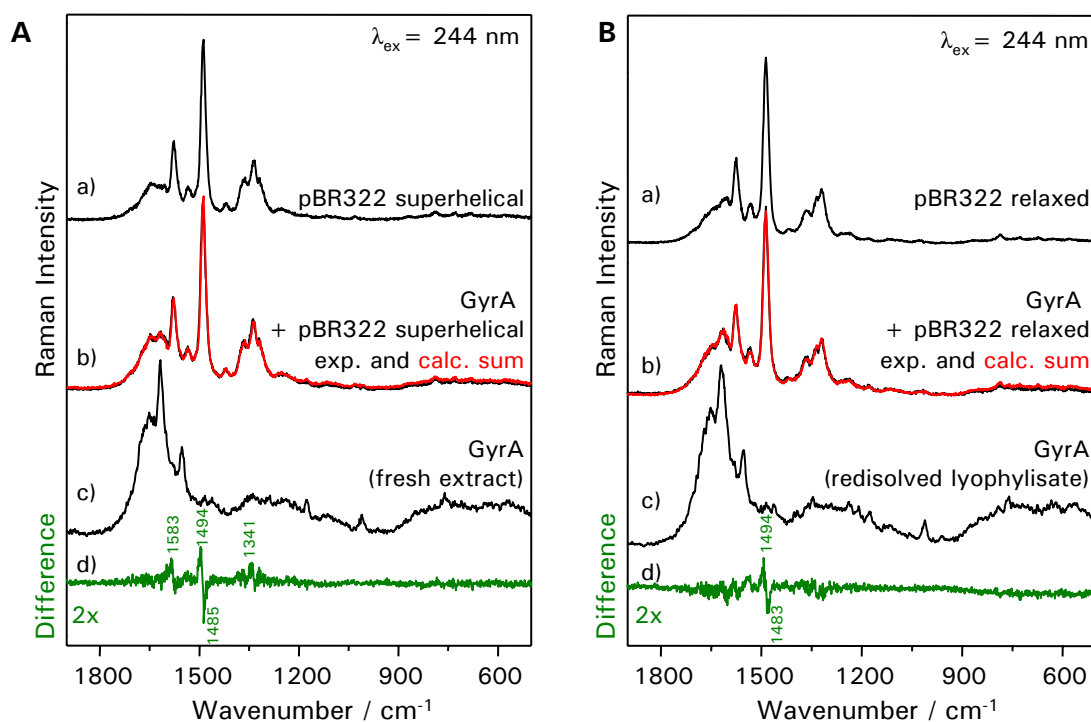
The GyrA subunit of the gyrase was used for investigating the specific interactions between the DNA double strand of different topology and the enzyme. As was explained above (section 8.1) DNA binding occurs in the DNA cleavage region GyrA59. In the absence of GyrB and ATP the DNA supercoiling process will stop after opening the G segment of the DNA double strand.

Figure 8.6A shows again the resonance Raman spectra of the fresh extract of GyrA (c) and the relaxed plasmid DNA pBR322 (a). In the middle (b) the resonance Raman spectrum of the complex formed upon mixing both components in a ratio 2:1 (volume of solution of GyrA : DNA solution (1.2 mg/ml)) is depicted. The spectrum is dominated by the Raman signatures of the plasmid pBR322. In order to find out if any spectral changes occur upon binding, the experi-



**Figure 8.6:** **A)** UV-resonance Raman spectra of fresh GyrA (c), relaxed pBR322 (a) and the mixture of both (b). **B)** Comparison of the experimental spectrum of the gyrA-relaxed DNA-complex (black) with the sum spectrum (red) from the individual components gyrA and relaxed pBR322 the green spectrum at the bottom is the computed difference between the experimental spectrum and the sum spectrum **C)** Comparison of the experimental spectrum of the gyrA-relaxed DNA-complex (black) with the sum spectrum (red) from gyrA and supercoiled pBR322 the green spectrum at the bottom is the computed difference between the experimental spectrum and the sum spectrum.

mental spectrum of the GyrA-DNA-complex (black) is compared to the calculated sum spectrum (red) in figure 8.6B. The sum spectrum (red) was obtained by adding the spectra of the individual components (GyrA and relaxed pBR322) in the appropriate ratio. The green spectrum in figure 8.6B depicts the differences between the experimental and the calculated spectrum, which is free of any specific interactions: significant spectral variations are detected in the spectral region around  $1340 \text{ cm}^{-1}$  and with a peak-trough feature around  $1490 \text{ cm}^{-1}$ . A smaller trough-peak feature occurs around  $1600 \text{ cm}^{-1}$ . This suggests structural changes involving the ribose sensitive modes of the purine (and pyrimidine) rings as well as changes in the hydrogen bonding sites of the DNA double strand. The pattern of the difference spectrum strongly resembles the one obtained when calculating the spectral difference between the resonance Raman spectra of supercoiled and relaxed DNA (see figure 7.13 in section 7.5). Therefore, the experimental spectrum of the complex formed by mixing GyrA with relaxed pBR322 was compared to a sum spectrum calculated by adding the spectral contributions from GyrA and supercoiled pBR322 (instead of



**Figure 8.7:** **A)** UV-resonance Raman spectra of fresh GyrA (c), superhelical pBR322 (a) and the mixture of both (b), the red spectrum in the middle (b) was obtained by calculating the sum of the individual components GyrA and supercoiled pBR322. The green spectrum at the bottom (d) is the computed difference between the experimental spectrum and the sum spectrum. **B)** UV-resonance Raman spectra of GyrA (redisolved from lyophilized GyrA) (c), relaxed pBR322 (a) and the mixture of both (b), the red spectrum in the middle (b) was obtained by calculating the sum of the individual components GyrA and relaxed pBR322. The green spectrum at the bottom (d) is the computed difference between the experimental spectrum and the sum spectrum.

relaxed pBR322). The result is depicted in figure 8.6C. The difference between the experimental and calculated spectrum is very small (the green spectrum in figure 8.6C is amplified 2fold) and the only significant structures are a peak-trough feature around  $1490 \text{ cm}^{-1}$  and a small peak around  $1585 \text{ cm}^{-1}$ . These vibrational bands are assumed to result from the binding of the DNA to the GyrA surface. In the absence of the GyrB subunit and ATP the DNA will not be released from the enzyme.

Figure 8.7A shows the results when the same mixing experiment is performed with GyrA and supercoiled DNA. Again the experimental spectrum of the mixture is shown in black (graph b) and the calculated sum spectrum from the individual components (GyrA and supercoiled pBR322, graph a and c, respectively) is depicted in red in the same diagram (graph b). The calculated difference spectrum between the experimental and the sum spectrum, that allows conclusions about the specific interactions in the complex, is shown in green in the bottom (d). The observed devi-



ations are not as striking as the ones for the relaxed DNA in figure 8.6B, but rather resemble the difference pattern shown in figure 8.6C. However the magnitude of the peak-and-trough features is slightly higher. This suggests that the DNA is bound to the enzyme causing the changes in the vibrational spectrum around  $1490\text{ cm}^{-1}$ ,  $1580\text{ cm}^{-1}$  and  $1340\text{ cm}^{-1}$ , but the changes in DNA topology are only minimal. This seems plausible as native supercoiled plasmid pBR322 as used in the experiment exists already in the state of maximum twist that is achieved by the action of gyrase from *E. coli*.

The same experiment was also performed using the redissolved lyophilized GyrA and the relaxed plasmid DNA pBR322. The corresponding spectra are shown in figure 8.7B. The difference spectrum (in green, graph d) calculated from the experimental spectrum of the mixture (black, graph b) and the sum spectrum (red, b) does not exhibit the large deviations as observed for the complex between the fresh extract of GyrA and relaxed DNA. The spectral signature rather suggests a specific binding as was recorded for the complex of the fresh GyrA extract and supercoiled DNA. This suggests a (partial) loss of the biological activity of the enzyme upon lyophilization and resolving. Since there are still interactions between the enzyme, the distortion of the tertiary structure might be either small or rather affect the CTD of GyrA which wraps the DNA double strand around the enzyme under strong bending of the DNA strand.

These experiments showed that the fresh extract of the GyrA subunit of the enzyme gyrase exhibits full biological activity and is capable of introducing structural changes in relaxed pBR322 that vary its topology towards the one of superhelical DNA. The lyophilized and redissolved fraction of the enzyme did not show such a high biological activity and only vibrational changes due to the binding of the DNA to the enzyme have been observed. When using supercoiled pBR322 as a target for GyrA only minor changes in topology are detectable. This can be explained by the fact that the native supercoiled pBR322 is already in the maximal state of supercoiling achievable by the action of GyrA from *E. coli*.

A concentration series with different mixing ratios of GyrA and plasmid DNA could provide further insights into the binding and supercoiling mechanism. In the next step the binary mixture of enzyme and drug is investigated.

#### 8.4.2 Interactions with the drug

To investigate the effect of the fluoroquinole drugs alone on the enzyme, resonance Raman spectra have been recorded from the GyrA subunit, moxifloxacin and the mixture of both (figure 8.8A). The spectral deviation between the experimental spectrum of the mixture (black) and the sum spectrum (red) obtained by adding the spectra of the two components is depicted in green in figure 8.8B. The difference spectrum is relatively noisy and suggests some variances in the spectral region of the most intense bands ( $1650\text{-}1250\text{ cm}^{-1}$ ). In the literature it is reported that there are neither specific interactions between the enzyme and the drug nor between the drug and the DNA. However, the spectra suggest some minor structural changes but for a detailed analysis more data

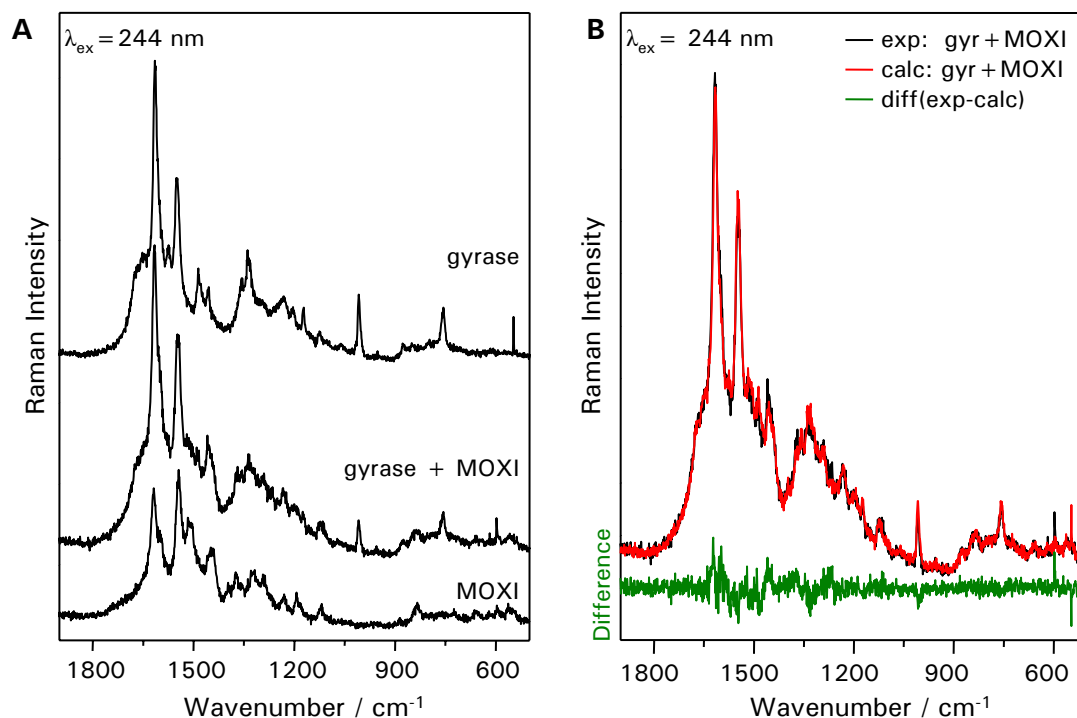


**Figure 8.8:** **A)** UV-resonance Raman spectra of GyrA (bottom), moxifloxacin (top) and the mixture of both (middle). **B)** Comparison of the experimental spectrum of the GyrA-moxifloxacin-complex (black) with the sum spectrum (red) from the individual components gyrase and moxifloxacin, the green spectrum at the bottom is the computed difference between the experimental spectrum and the sum spectrum.

points are necessary to allow the use of statistical analysis methods and a profound interpretation of the data.

## 8.5 Summary

Different amino acids have been characterized by means of vibrational spectroscopy and marker bands could be identified which could be also found in the Raman spectrum of extracted gyrase. While the micro-Raman spectrum of the enzyme gyrase excited at 532 nm exhibits rather broad and poorly resolved features the UV-resonance Raman spectrum excited at 244 nm shows sharp vibrational bands originating mainly from the aromatic amino acids. The fresh extract of the GyrA subunit of the enzyme displays biological activity and is able to change the topology of relaxed DNA. Care has to be taken when the enzyme is subjected to lyophilization, because it can cause a loss of activity.

## 9 Influence of fluoroquinolone drugs on bacterial growth

Many bacteria are cause of infectious diseases. In order to fight those diseases a large variety of antibiotics exists. They interfere with different vital processes of the bacteria. The fluoroquinolones are important broad band antibiotics which are bactericidal by attacking the gyrase-DNA complex and interfering with the action of the vital enzyme gyrase. The individual components of the ternary drug-target complex have been characterized by means of vibrational spectroscopy in the previous chapters: the fluoroquinolone drugs in chapter 6, the biological target DNA in chapter 7 and the enzyme gyrase in chapter 8. Also the unperturbed bacteria and their metabolic changes during bacterial growth have been discussed in chapter 4. In this chapter now, everything will be put together and the effect of fluoroquinolone drugs on the bacterial growth will be monitored by means of vibrational spectroscopic methods such as IR absorption, micro-Raman and UV-resonance Raman spectroscopy. Multivariate statistical analysis methods will help to extract the traits of interest from the complex bacterial spectra.

### 9.1 Minimal inhibition concentration

The minimal inhibition concentration (MIC) denotes the lowest antibiotic concentration at which no bacterial growth is observed after overnight incubation. Minimum inhibitory concentrations are used as characteristic in diagnostic laboratories to confirm resistance of microorganisms to an antimicrobial agent and also to monitor the activity of new antimicrobial agents. The MIC of four different drugs for *Bacillus pumilus* DSM 361 *Staphylococcus epidermidis* ATCC 35984 and *Escherichia coli* DSM 423 are shown in table 9.1.

**Table 9.1:** Minimal inhibition concentration of norfloxacin, ciprofloxacin, moxifloxacin and vancomycin on *B. pumilus* DSM 361 *S. epidermidis* ATCC 35984 and *E.coli* DSM 423.

drug bacterial strain	norfloxacin µg/ml	ciprofloxacin µg/ml	moxifloxacin µg/ml	vancomycin µg/ml
<i>B. pumilus</i> DSM 361	< 12	< 0.7	0.05	
<i>S. epidermidis</i> ATCC 35984	< 0.3	<1	< 0.06	4
<i>E.coli</i> DSM 423	< 0.6	< 0.07		

## 9 Influence of fluoroquinolone drugs on bacterial growth

A clear increase in the activity can be seen in the fluoroquinolone series norfloxacin – ciprofloxacin – moxifloxacin. The newest, third generation drug, moxifloxacin exhibits a clearly enhanced activity against Gram-positive bacteria compared to the older, second generation drugs. Increasing resistances of various bacteria against antibiotics make the development and design of new powerful drugs necessary. Therefore, it is of great interest to understand the action of antibiotics also on a molecular level. In this work the focus is set on the fluoroquinolones drugs, which are important and effective broad spectrum antibiotics [15, 102, 9, 69, 227] (see also chapter 6). Despite of many microbiological, chemical and spectroscopic investigations the exact impact mechanism on a molecular level is not yet fully understood [18, 98]. Exemplarily the influence of two different fluoroquinolones drugs (moxifloxacin and ciprofloxacin) applied in various concentrations on the growth of two different bacterial strains (*S. epidermidis* and *B. pumilus*) is studied in the following.

It was found that for the full activity of the fluoroquinone drugs a free carboxyl acid group is necessary in position 3 of the quinolone ring. The three precursor structures A, B and C shown in figure 6.2 in section 6.2 where the carboxyl group is blocked by ester formation exhibit no antibacterial activity while the analogous structures D and E (see figure 6.2) with free acids are highly active.

For comparison the MIC of vancomycin, a drug of the group of the glycopeptides which inhibit cell wall synthesis by blocking the murein synthesis, is shown in the last column of table 9.1. While glycopeptides had been one of the last effective weapons against multiresistant germs like methicillin resistant staphylococci (MRS), growing resistances of the bacteria seem to evolve [168], as is also seen in the example of *S. epidermidis* ATCC 35984. In the development of new and effective drugs and for the elucidation of the mechanisms of action of the drugs high resolution techniques that provide rich information in short times are required. In chapter 5 such a technique was introduced.

Increasing resistances of various bacteria against antibiotics make the development and design of new powerful drugs necessary. Therefore, it is of great interest to understand the action of antibiotics also on a molecular level. In this work the focus is set on the the fluoroquinolones drugs, which are important and effective broad spectrum antibiotics [15, 102, 9, 69, 227]. Despite of many microbiological, chemical and spectroscopic investigations the exact impact mechanism on a molecular level is not yet fully understood [18, 98]. Exemplarily the influence of two different fluoroquinolones drugs (moxifloxacin and ciprofloxacin) applied in various concentrations on the growth of two different bacterial strains (*S. epidermidis* and *B. pumilus*) is studied in the following.

### 9.2 Effect of moxifloxacin on *Staphylococcus epidermidis*

Moxifloxacin (see chapter 6) is one of the newer fluoroquinolone drugs which reached the (UK) market in 2000 as a powerful respiratory agent. The addition of an azabicyclo group in position 7 improves the activity against Gram-positive bacteria, and brings also a marked lipophilicity and half-lives of more than 10 hours [9]. Moxifloxacin retains activity against many staphylococcal

isolates that developed resistance to the older fluoroquinolone drug ciprofloxacin [142]. This testifies the recognized fact in pharmaceutical and medical research that the only solution to overcome the threat of growing resistances is to continuously develop new drugs [138]. In order to facilitate target-oriented research new techniques that provide a fast and reliable insight into the mode of action of antibiotics are in high demand.

Within this chapter different vibrational spectroscopic techniques will be used to gain a deeper insight into the mechanism of antibiotic action. IR absorption and micro-Raman spectroscopy with excitation at 532 nm, as well as UV-resonance Raman spectroscopy with excitation at 244 nm are applied as optical analytical tools to investigate the effect of the fluoroquinolone drug moxifloxacin on *Staphylococcus epidermidis* as an example of Gram-positive bacteria. Spectra are recorded of unperturbed bacteria and of bacteria that experienced varying antibiotic concentrations. With the help of statistical methods the spectral changes due to the action of the drug are pointed out and assigned to biological features within the cell. That way the actual model for the mode of action of the fluoroquinolone drugs can be supported, demonstrating once again the power of vibrational spectroscopy for biomedical and pharmaceutical problems.

The minimal inhibition concentration (MIC) of moxifloxacin on *S. epidermidis* ATCC 35984 was determined to be less than 0.06  $\mu\text{g/ml}$ . This value is in good agreement with the MICs of moxifloxacin on other staphylococcus strains as reported in the literature [9]. When the drug is applied target peak serum concentrations of 2.5  $\mu\text{g/ml}$  in the body have been reported [147]. We chose four different drug concentrations within this pharmaceutical relevant range to study the influence of moxifloxacin on the bacteria in order to learn more about the mode of action of this fluoroquinolone drug.

### 9.2.1 Growth curve under the influence of drug

Figure 9.1 shows the growth curves of *S. epidermidis* ATCC 35984 under batch conditions (CASO, 37°C) in the semi-logarithmic representation for bacterial cultures without (★) and with the addition of different moxifloxacin concentrations (● 0.8  $\mu\text{g/ml}$ , ▲ 0.16  $\mu\text{g/ml}$ , ▼ 0.27  $\mu\text{g/ml}$ , and ◆ 0.63  $\mu\text{g/ml}$ ). The growth curve of the unperturbed culture (★) features the typical growth phases as was described in more detail before (chapter 4.3): In the lag phase (< 100 min) the bacteria prepare their metabolism for the upcoming growth phase and no net-increase of biomass is observed. It follows the acceleration phase in which the growth rate increases until it reaches a constant value of  $\mu = 0.789 \text{ h}^{-1}$  (37°C in CASO) in the exponential growth phase (> 180 min). Finally, the growth rate decreases again in the retardation phase and is zero in the stationary phase (> 600 min, not shown). At the beginning of the exponential growth phase bacteria are most susceptible to changes in their environment. Therefore, moxifloxacin was added in different concentrations to the growing bacterial culture at this time (200 minutes after inoculation of the culture; marked by an arrow in figure 9.1). This causes a reduction of the overall biomass increase and finally results in a complete inhibition of the bacterial growth due to cell death, as can be seen in the growth curve at later

## 9 Influence of fluoroquinolone drugs on bacterial growth

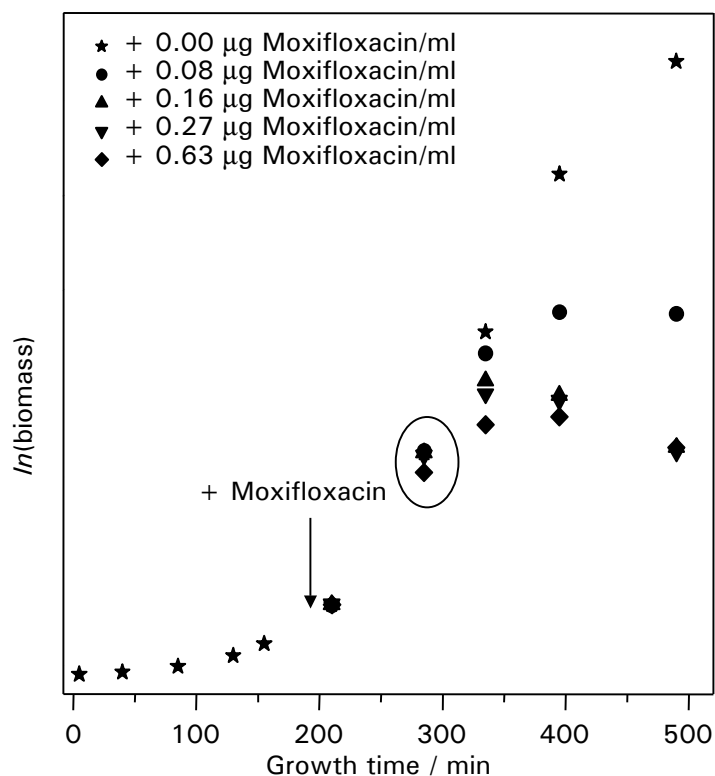


**Figure 9.1:** Growth curves of *S. epidermidis* ATCC 35984 under batch conditions (CASO, 37°C) in the semi-logarithmic representation for bacterial cultures without (★) and with the addition of different moxifloxacin concentration (● 0.8  $\mu\text{g/ml}$ , ▲ 0.16  $\mu\text{g/ml}$ , ▼ 0.27  $\mu\text{g/ml}$ , and ◆ 0.63  $\mu\text{g/ml}$ ). An arrow marks the time of the addition of the drug and the ellipse highlights the time at which the following vibrational spectra have been recorded.

growth times. The effect is more pronounced at higher moxifloxacin concentrations meaning that the extent of bacterial killing increases as drug concentrations increase. Several times after the addition of the drug, IR absorption, micro-Raman and resonance Raman spectra were recorded of the bacteria without and with drug addition. In the following the results are represented for a residence time of the drug of 80 minutes. This is enough time for the drug to diffuse into the bacterial cells, interact with its biological targets and cause cell death. From pharmacodynamic studies of moxifloxacin the time to kill 99.9% of *S. epidermidis* cells was determined to be between 90 and 180 minutes [142].

### 9.2.2 IR absorption spectra

Figure 9.2A shows representative IR absorption spectra for the different drug concentrations after an incubation time of 80 minutes (280 minutes of total growth time, marked with an ellipse in figure 9.1). On a first view all spectra look very similar. They are dominated by the strong amide I band at  $1654\text{ cm}^{-1}$  and the amide II band at  $1547\text{ cm}^{-1}$ . Other prominent features are the broad

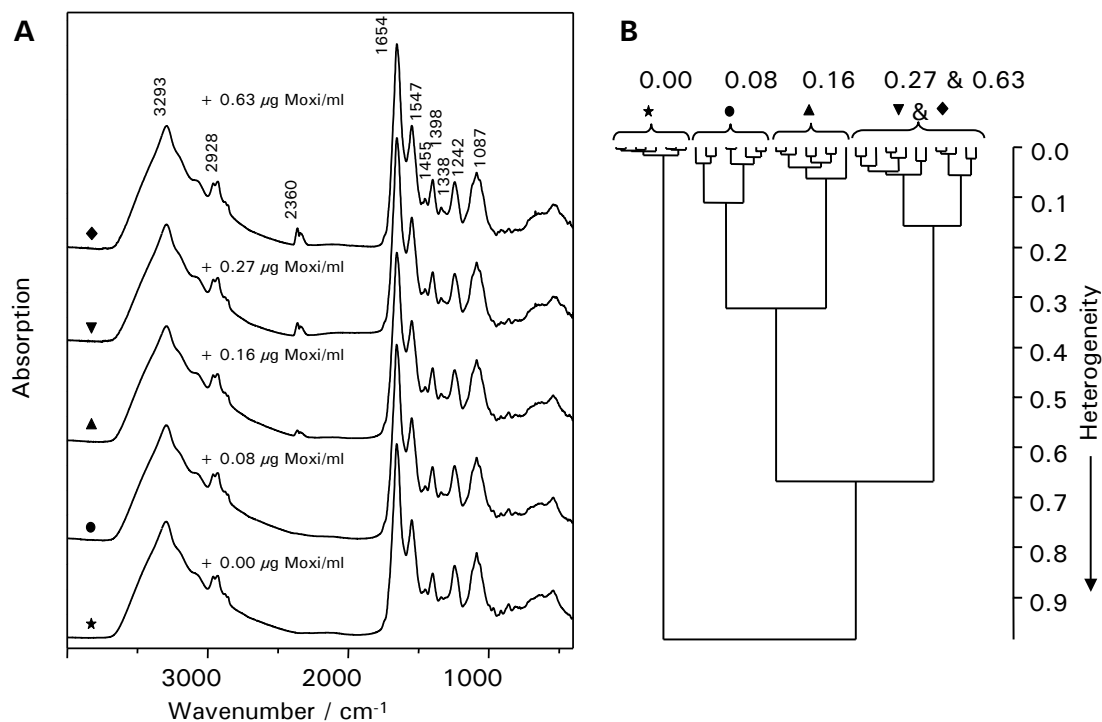


**Figure 9.2:** **A)** IR absorption spectra of *S. epidermidis* with different drug concentrations, recorded 80 minutes after drug addition. **B)** Hierarchical cluster analysis (HCA) of the vector normalized spectra shown in A). The numbers above the clusters name the added moxifloxacin concentration in  $\mu\text{g}/\text{ml}$ .

NH stretching band around  $3293\text{ cm}^{-1}$  and the various CH stretches of medium intensity around  $2930\text{ cm}^{-1}$ . The CH deformation mode is found at  $1242\text{ cm}^{-1}$  and the band at  $1087\text{ cm}^{-1}$  is due to the symmetric P=O stretching vibration. A more detailed discussion of the spectra of unperturbed *S. epidermidis* is given in chapter 4.1.

Even though, the spectra appear qualitatively very similar, quantitative differences according to the drug concentration can be found. Statistical methods help to point out the spectral traits of interest. In the hierarchical cluster analysis (HCA) shown in figure 9.2B the vector normalized spectra of bacteria without and with drug separate very well into two different clusters. The cluster of spectra of bacteria that were exposed to the antibiotics further splits according to the drug concentration. The two lowest moxifloxacin concentrations ( $0.08\text{ }\mu\text{g}/\text{ml}$  and  $0.16\text{ }\mu\text{g}/\text{ml}$ ) form each separate sub-clusters with a relatively small inner-cluster heterogeneity and are distinct from the spectra of bacteria which were treated with higher moxifloxacin concentrations ( $0.27\text{ }\mu\text{g}/\text{ml}$  and  $0.63\text{ }\mu\text{g}/\text{ml}$ ). The similarity of the spectra of the two highest drug concentrations is also in good agreement with a coinciding amount of biomass present in the culture at this growth time (figure 9.1).

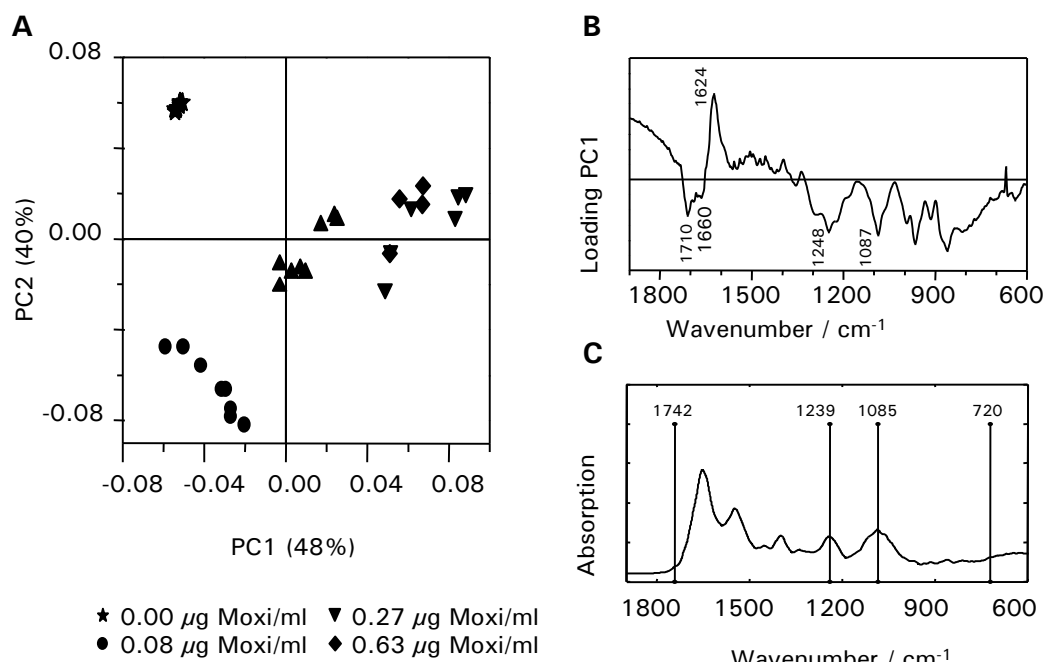


**Figure 9.3:** **A)** Scores plot of the first two principal components (PCs) of the IR absorption spectra of *S. epidermidis* with different drug concentrations, recorded 80 minutes after drug addition. **B)** Loading Plot for the first principal component (from A). **C)** Important wavenumbers determined by variable selection (REM-TS and LDA) plotted into an IR absorption spectrum of *S. epidermidis* grown in the presence of 0.16  $\mu\text{g/ml}$  moxifloxacin, recorded 80 minutes after drug addition.

The same vibrational spectra were used to perform a principal component analysis (PCA). The scores plot of the first two principal components (PC) which describe together 88% of the explained variance is shown in figure 9.3A. According to the drug concentration the bacterial spectra arrange along the first PC, with the bacteria with no moxifloxacin and with 0.08  $\mu\text{g/ml}$  moxifloxacin /ml displaced also along the second PC. As in the HCA no separation of the two highest moxifloxacin concentrations 0.27  $\mu\text{g/ml}$  and 0.63  $\mu\text{g/ml}$  is achieved.

Since the first principal component correlates to the drug concentration the loading of PC1 gives the wavenumbers that show the largest variation associated with the action of the drug (figure 9.3B). The largest spectral changes occur in the wavenumber region around 1624  $\text{cm}^{-1}$ . But also the wavenumbers around 1710  $\text{cm}^{-1}$ , 1660  $\text{cm}^{-1}$ , 1248  $\text{cm}^{-1}$ , 1087  $\text{cm}^{-1}$ , 965  $\text{cm}^{-1}$  and 860  $\text{cm}^{-1}$  contribute with markedly weight to PC1 (table 9.2).

Employing REM-TS with LDA for variable selection (see section 3.4) gives information about wavenumbers with high discriminative power. It turned out that a couple of variable subsets achieved extremely good classification results with LDA. As a consequence the search did not



**Table 9.2:** Assignment of the wavenumbers showing the highest discriminative power for the spectra (IR absorption, micro-Raman and UV-resonance Raman) of *S. epidermidis* experiencing different moxifloxacin concentrations as determined by means of PCA and REM-TS/LDA, respectively. The spectra were recorded after a growth time of 335 minutes, which is 80 minutes after the addition of the drug.

Experimental Method Evaluation Method	IR Absorption			Micro-Raman ( $\lambda_{\text{exc}}=532\text{ nm}$ )			UV RR ( $\lambda_{\text{exc}}=244\text{ nm}$ )		
	PCA (PC1)	REM-TS / LDA	Assignment	PCA (PC1)	REM-TS / LDA	Assignment	PCA (PC1)	REM-TS / LDA	Assignment
Wavenumber in $\text{cm}^{-1}$	1710	1742	amide I ( $\alpha$ -helix and $\beta$ -sheet) [152]	1660		amide I (C=O str, NH <sub>2</sub> bend, C=N str) [151, 152] C=C str (lipids) [185]	1650		amide I
	1660		intermolecular aggregated $\beta$ -sheet of denatured protein [255]					1639	T [145]
1624				1581	1450	nucleic acids (G+A ring str) [152]	1601	1609	Tyr + Trp [145]
				1462	1314	$\delta(\text{CH}_2)$ scissoring [151, 152, 283, 276]	1570	1475	G + A [145]
						$\delta(\text{CH})$ [151]			G + A [145]
1248			amide III; P=O str (asym) of PO <sub>2</sub> <sup>-</sup> (phosphodiester) [152]	1298		guanine, CH def (protein) [185]			
		1239		1263		amide III [151, 152]		1307	A + G + Tyr [145]
1087		1085	P=O str (sym) of PO <sub>2</sub> <sup>-</sup> [152], aliphatic esters [72]	1123	1242	stacking-sensitive marker of dT [24]			
965				1088		C-N and C-C str [151, 152], =C-C= (unsat. fatty acids in lipids) [230]			
860						CC skeletal, C-O-C asymmetric stretching in aliphatic esters, glycosidic link [152]			
		720	C-H rock of CH <sub>2</sub> [152]	741	782	n (CC) ring breathing (cytosine, uracil) [151, 152, 283, 276]			
						DNA components (stacking-sensitive marker of dA [24] or dT [151, 24])		1229	G + A + U [145]

## 9 Influence of fluoroquinolone drugs on bacterial growth

yield a definite result concerning which wavenumbers are most relevant for the discrimination. One out of many equally good variable subsets is:  $1742\text{ cm}^{-1}$  (C=O str),  $1239\text{ cm}^{-1}$  (P=O str (asym), amide III),  $1085\text{ cm}^{-1}$  (P=O str (sym)) and  $720\text{ cm}^{-1}$  (CH rock) (figure 9.3C). Using these variables for classification achieved an internal predictivity of 98% correctly classified spectra in LMO-CV. The external predictivity of the test set spectra obtained by major voting was 93%.

This indicates that in the interaction of moxifloxacin with its biological targets and the subsequent reactions mainly changes at the DNA (symmetric and asymmetric P=O stretch in the DNA backbone), but also in protein (amide III and amide I) are involved.

The contributions of the asymmetric and symmetric  $\text{PO}_2^-$  stretching vibration at  $1248\text{ cm}^{-1}$  and  $1087\text{ cm}^{-1}$ , to the loading of PC1 and the selection of those wavenumbers by the tabu search method indicate structural changes in the DNA backbone, which might be a reorientation of the phosphate groups due to DNA interactions. The negative correlation of this wavenumbers in the PCA suggests a decrease of phosphate binding which is in good agreement with the observation of DNA fragments after the incubation with fluoroquinolone drugs reported in earlier studies [162].

The principal component analysis reveals a positive correlation of the wavenumber region around  $1624\text{ cm}^{-1}$  to the loading of PC1 which indicates the increase of intermolecular aggregated  $\beta$ -sheet as they are found in denatured protein [255]. The concomitant negative correlation of PC1 with a broad region around  $1660\text{ cm}^{-1}$  marks the decrease of ordered  $\alpha$ -helical and  $\beta$ -sheet structures. The observed changes might not only be due to the pure action of the drug with its biological target, but also caused by successive reactions (in pharmacokinetic studies moxifloxacin was found to have a protein binding of 50% [9]).

### 9.2.3 Micro-Raman spectra with excitation at 532 nm

Figure 9.4A shows the micro-Raman spectra of the bacteria with and without drug addition in a spectral region between  $1900\text{ cm}^{-1}$  and  $600\text{ cm}^{-1}$ . As for the IR spectra no significant differences are visible on first sight and make a statistical analysis necessary. Due to different selection rules different vibrational bands are prominent in the Raman spectra compared to the IR spectra. Protein contributions are found around  $1660\text{ cm}^{-1}$  with the amide I band [151, 152], in the spectral region between  $1220\text{-}1300\text{ cm}^{-1}$  contribution from the amide III band [151, 152], and around  $1000\text{ cm}^{-1}$  with the aromatic ring stretching mode of phenylalanine [152]. The vibrational bands at  $1450\text{ cm}^{-1}$  and  $1333\text{ cm}^{-1}$  are assigned to  $\text{CH}_2$  and CH deformation modes, respectively [151, 152, 283, 276]. Nucleic acid vibrations are present with the guanine and adenine ring stretch at  $1574\text{ cm}^{-1}$  [152].

In order to keep the influence of the fluorescence background low the first derivative of the Raman spectra was used for the hierarchical cluster analysis (HCA) shown in figure 9.4B. Like for the IR spectra the HCA allows a clear discrimination between the spectra of untreated bacteria and the spectra of bacteria that have been exposed to moxifloxacin. The bacterial spectra of different

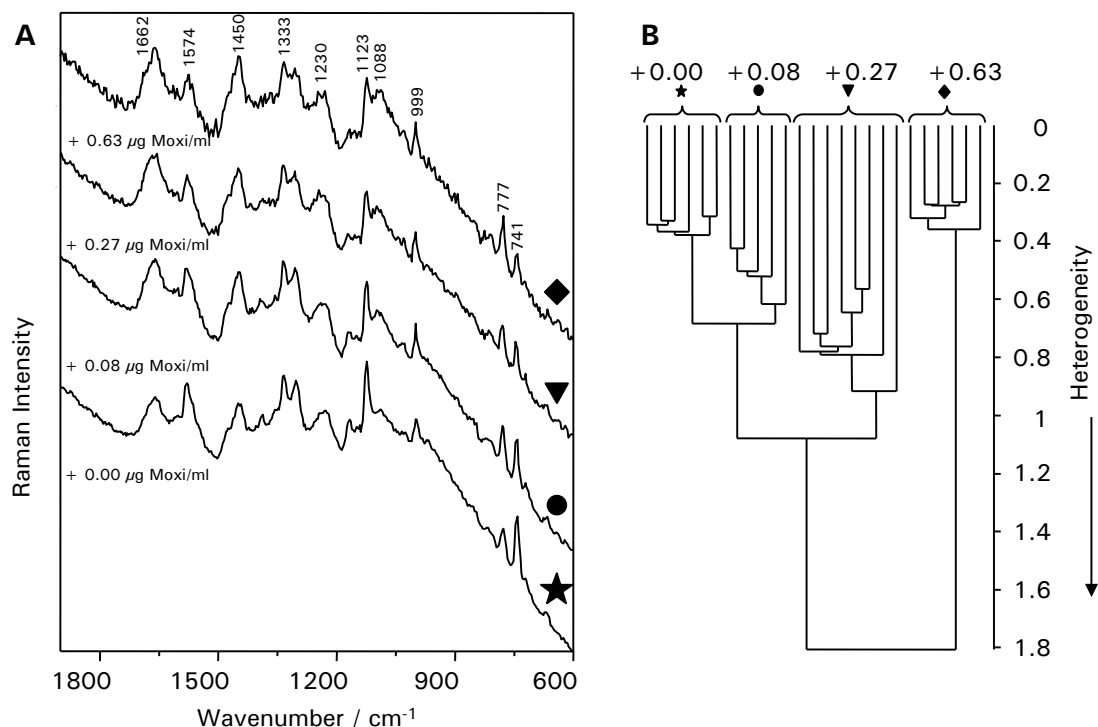


**Figure 9.4:** **A)** Micro-Raman spectra with excitation at 532 nm of *S. epidermidis* with different moxifloxacin concentrations, recorded 80 minutes after drug addition. **B)** Hierarchical cluster analysis (HCA) of the first derivative from the spectra shown in A). The numbers above the clusters name the added moxifloxacin concentration in  $\mu\text{g/ml}$ .

drug concentration form individual sub-clusters within the moxifloxacin-cluster, but the inner-class variance is quite high.

For performing the principal component analysis (PCA) and the REM-TS/LDA the markedly fluorescence background of the Raman spectra was removed by baseline correction rather than by using the first derivative, because information about exact peak position and intensity are desirable when assigning the loadings for the principal components. The scores plot of the first two principal components of the PCA is shown in figure 9.5A. No clean separation of the individual antibiotic concentrations is achieved when using only two PCs. However, as for the IR spectra it is again the first principal component that correlates with the addition of the drug. Figure 9.5B indicates strong contributions of the wavenumbers due to DNA to the loading of PC1. The strong positive loadings at  $1581\text{ cm}^{-1}$ ,  $1123\text{ cm}^{-1}$  and  $741\text{ cm}^{-1}$  can be assigned to ring stretching vibrations in guanine and adenine [152], to C-N and C-C stretching vibrations [151, 152], and to stacking sensitive vibrations of adenosine and thymidine [151, 24], respectively. Further DNA contributions are present with the band at  $1088\text{ cm}^{-1}$  from glycosidic linkages and symmetric  $\text{PO}_2^-$  stretching vibrations of the DNA backbone. Changes in the protein structure are indicated by the loadings of the amide I band around  $1660\text{ cm}^{-1}$  and the amide III band around  $1263\text{ cm}^{-1}$ . The negative

## 9 Influence of fluoroquinolone drugs on bacterial growth

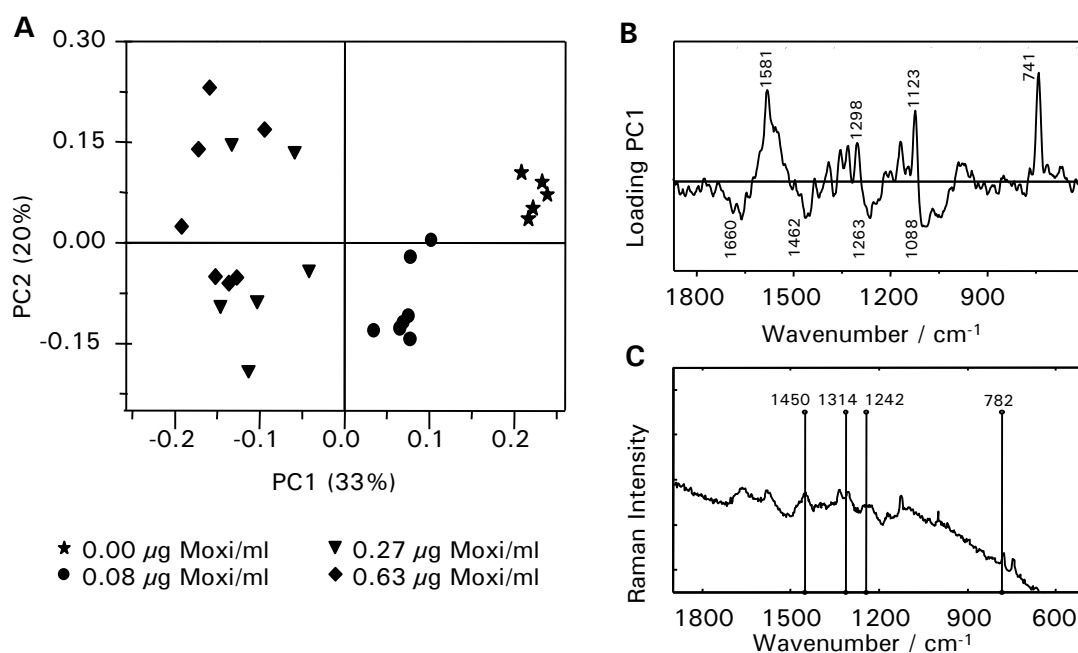


**Figure 9.5:** **A)** Scores plot of the first two principal components (PCs) when using base-line corrected micro-Raman spectra with excitation at 532 nm of *S. epidermidis* with different drug concentrations, recorded 80 minutes after drug addition. **B)** Loading Plot for the first principal component (from A) **C)** Important wavenumbers determined by variable selection (REM-TS and LDA) plotted into a micro-Raman spectrum of *S. epidermidis* grown in the presence of 0.08  $\mu\text{g}/\text{ml}$  Moxifloxacin, recorded 80 minutes after drug addition.

correlation of these bands denotes an increase of random coil structure [49] upon the addition of the drug. This is in good agreement with the results from the IR absorption measurements. The loadings around 1462  $\text{cm}^{-1}$  are due to molecular changes affecting CH-deformation modes.

As for the IR absorption spectra REM-TS coupled to LDA was employed to reveal important spectral regions in the micro-Raman spectra. Especially wavenumbers that are associated with changes in the DNA have selected in that procedure. The wavenumber at 782  $\text{cm}^{-1}$  can be assigned to the ring breathing mode in cytosine (and also uracil) [151, 152, 283, 276], the wavenumber 1242  $\text{cm}^{-1}$  can be assigned to stacking sensitive vibrations of thymine. The wavenumbers at 1314  $\text{cm}^{-1}$  and 1450  $\text{cm}^{-1}$  could be due to CH vibrations of the sugar moiety of the DNA (figure 9.5C, table 9.2). However, a definite ranking concerning the importance of the wavenumbers could not be obtained as the classification by LDA showed an equally good performance for many subsets. The chosen variable subset (1242  $\text{cm}^{-1}$  and 782  $\text{cm}^{-1}$  as well as 1450  $\text{cm}^{-1}$  and 1314  $\text{cm}^{-1}$ , figure 9.5C) showed very good recognition rates and 100% of the spectra could be classified cor-

rectly in LMO-CV (internal predictivity). The test set recognition rate obtained by major voting was 96% (external predictivity).

The selected wavenumbers that experience changes upon addition of moxifloxacin support the proposed mechanism of action of the fluoroquinolone drugs. The drug, in our case moxifloxacin, interacts simultaneously with the DNA double strand while binding to the protein gyrase. Therefore, vibrational bands due to DNA and protein should be affected by the addition of the drug. However, it should be noted that 80 minutes after drug addition further reactions might have occurred. Contributions of the drug itself to the Raman spectra of the bacteria can be neglected, since moxifloxacin is so effective against staphylococci ( $MIC < 0.06 \mu\text{g/ml}$ ) that only low antibiotic concentrations are required in the cultivation flasks to kill the bacteria. Aqueous solutions of moxifloxacin at concentrations below  $1.5 \mu\text{g}/\mu\text{l}$  did not result in any Raman spectra with noticeable signal. Therefore, the direct influence of the pure presence of the drug on the variance of the bacterial spectra with different drug concentration can be neglected. The observed variances within the spectra must be due to changes within the bacteria that are caused by the action of the drug.

#### 9.2.4 UV-resonance Raman spectra with excitation at 244 nm

In the proposed mechanisms of action of the fluoroquinolone drugs the DNA and the enzyme gyrase are involved. It was shown above, that indeed changes in the protein and DNA moieties of the bacteria can be found in the spectra upon drug addition. UV-resonance Raman spectroscopy with an excitation wavelength of 244 nm allows especially focusing on the purine and pyrimidine bases of the nucleic acids and on the aromatic amino acids in the proteins (see also sections 7.1.3, 7.4.3 and 8.3.2).

The UV-resonance Raman spectra of the bacteria without and with different drug concentration shown in figure 9.6A are dominated by contributions from the purine and to a lesser extend the pyrimidine bases of the nucleic acids. Guanine and adenine moieties account for the vibrational bands at  $1479 \text{ cm}^{-1}$  and  $1566 \text{ cm}^{-1}$ . Cytosine is responsible for the weak band at  $1525 \text{ cm}^{-1}$  and thymine and adenine contribute to the band at  $1365 \text{ cm}^{-1}$ . Amino acid vibrations are present with the aromatic amino acids tyrosine and tryptophan which show up at  $1612 \text{ cm}^{-1}$  and  $1167 \text{ cm}^{-1}$ . The band at  $1324 \text{ cm}^{-1}$  results from vibrations in the adenine, guanine and tyrosine moieties.

Unlike for the IR and non-resonance Raman spectra the hierarchical cluster analysis of the UV-resonance Raman spectra (figure 9.6B) reveals a high heterogeneity of the bacteria which were exposed to high moxifloxacin concentrations ( $0.63$  and  $0.27 \mu\text{g/ml}$ ) and those which experienced no or a lower moxifloxacin concentration. Within the low-moxifloxacin concentration cluster the bacterial spectra of the reference culture (no drug) are very well separated from those which were treated with the drug. The two lowest drug concentrations ( $0.08$  and  $0.16 \mu\text{g/ml}$ ) form sub-clusters which contain also one spectrum of the other drug concentration. Within the cluster of the high moxifloxacin concentrations no clear sub-cluster formation according to the concentration

## 9 Influence of fluoroquinolone drugs on bacterial growth

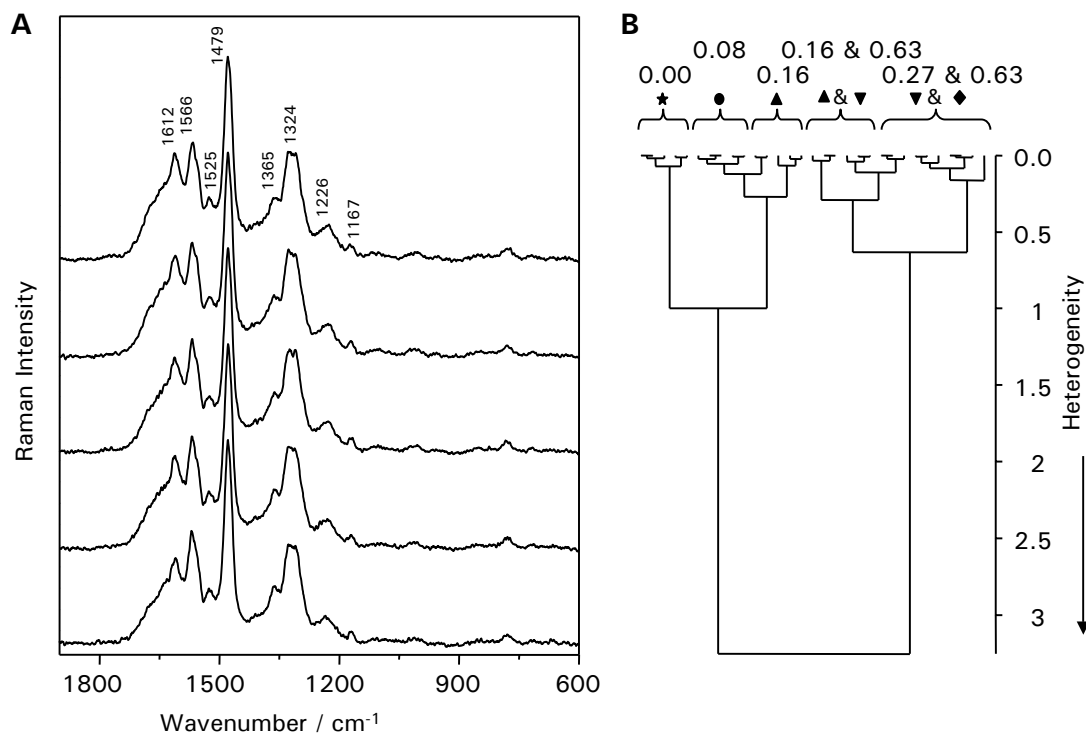


**Figure 9.6:** **A)** UV-resonance Raman spectra with excitation at 244 nm of *S. epidermidis* with different drug concentrations recorded 80 minutes after drug addition. **B)** Hierarchical cluster analysis (HCA) of the vector normalized spectra shown in A). The numbers above the clusters name the added moxifloxacin concentration in  $\mu\text{g/ml}$ .

is observed. This suggests that the changes within the bacteria due to the drug are the same for the two highest drug concentrations of 0.27  $\mu\text{g/ml}$  and 0.63  $\mu\text{g/ml}$  as was already observed for the IR absorption spectra. Those concentrations are well above the MIC of moxifloxacin for *S. epidermidis* while 0.08  $\mu\text{g/ml}$  and 0.16  $\mu\text{g/ml}$  are in the order of magnitude of the MIC (0.06  $\mu\text{g}$  moxifloxacin/ml bacterial culture).

The scores plot of the first two principal components of the PCA shown in figure 9.7A features the same classification pattern as the HCA: the spectra of the bacteria without drug and with low drug concentration are found on the positive side of the first principal component while the spectra of bacteria with high drug concentrations form a mixed cluster on the negative end of PC1. Even though no clear, well separated clusters are formed, the variation within the spectra due presence and action of the drug can be correlated with the first principal component. In particular the vibrational bands around 1650  $\text{cm}^{-1}$  and 1601  $\text{cm}^{-1}$  (negatively correlated) as well as the bands at 1570  $\text{cm}^{-1}$  and 1477  $\text{cm}^{-1}$  (positively correlated) contribute to this principal component as can be seen from the loading plot in figure 9.7B.

The importance of the wavenumbers around 1609  $\text{cm}^{-1}$  and 1475  $\text{cm}^{-1}$  for the classification of the data is also reproduced by subset selection by REM-TS and LDA. The wavenumbers

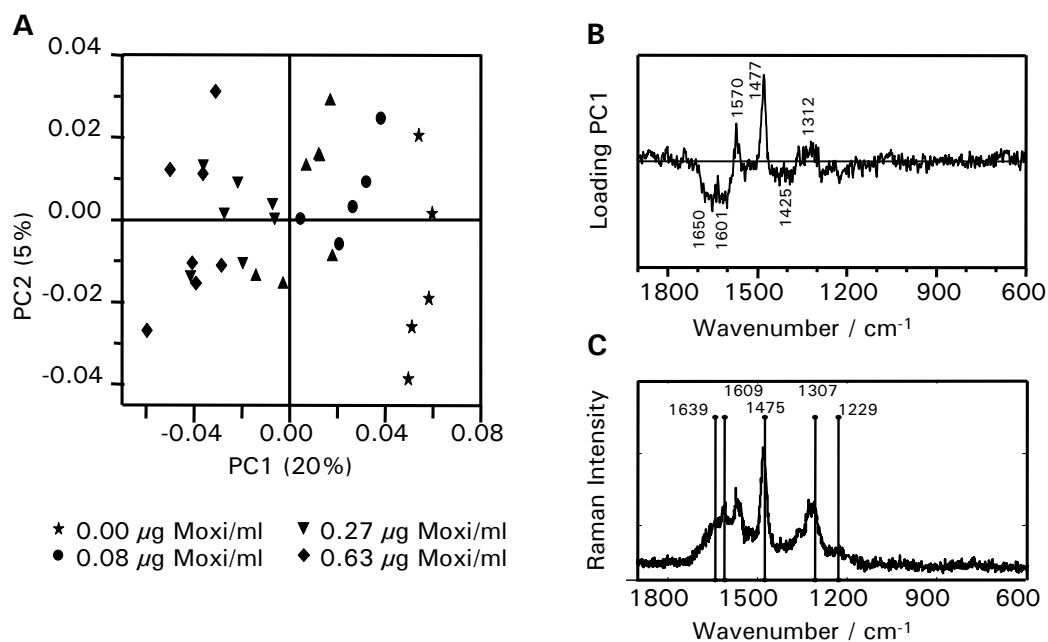


**Figure 9.7:** **A)** Scores plot of the first two principal components (PCs) of the UV-resonance Raman spectra with excitation at 244 nm of *S. epidermidis* with different drug concentrations recorded 80 minutes after drug addition. **B)** Loading Plot for the first principal component (from A). **C)** Important wavenumbers determined by variable selection (REM-TS and LDA) plotted into a UV-resonance Raman spectrum of *S. epidermidis* grown in the presence of 0.08 µg/ml moxifloxacin, recorded 80 minutes after drug addition.

1609  $\text{cm}^{-1}$  and 1229  $\text{cm}^{-1}$  were selected most often during the search procedure with an occurrence of  $> 80$  out of the 100 runs with different splits into training set and test set. Moreover, the spectral regions at 1639  $\text{cm}^{-1}$ , 1475  $\text{cm}^{-1}$  and 1307  $\text{cm}^{-1}$  were selected more than 30 times out of the 100 runs (figure 9.7C). A combination of the five strongest regions of wavenumbers with an occurrence of more than 30 times out of the 100 runs achieved a recognition rate of 74% by LMO-CV and LDA (internal predictivity). By major voting 69% of the spectra were classified correctly (external predictivity). This relative low internal predictivity is in line with the mixed clusters in the HCA and PCA. Nevertheless, the selection of the relevant wavenumbers is quite clear and supports the proposed mechanism by putting special focus on the DNA (especially adenine and guanine) and protein moieties (especially amide I and the aromatic amino acids tryptophan and tyrosine). It should be noted that the binding of the DNA double strand to the gyrase occurs via an ester linkage to tyrosine Tyr122 of the enzyme (see also section 8.1.2). The presence of different moxifloxacin concentrations within the bacterial cells does not seem to influence the classification since the wavenumbers of the two strongest vibrational bands of the resonance Raman spectrum

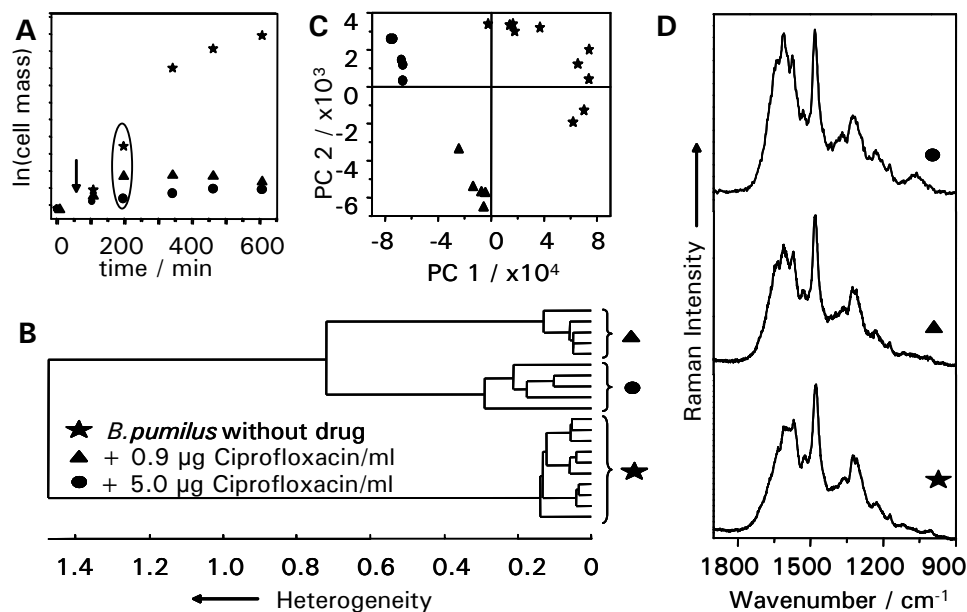


**Figure 9.8:** **A**) Growth curve of *B. pumilus* without (★) and with 0.9 µg (▲) and 5.0 µg (●) ciprofloxacin/ml. The arrow marks the time after inoculation (60 min) when the drug was added. **B**) Hierarchical cluster analysis (HCA) of the spectra of the bacteria after 190 min growth time, marked in A with an ellipse **C**) 2D plot of the scores of the principle component analysis (PCA) of the bacterial spectra after 190 min of growth time. **D**) UV-resonance Raman spectra ( $\lambda_{ex}= 244$  nm) of *B. pumilus* used for the shown chemometrical analysis.

of moxifloxacin ( $1619\text{ cm}^{-1}$  and  $1548\text{ cm}^{-1}$ ) have neither been selected by REM-TS/LDA nor showed markedly contributions to the loadings of PC1 from the PCA.

### 9.3 Effect of ciprofloxacin on *Bacillus pumilus*

In analogy to the experiments with moxifloxacin and *S. epidermidis*, the influence of another fluoroquinolone drug (ciprofloxacin) on another Gram-positive bacterium *Bacillus pumilus* is investigated by means of UV-resonance Raman spectroscopy in this section.

In order to observe the largest effects the drug ciprofloxacin is added to a batch culture of *Bacillus pumilus* DSM 361 at the beginning of the exponential growth phase when the cells are most susceptible to changes in the environment. Two different ciprofloxacin concentrations are added ca. 60 min after inoculation. The growth curves of the bacteria with and without addition of the drug are shown in figure 9.8A, the arrow indicates the time when the drug was added. Without



any drug (★) the batch culture follows the typical growth curve of an unperturbed cell culture (for a detailed discussion of the growth phases see section 4.3) with the cell mass increasing exponentially in the logarithmic growth phase. In the presence of the drug the bacterial growth is inhibited. The effect is more pronounced at the higher ciprofloxacin concentration (5.0 µg/ml, ●) than with a concentration of only 0.9 µg/ml of ciprofloxacin (▲) which is just above the minimal inhibition concentration (MIC). Raman spectra were taken after different growth times and unsupervised multivariate statistical analysis was carried out to visualize the spectral differences. As an example, the UV-resonance Raman spectra of *Bacillus pumilus* with three different ciprofloxacin concentrations after a growth time of 190 min, which is 130 min after the addition of the drug, are shown in figure 9.8D. Spectral changes are visible especially in the wavenumber regions around 1620 and 1480 cm<sup>-1</sup>. To confirm this observation, statistical data analysis was carried out. Figure 9.8B shows the dendrogram generated by a hierarchical cluster analysis (HCA) of these Raman spectra. The spectra of *B. pumilus* with and without drug are well separated into two clusters with a relatively large spectral distance, while the two different drug concentrations also form two well separated sub-clusters within the cluster of the spectra with drug. Within the clusters the heterogeneity is much smaller than between different clusters and these spectral distances within one cluster are caused by inhomogeneities of the sample (bulk measurement). By calculating the B/W ratio (see section 3.4) the wavenumbers having the most significant discriminative power were determined to be 1607 cm<sup>-1</sup>, 1606 cm<sup>-1</sup>, 1477 cm<sup>-1</sup> and 1476 cm<sup>-1</sup> (B/W ratio > 40). These wavenumbers have also been selected by REM-TS from the UV-resonance Raman spectra of *S. epidermidis* under the influence of different moxifloxacin concentrations (see table 9.2 last 3 columns). The increased relative band intensity of the Raman band at 1607 cm<sup>-1</sup> in the spectra of bacteria with addition of drug can tentatively be assigned to the CC-stretching vibration of the drug ciprofloxacin itself (1617 cm<sup>-1</sup> see chapter 6), which is accumulated within the cell. The spectral changes observed around 1480 cm<sup>-1</sup> are due to changes at the DNA within the bacteria caused by the drug. Principle component analysis (PCA) was performed for the same data set as for the cluster analysis. The first principle component (PC) describes already 99% of the data set, the following four PCs also contain valuable information about the data set, even though only to a vanishing amount as can be seen from the loading (not shown). Figure 9.8C shows a two-dimensional scores plot in which the second PC is plotted against the first PC. The individual concentrations form separated clusters with increasing drug concentration along the negative PC1-axis.

## 9.4 Summary and Conclusion

IR absorption, micro-Raman and UV-resonance Raman spectra were recorded to monitor the effect of the gyrase-inhibitors moxifloxacin and ciprofloxacin on *Staphylococcus epidermidis* and *Bacillus pumilus*, respectively. With the help of multivariate statistical methods it was possible to distinguish between bacterial cells that grew under unperturbed conditions and those cells that

## 9 Influence of fluoroquinolone drugs on bacterial growth

were exposed to different concentrations of the antibiotics. It was even possible to classify the bacterial spectra according to the added drug concentrations. In the experiments with moxifloxacin and *S. epidermidis* the two highest drug concentrations (0.27 µg/ml and 0.63 µg/ml) could hardly be distinguished and their spectra mix in the statistical analysis. This suggests that the same biological processes occur within the cell upon drug addition when the drug concentration is well above the MIC. This assumption is in agreement with the very similar biomass concentrations of the bacterial suspensions of those two antibiotic concentrations at the sampling time as can be seen in the growth curve (figure 9.1). The wavenumbers that are responsible for the classification of the spectra could be determined by the data-driven selection procedure of reverse elimination tabu search coupled to Fisher's discriminant analysis (REM-TS/LDA) for the *S. epidermidis* - moxifloxacin data set and from the B/W ratio for the *B. pumilus* - ciprofloxacin data set. Furthermore, it was possible to find a correlation between the first principal component and the drug concentration in the bacterial suspension when using principal component analysis to identify the wavenumbers that experience the largest variations upon drug addition. Even though, the different spectroscopic techniques focus on different aspects of the cells, they all agree that the drug causes changes within the cell being mainly associated with changes in the DNA and protein moieties (table 9.2). The two different fluoroquinolone drugs moxifloxacin and ciprofloxacin cause similar spectral changes in the UV-resonance Raman spectra of the affected bacteria. This supports the proposed mechanism of the action of the drugs of the fluoroquinolone type: they attack the gyrase-DNA complex which causes subsequent reactions that affect the DNA and protein structure.

This chapter clearly demonstrates that vibrational spectroscopy, namely IR absorption, micro-Raman spectroscopy with excitation in the visible, as well as UV-resonance Raman spectroscopy can be used in combination with advanced statistical data analysis to study the influence of drugs on microorganisms. Furthermore, resonance Raman spectroscopy allows the selective enhancement of the Raman signals of certain chromophoric segments within the bacterial cell. Valuable information corresponding to the molecular interactions of the drug and its following metabolic changes can be extracted from the multidimensional spectra by means of multivariate statistical methods. These techniques bear high potential for the characterization of the mode of action of various drugs in a fast and reliable manner, and therefore could assist on the way to develop new and powerful drugs.

# 10 Summary and Outlook

## Summary

In this work it was shown how vibrational spectroscopy can be applied to fully characterize bacteria. This was done exemplarily for *S. epidermidis* in great detail and for *B. pumilus* in a basic approach utilizing the different vibrational spectroscopic methods such as IR absorption, micro-Raman, UV-resonance Raman and tip-enhanced Raman spectroscopy. The scheme in figure 10.1 summarizes the different techniques used in this work and how they contribute to a deepened insight and increased knowledge about special phenotypic characteristics and the chemical composition of bacteria, the bacterial metabolism and the interaction with its environment, including the influence of antibiotics.

IR absorption spectroscopy reveals the overall chemical composition of the bacteria, with special focus on the protein components (especially due to intense peptide bond vibrations). It was

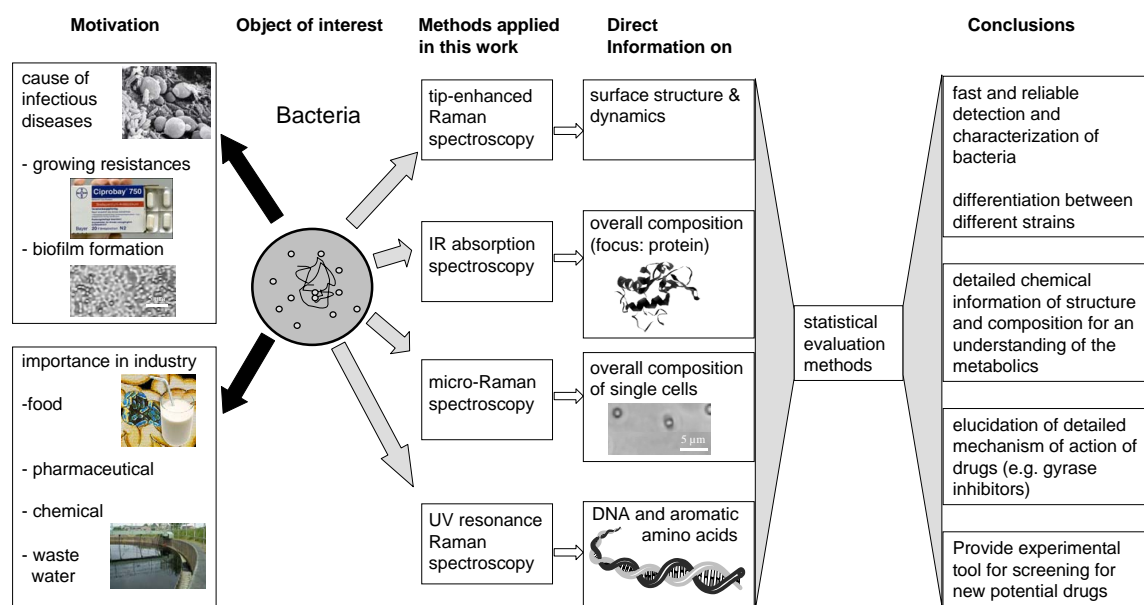


**Figure 10.1:** Characterization of bacteria by means of different vibrational spectroscopic techniques.

## 10 Summary and Outlook

found that during the exponential growth phase the protein content within the bacterial cells is increasing due to an augmented synthesis of ribosomes for the translation and later due to an augmented synthesis of enzymes and other functional proteins. In the stationary phase the total amount of proteins reaches a relative constant level, even though the type of proteins might vary according to the special function of the cell. This is reflected by a relative increase of the amide I band within the bacterial spectrum during the exponential growth phase and a constant amide band intensity in the stationary phase. IR absorption spectroscopy is also suited to monitor RNA and DNA backbone vibrations via the prominent P=O vibrations. A decrease of the relative intensity of these vibrations during the logarithmic growth phase points out an increased RNA content at the beginning of the exponential growth phase. This is produced during the lag phase and necessary for a quick and efficient translation prior to cell division. These characteristic metabolic activities are reflected in the chemical composition of the bacteria and allow a classification of the bacterial spectra according to the growth phase.

These findings were supported by micro-Raman spectroscopy, where also the overall chemical composition of the bacterial cells is probed. Furthermore, with micro-Raman spectroscopy it was also possible to investigate bacteria at the single cell level. This introduced a slightly increased variability between the individual spectra of the bacterial cells in the logarithmic growth phase, because the cell culture was not synchronous, i.e. some cells were dividing while others had just finished this process and were preparing for the next dividing process.

Deep UV-resonance Raman spectroscopy with excitation at 244 nm proved to be especially suited to monitor the vibrational modes of the nucleic acid bases and the aromatic amino acids. Clearly the effect of a high nucleic acid content (especially RNA) at the beginning of the exponential growth phase and the increased relative protein content in the stationary phase were observed as was already deduced from the IR absorption spectra.

Even though the vibrational spectra of different bacteria from different strains often look very similar by eye, they contain characteristic information that allow the differentiation and classification of bacteria with the help of multivariate statistical analysis methods.

Using tip-enhanced Raman spectroscopy (TERS) detailed information from the bacterial surface are assessable. With a high spatial resolution below the diffraction limit ( $<50$  nm) rich chemical information about the chemical composition and the dynamics taking place on the outermost bacterial surface can be gained. It was found that protein and sugar moieties dominate the bacterial surface of the Gram-positive bacterium *S. epidermidis*. In a variety of TERS spectra the spectral signature of N-acetylglucosamine (NAG) was recognized. NAG is known to be a major building block of the cell wall, the extracellular teichoic acids and the polysaccharide intercellular adhesin (PIA) which is supposed to be responsible for biofilm formation of *S. epidermidis*. Using silver-coated tips and an excitation wavelength of 568 nm enhancement factors up to  $10^6$ - $10^8$  compared to normal Raman spectroscopy have been achieved which allows integration times as short as 1s. At this time scale fluctuations within the TERS spectra recorded on one spot of the bacterial surface have been detected and it is very likely that a glimpse of the molecular motions on the

bacterial surface is caught. Since only small volume elements (ca.  $50 \times 50 \times 10 \text{ nm}^3$ ) experience the strong (oriented) field enhancement, already a change of orientation of the probed molecule effects the TERS spectrum. This quite new approach of investigating complex biological surfaces, such as bacterial cells, opens new ways for a direct investigation of surface processes as bacterial adhesion, biofilm formation or bacterial communication, which are all of utmost interest and also not completely understood. It is also imaginable to use the TERS technique for the study of the mode of action of cell wall attacking drugs such as vancomycin.

Within the frame of this work the focus was set on a different type of antibiotics: the gyrase inhibitors of the fluoroquinolone type. Several structural variations of the drugs have been characterized by IR absorption, micro-Raman, UV-resonance Raman and surface-enhanced Raman spectroscopy. The spectra revealed the similarities in the framework of the quinolone drugs, but also the special structural characteristics of each drug. The band assignment was assisted by DFT calculations. Vibrational spectroscopy proved to be capable to detect small changes in the chemical environments of the drugs in *in vitro* experiments, such as hydrogen bonding interactions. Furthermore, the carbonyl group in 3 position on the quinolone skeleton was shown to be essential for the *in-vivo* action of the drug. The different substituents on the quinolone skeleton caused a changed activity against different bacterial strains as was determining by antibiotic susceptibility tests.

The biological target of the fluoroquinolone drugs is the gyrase-DNA complex. The antibiotics interfere with the introduction of negative supercoils into the DNA by the enzyme gyrase which finally causes cell death. To perform *in vitro* experiments DNA and the enzyme gyrase have been extracted from bacteria. When using resonance Raman spectroscopy with excitation in the UV (244 and 257 nm) aqueous solution at biological low concentrations of DNA and gyrase could be investigated. The spectra contained the vibrational bands of aromatic amino acids and the nucleic acid bases. In the UV-resonance Raman spectra of plasmid DNA characteristic marker bands of the DNA tertiary structure could be identified that allow a distinction of the DNA before and after the action of the gyrase (relaxed and supercoiled form). In the presence of the DNA-binding subunit GyrA of the enzyme gyrase relaxed DNA could be converted into supercoiled DNA, however, in the absence of GyrB and ATP the process stopped in a stage where the DNA is still bound to the enzyme. Already supercoiled DNA could also bind to the GyrA-subunit of the enzyme, but no further increase in superhelicity could be detected.

The detailed knowledge about the bacterial composition and growth phenomena gained earlier in this work was used when analyzing the metabolic changes within bacterial cells caused by the action of the fluoroquinolone drugs added at varying concentrations. The pronounced effects on living bacterial cells was observed when the drug was added to the bacterial culture in the beginning of the exponential growth phase. The antibiotics caused a reduced growth and high enough drug concentrations (above the MIC (minimal inhibition concentration)) completely killed the cells. Multivariate statistical analysis methods (PCA and REM-TS with LDA) helped to identify the vibrational bands that are most affected by the action of the drug. In agreement with

the proposed mechanism of action of the fluoroquinolones vibrational bands involving protein and DNA moieties showed the highest discriminative power when comparing the IR absorption, micro-Raman and also the UV-resonance Raman spectra of untreated bacteria and bacteria under the influence of drug. At drug concentrations around the MIC the bacterial spectra can be classified according to the added drug concentration. If the antibiotic concentration is well above the MIC no distinction between the bacterial spectra of different drug concentration is possible, indicating that the same biological processes occur and the maximum effect of the drug is reached.

The experiments performed in this work showed how different vibrational spectroscopic techniques (IR absorption, micro-Raman, UV-resonance Raman spectroscopy) can be used in combination with multivariate statistical analysis methods to characterize and classify bacteria and to gain insights into their metabolism during unperturbed growth and under the influence of drugs. The results encourage the continuation of the research in this field and some possible future experiments will be presented in the next paragraph.

### **Outlook: Further experiments**

The results presented in this work give an insight into the bacterial metabolism during bacterial growth and analyze drug-target interactions involving gyrase inhibitors of the fluoroquinolone type. The experiments could reproduce the information that were gained previously by tedious and time consuming biological experiments and therefore established vibrational spectroscopy as useful methods in the search for new and effective antibiotics.

It was shown that the effect of drugs can be detected via vibrational spectroscopy (IR absorption, Raman spectroscopy and UV-resonance Raman spectroscopy). This was shown for three different fluoroquinolones at different concentrations around and above the MIC. In future experiments also concentrations well below the MIC should be incorporated to detect early stage effects that are very specific to that special drug and that arise before population effects (i.e. a reduction in cell growth) can be detected.

Further insights into the mode of action of the gyrase inhibitors of the fluoroquinolone type can be gained when continuing the *in vitro*-experiments started in this work. A concentration series with different mixing ratios of GyrA and plasmid DNA could provide further insights into the binding and supercoiling mechanism. In order to find out more about the mechanism of action on a molecular level of the fluoroquinolones, the drug should be added to the binary mixture GyrA and pBR322 in varying concentrations. It is known that the fluoroquinolone drugs interfere with the supercoiling process close to the GyrA59 binding region. This should be detectable in the vibrational spectra. In the absence of GyrB and ATP the supercoiling reaction stops after the second stage (recall from section 8.1) which provides an unique opportunity to investigate the individual reactions in a stepwise manner. Later on, the experiment could be repeated in the presence of GyrB and ATP in order to show whether further interference is caused by the drug

(e.g. when adding GyrB, ATP and the drug successively and in different order to the mixture of GyrA and relaxed DNA).

So far, the enzymes gyrase was only extracted from *E. coli*. However, the extraction protocol could be used to extract the enzyme also from different bacteria, including those that developed resistances against the fluoroquinolone drugs. Gyrase from *Streptomyces noursei*, for example, exhibits 10fold more resistance to quinolones than the enzyme from *E. coli* [248]. Those experiments could help to identify whether the resistance is due pharmacokinetic processes or due to changes in the enzyme.

Furthermore, the drug-target research by means of vibrational spectroscopic techniques could be extended to other types of drugs following a different mode of of action, e.g. to those that inhibit the protein synthesis. Comparing those results to the results obtained with the gyrase inhibitors should allow a separation of the characteristic wavenumbers (vibrational bands) associated specifically with the action of the drug and those which indicate the following cell death.

Great potential for further experiment is offered also by tip-enhanced Raman spectroscopy. The non-invasive characterization of the bacterial surfaces with a high spatial resolution opens the way for a direct and in-vivo investigation of the chemical composition and spatial arrangement of the bacterial surface. This should provide useful information towards the understanding of bacterial "communication", biofilm formation or bacterial adhesion. Of utmost interest are also the investigation of the mode of action of cell wall synthesis inhibition drugs such as vancomycin on a molecular level.





# 11 Zusammenfassung und Ausblick

## Zusammenfassung

In dieser Arbeit wurde gezeigt, wie die Schwingungsspektroskopie mit all ihren Unterarten zur umfassenden Charakterisierung von Bakterien verwendet werden kann. Beispielhaft wurden für *Staphylococcus epidermidis* und zum Teil für *Bacillus pumilus* IR-Absorptionsspektren, Raman-Spektren, Resonanz-Raman-Spektren und spitzenverstärkte Raman-Spektren aufgenommen, um einen tieferen Einblick in die phenotypischen Merkmale und die chemische Zusammensetzung der Bakterien zu erlangen, sowie umfassendere Kenntnisse über den Bakterienstoffwechsel und die Wechselwirkung der Bakterien mit ihrer Umgebung, einschließlich der Wirkung von Antibiotika, zu gewinnen. Spezielles Augenmerk lag dabei auf den Gyrasehemmstoffen aus der Gruppe der Fluorochinolone. Die Wirkstoffe und die extrahierten biologischen Zielstrukturen DNA und Gyrase wurden in *in-vitro*-Experimenten charakterisiert, und die so identifizierten Markerbanden halfen bei der Interpretation der *in-vivo*-Experimente mit Bakterien und Antibiotika. Das Schema in Abbildung 11.1 fasst die verschiedenen angewandten spektroskopischen Techniken und die spezifischen Informationen, die durch diese zugänglich sind, zusammen.

Mit Hilfe der IR-Absorptionsspektroskopie können Informationen über die chemische Zusammensetzung der Bakterien gewonnen werden. Spezieller Fokus liegt dabei auf den Proteinkomponenten, da die Peptidschwingungen mit intensiven Schwingungsbanden im Spektrum vertreten sind. Es wurde herausgefunden, dass während der exponentiellen Phase des Bakterienwachstums der relative Proteingehalt innerhalb der Bakterien leicht ansteigt. Dies ist zunächst auf eine erhöhte Synthese von Ribosomen für die Translation und später auf eine verstärkte Synthese von Enzymen und anderen funktionalen Proteinen zurückzuführen. In der stationären Phase des Bakterienwachstums erreicht der Proteingehalt ein konstantes Level, das von wechselnden Proteinen aufrecht erhalten wird. Im IR-Absorptionsspektrum der Bakterien zeigen sich diese Veränderungen in einem Anstieg der relativen Intensität der Amid I-Bande während der exponentiellen Wachstumsphase und einer konstanten Intensität in der stationären Phase.

Intensive IR-Banden resultieren auch von der P=O-Schwingung im Rückgrat der Nukleinsäuren. IR-Absorptionsspektroskopie ist daher auch gut geeignet, um Veränderungen der RNA und DNA zu verfolgen. Während des Bakterienwachstums (exponentielle Phase) wurde eine Abnahme dieser Bande und damit des Nukleinsäuregehaltes beobachtet. Das Maximum des RNA-Gehalts zu Beginn der exponentiellen Wachstumsphase wird durch eine verstärkte Transkription in der Lag-Phase erzeugt und ist für eine schnelle und effiziente Translation vor der Zellteilung nötig. Diese

## 11 Zusammenfassung und Ausblick

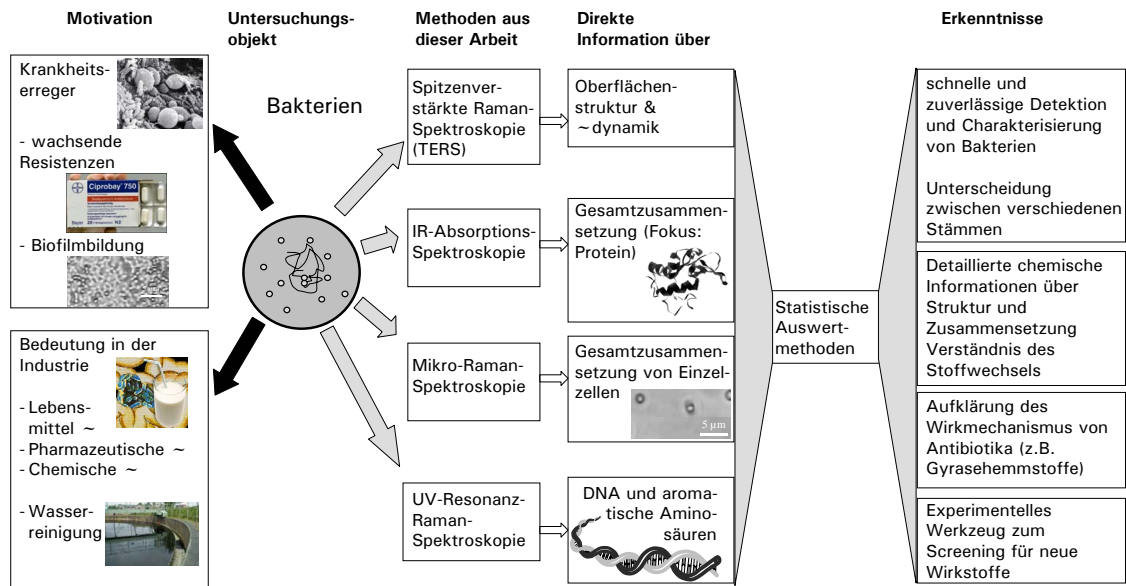


**Abbildung 11.1:** Charakterisierung von Bakterien mit Hilfe verschiedener schwingungsspektroskopischer Methoden.

Stoffwechselaktivitäten ändern die chemische Zusammensetzung der Bakterienzelle, was sich in den Spektren niederschlägt und eine Klassifizierung der Spektren anhand ihrer Wachstumsphasen ermöglicht.

Ähnliche Ergebnisse wurden mittels der Raman-Spektroskopie erhalten. Bei Verwendung der Mikro-Raman-Spektroskopie ist es zudem möglich einzelne Bakterienzellen zu untersuchen. Zeit- und arbeitsaufwendige Kultivierungsschritte sind nicht nötig, um Informationen über die allgemeine chemische Zusammensetzung der Bakterien zu gewinnen. Es wurde jedoch eine erhöhte Variabilität zwischen den Einzelspektren der Bakterien in der exponentiellen Wachstumsphase beobachtet. Dies kann mit der Nicht-Synchronität der Bakterienkultur erklärt werden, d.h. während sich einzelne Zelle gerade teilen, befinden sich andere Zellen gerade im Größenwachstum zwischen zwei Teilungsschritten.

Mit Hilfe der UV-Resonanz-Raman-Spektroskopie mit Anregung im Tief-UV bei 244 nm werden fast ausschließlich die Schwingungsmoden der Nukleinsäurebasen und der aromatischen Aminosäuren verstärkt. In den wachstumsphasenabhängigen Bakterienspektren wird deutlich ein erhöhter Nukleinsäure-Gehalt (RNA) zu Beginn der exponentiellen Wachstumsphase, sowie ein steigender und schließlich konstanter Proteingehalt wiedergegeben. Dies ist in guter Übereinstimmung mit den Ergebnissen, die aus den IR-Absorptionsspektren gewonnen wurden.

Obwohl die Schwingungsspektren von verschiedenen Bakterienstämmen zunächst auf den ersten Blick sehr ähnlich erscheinen, so enthalten sie doch charakteristische Informationen, die eine Klassifizierung mit Hilfe multivariater statistischer Analysemethoden, wie z. B. der hierarchi-

schen Clusteranalyse (HCA), der Hauptkomponentenanalyse (PCA) oder REM-TS (engl. *reverse elimination tabu-search*) in Kombination mit linearer Diskriminanzanalyse ermöglichen.

Ein neuer Ansatz, der in dieser Arbeit verfolgt wurde, ist die Untersuchung der Oberfläche von Bakterien mit Hilfe der spitzenverstärkten Raman-Spektroskopie (TERS, engl. *tip-enhanced Raman spectroscopy*). Detaillierte Informationen über die äußerste Bakterienoberfläche sind notwendig, um wichtige biologische Prozesse, wie die Zellanhaftung an Oberflächen, die Biofilmbildung, oder auch die Wirkungsweise von zellwandangreifenden Antibiotika auf molekularer Ebene zu verstehen. Mit TERS können reichhaltige chemische Informationen aus Schwingungsspektren mit einer Ortsauflösung im Nanometerbereich (ca. 50 nm) erhalten werden. Es wurde gefunden, dass die Zelloberfläche des Gram-positiven Bakteriums *S. epidermidis* von Protein- und Zuckerstrukturen dominiert wird. Sehr häufig war in den TERS-Spektren die Schwingungsstruktur des N-Acetylglucosamins (NAG) enthalten. NAG ist ein wichtiger Baustein der Zellwand, der extrazellulären Teichonsäuren, sowie des Polysaccharids PIA (engl. *polysaccharide intercellular adhesin*), das zu einem entscheidenden Teil an der Biofilmbildung beteiligt sein soll. Mit silberbeschichteten Spitzen und einer Anregungswellenlänge von 568 nm wurden Verstärkungsfaktoren von  $10^6$ - $10^8$  im Vergleich zur normalen Raman-Streuung beobachtet. Dies gestattet kurze Integrationszeiten von nur 1 s. Auf dieser Zeitskala wurden Fluktuationen des TERS-Signals in einem Punkt auf der Bakterienoberfläche beobachtet und es scheint sehr wahrscheinlich, dass diese Fluktuationen die Moleküldynamik auf der Bakterienoberfläche widerspiegeln. Da mit Hilfe der spitzenverstärkten Raman-Spektroskopie nur ein kleines Volumenelement (ca.  $50 \times 50 \times 10 \text{ nm}^3$ ) auf der Bakterienoberfläche das verstärkte (evaneszente) elektromagnetische Feld verspürt, bewirkt schon eine Änderung der Orientierung der Moleküle auf der Zelle eine Änderung im Spektrum. Dieser neuartige Ansatz zur Untersuchung komplexer biologischer Oberflächen eröffnet eine Vielzahl von Möglichkeiten zur direkten Untersuchung von biologischen Prozessen, die bis heute noch nicht vollständig verstanden sind (z. B. Bakterienkommunikation, Biofilmbildung). Des Weiteren sind auch zahlreiche Anwendungen in der Wirkstoffforschung zur Aufklärung von Wirkmechanismen von Zellwand-angreifenden Antibiotika, wie z. B. Vancomycin oder auch bei der Suche von neuartigen Wirkstoffen denkbar.

Im Rahmen dieser Arbeit lag der Fokus auf einer anderen Wirkstoffklasse, auf den Gyrasehemmstoffen aus der Gruppe der Fluorochinolone. Verschiedene Vertreter mit modifizierter chemischer Struktur wurden mit Hilfe der IR-Absorptions-, Mikro-Raman-, UV-Resonanz-Raman- sowie der oberflächenverstärkten Raman-Spektroskopie (SERS, engl. *surface enhance Raman spectroscopy*) untersucht. Die Spektren spiegelten die Ähnlichkeiten im Grundgerüst, aber auch die strukturellen Eigenheiten wider. Eine detaillierte Zuordnung der einzelnen Schwingungsbanden wurde durch DFT-Rechnungen (engl. *density functional theory*) unterstützt. Mit Hilfe der Schwingungsspektroskopie war es möglich, kleine Änderungen in der chemischen Umgebung der Wirkstoffe, wie z. B. veränderte Wasserstoffbrückenbindungen, in *In-vitro*-Experimenten nachzuweisen. Außerdem wurde in *In-vivo*-Experimenten mit Bakterien nachgewiesen, dass die Carbonylgruppe in 3-Stellung am Chinolonring (benachbart zur Ketogruppe) essentiell für die Wirk-

## 11 Zusammenfassung und Ausblick

samkeit der Gyrasehemmstoffe ist. Die verschiedenen Substituenten am Chinolongrundgerüst bewirken eine Modifizierung der Aktivität gegenüber verschiedenen Bakterienstämmen.

Die biologische Zielstruktur der Fluorochinolone ist der Gyrase-DNA-Komplex innerhalb der Bakterie. Das Antibiotikum stört die Funktion des Enzyms Gyrase und verhindert damit die Einführung von negativen Verdrillungen in die Bakterien-DNA, was schließlich zum Zelltod führt. Für *In-vitro*-Experimente wurden DNA und Enzym aus den Bakterien extrahiert. Vorversuche mit den DNA- und Proteinbausteinen, den Nukleinsäurebasen und den Aminosäuren, bildeten die Grundlage für die Zuordnung der Schwingungsbanden der polymeren Strukturen. Die wässrigen Lösungen der beiden Zielstrukturen wurden in biologisch niedrigen Konzentrationen mit Hilfe der Resonanz-Raman-Spektroskopie mit Anregung im Tief-UV (244 und 257 nm) untersucht. Bei diesen Anregungswellenlängen dominieren die Schwingungsbanden der Nukleinsäurebasen bzw. der aromatischen Aminosäuren die Raman-Spektren. Im UV-Resonanz-Raman-Spektrum der DNA konnten Markerbanden für die beiden verschiedenen Tertiärstrukturen „entspannt“ und „superhelikal“ identifiziert werden, die vor und nach dem Einfluss der Gyrase vorliegen. Durch Zusatz von GyrA, der DNA-bindenden Untereinheit der Gyrase, kann entspannte DNA in den superhelikalen Zustand überführt werden. Jedoch erfolgt die Änderung des Topologiezustandes der DNA in Abwesenheit der GyrB-Untereinheit und von ATP nicht vollständig, sondern stoppt in einem Zwischenstadium, in dem die DNA noch an das Enzym gebunden ist. Superhelikale DNA kann ebenfalls an die GyrA-Untereinheit des Enzyms binden, jedoch findet keine weitere Erhöhung der Superhelizität statt.

Diese Vorexperimente und die Kenntnisse über die Zusammensetzung und das Wachstumsverhalten der Bakterien wurden bei der Analyse der *In-vivo*-Experimente genutzt, bei denen der Einfluss der Fluorochinolone in verschiedenen Konzentrationen auf das Bakterienwachstum untersucht wurde. Den größten Einfluss auf das Wachstum hat das Antibiotikum, wenn es zu Beginn der exponentiellen Phase zur Bakterienkultur gegeben wird. Es bewirkt eine Reduzierung des Bakterienwachstums und Konzentrationen oberhalb der minimalen Hemmkonzentration (MHK) verursachen vollständigen Zelltod. Mit Hilfe von statischen Analysemethoden (HCA, PCA) können die Bakterienspektren entsprechend der zugesetzten Antibiotikakonzentration klassifiziert werden. Dies ist jedoch nur bei Wirkstoffkonzentrationen um die MHK möglich; bei Konzentrationen weit über der MHK tritt eine Sättigung im erreichbaren Effekt auf, die keine weitere Unterscheidung der Bakterienspektren mit Antibiotikum ermöglicht. Multivariate statistische Auswertemethoden (PCA, REM-TS) dienen außerdem zur Identifizierung der Schwingungsbanden in den komplexen Bakterienspektren, die unter dem Einfluss des Fluorochinolons eine Veränderung erfahren. Sowohl in den IR-Absorptions-, den Mikro-Raman- als auch in den UV-Resonanz-Raman-Spektren sind Schwingungsmoden von Protein- und DNA-Bausteinen für eine Klassifizierung der Bakterienspektren (unbehandelte Bakterien vs. Bakterien unter dem Einfluss verschiedener Antibiotikakonzentrationen) verantwortlich. Ein solches Verhalten wird auch aus dem angenommenen Wirkmechanismus (Angriff des Gyrase-DNA-Komplexes) der Fluorochinolone erwartet.

Die Ergebnisse dieser Arbeit zeigen, wie verschiedene schwingungsspektroskopische Techniken in Verbindung mit multivariaten statistischen Analysemethoden zur Charakterisierung und Klassifizierung von Bakterien verwendet werden können. Des Weiteren konnte ein Einblick in die Stoffwechselfvorgänge während des ungestörten Bakterienwachstums sowie unter dem Einfluss von Antibiotika gewonnen werden. Die Ergebnisse eröffnen zahlreiche weiterführende Experimente und einige davon sollen im nächsten Abschnitt vorgestellt werden.

## Ausblick

Die Ergebnisse dieser Arbeit geben einen Einblick in den Bakterienstoffwechsel und analysieren die Wirkstoff-Zielstruktur-Wechselwirkungen der Gyrasehemmstoffe aus der Gruppe der Fluorochinolonklasse mit ihren biologischen Targets. Die Schwingungsspektroskopie ermöglicht es, innerhalb relativ kurzer Mess- und Präparationszeiten Ergebnisse zu gewinnen, die sonst nur in zeit- und arbeitsaufwendigen (biologischen) Experimenten zugänglich sind. Dies macht die Schwingungsspektroskopie zu einer geeigneten Methode für die Beantwortung zahlreicher biologischer und biomedizinischer Fragestellungen, u. a. bei der Suche nach neuen und effektiven Wirkstoffen.

Der Einfluss von drei verschiedenen Fluorochinolonen in verschiedenen Konzentrationen auf das Bakterienwachstum konnte mit Hilfe der Schwingungsspektroskopie nachgewiesen und analysiert werden. In dieser Arbeit wurden hauptsächlich Antibiotikakonzentrationen um und oberhalb der MHK angewendet. In zukünftigen Experimenten sollten auch Konzentrationen weit unterhalb der MHK angewendet werden, um frühzeitige Effekte, die spezifisch für das verwendete Antibiotikum sind und vor äußerlich sichtbaren Populationseffekten (z. B. Reduzierung des Bakterienwachstums und Absterben der Kultur) auftreten, zu detektieren.

Weitere detaillierte Einblicke in den Wirkmechanismus der Fluorochinolone auf molekularer Ebene können in einer Fortsetzung der *in-vitro*-Experimente mit extrahierter Gyrase, DNA und Wirkstoff gewonnen werden. Werden nur GyrA und DNA verwendet, und keine GyrB und ATP zugesetzt, so stoppt der Verdrillungsprozess der DNA auf der 2. Stufe (siehe Abschnitt 8.1). Dies eröffnet die Möglichkeit den Hemmprozess durch die Fluorochinolone in verschiedenen Etappen zu untersuchen, zunächst in Konzentrationsserien mit ausschließlich GyrA und relaxierter DNA, und später mit GyrA, DNA, GyrB und ATP.

In den bisherigen Experimenten wurde die Gyrase ausschließlich aus *E. coli* gewonnen. Das Extraktionsprotokoll kann jedoch auch auf andere Bakterien übertragen werden, einschließlich derer die eine Resistenz gegenüber einzelnen Fluorochinolonen entwickelt haben (bei Gram-positiven Bakterien müsste evtl. der Lysis-Schritt zu Beginn des Extraktionsprozesses ausgeweitet werden, um die stabilere Zellwand vollständig zu zerstören). Solche Experimente könnten bei der Feststellung behilflich sein, ob die Resistenzen pharmakokinetisch bedingt sind oder tatsächlich durch Veränderungen am Enzym hervorgerufen werden.

Weiterhin könnte schwingungsspektroskopische Untersuchung von Wirkstoff-Zielstruktur-Wechselwirkungen auch auf andere Antibiotika mit anderen Wirkmechanismen (z. B. Hemmung der

## 11 Zusammenfassung und Ausblick

Proteinsynthese) ausgeweitet werden. Der Vergleich dieser Ergebnisse mit denen von den Gyrasehemmstoffen sollte zusätzliche Informationen liefern, welche Wellenzahlen in den Schwingungsspektren spezifisch für die Wirkungsweise des Antibiotikums sind und welche durch unspezifischere Folgereaktionen bis hin zum Zelltod hervorgerufen werden.

Sehr großes Potential für weiterführende Experimente bietet die spitzenverstärkte Raman-Spektroskopie (TERS). Diese nicht-invasive Charakterisierungsmöglichkeit der Oberfläche von lebenden Zellen mit einer sehr hohen Ortsauflösung unterhalb des Beugungslimits eröffnet den Weg für die direkte *in-vivo*-Untersuchung der chemischen Zusammensetzung sowie der räumlichen Verteilung der einzelnen Komponenten. So können wertvolle Informationen gewonnen werden, die zum Verständnis von Bakterienkommunikation, Biofilmbildung oder Bakterienanhaftung beitragen. Von äußerstem Interesse ist auch die Erforschung von Wirkmechanismen von Antibiotika, die die Zellwandsynthese hemmen, wie z. B. Vancomycin.

# Appendix





# A Chemicals and Media

## A.1 Antibiotics

### A.1.0.1 Gyrase Inhibitors of the Group of the Fluoroquinolones

The quinolones nalidixic acid (NAL), oxolinic acid (OXO), cinoxacin (CIN), flumequine (FLU), norfloxacin (NOR), ciprofloxacin (CIPRO), lomefloxacin (LOM), ofloxacin (OFL) and enoxacin (ENO) were purchased from Sigma and Aldrich. Sarafloxacin (SARA) and Moxifloxacin (MOXI) are kind gifts of the group of Prof. U. Holzgrabe from the university of Würzburg where they have been synthesized. Also 5 different precursor of moxifloxacin have been obtained from the Holzgrabe-group (see figure 6.2 in section 6.2).

The hydrated compounds were prepared by mixing the anhydrous fluoroquinolones (FQ) with water in a ratio of FQ:6H<sub>2</sub>O. A chemical structure of the investigated quinolones is shown in chapter 6.

### A.1.0.2 Glycopeptides

Vancomycin is a kind gift of the group of PD. Dr. Wilma Ziebuhr from the University of Würzburg.

## A.2 Cellular Components

### A.2.1 Nucleic acids

#### A.2.1.1 Nucleic acid bases, nucleosides and nucleotides

The **nucleic acid bases** have been obtained commercially.

nucleotide	company	sum formula	molecular weight in g/mol
adenine (9H-purin-6-amine, 6-aminopurin)	Fluka	$C_5H_5N_5$	135.1
$\beta$ -(-)-adenosine	Aldich	$C_{10}H_{13}N_5O_4$	267.2
adenosine-5'-monophosphate disodium salt	Fluka	$C_{10}H_{12}N_5Na_2O_7P$	391.1
guanine	Fluka	$C_5H_5N_5O$	151.1
guanosine	Sigma	$C_{10}H_{13}N_5O_5$	283.2
guanosine-5'-monophosphate disodium salt	Fluka	$C_{10}H_{12}N_5Na_2O_8P$	407.2
cytosine	Fluka	$C_4H_5N_3O$	111.1

## A Chemicals and Media

cytidine	Aldrich	$C_9H_{13}N_3O_5$	243.2
cytidine-5'-monophosphate	Sigma	$C_9H_{14}N_3O_8P$	323.2
thymine	Sigma	$C_5H_6N_2O_2$	126.1
thymidine	Fluka	$C_{10}H_{14}N_2O_5$	242.2
thymidine-5'-monophosphate disodium salt (hyd)		$C_{10}H_{13}N_2Na_2O_8P \cdot aq$	366.2 aq

The **deoxynucleotides** have been obtained as aqueous solutions from Fermentas GmbH. (pH7, 25 µl of aqueous solution of dATP, dCTP, dGTP and dTTP; 100 mM).

### A.2.1.2 Polynucleotides

The polynucleotides have commercially obtained from Sigma as lyophilized sodium salts:

Poly(deoxyadenylic-thymidylic) acid sodium salt

p(dA-dT)·p(dA-dT), P0883, LOT124K16461

22 A<sub>260</sub> units/mg (one unit will yield an A<sub>260</sub> OF 1.0 in 1 ml of water)

average length 8778 bp

Poly(deoxyguanylic-deoxycytidylic) acid sodium salt

Poly(dG-dC)·Poly(dG-dC), P9389, LOT124K16841

19 A<sub>260</sub> units/mg, length ca. 1014 bp

Polydeoxyguanylic acid ·Polydeoxycytidylic acid sodium salt

Poly(dG)·Poly(dC), P3136, LOT064K14911

14.5 A<sub>260</sub> units/mg, appr. length 7168 bp

Poly(deoxyadenylic-deoxycytidylic) acid·Poly(deoxyguanylic-thymidylic) acid sodium salt

Poly(dA-dC)·Poly(dG-dT) sodium salt, P0307, LOT045K1483

12 A<sub>260</sub> units/mg, MW 2.9·10<sup>6</sup> g/mol.

## A.3 Bacteria

### A.3.1 Bacterial strains

For the spectroscopic investigations following bacterial strains have been used (the location in brackets assigns the source):

<i>Bacillus pumilus</i> DSM 27	(DSMZ, Braunschweig)
<i>Bacillus pumilus</i> DSM 361	(DSMZ, Braunschweig)
<i>Bacillus subtilis</i> DSM 10	(DSMZ, Braunschweig)
<i>Bacillus subtilis</i> DSM 347	(DSMZ, Braunschweig)
<i>Escherichia coli</i> DSM 423	(DSMZ, Braunschweig)
<i>Staphylococcus epidermidis</i> RP62A (ATCC 35984)	(Universität Würzburg)

In addition the following *E. coli* strains have been cultivated for the extraction of plasmid DNA and the enzyme gyrase. The strains were obtained from the Lehrstuhl für Genetik at the Universität Jena.

*Escherichia coli* K12 and *Escherichia coli* JM109 for the extraction of the plasmid pBR322,

*Escherichia coli* DSM 436 for the gyrase extraction,

*Escherichia coli* M15 (pQE30/GyrAliv, pQE30/GyrAnou, pREP4) for the extraction of 6xHis tagged GyrA.

### A.3.2 Media for the bacterial cultivation

**LB** (lysogeny broth, or sometimes called Luria-Bertani medium) is a common used complex medium for the cultivation of bacteria, especially *Escherichia coli*. The recipe was first published by Giuseppe Bertani in 1951.

In 1 L distilled water the following ingredients are dissolved:

10 g tryptone

5 g yeast extract

10 g NaCl

The pH is adjusted with NaOH to pH7, and the medium is autoclaved at 121°C prior to use.

**CASO** tryptic soy broth (casein-peptone soymeal-peptone)

30 g CASO (Merck) in 1 L distilled water, pH 7.3 ± 0.2

**NA** nutrient broth

25 nutrient broth (Merck) in 1 L of distilled water, pH 7.5 ± 0.2

**Agar plates** To prepare agar plates of the respective media 15 g/L agar are added prior to autoclavation. The still hot and liquid medium is poured into petri dishes where it cools and hardens.

## A.4 Buffer

**PBS** (10xbuffer, 0.1M PBS, pH 7.2)

10.9 g Na<sub>2</sub>HPO<sub>4</sub> (water free)

3.2 g Na<sub>2</sub>HPO<sub>4</sub> (water free)

90 g NaCl

fill up to 1000 ml with distilled water

adjust pH.

**TAE** is a buffer solution used in agarose electrophoresis, typically for the separation of nucleic acids such as DNA and RNA. It is made up of Tris-acetate buffer, usually at pH 8.0, and EDTA, which sequesters divalent cations.

**TAE (Beutenberg)** pH 8.5

50 mM Tris

20 mM Na-Acetate

18 mM NaCl

2 mM EDTA

## A Chemicals and Media

**TNE** buffer used in the DNA relaxation  
Tris-HCl  
NaCl  
EDTA

### A.4.1 Buffer for the DNA extraction (pBR322)

The DNA extraction was performed using the Nucleobond AX-Set by Macherey-Nagel. The following buffers were included in this set:

**buffer S1** , pH 8.0:  
50 mM Tris/HCl  
10 mM EDTA  
100 ml RNase, A/ml

**buffer S2** :  
200 mM NaOH  
1% SDS

**buffer S3** :  
2.80 M KAc, pH 5.1

**buffer N1** , pH 6.3:  
100 mM Tris/H<sub>3</sub>PO<sub>4</sub>  
15% EtOH  
400 mM KCl

**buffer N2** , pH 6.3:  
100 mM Tris/H<sub>3</sub>PO<sub>4</sub>  
15% EtOH  
900 mM KCl  
0.15% Triton X-100

**buffer N3** , pH 6.3:  
100 mM Tris/H<sub>3</sub>PO<sub>4</sub>  
15% EtOH  
1150 mM KCl

**buffer N5** , pH 8.5:  
100 mM Tris/H<sub>3</sub>PO<sub>4</sub>  
15% EtOH  
1000 mM KCl

### A.4.2 Buffer for the gyrase extraction

**digestion buffer** , total volume 150 ml:  
15 ml 0.5M potassium phosphate buffer (pH 7.4)  
15 g saccharose  
150 ml 0.1M DTT (0.077 g in 5 ml)  
6.5 ml 2M KCl (Mr 74.56; 7.46 g in 50 ml aq. dest)  
127 ml aqua dest.

**0.5M potassium phosphate buffer pH7.4**

1.141 g  $K_2HPO_4 \cdot 3H_2O$  in 10 ml aq. dest  
0.6805 g  $KH_2PO_4$  in 10 ml distilled water  
start with  $K_2HPO_4 \cdot 3H_2O$ , adjust pH with  $KH_2PO_4$

**10-fold storage buffer :**

500 mM  $KH_2PO_4$  (68.05 g)  
2 mM EDTA (8 ml 0.25M EDTA)  
10 mM DTT (1.54 g)  
adjust pH with KOH to pH 7.5, fill up to 1000 ml

**storage buffer 10% glycerin , pH7.5**

100 ml storage buffer 10fold  
112 ml glycerin  
adjust pH with KOH  
fill up to with 1000 ml with aq. dest.

**storage buffer 50% glycerin pH 7.6**

100 ml storage buffer 10fold  
500 ml glycerin  
adjust pH with KOH  
fill up with aq.dest to 1000ml

**TKK, 10x , pH7.5 (Tris potassium chloride - potassium phosphate)**

400 mM Tris (4.84 g)  
190 mM  $KH_2PO_4$  (2.58 g)  
340 mM KCl (2.53 g)  
100 ml aq.dest. (decoct, or autoclave buffer)  
adjust pH with HCl

**A.4.3 Buffer for the affinity chromatography of GyrA with  $Ni^{2+}$ -NTA agarose**

**lysis buffer (native)**

50 mM  $KH_2PO_4$ , pH 8.0  
300 mM KCl  
10 mM imidazol  
10% glycerin  
1 mg/ml lysozyme

**washing buffer (native)**

as lysis buffer, but with 20 mM imidazol

**elution buffer (native)**

as lysis buffer, but with 250 mM imidazol

0.8

$Ni^{2+}$ -NTA agarose was obtained from QIAGEN and is composed of Ni-nitrolo tri acetic acid (NTA) coupled to Sepharose CL-6B. The nickel atom is fourfold complexed by NTA and has two open binding positions for the imidazol nitrogen of the histidine moieties. The surface concentration of the NTA ligand in the  $Ni^{2+}$ -NTA agarose from QIAGEN is sufficient for the binding of approximately 5-10 mg of 6xHis-tagged protein per ml of resin.

#### A.4.4 Coupling Novobiocin-Sepharose

**procedure :**

let 4.67 g epoxyactivated sepharose swell in  
500 ml aq.dest. for 2 h  
filtrate the white gel  
wash with 500 ml 0.3 M Na<sub>2</sub>CO<sub>3</sub> (31.977 g Na<sub>2</sub>CO<sub>3</sub> in 1.1 L aq.dest.)  
add Novobiocin solution (470 mg in 14.7 ml 0.3 M Na<sub>2</sub>CO<sub>3</sub>)  
add 0.9162 g (0.905 ml) Ethanolamin to the pale red-yellow solution, cend=1M)  
shake for 5 h at 37°C  
wash with 500 ml 0.5 M NaCl in buffer A (14.61 g NaCl in 500 ml buffer A)  
wash with 500 ml aq.dest  
wash with 500 ml 0.5 M NaCl in 0.1M Naac (pH4) (6.804 g Naac\*3H<sub>2</sub>O in 500 ml aq.dest.)  
gel turns slowly into white again, but keeps it reddish touch) wash with 500 ml aq.dest.

**0.3M Na<sub>2</sub>CO<sub>3</sub> pH 9.5**

15.899 g in 500 ml  
31.797 g in 1000 ml  
34.977 g in 1100 ml

**buffer A** 0.3M Na<sub>2</sub>CO<sub>3</sub>, pH 9.5

**1M ethanolamin** 0.9162 g (0.905 ml) in 15 ml

**0.5M NaCl** 14.61 g in 500 ml

**0.1M NaAc** 6.804 g NaAc\*3H<sub>2</sub>O in 500 ml

**ATP-buffer** 0.1102 g ATP (Mr 551.1) (0.02M)  
0.0536 g Mg-acetat (0.025M)  
0.149 g KCl (0.2M)  
in 10 ml

**buffer B** 0.8 M KCl (14.912 g KCl in 250 ml distilled water)

**5M urea** (Carbamid) Mr 60.06, d=1.335, R36/37/38, S26-36  
15.015 g in 50 ml

**5xTNE II pH7.8**

2.5ml Tris 1M, pH 8  
100 ml EDTA 0.5M, pH8  
5 ml NaCl 1M  
adjust pH with HCl to pH7.8  
fill up to 10 ml

## A.5 Gel electrophoreses

### A.5.1 Agarose gel

Agarose gels are used for the electropherographic separation of nucleic acids. The concentration of the agarose depends on the size of the applied particles. For the small PCR products a 2% agarose gel was used and for the plasmid pBR322 a 1% agarose gel.

**1% agarose gel** for the analysis of the DNA topology

0.4 g agarose  
 fill up to 40 ml with TAE (Beutenberg) buffer  
 heat in microwave till everything is dissolved  
 fill into a gel rack  
 load DNA when gel is dried.  
 Run gel for 8 hours at 20 Volt.

**A.5.2 SDS-PAGE**

SDS-PAGE (sodium dodecylsulfate polyacrylamide gel electrophoresis) is a common form of gel electrophoreses, which is used for the analysis of proteins (here: gyrase).

	10%T, 2.7%C separation gel	4%T, 2.7%C collection gel
30%T, 2.7%C (1) buffer (3)	3.33 ml 2.50 ml	0.67 ml -
buffer (4)	-	1.25 ml
10% SDS (5)	0.10 ml	50 ml
H <sub>2</sub> O	4.0 ml	3.0 ml
APS 10% (6)	50 ml	25 ml
TEMED	10 ml	7 ml
total volume	10 ml	5 ml

TEMED needs to be added at the end, because it starts the polymerization.

The separation gel is put between two clean glass plates, which are separated by a spacer. In order to seal the reaction mixture (the polymerization occurs only under O<sub>2</sub>-exclusion) it is covered with a layer of water. After about 45 minutes the water is removed and the separation gel is added. A special comb is used to obtain the pockets for loading the protein.

Following buffers were used for the gel preparation:

**(1) monomer solution** 30%T, 2.7%Bis, stock solution:

Acrylamid	58.4 g	73 g
Bis	1.6 g	2 g
H <sub>2</sub> O	to 200 ml	to 250 ml

keep at 4°C in the dark

**(3) resolving gel buffer** 1.5M TrisHCl, pH 8.8, separation gel buffer

Tris	36.3 g	adjust with HCl to pH8.8
H <sub>2</sub> O	to 200 ml	

**(4) stacking gel buffer** 0.5 M Tris-HCl, pH 6.8, collection gel buffer**(5) 10% SDS :**

SDS	50 g
H <sub>2</sub>	to 50 ml

## A Chemicals and Media

### (6) Initiator 10% ammonium persulfate

ammonium persulfat	100 mg
H <sub>2</sub> O	to 1 ml

### (8) 2x treatment buffer (stock solution)

Tris-HCl, pH 6.8 (solution (4))	2.5 ml	0.125M
SDS (solution (5))	4 ml	4%
Glycerol	2.0 ml	20%
2-mercapto-ethanol	1.0 ml	10%
H <sub>2</sub> O	to 10 ml	

divide into aliquots and freeze  
use for the samples by diluting 1:1

### (9) tank buffer :

Tris	12 g	0.025 M
Glycine	57.6 g	0.192 M
SDS	40 ml	0.1%
H <sub>2</sub> O	to 4 L	

The gel is run at 130 V and about 40 mW for circa 1 hour.

## A.6 Further biological assays

### A.6.1 Bradford protein test

#### Bradford reagent ,

100 mg Coomassie Brilliant Blue G-250  
50 ml 96% ethanol  
100 ml 85% phosphoric acid  
fill up to 1 L with distilled water, filtrate and store in the dark.

#### Bradford protein test :

100 ml sample solution  
1 ml Bradford reagent  
after 2-15 min changed absorbance at 630 nm (red in alcoholic-acidic media, changes to blue upon binding to proteins).

### A.6.2 Gyrase activity test

2 ml 10x TKK  
2 ml 50 mM MgCl<sub>2</sub>  
2 ml Spermidin (20 mg/ml) to accelerate reaction  
2 ml RSA (20 mg/ml)  
2 ml ATP (20 mg/ml)  
DNA  
enzyme (DNA:Gyrase 1:1, 2-4 mg/ml)  
fill up with H<sub>2</sub>O to 20 ml  
1h, 30°C



## B Additional spectra and tables

### B.1 DNA and DNA building blocks

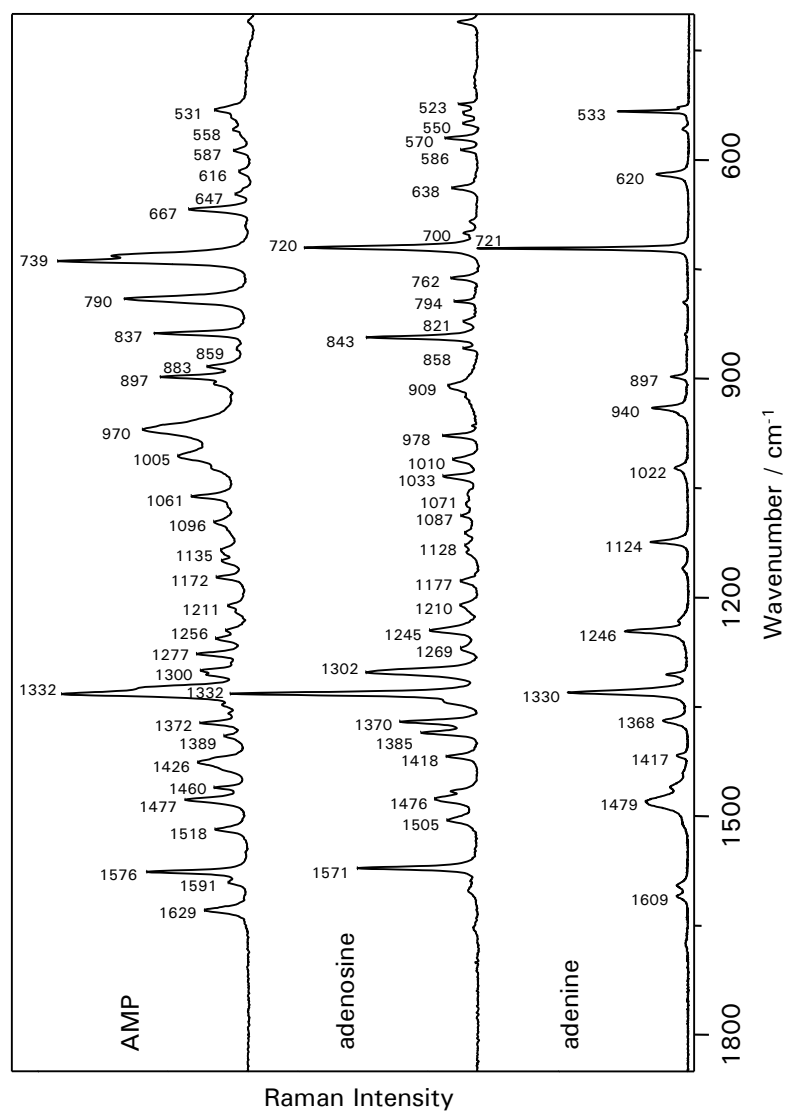


**Figure B.1:** Micro-Raman spectra of adenine, adenosine and AMP ( $\lambda_{ex} = 532$  nm).

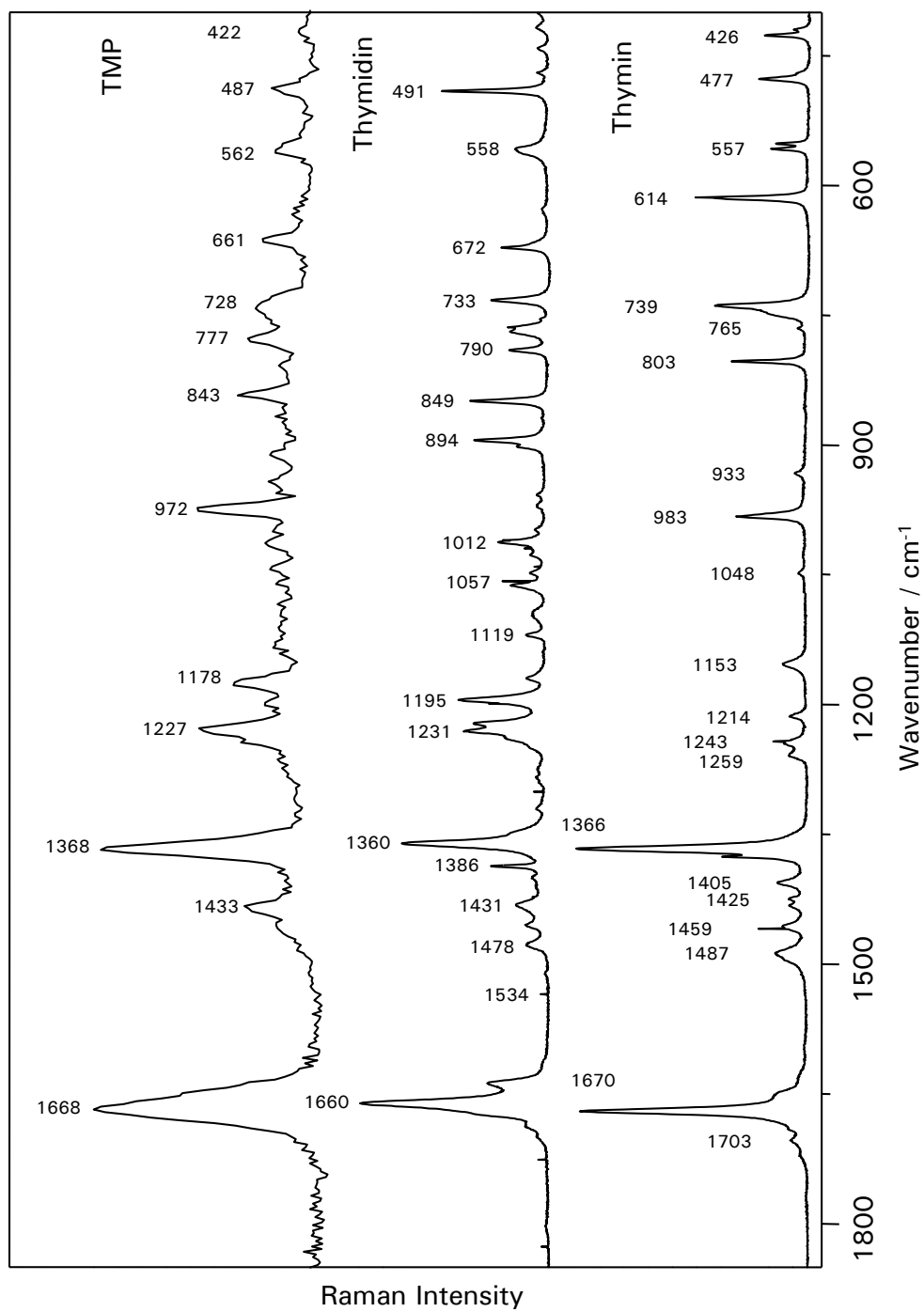


Figure B.2: Micro-Raman spectra of thymine, thymidine and TMP ( $\lambda_{ex} = 532$  nm).

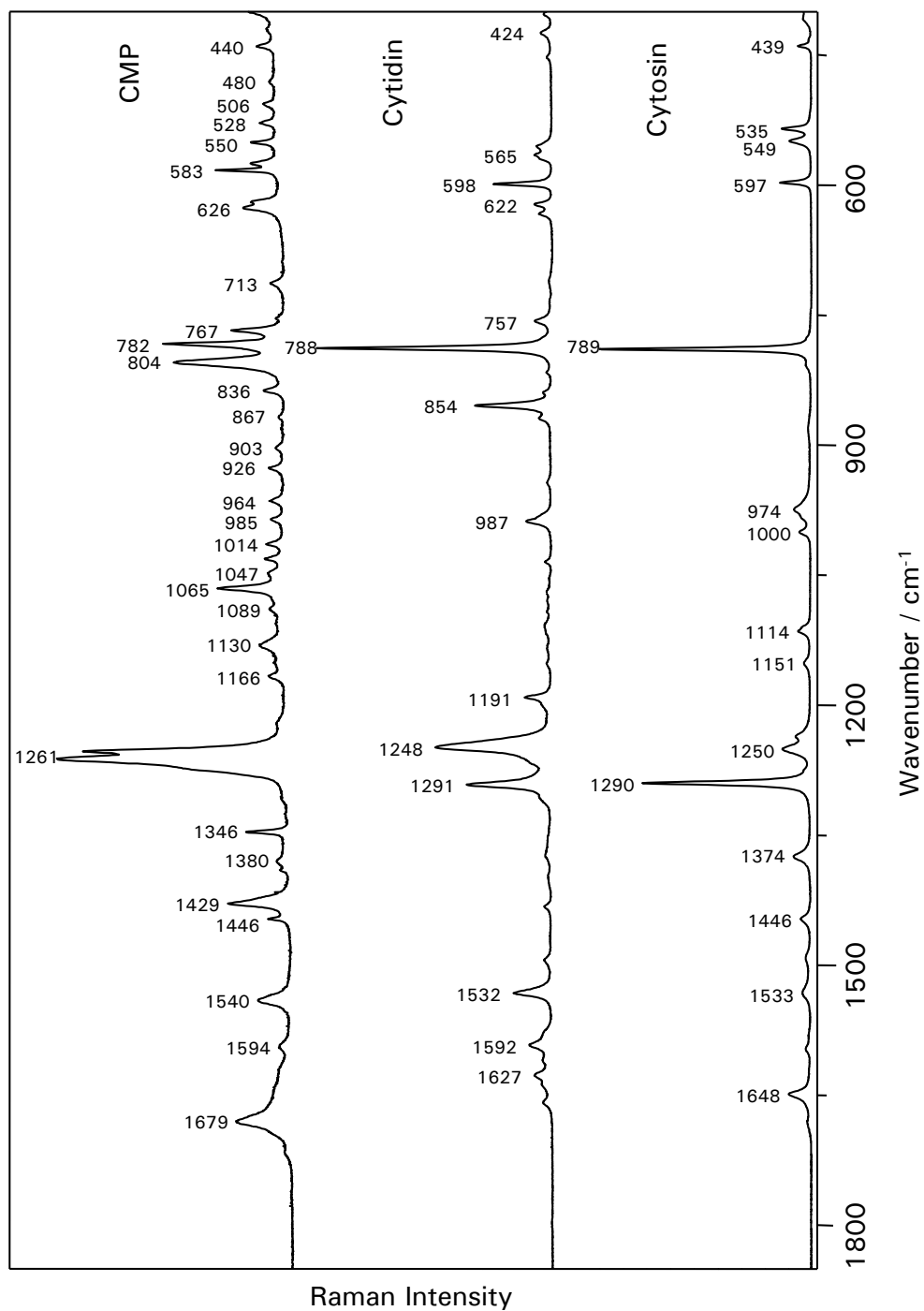


Figure B.3: Micro-Raman spectra of cytosine, cytidine and CMP ( $\lambda_{ex}=532$  nm).

## B Additional spectra and tables

**Table B.1** : Assignment of the Raman bands of guanine, guanosine and guanosine-5'-monophosphate. The experimental spectra have been recorded with excitation at 532 nm, DFT calculations have been performed using B3PW91/6-31+G(d,p), for scaling (DFT sc.) a scaling factor of 0.9614 was used, the values in the three last columns have been obtained from the literature [84] and were calculated using B3LYP/6-31++G(d,p).

guanine		guanosine		GMP		guanine [84]	
DFT	exp.	DFT	exp.	DFT	exp.	DFT	exp.
cm <sup>-1</sup>	cm <sup>-1</sup>	cm <sup>-1</sup>	cm <sup>-1</sup>	cm <sup>-1</sup>	cm <sup>-1</sup>	cm <sup>-1</sup>	cm <sup>-1</sup>
Assignment		Assignment		Assignment		Assignment	
138	133	22	22	18	18	18	18
		35	34	45	43	45	43
		59	56	52	50	52	50
		76	73	56	54	56	54
				75	72	75	72
				77	74	77	74
		98	95	84	80	84	80
		115	110	101	97	101	97
		139	134	109	105	109	105
	pu ring def out, C2N out			141	136	141	136
161	155	162	155	144	139	144	139
		170	164	162	155	162	155
200	192	188	181	175	168	175	168
		211	203	185	178	185	178
				200	192	200	192
		242	232	214	206	214	206
				253	243	253	243

Table B.1: continued

guanine		guanosine		GMP		guanine [84]	
DFT $\text{cm}^{-1}$	exp. $\text{cm}^{-1}$	DFT $\text{cm}^{-1}$	exp. $\text{cm}^{-1}$	DFT $\text{cm}^{-1}$	exp. $\text{cm}^{-1}$	DFT $\text{cm}^{-1}$	exp. $\text{cm}^{-1}$
318	305	250	240	265	255	317	340
328	315	292	280	275	265	327	
335	322	296	285	282	271	335	397
360	346	312	300	287	276	357	357
		323	311	304	292		
		332	319	312	300		
		351	338	315	302		
		387	372	339	326		
		400	384	344	331		
		431	415	370	356		
				378	363		
				383	368		
				417	401		
				419	403		
				431	414		

B Additional spectra and tables

Table B.1: continued

guanine		guanosine		GMP		guanine [84]				
DFT	Assignment	DFT	Assignment	DFT	Assignment	DFT				
cm <sup>-1</sup>	cm <sup>-1</sup>	cm <sup>-1</sup>	cm <sup>-1</sup>	cm <sup>-1</sup>	cm <sup>-1</sup>	cm <sup>-1</sup>				
487	468	493	pyr ring breath	490	471	493	474	495	def R6 (sqz groups C5C6N1, C2N3C4)	
528	507	N2H <sub>2</sub> def, ring def	N2H <sub>2</sub> def, O3'H def	517	497	517	497	527	def R6 (sqz groups C6NIC2, N3C4C5), wag N9H, NH <sub>2</sub> , combination tone	
544	523	N9H out, N2H <sub>2</sub> wag	O3'H def, O2'H def	536	499	536	515	536	furanose ring def, PO <sub>2</sub> wag	
545	523	N9H out, N2H <sub>2</sub> wag	O3'H def, O2'H def, skeletal	556	506	556	535	536	skeletal (ring def, O'H bend)	
600	577	561	N1H out	600	576	604	581	548	O2'H bend, NH <sub>2</sub>	
631	607	pur ring breath	O2'H def, pur ring def, furanose ring def	556	534	566	544	566	O2'H bend, PO bend, N2H	
662	637	im ring out	furanose ring def, C5'H <sub>2</sub> def, N1H out	581	559	584	561	595	wag N1H	
669	644	647	pur ring def, C6O bend, NH def	627	603	634	609	626	breath R6	
697	670	pur ring out	pur ring out, furanose ring def,	661	636	658	632	660	def R5 (wag N7C8N9)	
				671	645	675	649	668	710	def R6 (sqz N1C2N10), bend C6O
				695	668	686	659			

Table B.1: continued

guanine		guanosine		GMP		guanine [84]	
DFT	Assignment	DFT	Assignment	DFT	Assignment	DFT	Assignment
cm <sup>-1</sup>	cm <sup>-1</sup>	cm <sup>-1</sup>	cm <sup>-1</sup>	cm <sup>-1</sup>	cm <sup>-1</sup>	cm <sup>-1</sup>	cm <sup>-1</sup>
701		674	pur ring out, NIH out, furanose ring str, O2'H def	696	pur out, NIH out	694	def R6 (wag N3C4C5, C6NIC2), wag N1H
733	705 708 ring out (esp. pyr)	732 703 694	pyr ring out, C8H out	715 688	skeletal def	729	def R6 (wag C2N3C4, C5C6N1), wag N1H
766	736 ring out	743 714	furanose ring str, skeletal	728 700	furanose ring breath, C5'OP, pur ring str	766	def R6 (wag C4C5C6, NIC2N3), R5 (tors N7C8), wag C8H
823	791 C8H out	765 735	pur ring out	731 703	pyr ring out, sugar skeletal	822	wag C8H
839	807 846 pur ring def	828 796 785	pur ring str	761 732	pur ring out		
945	908 936 im ring def	833 801	C8H out	815 784	furanose ring def, CN str, CC str, C5'O def		
		879 845 878	im ring def, C5'H2 def, furanose ring breath, pyr ring	833 801	pur ring def, C1' def		
		889 855 915	im ring def, furanose ring def, C'H def, O5'H def	876 843 827	C8H out, pur ring breath, C5'H2 def, N9C1'		
		922 886	furanose ring str (C2'C3' str), C5'H2 twist,	887 853	C8H out, furanose ring str, C5'H2 def		
		1013 974	furanose ring str (C1'C2' str), C4'H, O'H def	893 858	furanose ring breath, C5'H rock, im ring breath	835	def R5 (sqz C4N9C8, str C5N7), R6 (sqz NIC2N3)
		1028 988	N2H2 def, pur ring str, furanose ring (C3'C4' ring str), O'H bend	913 878	C2'C3' str, C5'H2 rock, C'H def	945	def R5 (sqz N7C8N9)
1054	1013 NIH, N2H2 def	1044 1004	N2H2 def, N1H1 def, C1'C2' str, O'H def	932 896 892	PO str sym.		
				942 906	C2'C3', C4'C5', C5'H2, C4'H, C3'H, N9C1'		
				1005 967 973	C4'H, C3'H, C4'C5', furanose ring str, C1'H		





Table B.1: continued

guanine		guanosine		GMP		guanine [84]					
DFT sc. exp.	Assignment	DFT sc. exp.	Assignment	DFT sc. exp.	Assignment	DFT exp.					
cm <sup>-1</sup>	cm <sup>-1</sup>	cm <sup>-1</sup>	cm <sup>-1</sup>	cm <sup>-1</sup>	cm <sup>-1</sup>	cm <sup>-1</sup>					
1185	1139	1243	1195	1248	1241	1193	1176	1186	bend C8H, str C5N7, def R6 (sqz N3C4C5)		
	C8H def, N9H def, ring		C8H def, C1'H def, C8N9 str, C'H sugar, O'H sugar, pur ring str		C8H def, C'H def, ring		C8H def, C'H def, ring				
		1264	1215		1259	1210			C5'H <sub>2</sub> twist, C'H def		
		1268	1219		1280	1230			C8N9 str, C1'H, C8H, C5'H <sub>2</sub> twist, C'H def		
		1276	1226		1282	1233			C'H def, O2'H def, C8H, ring		
		1307	1257		1297	1247			C'H def, O2'H def, C8H		
		1318	1267		1325	1274			C'H def		
1316	1266	1330	1279		1336	1285			NIH def, C8H def, C1'H, C3'H, C4'H, C2N str, N2H def		
	NIH def, C8H def, N9H	1337	1285		1353	1301			1310	1234	bend N1H, N9H, C8H, str C2N10-N7C8
1343	1291	1356	1304		1361	1309			1337	1265	bend N1H, N10H12 (str C5N7-C2N10-N3C4)
	NIH def, N2H def, N3C4 str, C8H		C'H def (sugar), O3'H def, C8H def, N1H def, C5'H def, N2H <sub>2</sub> def, O2'H def		C'H def (sugar), O3'H def, C8H def, N1H def, C5'H def, N2H <sub>2</sub> def, O2'H def		C4'H def, C'H def, N1H def, C8H def, ring def				
		1367	1314	1365	1373	1320	1325				
			C'H def (sugar), C8H def, N1H def, pur ring (C5N7, C4N3), N2H <sub>2</sub> def		C'H def (sugar), C8H def, N1H def, pur ring (C5N7 str)		C'H def, O3'H def, N1H, ring def				
		1369	1316		1393	1340					
			C'H def (sugar), O3'H def, C8H def		C'H def (sugar), O3'H def, C8H def		C'H def, O'H def, im ring breath				

B Additional spectra and tables

Table B.1: continued

guanine		guanosine		GMP		guanine [84]	
DFT	Assignment	DFT	Assignment	DFT	Assignment	DFT	Assignment
cm <sup>-1</sup>	cm <sup>-1</sup>	cm <sup>-1</sup>	cm <sup>-1</sup>	cm <sup>-1</sup>	cm <sup>-1</sup>	cm <sup>-1</sup>	cm <sup>-1</sup>
1383	1330 1390	1384 1331	C'H def (sugar)/O2'H def	1401 1347	C5'H <sub>2</sub> wag, C'H, O'H sugar	1365 1361	str C5N7+C4N9-C5C6-N3C4, A bend C8H, N9H
1405	1351 1420	1411 1356	C5C6 str, C5N7 str, pur ring str, N2H <sub>2</sub> def, C'H def (sugar)	1413 1358	C1'H def, C2'H def, O3'H def, im ring str	1390 1390	str NIC2+N7C8+C4N9, bend NIH, rock NH <sub>2</sub> , bend N9H, str C8N9-C5N7
1458	1402 1464	1433 1377	C'H def (sugar), O3'H def	1418 1363	pur ring str (C5C7), C'H def, O3'H def		
		1439 1384	C1'H def, CH sugar	1423 1368	C'H def, O'H def, im ring breath		
		1465 1408	C5'H <sub>2</sub> wag, O5'H def, C4'H, C1'H, skeletal	1447 1391 1383	O2'H bend, C2'H bed, C1'H def, C'H def, im breath		
1534	1475 1547	1468 1412 1481	pur ring str, N1H def, CH sugar	1453 1397 1401	ring str (im), C8H def, C1'H def, NIH def	1441 1421	str N7C8-N3C4-NIC2, bend C8H, NIH
		1503 1445	C5'H <sub>2</sub> scis	1499 1441 1416	C5'H <sub>2</sub> scis		
1573	1512	1539 1479 1542	NIH def, pur ring str, C8H def, N2H <sub>2</sub> def, C1'H def	1530 1471	C8H def, NIH def, NH <sub>2</sub> scis, pur ring str (CN)	1517 1468	bend NIH, sciss NH <sub>2</sub>
1623	1561	1578 1517	C8H def, NIH def, N2H <sub>2</sub> def, pur ring str, C1'H	1579 1518	C8H def, NIH def, NH <sub>2</sub> scis, ring	1559 1479	str C2N10+C4N9-N7C8-NIC2+C5C6+C6O,
		1607 1544	C4C5 str, C8H def, C1'H, C2N1 str, NIH def, N2H def	1611 1549 1492	C4C5 str, NIH def, pur ring str		

Table B.1: continued

guanine		guanosine		GMP		guanine [84]								
DFT	exp.	DFT	exp.	DFT	exp.	DFT	exp.							
cm <sup>-1</sup>	cm <sup>-1</sup>	cm <sup>-1</sup>	cm <sup>-1</sup>	cm <sup>-1</sup>	cm <sup>-1</sup>	cm <sup>-1</sup>	cm <sup>-1</sup>							
	Assignment		Assignment		Assignment		Assignment							
1635	1571	1630	1567	1574	1537	1610	1551	N2H <sub>2</sub> scis, N9H, ring (C4)	N2H <sub>2</sub> scis, N1H def, pyr ring str, C8H def, C1'H def	NH <sub>2</sub> scis, N1H C2N1, C2N3 str	1610	1551	str	N3C4- C4C5+C2N3, sciss NH <sub>2</sub>
1677	1613	1674	1610	1630	1630	1677	1613	N2H <sub>2</sub> scis, C2N3 str, C2N1 str, N1H def	N2H <sub>2</sub> scis, N1H def, C2N3 str, C2N1 str	NH <sub>2</sub> scis, N1H def	1621	1551	str	C2N3-N3C4, sciss NH <sub>2</sub> , bend N1H
1818	1748	1680	1819	1749	1699	1808	1739	C6O str, N1C6, C5C6, N1H	C6O str, N1C6, C5C6, N1H	C6=O str, N1H def	1667	1602	sciss	NH <sub>2</sub> , str
			3001	2886	2832	3023	2906	C5'H <sub>2</sub> str (sym)	C5'H <sub>2</sub> str (sym)	C5H <sub>2</sub> str sym	1797	1675	str	C6O-C5C6, bend N1H
3276	3149	3124	3035	2918	2897	3057	2939	C4'H, C5'H <sub>2</sub> str (sym)	C4'H, C5'H <sub>2</sub> str (sym)	C3'H str, C1'H str				
3609	3469		3057	2939	2926	3059	2941	C5'H <sub>2</sub> str (asym), C4'H	C5'H <sub>2</sub> str (asym), C4'H	C1'H str, C3'H str				
			3070	2952	2958	3076	2957	C2'H str, C3'H	C2'H str, C3'H	C5'H <sub>2</sub> str asym				
			3078	2959		3101	2981	C1'H str	C1'H str	C2'H str				
			3100	2980		3104	2984	C3'H str, C2'H, C4'H	C3'H str, C2'H, C4'H	C4'H str				
3621	3482	3321	3267	3141	3143	3300	3172	C8H str	C8H str	C8H str				
3682	3540		3609	3470		3614	3474	N2H <sub>2</sub> str (sym), N1H str	N2H <sub>2</sub> str (sym), N1H str	NH <sub>2</sub> str symm, N1H str				
3730	3586		3621	3481		3621	3481	N1H str, N2H <sub>2</sub> str (sym)	N1H str, N2H <sub>2</sub> str (sym)	N1H str, NH <sub>2</sub> str symm				
			3729	3585		3695	3553	N2H <sub>2</sub> str (asym)	N2H <sub>2</sub> str (asym)	O2'H str				
			3748	3603		3734	3590	O2'H str	O2'H str	NH <sub>2</sub> str asym				
			3876	3727		3790	3644	O3'H str	O3'H str	O3'H str				
			3880	3730				O5'H str	O5'H str					

B.1.0.1 IR absorption spectra

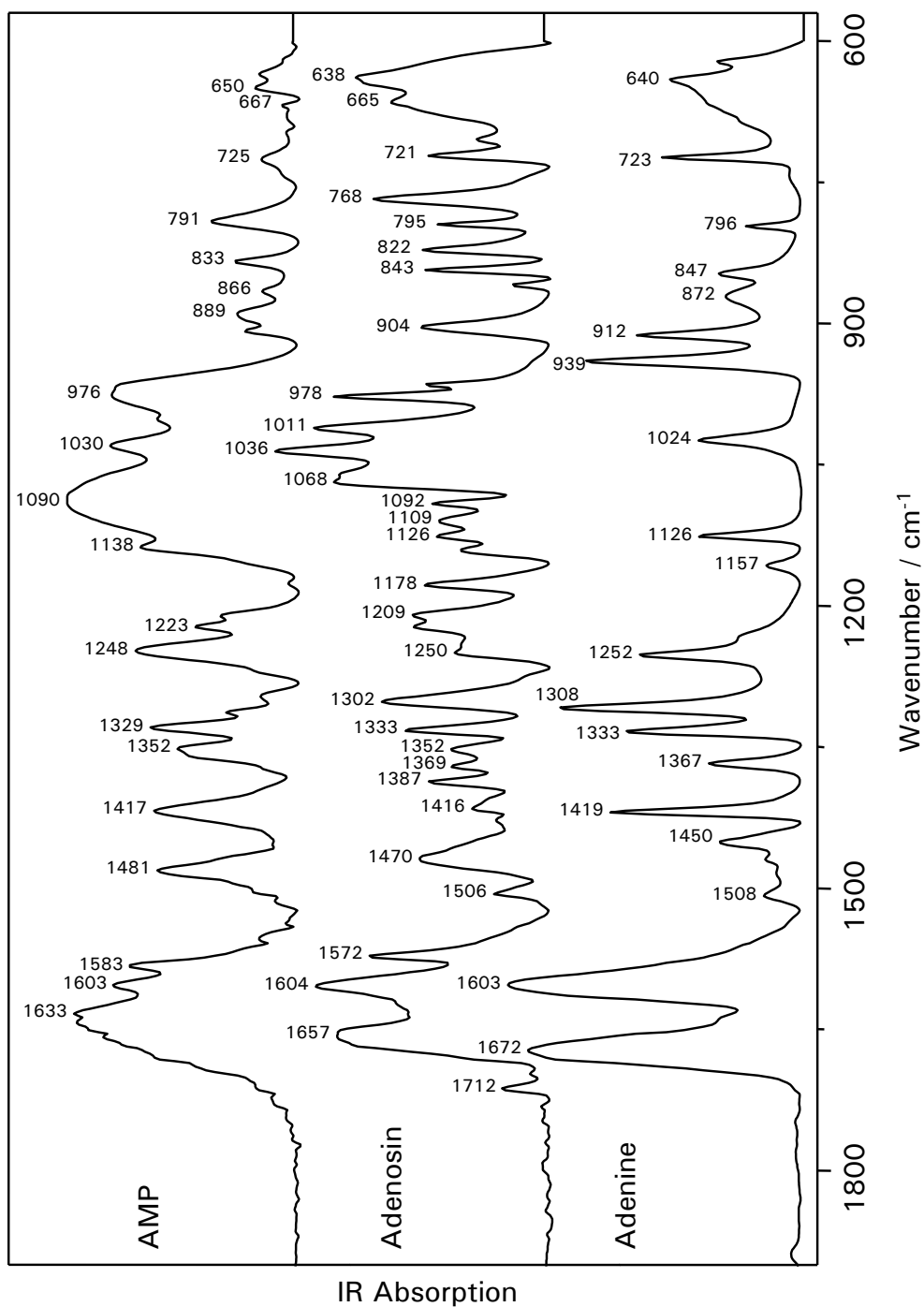
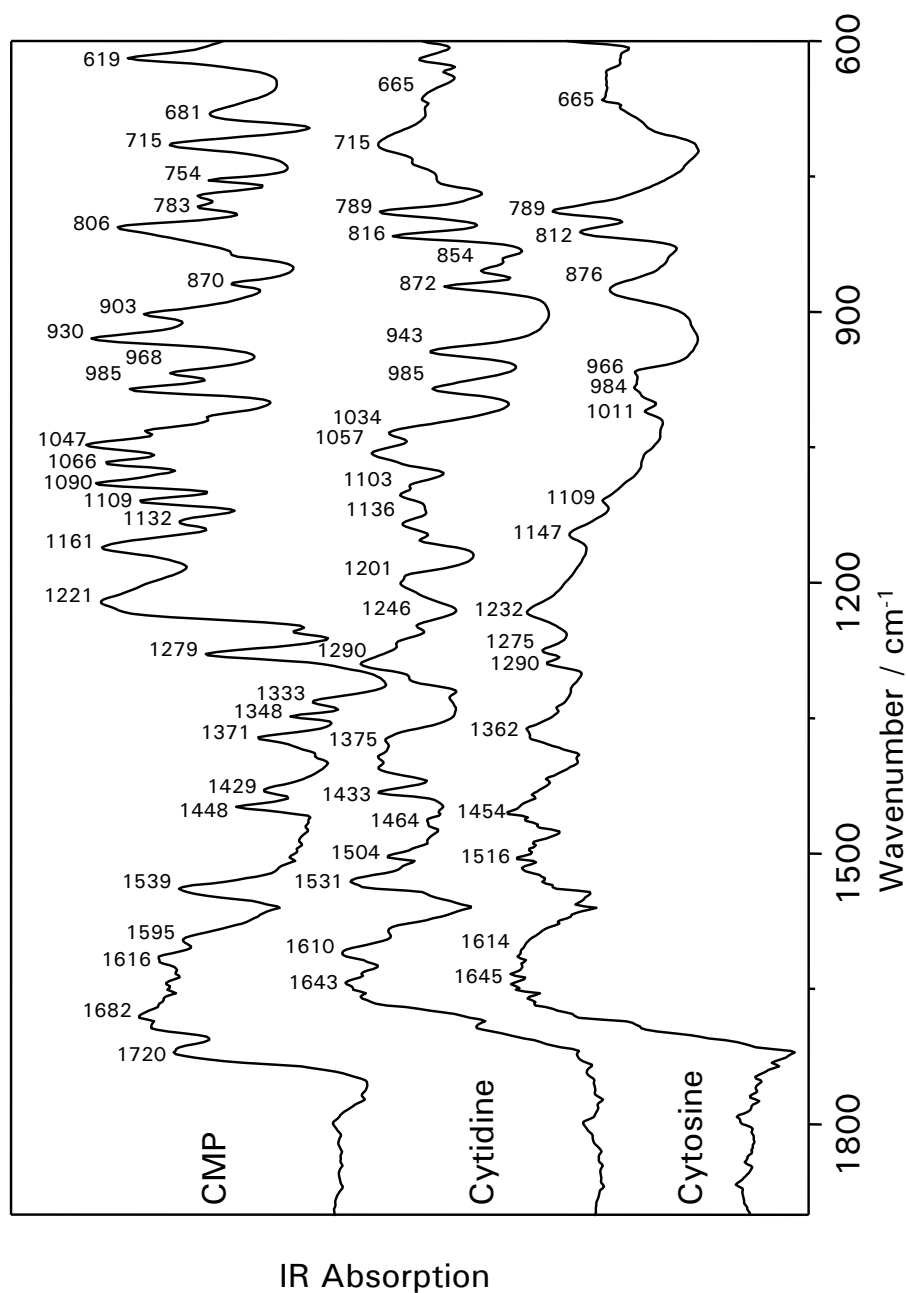
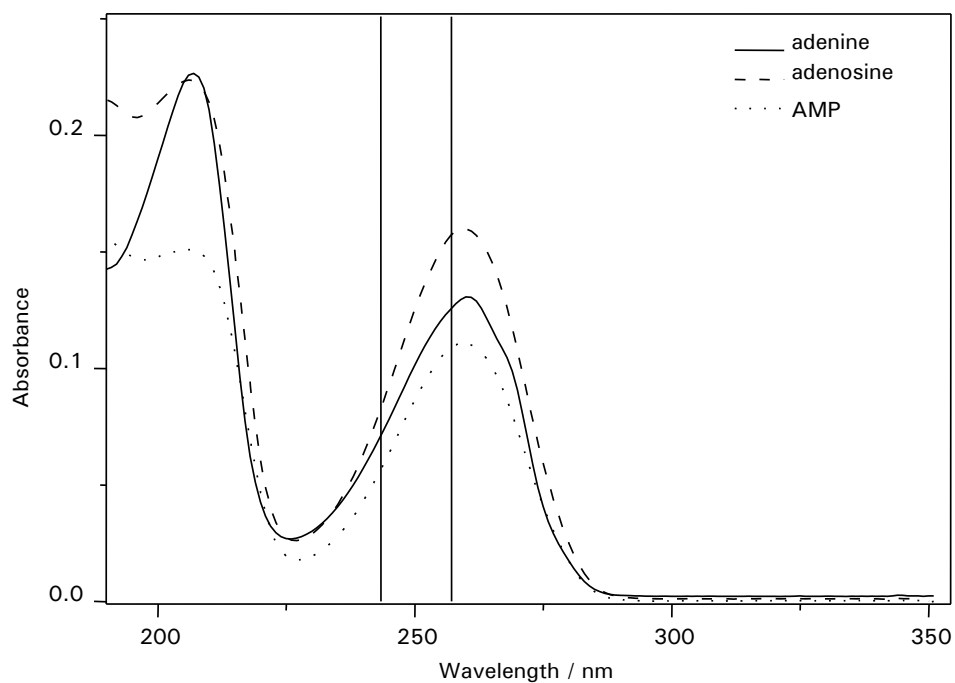


Figure B.4: IR absorption spectra of adenine, adenosine and adenosine-5'-monophosphate (AMP) (IR microscope).



**Figure B.5:** IR absorption spectra of cytosine, cytidine and cytidine-5'-monophosphate (CMP) (IR microscope).

### B.1.1 UV absorption spectra



**Figure B.6:** UV absorption spectra of adenine, adenosine and AMP in aqueous solution.

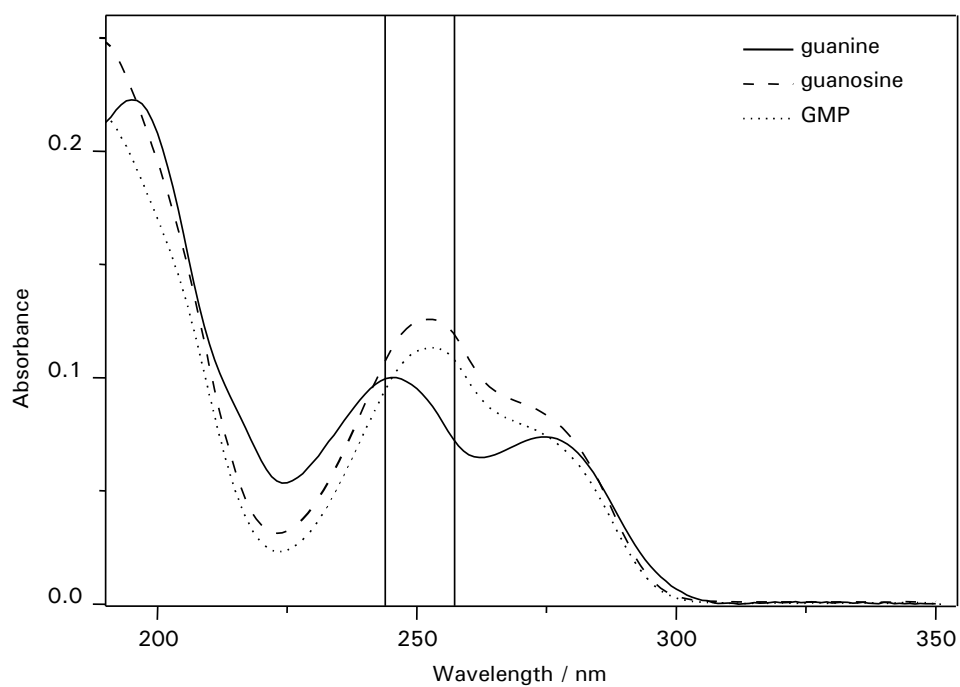


**Figure B.7:** UV absorption spectra of adenine, adenosine and AMP in aqueous solution .

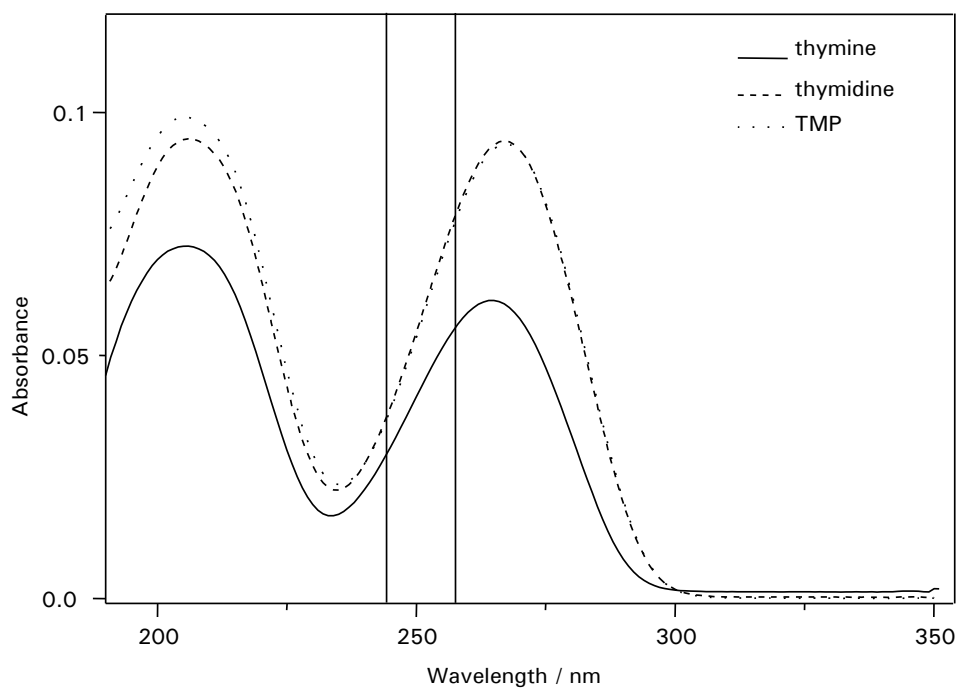


**Figure B.8:** UV absorption spectra of thymine, thymidine and TMP in aqueous solution.

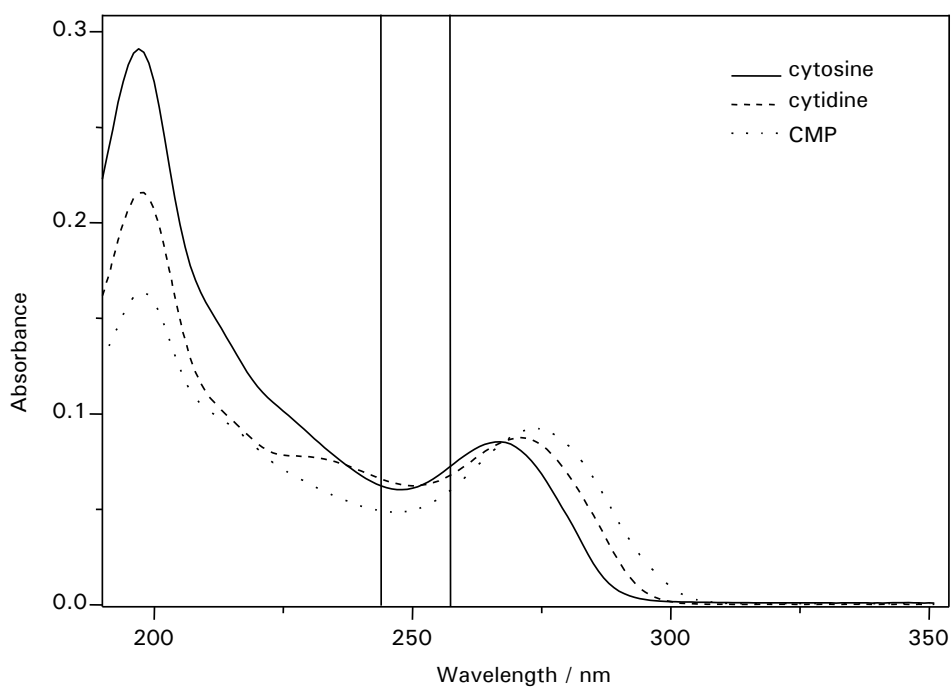


**Figure B.9:** UV absorption spectra of cytosine, cytidine and CMP in aqueous solution.

## B.2 Gyrase and amino acids

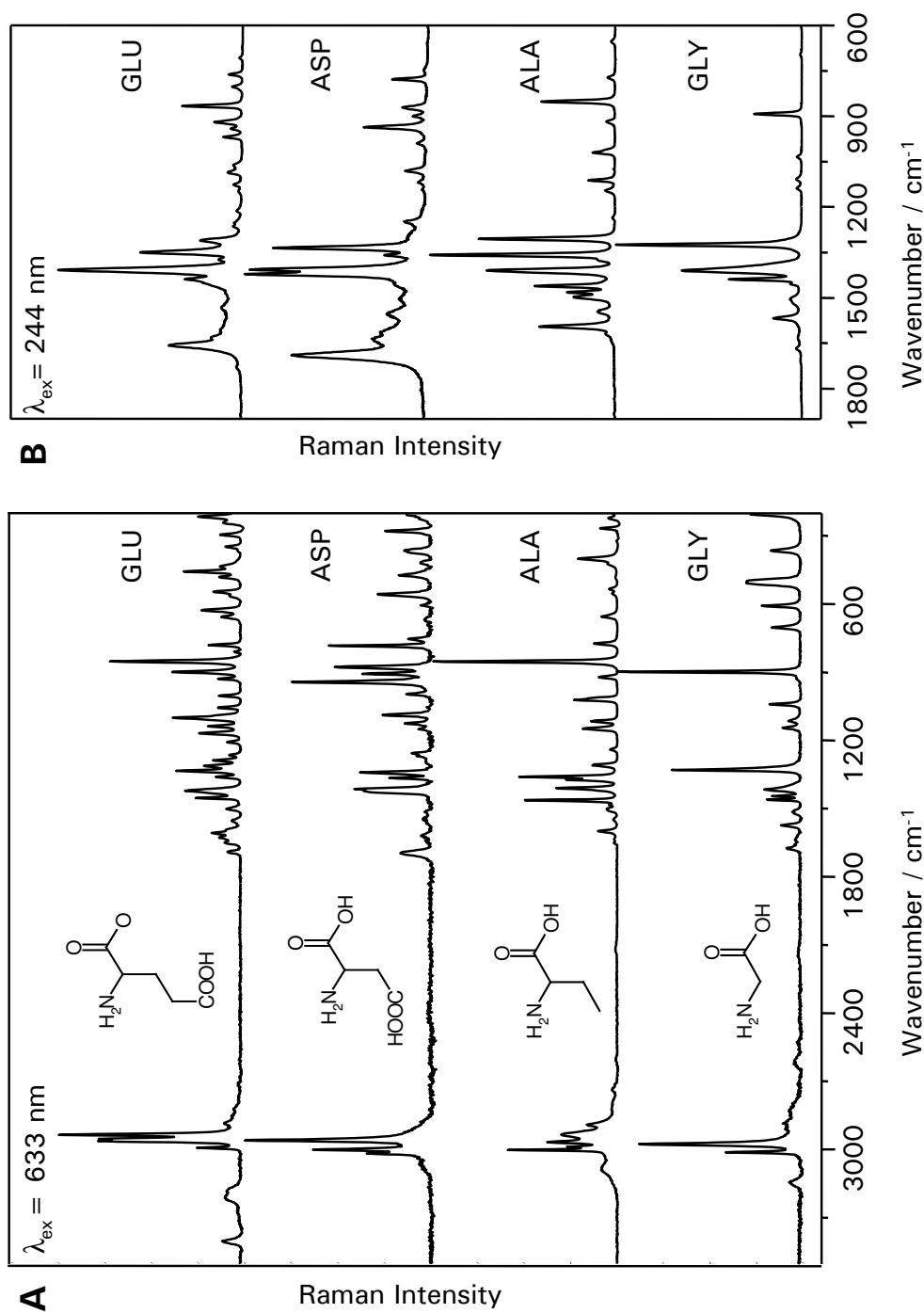


**Figure B.10:** Raman (A,  $\lambda_{ex} = 633$  nm) and UV-resonance Raman (B,  $\lambda_{ex} = 244$  nm) spectra of some aliphatic amino acids: from bottom to top glycine (GLY), alanine (ALA), aspartic acid (ASP) and glutamic acid (GLU).



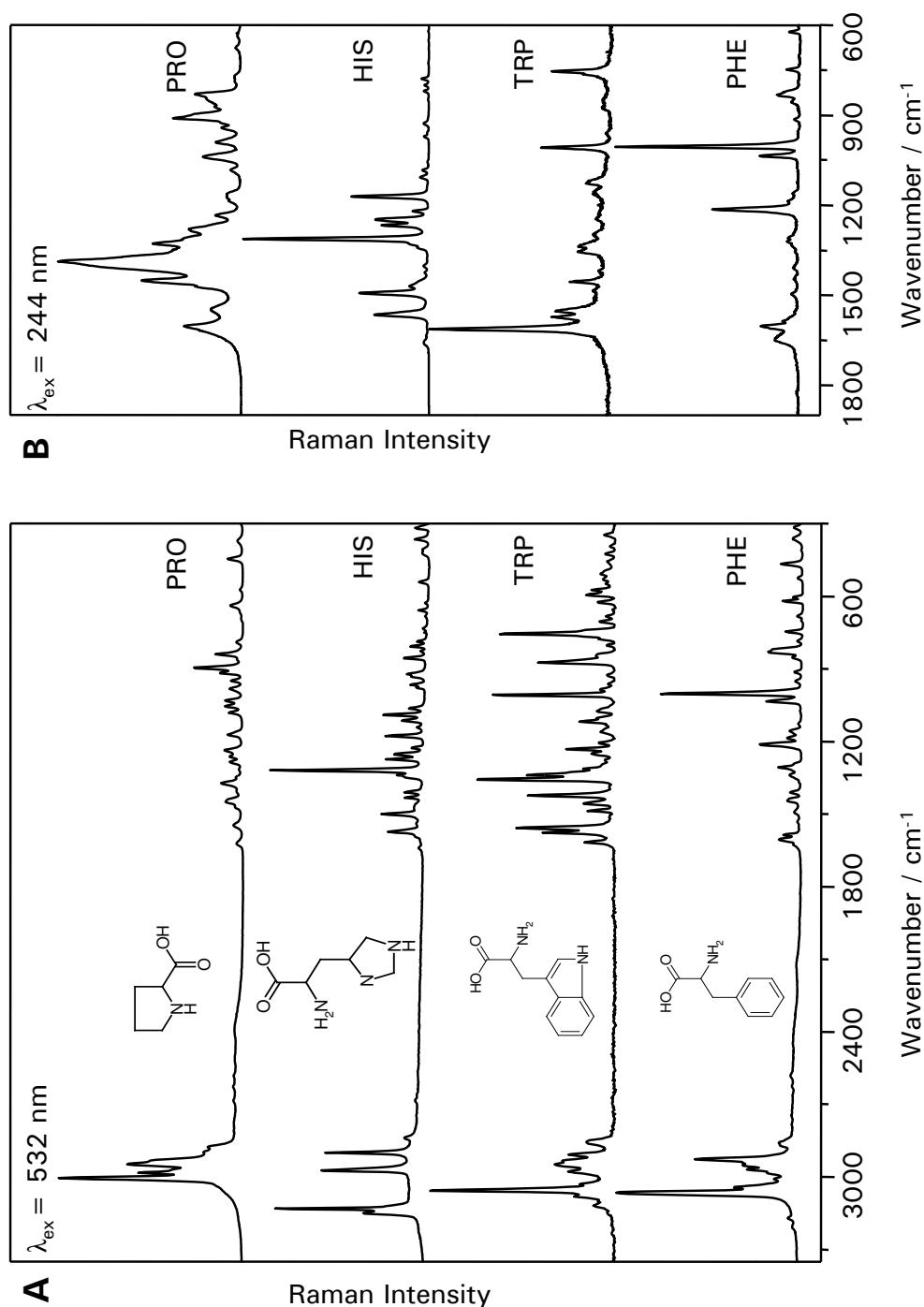


**Figure B.11:** Raman (A,  $\lambda_{\text{ex}} = 532 \text{ nm}$ ) and UV-resonance Raman (B,  $\lambda_{\text{ex}} = 244 \text{ nm}$ ) spectra of the aromatic and heterocyclic amino acids: from bottom to top phenylalanine (PHE), tryptophan (TRP), histidine (HIS) and proline (PRO).



## Abbreviations

ADP	adenosine diphosphate
ATCC	American Type Culture Collection
ATP	adenosine triphosphate
bp	base pair
CASO	casein-peptone - soy meal-peptone, common media for staphylococci
CTD	carboxyl-terminal domain (in proteins)
DFT calculations	density functional theoretical calculations
DSMZ	Deutsche Sammlung von Mikroorganismen und Zellkulturen GmbH (German Collection of Microorganisms and Cell Cultures)
Fig.	figure
FRET	fluorescence resonance energy transfer
GC content	the proportion of guanine-cytosine base pairs in the DNA/RNA molecule or a genome sequence, usually expressed as a percentage, it is a characteristic of the genome of any given organism or any other piece of DNA or RNA
HCA	hierarchical cluster analysis
im	imidazole
IR	infrared
$\lambda_{ex}$	excitation wavelength
LDA	linear discriminant analysis
$Lk$	linking number
LMO-CV	leave multiple out cross-validation
MIC	minimal inhibition concentration
MRS	methicillin resistant staphylococci
NIR	near infrared
NMR	nuclear magnetic resonance
NTD	amino-terminal domain (in proteins)
pH	negative decade logarithm of the $H^+$ concentration
PC	principal component
PCA	principal component analysis

## Abbreviations

PCR	Polymerase Chain Reaction, used for amplification of DNA sequences
ped	potential energy distribution
PIA	polysaccharide intercellular adhesin
pur	purine
pyr	pyrimidine
rcf	relative centrifugal force (measurement of the force applied to a sample within a centrifuge. Can be calculated from the rpm and the rotational radius $r$ in cm using the following equation: $rcf = 0.00001118r(rpm)^2$ )
Ref.	reference
REM-TS	reverse elimination method tabu search
rpm	revolutions per minute
RR	resonance Raman
$\sigma$	superhelical density parameter
SDS-PAGE	sodium dodecylsulfate polyacrylamide gel electrophoresis
SEM	scanning electron microscopy
SERS	surface enhanced Raman spectroscopy
SNR	signal-to-noise ratio
TERS	tip-enhanced Raman spectroscopy
UV	ultraviolet

### Assignment of vibrational modes

str	stretching vibration
def	deformation vibration
rock	rocking vibration
sciss	scissoring vibration
wag	wagging vibration
out	out of plane

### Nucleic acids and nucleic acid bases

A	adenine
C	cytosine
DNA	deoxyribo nucleic acid
G	guanine
RNA	ribo nucleic acid
T	thymine
U	uracil

**Amino acids**

one letter code	three letter code	full name
A	Ala	alanine
C	Cys	cystein
D	Asp	asparaginic acid
E	Glu	glutamic acid
F	Phe	phenylalanine
G	Gly	glycin
H	His	histidine
I	Ile	isoleucin
K	Lys	lysin
L	Leu	leucin
M	Met	methionin
N	Asn	asparagin
P	Pro	prolin
Q	Gln	glutamin
R	Arg	arginin
S	Ser	serin
T	Thr	threonin
V	Val	valin
W	Trp	tryptophan
Y	Tyr	tyrosin

**Fluoroquinolone drugs**

CIN	cinoxacin
CIPRO	ciprofloxacin
ENO	enoxacin
FLU	flumequine
LOM	lomefloxacin
MOXI	moxifloxacin
NAL	nalidixic acid
NOR	norfloxacin
OFL	ofloxacin
O XO	oxolinic acid
SARA	sarafloxacin

## Abbreviations

### Chemicals

EDTA	ethylenediaminetetraacetic acid
EthBr	ethidium bromide
Glc	glucose
GlcN	glucosamine
IPTG	isopropyl- $\beta$ -D-thiogalactopyranoside, an artificial inductor for the <i>lac</i> operon in <i>Escherichia coli</i> .
KAc	potassium acetate
LB medium	lysogeny broth, sometimes called Luria-Bertani media (complex media for the growth of bacteria, especially <i>E. coli</i> )
NAM	N-Acetyl muramic acid
NAG	N-acetylglucosamine
PIA	polysaccharide intercellular adhesin
PBS	Phosphat buffered saline, popular phosphate buffer
SDS	sodium dodecylsulfate, added to compensate the negative charges of the protein and facilitate gel electrophoreses
TA	teichoic acid
TAE buffer	typical buffer solution for agarose electrophoresis of DNA and RNA, made up of Tris-acetate buffer, usually at pH 8.0, and EDTA
TEMED	tetramethylethylenediamin (polymerization catalyst)
TNE buffer	
Tris	tris(hydroxy methyl)aminomethane

**Units**

quantity		unit	conversion
energy	J	Joule	4.18 J = 1 cal
	kJ	kilo Joule	1 kJ = 10 <sup>3</sup> J
	eV	electron Volt	1 eV = 1.6 · 10 <sup>-18</sup> J
	cm <sup>-1</sup>	reciprocal centimeter	1 eV = 8065.5 cm <sup>-1</sup>
	Ha	Hartree	1 Ha = 4.3597 · 10 <sup>-18</sup> J
force constant	N/m	Newton/metre	
frequency	Hz	Hertz	1 Hz = 1/s
concentration	M	molar	mol L <sup>-1</sup>
	mM	millimolar	1 mM = 10 <sup>-3</sup> M
length	nm	nanometer	1 nm = 10 <sup>-9</sup> m
	µm	micrometer	1 µm = 10 <sup>-6</sup> m
amount of substance	mol		
temperature	°C	degree Celsius	
	K	Kelvin	
volume	L	liter	1 L = 10 <sup>-3</sup> m <sup>3</sup> = 10 <sup>24</sup> nm <sup>3</sup>
	mL	milliliter	1 mL = 10 <sup>-3</sup> L
	nm <sup>3</sup>	cubic nanometer	1 nm <sup>3</sup> = 10 <sup>-27</sup> m <sup>3</sup>
	Vol%	volume percent	
time	s	second	
	min	minute	1 min = 60 s
molecular weight	kDa	kilo-Dalton	1 kDa = 1.66054 · 10 <sup>-24</sup> kg
wavenumber	cm <sup>-1</sup>	reciprocal centimeter	1 eV = 8065.5 cm <sup>-1</sup>

**Constants**

constant	value	meaning
<i>c</i>	2.99792458 · 10 <sup>8</sup> ms <sup>-1</sup>	speed of light
<i>g</i>	9.80665 ms <sup>-2</sup>	acceleration of gravity
<i>h</i>	6.6260755 · 10 <sup>-34</sup> Js	Planck's constant
<i>ħ</i>	1.05457 · 10 <sup>-34</sup> Js	$\hbar = h/2\pi$
<i>k</i>	1.38066 · 10 <sup>-23</sup> JK <sup>-1</sup>	Boltzmann's constant
<i>N<sub>A</sub></i>	6.0221367 · 10 <sup>23</sup> mol <sup>-1</sup>	Avogadro's number
<i>R</i>	8.31451 JK <sup>-1</sup> mol <sup>-1</sup>	gas constant





## Bibliography

- [1] *Vorschrift für das biochemische Praktikum, Uni Würzburg Versuch 3.*
- [2] *Opus/Ident Handbuch Version 2.2.* Bruker Analytische Messtechnik GmbH, **1995.**
- [3] <http://www.uccs.edu/rmelamed/MicroFall2002/Chapter%204/ch04.htm> **Jan. 2006.**
- [4] A. Abbott. 'Hopping Fences'. *Nature* **2005.** 433, 680–682.
- [5] H. G. Abdelhady, S. Allen, S. J. Ebbens, C. Madden, N. Patel, C. J. Roberts, & J. Zhang. 'Towards nanoscale metrology for biomolecular imaging by atomic force microscopy'. *Nanotechnology* **2005.** 16, 966–973.
- [6] R. Ahmad, H. Arakawa, & H. A. Tajmir-Riahi. 'A Comparative Study of DNA Complexation with Mg(II) and Ca(II) in Aqueous Solution: Major and Minor Grooves Bindings'. *Biophys. J.* **2003.** 84(4), 2460–2466.
- [7] M. G. Albrecht & J. A. Creighton. 'Anomalously Intense Raman Spectra of Pyridine at a Silver Electrode'. *J. Am. Chem. Soc.* **1977.** 99(15), 5215–5217.
- [8] C. A. Andersson. 'Direct orthogonalization'. *Chemom. Intell. Lab. Syst.* **1999.** 47, 51–63.
- [9] M. I. Andersson & A. P. MacGowan. 'Development of the quinolones'. *J. Antimicrob. Chemother.* **2003.** 51 (Suppl. S1), 1–11.
- [10] J. F. Arenas, I. Lopez-Tocon, J. L. Castro, S. P. Centeno, M. R. Lopez-Ramirez, & J. C. Otero. 'Resonant charge transfer on the nanoscale: studying doublet states of adsorbates by surface-enhanced Raman scattering'. *J. Raman Spectrosc.* **2005.** 36, 515–521.
- [11] S. A. Asher. 'UV Resonance Raman Spectroscopy for Analytical, Physical and Biophysical Chemistry 2'. *Anal. Chem.* **1993.** 65, A201–A210.
- [12] S. A. Asher, A. Ianoul, G. Mix, M. N. Boydon, A. S. Karnoup, M. Diem, & R. Schweitzer-Stenner. 'Dihedral Psi Angle Dependence of the Amide III Vibration: A Uniquely Sensitive UV Resonance Raman Secondary Structural Probe'. *J. Am. Chem. Soc.* **2001.** 123, 11 775–11 781.
- [13] S. A. Asher, A. V. Mikhonin, & S. Bykov. 'UV Raman Demonstrates that  $\alpha$ -Helical Polyalanine Peptides Melt to Polyproline II Conformations'. *J. Am. Chem. Soc.* **2004.** 126, 8433–8440.
- [14] K. Bacia, I. V. Majoul, & P. Schwille. 'Probing the Endocytic Pathway in Live Cells Using Dual-Color Fluorescence Cross-Correlation Analysis'. *Biophys. J.* **2002.** 83, 1184–1193.
- [15] P. Ball. 'Quinolone generations: natural history or natural selection?' *J. Antimicrob. Chemother.* **2000.** 46(Topic T1), 17–24.
- [16] P. Ball. 'Adverse drug reactions: implications for the development of fluoroquinolones'. *J. Antimicrob. Chemother.* **2003.** 51 (Suppl. S1), 21–27.
- [17] P. Ball, L. Mandell, Y. Niki, & G. Tillotson. 'Comparative tolerability of the newer fluoroquinolone antibacterials'. *Drug Safety* **1999.** 21, 407–421.
- [18] F. M. Barnard & A. Maxwell. 'Interaction between DNA gyrase and quinolones: effects of alanine mutations at GyrA subunit residues Ser83 and Asp87'. *Antimicrob. Agents Chemother.* **2001.** 45(7), 1994–2000.

## Bibliography

- [19] K. Baumann. 'Chance correlation in variable subset regression: Influence of the objective function, the selection mechanism, and ensemble averaging.' *QSAR Comb. Sci.* **2005**. 24, 1033–1046.
- [20] K. Baumann, H. Albert, & M. von Korff. 'A systematic evaluation of the benefits and hazards of variable selection in latent variable regression. Part I: Theory and simulations'. *J. Chemom.* **2002**. 16, 339–350.
- [21] A. D. Becke. 'Density-functional thermochemistry. III. The role of exact exchange'. *J. Chem. Phys.* **1993**. 98(7), 5648–5652.
- [22] K. R. Beebe, R. J. Pell, & M. B. Seasholtz. *Chemometrics - A practical guide*. John Wiley & Sons, Inc., New York, **1998**.
- [23] J. M. Benevides, S. A. Overman, & G. J. Thomas Jr. 'Raman, polarized Raman and ultraviolet resonance Raman spectroscopy of nucleic acids and their complexes'. *J. Raman Spectrosc.* **2005**. 36, 279–299.
- [24] J. M. Benevides, D. Serban, & G. J. Thomas Jr. 'Structural Perturbations Induced in Linear and Circular DNA by the Architectural Protein HU from *Bacillus stearothermophilus*'. *Biochemistry* **2006**. 45(16), 5359–5366.
- [25] J. M. Benevides & G. J. Thomas Jr. 'Local Conformational Changes Induced in B-DNA by Ethidium Intercalation'. *Biochemistry* **2005**. 44, 2993–2999.
- [26] J. M. Benevides, A. H.-J. Wang, G. A. v. d. Marel, J. H. v. Boom, & G. J. Thomas Jr. 'Effect of the G\*T Mismatch on Backbone and Sugar Conformations of Z-DNA and B-DNA: Analysis by Raman Spectroscopy of Crystal and Solution Structures of d(CGCGTG) and d(CGCGCG)'. *Biochemistry* **1989**. 28, 304–310.
- [27] C. J. Benham. 'Torsional stress and local denaturation in supercoiled DNA'. *Proc. Natl. Acad. Sci. USA* **1979**. 76(8), 3870–3874.
- [28] M. L. Bennink, D. N. Nikova, K. O. van der Werf, & J. Greve. 'Dynamic imaging of single DNA-protein interactions using atomic force microscopy'. *Anal. Chim. Acta* **2003**. 479(1), 3–15.
- [29] J. M. Berger, S. J. Gamblin, S. C. Harrison, & J. C. Wang. 'Structure and mechanism of DNA topoisomerase II'. *Nature* **1996**. 379(6562), 225–232.
- [30] B. E. Billingham & G. R. Loppnow. 'Excited-State Structural Dynamics of Cytosine from Resonance Raman Spectroscopy'. *J. Phys. Chem. A* **2006**. 110(7), 2353–2359.
- [31] L. Billot, M. Lamy de la Chapelle, A.-S. Grimault, A. Vial, D. Barchiesi, J.-L. Bijeon, P.-M. Adam, & P. Royer. 'Surface enhanced Raman scattering on gold nanowire arrays: Evidence of strong multipolar surface plasmon resonance enhancement'. *Chem. Phys. Lett.* **2006**. 422, 303–307.
- [32] G. Binnig, H. Rohrer, C. Gerber, & E. Weibel. 'Surface studies by scanning tunneling microscopy'. *Physical Review Letters* **1982**. 49(1), 57–61.
- [33] H. C. Birnboim & J. Doly. 'A rapid alkaline extraction procedure for screening recombinant plasmid DNA'. *Nucleic Acids Res.* **1979**. 7(6), 1513–1523.
- [34] G. M. Blackburn & M. J. Gait. *Nucleic Acids in Chemistry and Biology*. Oxford University Press, New York, **1996**.
- [35] M. Bolboaca, W. Kiefer, & J. Popp. 'Fourier Transform Raman and Surface-enhanced Raman Spectroscopy of some Quinoline Derivatives'. *J. Raman Spectrosc.* **2002**. 33, 207–212.
- [36] M. G. Bowden, W. Chen, J. Singvall, Y. Xu, S. J. Peacock, V. Valtulina, P. Speziale, & M. Höök. 'Identification and preliminary characterization of cell-wall-anchored proteins of *Staphylococcus epidermidis*'. *Microbiology* **2005**. 151, 1453–1464.
- [37] M. N. Boydon & S. A. Asher. 'UV Raman Studies of Peptide Conformation Demonstrate Demonstrate That Betanovine Does Not Cooperatively Unfold'. *Biochemistry* **2001**. 40, 13 723–13 727.

- [38] S. Brahms, S. Nakasu, A. Kikuchi, & J. G. Brahms. 'Structural changes in positively and negatively supercoiled DNA'. *Eur. J. Biochem. (FEBS)* **1989**. 184, 297–303.
- [39] C. S. Braun, G. S. Jas, S. Choosakoonkriang, G. S. Koe, J. G. Smith, & C. R. Middaugh. 'The structure of DNA within cationic lipid/DNA complexes'. *Biophys. J.* **2003**. 84(2, Pt. 1), 1114–1123.
- [40] L. Breiman. 'Bagging Predictors'. *Mach. Learn.* **1996**. 24, 123–140.
- [41] L. Brino, A. Urzhumtsev, M. Mousli, C. Bronner, A. Mitschler, P. Oudet, & D. Moras. 'Dimerization of Escherichia coli DNA-gyrase B Provides a Structural Mechanism for Activating the ATPase Catalytic Center'. *J. Biol. Chem.* **2000**. 275(13), 9468–9475.
- [42] P. O. Brown & N. R. Cozzarelli. 'A sign inversion mechanism for enzymatic supercoiling of DNA'. *Science* **1979**. 206, 1081–1083.
- [43] R. Brown, J. Gallop, & M. Milton. 'Review of Techniques for Single Molecule Detection in Biological Applications'. *National Physical Laboratory Report COAM2* **2001**.
- [44] G. Burckhardt, A. Walter, H. Triebel, K. Stoerl, H. Simon, J. Stoerl, A. Opitz, E. Roemer, & C. Zimmer. 'Binding of 2-Azaanthraquinone Derivatives to DNA and Their Interference with the Activity of DNA Topoisomerases in Vitro'. *Biochemistry* **1998**. 37(14), 4703–4711.
- [45] J. H. M. Cabral, A. P. Jackson, C. V. Smith, N. Shikotra, A. Maxwell, & R. C. Liddington. 'Crystal Structure of the Breakage-Reunion Domain of DNA Gyrase'. *Nature* **1997**. 388, 903–906.
- [46] P. R. Callis. 'Electronic states and luminescence of nucleic acid systems'. *Annu. Rev. Phys. Chem.* **1983**. 34, 329–357.
- [47] P. Carmona, M. Molina, A. Lasagabaster, R. Escobar, & A. Ben Altabef. 'Vibrational analysis of the hydrogen bonding of cytidine and guanosine derivatives'. *J. Phys. Chem.* **1993**. 97(37), 9519–9524.
- [48] J. J. Champoux. 'DNA Topoisomerases: Structure, Function, and Mechanism'. *Annu. Rev. Biochem.* **2001**. 70, 369–413.
- [49] M. C. Chen, R. C. Lord, & R. Mendelsohn. 'Laser-Excited Raman Spectroscopy of Biomolecules. V. Conformational Changes Associated with the Chemical Denaturation of Lysozyme'. *J. Am. Chem. Soc.* **1974**. 96(10), 3038–3042.
- [50] Z. Chi, X. G. Chen, J. S. W. Holtz, & S. A. Asher. 'UV Resonance Raman-Selective Amide Vibrational Enhancement: Quantitative Methodology for Determining Protein Secondary Structure'. *Biochemistry* **1998**. 37, 2854–2864.
- [51] L.-P. Choo-Smith, K. Maquelin, T. v. Vreeswijk, H. A. Bruining, G. J. Puppels, N. A. Ngo Thi, K. C., D. Naumann, D. Ami, A. M. Villa, F. Orsini, S. M. Doglia, L. H., G. D. Sockalingum, M. Manfait, P. Allouch, & H. P. Endtz. 'Investigating Microbial (Micro)colony Heterogeneity by Vibrational Spectroscopy'. *Appl. Environ. Microbiol.* **2001**. 67(4), 1461–1469.
- [52] R. J. H. Clark & P. D. Mitchell. 'Resonance Raman and Preresonance Raman Spectra of Titanium Tetraiodide'. *J. Am. Chem. Soc.* **1973**. 95(25), 8300–8304.
- [53] L. Clowney, S. C. Jain, A. R. Srinivasan, J. Westbrook, W. K. Olson, & H. M. Berman. 'Geometric Parameters in Nucleic Acids: Nitrogenous Bases'. *J. Am. Chem. Soc.* **1996**. 118, 509–518.
- [54] K. D. Corbett, R. K. Shultzaberger, & J. M. Berger. 'The C-terminal domain of DNA gyrase A adopts a DNA-bending beta-pinwheel fold'. *Proc. Natl. Acad. Sci. U. S. A.* **2004**. 101(19), 7293–7298.
- [55] L. Costenaro, J. G. Grossmann, C. Ebel, & A. Maxwell. 'Small-Angle X-Ray Scattering Reveals the Solution Structure of the Full-Length DNA Gyrase A Subunit'. *Structure* **2005**. 13, 287–296.
- [56] T. M. Cotton, R. A. Uphaus, & D. Möbius. 'Distance Dependence of Surface-Enhanced Resonance Raman Enhancement in Langmuir-Blodgett Dye Multilayers'. *J. Phys. Chem.* **1986**. 90(23), 6071–6073.

## Bibliography

- [57] V. W. Couling, P. Fischer, D. Klenerman, & W. Huber. 'Ultraviolet resonance Raman study of drug binding in dihydrofolate reductase, gyrase, and catechol O-methyltransferase'. *Biophys. J.* **1998**. 75(2), 1097–1106.
- [58] V. W. Couling, N. W. Foster, & D. Klenerman. 'Ultraviolet resonance Raman spectroscopic study of the average environment of tyrosine in native and denatured barnase'. *J. Raman Spectrosc.* **1997**. 28(1), 33–38.
- [59] L. V. Crawford & M. J. Waring. 'Supercoiling of Polyoma Virus DNA measured by its Interaction with Ethidium Bromide'. *J. Mol. Biol.* **1967**. 25, 23–30.
- [60] J. A. Creighton. 'The Selection Rules for Surface Enhanced Raman Spectroscopy'. In R. J. H. Clark & R. Hester (eds.), *Spectroscopy of Surfaces*. John Wiley & Sons, **1988**.
- [61] K. De Gussem, P. Vandenabeele, A. Verbeken, & L. Moens. 'Raman spectroscopic study of Lactarius spores (Russulales, Fungi)'. *Spectrochim. Acta, Part A* **2004**. 61, 2896–2908.
- [62] H. Deng, V. A. Bloomfield, J. M. Benevides, & G. J. Thomas Jr. 'Dependence of the Raman Signature of Genomic B-DNA on Nucleotide Base Sequence'. *Biopolymers* **1999**. 50, 656–666.
- [63] J. A. Dieringer, A. D. McFarland, N. C. Shah, D. A. Stuart, A. V. Whitney, C. R. Yonzon, M. A. Young, X. Zhang, & R. P. Van Duyne. 'Surface enhanced Raman spectroscopy: new materials, concepts, characterization tools, and applications'. *Faraday Discuss.* **2005**. 1–18.
- [64] T. G. Dietterich. *Ensemble Methods in Machine Learning*. Multiple Classifier Systems, Lecture Notes in Computational Sciences 1857. Springer, **2001**.
- [65] H. G. M. Edwards, N. C. Russell, R. Weinstein, & D. D. Wynn-Williams. 'Fourier Transform Raman Spectroscopic Study of Fungi'. *J. Raman Spectrosc.* **1995**. 26, 911–916.
- [66] S. Efrima, B. V. Bronk, & J. Czege. 'Surface enhanced Raman spectroscopy of bacteria coated by silver'. *Proc. SPIE* **1999**. 3602, 164–171.
- [67] T. Egawa & S.-R. Yeh. 'Structural and functional properties of hemoglobins from unicellular organisms as revealed by resonance Raman spectroscopy'. *Journal of Inorganic Biochemistry* **2005**. 99(1), 72–96.
- [68] J. S. Ellis, H. G. Abdelhady, S. Allen, M. C. Davies, C. J. Roberts, S. J. B. Tendler, & P. M. Williams. 'Direct atomic force microscopy observations of monovalent ion induced binding of DNA to mica'. *J. Microscopy* **2004**. 215, 297–301.
- [69] A. M. Emmerson & A. M. Jones. 'The quinolones: decades of development and use'. *J. Antimicrob. Chemother.* **2003**. 51 (Suppl. S1), 13–20.
- [70] S. C. Erfurth, E. J. Kiser, & W. L. Peticolas. 'Determination of the Backbone Structure of Nucleic Acids and Nucleic Acid Oligomers by Laser Raman Scattering'. *Proc. Natl. Acad. Sci. USA* **1972**. 69(4), 938–941.
- [71] D. W. Feldman, J. Parker, James H., & M. Ashkin. 'Raman Scattering by Optical Modes of Metals'. *Phys. Rev. Lett.* **1968**. 21(9), 607–608.
- [72] Z. Filip, S. Herrmann, & J. Kubat. 'FT-IR spectroscopic characteristics of diefferently cultivated *Bacillus subtilis*'. *Microbiol. Res.* **2004**. 159, 257–262.
- [73] M. Fleischmann, P. J. Hendra, & A. J. McQuillan. 'Raman spectra of pyridine adsorbed at a silver electrode'. *Chem. Phys. Lett.* **1974**. 26(2), 163–166.
- [74] A. J. Florence, A. R. Kennedy, N. Shankland, E. Wright, & A. Al-Rubayi. 'Norfloxacin Dihydrate'. *Acta Cryst.* **2000**. C56, 1372–1373.
- [75] J. Florian. 'Scaled Quantum Mechanical Force Fields and Vibrational Spectra of Solid-state Nucleic Acid Constituents, 6. Guanine and Guanine Residue'. *J. Phys. Chem.* **1993**. 97, 10 649–10 658.

- [76] J. Florian, V. Baumruk, & J. Leszczynski. 'IR and Raman Spectra, Tautomeric Stabilities, and Scaled Quantum Mechanical Force Fields of Protonated Cytosine'. *J. Phys. Chem.* **1996**. 100(13), 5578–5589.
- [77] S. P. A. Fodor, R. P. Rava, T. R. Hays, & T. G. Spiro. 'Ultraviolet Resonance Raman Spectroscopy of the Nucleotides with 266-, 240-, 218-, and 200-nm Pulsed Laser Excitation'. *J. Am. Chem. Soc.* **1985**. 107, 1520–1529.
- [78] S. P. A. Fodor & T. G. Spiro. 'Ultraviolet Resonance Raman Spectroscopy of DNA with 200-266-nm Laser Excitation'. *J. Am. Chem. Soc.* **1986**. 108, 3198–3205.
- [79] N. Fujimoto, A. Toyama, & H. Takeuchi. 'Effects of hydrogen bonding on the UV resonance Raman bands of the adenine ring and its C8-deuterated analog'. *J. Mol. Struct.* **1998**. 447, 61–69.
- [80] X. Gao, J. P. Davies, & M. J. Weaver. 'A Test of Surface Selection Rules for Surface-Enhanced Raman Scattering: The Orientation of Adsorbed Benzene and Monosubstituted Benzenes on Gold'. *J. Phys. Chem.* **1990**. 94(17), 6858–6864.
- [81] K. Gaus. 'Klassifizierung von Milchsäurebakterien aus Joghurt mit schwingungsspektroskopischen Methoden'. Diplomarbeit, Friedrich-Schiller-Universität Jena, **2005**.
- [82] K. Gaus, P. Roesch, R. Petry, K. D. Peschke, O. Ronneberger, H. Burkhardt, K. Baumann, & J. Popp. 'Classification of lactic acid bacteria with UV-resonance Raman spectroscopy'. *Biopolymers* **2006**. 82(4), 286–290.
- [83] R. A. Gaussian 98, M. J. Frisch, G. W. Trucks, H. B. Schlegel, G. E. Scuseria, M. A. Robb, J. R. Cheeseman, V. G. Zakrzewski, J. J. A. Montgomery, R. E. Stratmann, J. C. Burant, S. Dapprich, J. M. Millam, A. D. Daniels, K. N. Kudin, M. C. Strain, O. Farkas, J. Tomasi, V. Barone, M. Cossi, R. Cammi, B. Mennucci, C. Pomelli, C. Adamo, S. Clifford, J. Ochterski, G. A. Petersson, P. Y. Ayala, Q. Cui, K. Morokuma, N. Rega, P. Salvador, J. J. Dannenberg, D. K. Malick, A. D. Rabuck, K. Raghavachari, J. B. Foresman, J. Cioslowski, J. V. Ortiz, A. G. Baboul, B. B. Stefanov, G. Liu, A. Liashenko, P. Piskorz, I. Komaromi, R. Gomperts, R. L. Martin, D. J. Fox, T. Keith, M. A. Al-Laham, C. Y. Peng, A. Nanayakkara, M. Challacombe, P. M. W. Gill, B. Johnson, W. Chen, M. W. Wong, J. L. Andres, C. Gonzalez, M. Head-Gordon, E. S. Replogle, J. A. Pople, & P. P. Gaussian, Inc. **2002**.
- [84] B. Giese & D. McNaughton. 'Density functional theoretical (DFT) and surface-enhanced Raman spectroscopic study of guanine and its alkylated derivatives Part 1. DFT calculations on neutral, protonated and deprotonated guanine'. *Phys. Chem. Chem. Phys.* **2002**. 4, 5161–5170.
- [85] B. Giese & D. McNaughton. 'Surface-Enhanced Raman Spectroscopic and Density Functional Theory Study of Adenine Adsorption to Silver Surfaces'. *J. Phys. Chem. B* **2002**. 106, 101–112.
- [86] R. Goodacre, E. M. Timmins, R. Burton, N. Kaderbhai, A. M. Woodward, D. B. Kell, & P. J. Rooney. 'Rapid identification of urinary tract infection bacteria using hyperspectral whole-organism fingerprinting and artificial neural networks'. *Microbiology* **1998**. 144, 1157–1170.
- [87] J. Grand, S. Kostcheev, J.-L. Bijeon, M. Lamy de la Chapelle, P.-M. Adam, A. Romyantseva, G. Lerondel, & P. Royer. 'Optimization of SERS-active substrates for near-field Raman spectroscopy'. *Synth. Met.* **2003**. 139, 621–624.
- [88] C. H. Gross, J. D. Parsons, T. H. Grossman, P. S. Charifson, S. Bellon, J. Jernee, M. Dwyer, S. P. Chambers, W. Markland, M. Botfield, & S. A. Raybuck. 'Active-Site Residues of Escherichia coli DNA Gyrase Required in Coupling ATP Hydrolysis to DNA Supercoiling and Amino Acid Substitutions Leading to Novobiocin Resistance'. *Antimicrob. Agents Chemother.* **2003**. 47(3), 1037–1046.
- [89] A. J. Haes, S. Zou, J. Zhao, G. C. Schatz, & R. P. Van Duyne. 'Localized Surface Plasmon Resonance Spectroscopy near Molecular Resonances'. *J. Am. Chem. Soc.* **2006**. 128, 10905–10914.
- [90] R. Hande, Kenneth. 'Clinical applications of anticancer drugs targeted to topoisomerase II'. *Biochim. Biophys. Acta* **1998**. 1400(1-3), 173–184.

## Bibliography

- [91] H. G. Hansma. 'Surface biology of DNA by atomic force microscopy'. *Annu. Rev. Phys. Chem.* **2001**. 52, 71–92.
- [92] I. Harada & H. Takeuchi. *Advances in Spectroscopy: Spectroscopy of Biological Systems*. Wiley, New York, **1986**.
- [93] A. Hartschuh, M. R. Beversluis, A. Bouhelier, & L. Novotny. 'Tip-enhanced optical spectroscopy'. *Phil. Trans. R. Soc. Lond. A* **2004**. 362, 807–819.
- [94] A. Hartschuh, E. J. Sanchez, X. S. Xie, & L. Novotny. 'High-Resolution Near-Field Raman Microscopy of Single-Walled Carbon Nanotubes'. *Phys. Rev. Lett.* **2003**. 90(9), 095 503.
- [95] M. Harz, U. Neugebauer, P. Rösch, & J. Popp. 'Raman spectroscopy: A powerful tool for the investigations and identification of bacterial cells'. *G.I.T. Laboratory Journal Europe* **2006**. 3, 26–28.
- [96] M. Harz, P. Rösch, K.-D. Peschke, O. Ronneberger, H. Burkhardt, & J. Popp. 'Micro-Raman spectroscopic identification of bacterial cells of the genus *Staphylococcus* and dependence on their cultivation conditions'. *Analyst* **2005**. 130, 1543–1550.
- [97] J. Heddle & A. Maxwell. 'Quinolone-binding pocket of DNA gyrase: role of GyrB'. *Antimicrob. Agents Chemother.* **2002**. 46(6), 1805–1815.
- [98] J. G. Heddle, F. M. Barnard, L. M. Wentzell, & A. Maxwell. 'The Interaction of Drugs With DNA Gyrase: A Model For The Molecular Basis Of Quinolone Action'. *Nucleosides, Nucleotides Nucleic Acids* **2000**. 19(8), 1249–1264.
- [99] J. G. Heddle, S. Mittelheiser, A. Maxwell, & N. H. Thomson. 'Nucleotide Binding to DNA Gyrase Causes Loss of DNA Wrap'. *J. Mol. Biol.* **2004**. 337, 597–610.
- [100] R. Henrion & G. Henrion. *Multivariate Datenanalyse - Methodik und Anwendung in der Chemie und verwandten Gebieten*. Springer-Verlag, Berlin, Heidelberg, **1995**.
- [101] U. Holzgrabe. 'Gyrasehemstoffe im Abwind?' *Pharmazeutische Zeitung* **2000**. 42.
- [102] D. C. Hooper. 'Clinical application of quinolones'. *Biochim. Biophys. Acta* **1998**. 1400, 45–61.
- [103] W. E. Huang, R. I. Griffiths, I. P. Thompson, M. J. Bailey, & W. A. S. 'Raman Microscopic Analysis of Single Microbial Cells'. *Anal. Chem.* **2004**. 76, 4452–4458.
- [104] D. Hutsebaut, K. Maquelin, P. De Vos, P. Vandenabeele, L. Moens, & G. J. Puppels. 'Effect of Culture Conditions on the Achievable Taxonomic Resolution of Raman Spectroscopy Disclosed by Three *Bacillus* Species'. *Anal. Chem.* **2004**. 76, 6274–6281.
- [105] N. R. Isola, D. L. Stokes, & T. Vo-Dinh. 'Surface-Enhanced Raman Gene Probe for HIV Detection'. *Anal. Chem.* **1998**. 70, 1252–1356.
- [106] R. M. Jarvis, A. Brooker, & R. Goodacre. 'Surface-Enhanced Raman Spectroscopy for Bacterial Discrimination Utilizing a Scanning Electron Microscope with a Raman Spectroscopy Interface'. *Anal. Chem.* **2004**. 76, 5198–5202.
- [107] R. M. Jarvis & R. Goodacre. 'Discrimination of Bacteria Using Surface-Enhanced Raman Spectroscopy'. *Anal. Chem.* **2004**. 76, 40–47.
- [108] R. M. Jarvis & R. Goodacre. 'Ultra-violet resonance Raman spectroscopy for the rapid discrimination of urinary tract infection bacteria'. *FEMS Microbiol. Lett.* **2004**. 232, 127–132.
- [109] U. Jayasooriya & R. D. Jenkins. 'Introduction to Raman Spectroscopy'. In D. L. Andrews & A. A. Demidov (eds.), *Laser Spectroscopy*, 2nd ed. Kluwer Academic/Plenum Publishers, New York, **2002** 77ff.
- [110] D. L. Jeanmaire & R. P. van Duyne. 'Surface Raman Spectroelectrochemistry Part I. Heterocyclic, Aromatic, and Aliphatic Amines Adsorbed on the Anodized Silver Electrode'. *J. Electroanal. Chem.* **1977**. 84, 1–20.

- [111] E. Jimenez-Lonzano, I. Marques, D. Barron, J. L. Beltran, & J. Barbosa. 'Determination of pka values of quinolones from mobility and spectroscopic data obtained by capillary electrophoresis and a diode array detector'. *Anal. Chim. Acta* **2002**. 464, 37–45.
- [112] S. Kampranis & A. Maxwell. 'Conversion of DNA gyrase into a conventional type II topoisomerase'. *Proc. Natl. Acad. Sci. U. S. A.* **1996**. 93, 14416–14421.
- [113] W. Kiefer & H. J. Bernstein. 'Vibrational-Rotational Structure in the Resonance Raman Effect of Iodine Vapor'. *J. Mol. Spectrosc.* **1972**. 43, 366–381.
- [114] J. R. Kincaid. 'Resonance raman spectra of heme proteins and model compounds'. *Porphyrin Handbook* **2000**. 7, 225–291.
- [115] J. R. Kincaid & K. Czarnecki. 'Resonance Raman: bioinorganic applications'. *Comprehensive Coordination Chemistry II* **2004**. 2, 131–140.
- [116] T. Kitagawa. 'Resonance Raman spectroscopy'. *Journal of Porphyrins and Phthalocyanines* **2002**. 6(4), 301–302.
- [117] T. Kitagawa & Y. Mizutani. 'Resonance Raman spectra of highly oxidized metalloporphyrins and heme proteins'. *Coordination Chemistry Reviews* **1994**. 135/136, 685–735.
- [118] P. H. Klesius & V. T. Schuhardt. 'Use of Lysostaphin in the Isolation of Highly Polymerized Deoxyribonucleic Acid and in the Taxonomy of Aerobic Micrococcaceae'. *J. Bacteriol.* **1968**. 95(3), 739–743.
- [119] K. Kneipp, A. S. Haka, H. Kneipp, K. Badizadegan, N. Yoshizawa, C. Boone, K. E. Shafer-Peltier, J. T. Motz, R. R. Dasari, & M. S. Feld. 'Surface-Enhanced Raman Spectroscopy in Single Living Cells Using Gold Nanoparticles'. *Appl. Spectrosc.* **2002**. 56(2), 150–154.
- [120] K. Kneipp, H. Kneipp, I. Itzkan, R. R. Dasari, & M. S. Feld. 'Ultrasensitive Chemical Analysis by Raman Spectroscopy'. *Chem. Rev.* **1999**. 99, 2957–2975.
- [121] K. Kneipp, H. Kneipp, I. Itzkan, R. R. Dasari, & M. S. Feld. 'Surface-enhanced Raman scattering and biophysics'. *J. Phys.: Condens. Matter* **2002**. 14, R597–R624.
- [122] K. Kneipp, W. Yang, R. R. Dasari, & M. S. Feld. 'Approach to Single Molecule Detection Using Surface-Enhanced Resonance Raman Scattering (SERRS): A Study Using Rhodamine 6G on Colloidal Silver'. *Appl. Spectrosc.* **1995**. 49(6), 780–785.
- [123] A. L. Koch. *Bacterial Growth and Form*. Chapman & Hall, **1995**.
- [124] C. Krafft, J. M. Benevides, & G. J. Thomas Jr. 'Secondary structure polymorphism in *Oxytricha nova* telomeric DNA'. *Nucleic Acids Res.* **2002**. 30(18), 3981–3991.
- [125] U. Kreibig & M. Vollmer. *Optical Properties of Metal Clusters*, vol. 25 of *Springer Series in Optical Sciences*. Springer, Berlin, **1995**.
- [126] A. Kudelski & B. Pettinger. 'SERS on carbon chain segments: monitoring locally surface chemistry'. *Chem. Phys. Lett.* **2000**. 321, 356–362.
- [127] D. M. Kuncicky, S. D. Christensen, & O. D. Velev. 'Role of the Micro- and Nanostructure in the Performance of Surface-Enhanced Raman Scattering Substrates Assembled from Gold Nanoparticles'. *Appl. Spectrosc.* **2005**. 59(4), 401–409.
- [128] A. Kusumi, Y. Sako, & M. Yamamoto. 'Confined lateral diffusion of membrane receptors as studied by single particle tracking (nanovid microscopy). Effects of calcium-induced differentiation in cultured epithelial cells'. *Biophys. J.* **1993**. 65, 2021–2040.
- [129] Landolt-Börnstein. *Numerical Data and Functional Relationships in Science and Technology*, vol. Volume 1, Subvolume d of *Group VII: Biophysics*. Springer Verlag, Berlin Heidelberg, **1990**.

## Bibliography

- [130] S. Lecomte & M. H. Baron. 'Surface-enhanced Raman spectroscopy investigation of fluoroquinolones-DNA-DNA gyrase-Mg<sup>2+</sup> interactions. II. Interaction of pefloxacin with Mg<sup>2+</sup> and DNA'. *Biospectroscopy* **1997**. 3(1), 31–45.
- [131] S. Lecomte, N. J. Moreau, & M.-T. Chenon. 'NMR investigation of pefloxacin-cation-DNA interactions: the essential role of Mg<sup>2+</sup>'. *Int. J. Pharm.* **1998**. 164, 57–65.
- [132] C. Lee, W. Yang, & R. G. Parr. 'Development of the Colle-Salvetti correlation-energy formula into a functional of the electron density'. *Phys. Rev. B: Condens. Matter Mater. Phys.* **1988**. 37(2), 785–789.
- [133] S. A. Lee, A. Anderson, W. Smith, R. H. Griffey, & V. Mohan. 'Temperature-dependent Raman and infrared spectra of nucleosides. Part I - adenosine'. *J. Raman Spectrosc.* **2000**. 31, 891–896.
- [134] S. A. Lee, J. Li, A. Anderson, W. Smith, R. H. Griffey, & V. Mohan. 'Temperature-dependent Raman and infrared spectra of nucleosides. II - Cytidine'. *J. Raman Spectrosc.* **2001**. 32, 795–802.
- [135] S. A. Lee, A. Rupprecht, & Y. Z. Chen. 'Drug binding to DNA: observation of the drug-DNA hydrogen-bond-stretching modes of netropsin bound to DNA via Raman spectroscopy'. *Phys. Rev. Lett.* **1998**. 152, 2241–2244.
- [136] S. A. Lee, M. Schwenker, A. Anderson, & L. Lettress. 'Temperature-dependent Raman and infrared spectra of nucleosides. IV - Deoxyadenosine'. *J. Raman Spectrosc.* **2004**. 35, 324–331.
- [137] W. Lee, M. Alexe, K. Nielsch, & U. Gösele. 'Metal Membranes with Hierarchically Organized Nanotube Arrays'. *Chem. Mater.* **2005**. 17, 3325–3327.
- [138] M. Leeb. 'A shot in the arm'. *Nature* **2004**. 431(7011), 892–893.
- [139] J. Li, S. A. Lee, A. Anderson, L. Lettress, R. H. Griffey, & V. Mohan. 'Temperature-dependent Raman and infrared spectra of nucleosides. III - deoxycytidine'. *J. Raman Spectrosc.* **2003**. 34(3), 183–191.
- [140] D. M. J. Lilley. 'The inverted repeat as a recognizable structural feature in supercoiled DNA molecules'. *Proc. Natl. Acad. Sci. USA* **1980**. 77(11), 6468–6472.
- [141] J. L. Lippert, D. Tyminski, & P. J. Desmeules. 'Determination of the Secondary Structure of Proteins by Laser Raman Spectroscopy'. *J. Am. Chem. Soc.* **1976**. 98(22), 7075–7080.
- [142] P. D. Lister. 'Pharmacodynamics of Moxifloxacin and Levofloxacin against *Staphylococcus aureus* and *Staphylococcus epidermidis* in an In Vitro Pharmacodynamic Model'. *Clin. Infect. Dis.* **2001**. 32(Suppl 1), S33–38.
- [143] L. F. Liu & J. C. Wang. 'Micrococcus luteus DNA gyrase: active components and a model for its supercoiling of DNA'. *Proc. Natl. Acad. Sci.* **1978**. 75, 2098–2102.
- [144] D. Lockshon & D. r. Morris. 'Sites of Reaction of *Escherichia coli* DNA Gyrase on pBR322 in *Viva* as Revealed by Oxolinic Acid-induced Plasmid Linearization'. *J. Mol. Biol.* **1985**. 181, 63–74.
- [145] E. C. Lopez-Diez & R. Goodacre. 'Characterization of microorganisms using UV resonance Raman spectroscopy and chemometrics'. *Anal. Chem.* **2004**. 76(3), 585–591.
- [146] E. C. Lopez-Diez, C. L. Winder, L. Ashton, F. Currie, & R. Goodacre. 'Monitoring the Mode of Action of Antibiotics Using Raman Spectroscopy: Investigating Subinhibitory Effects of Amikacin on *Pseudomonas aeruginosa*'. *Anal. Chem.* **2005**. 77, 2901–2906.
- [147] A. P. MacGowan, K. E. Bowker, M. Wootton, & H. A. Holt. 'Exploration of the in-vitro pharmacodynamic activity of moxifloxacin for *Staphylococcus aureus* and streptococci of Lancefield Groups A and G'. *J. Antimicrob. Chemother.* **1999**. 44, 761–766.
- [148] M. Manfait, A. J. P. Alix, P. Jeannesson, J.-C. Jardillier, & T. Theophanides. 'Interaction of adriamycin with DNA as studied by resonance Raman spectroscopy'. *Nucleic Acids Res.* **1982**. 10(12), 3803–3816.



- [149] R. Manoharan, E. Ghiamati, S. Chadha, W. H. Nelson, & J. F. Sperry. 'Effect of Cultural Conditions on Deep UV Resonance Raman Spectra of Bacteria'. *Appl. Spectrosc.* **1993**. 47(12), 2145–2150.
- [150] K. Maquelin, L.-P. Choo-Smith, H. P. Endtz, H. A. Bruining, & G. J. Puppels. 'Rapid Identification of Candida Species by Confocal Raman Microspectroscopy'. *J. Clin. Microbiol.* **2002**. 40(2), 594–600.
- [151] K. Maquelin, L.-P. Choo-Smith, T. v. Vreeswijk, H. P. Endtz, B. Smith, R. Bennett, H. A. Bruining, & G. J. Puppels. 'Raman Spectroscopic Method for Identification of Clinically Relevant Microorganisms Growing on Solid Culture Medium'. *Anal. Chem.* **2000**. 72, 12–19.
- [152] K. Maquelin, C. Kirschner, L.-P. Choo-Smith, N. v. d. Braak, H. P. Endtz, D. Naumann, & G. J. Puppels. 'Identification of medically relevant microorganisms by vibrational spectroscopy'. *J. Microbiol. Methods* **2002**. 51, 255–271.
- [153] J. M. L. Martin & U. van Alsenoy, C.; modified by Uhlemann. 'gar2ped', **1995**.
- [154] Y. Maruyama & M. Futamata. 'Elastic scattering and emission correlated with single-molecule SERS'. *J. Raman Spectrosc.* **2005**. 36, 581–592.
- [155] M. Matsuno, H. Takeuchi, S. A. Overman, & G. J. Thomas Jr. 'Orientation of Tyrosines 21 and 24 in Coat Subunits of Ff Filamentous Virus: Determination by Raman Linear Intensity Difference Spectroscopy and Implications for Subunit Packing'. *Biophys. J.* **1998**. 74, 3217–3225.
- [156] A. Maxwell & D. M. Lawson. 'The ATP-binding site of type II topoisomerases as a target for antibacterial drugs'. *Curr. Top. Med. Chem.* **2003**. 3(3), 283–303.
- [157] V. Mazeta, C. Carteret, D. Brie, J. Idier, & B. Humbert. 'Background removal from spectra by designing and minimizing a non-quadratic cost function'. *Chemom. Intell. Lab. Syst.* **2005**. 76, 121–133.
- [158] C. J. McAllister, M. A. Karymov, Y. Kawano, A. Y. Lushnikov, A. Mikheikin, V. N. Uversky, & Y. L. Lyubchenko. 'Protein Interactions and Misfolding Analyzed by AFM Force Spectroscopy'. *J. Mol. Biol.* **2005**. 354(5), 1028–1042.
- [159] S. L. McCall, P. M. Platzman, & P. A. Wolff. 'Surface Enhanced Raman Scattering'. *Physics Letters* **1980**. 77A(5), 381–383.
- [160] C. R. Middaugh, R. K. Evans, D. L. Montgomery, & D. R. Casimiro. 'Analysis of Plasmid DNA from a Pharmaceutical Perspective'. *J. Pharm. Sci.* **1998**. 87(2), 130–146.
- [161] A. V. Mikhonin, N. S. Myshakina, S. Bykov, & S. A. Asher. 'UV Resonance Raman Determination of Polyproline II, Extended 2.51-Helix, and beta-Sheet Psi-Angle Energy Landscape in Poly-L-Lysine and Poly-L-Glutamic Acid'. *J. Am. Chem. Soc.* **2005**. 127, 7712–7720.
- [162] L. A. Mitscher. 'Bacterial Topoisomerase Inhibitors: Quinolone and Pyridone Antibacterial Agents'. *Chem. Rev.* **2005**. 105, 559–592.
- [163] I. Morrissey, K. Hoshino, K. Sato, A. Yoshida, I. Hayakawa, M. G. Bures, & L. L. Shen. 'Mechanism of Differential Activities of Ofloxacin Enantiomers'. *Antimicrob. Agents Chemother.* **1996**. 40(8), 1775–1784.
- [164] M. Moskovits. 'Surface-enhanced Raman spectroscopy: a brief retrospective'. *J. Raman Spectrosc.* **2005**. 36, 485–496.
- [165] M. Moskovits & J. S. Suh. 'Surface Selection Rules for Surface-Enhanced Raman Spectroscopy: Calculations and Application to the Surface-Enhanced Raman Spectrum of Phthalazine on Silver'. *J. Phys. Chem.* **1984**. 88(23), 5526–5530.
- [166] L. Movileanu, J. M. Benevides, & G. J. Thomas Jr. 'Determination of base and backbone contributions to the thermodynamics of premelting and melting transitions in B DNA'. *Nucleic Acids Res.* **2002**. 30(17), 3767–3777.

## Bibliography

- [167] L. Movileanu, J. M. Benevides, & G. J. Thomas Jr. 'Temperature Dependence of the Raman Spectrum of DNA. II. Raman Signatures of Premelting and Melting Transitions of Poly(dA)\*Poly(dT) and Comparison with Poly(dA-dT)\*Poly(dA-dT)'. *Biopolymers* **2002**. 63, 181–194.
- [168] E. Mutschler. *Arzneimittelwirkungen, Lehrbuch der Pharmakologie und Toxikologie*. 7th ed. Wissenschaftliche Verlagsgesellschaft mbH, Stuttgart, **1996**.
- [169] A. B. Myers & R. A. Mathies. *Biological Applications of Raman Spectroscopy*, vol. 2. Wiley, New York, **1987**.
- [170] A. B. Myers, R. A. Mathies, D. J. Tannor, & E. J. Heller. 'Excited state geometry changes from preresonance Raman intensities: Isoprene and hexatriene'. *J. Chem. Phys.* **1982**. 77, 3857.
- [171] I. Nabiev, K. V. Sokolov, & M. Manfait. 'Surface-enhanced Raman spectroscopy and its biomedical applications'. In R. J. H. Clark & R. Hester (eds.), *Advances in Spectroscopy*, vol. 20 Biomolecular Spectroscopy Part A. John Wiley & Sons, Chichester, **1993** 267–338.
- [172] D. Naumann. 'Infrared Spectroscopy in Microbiology'. In R. A. Meyers (ed.), *Encyclopedia of Analytical Chemistry*. John Wiley & Sons Ltd., Chichester, **2000** 102–131.
- [173] D. Naumann, D. Helm, & H. Labischinski. 'Microbiological characterization by FT-IR spectroscopy'. *Nature* **1991**. 351(6321), 81–82.
- [174] D. Naumann, D. Helm, H. Labischinski, & P. Giesbrecht. *The characterization of microorganisms by Fourier-transform infrared spectroscopy (FT-IR)*. Modern Techniques for Rapid Microbiological Analysis. VCH Publishers, New York, **1991**.
- [175] D. Naumann, S. Keller, D. Helm, C. Schultz, & B. Schrader. 'FT-IR Spectroscopy and FT-Raman Spectroscopy are powerful analytical tools for the non-invasive characterization of intact microbial cells'. *J. Mol. Struct.* **1995**. 347, 399–406.
- [176] W. W. Navarre & O. Schneewind. 'Surface Proteins of Gram-Positive Bacteria and Mechanisms of Their Targeting to the Cell Wall Envelope'. *Microbiol. Molecul. Biol. Rev.* **1999**. 63(1), 174–229.
- [177] W. H. Nelson, R. Manoharan, & J. F. Sperry. 'UV Resonance Raman Studies of Bacteria'. *Appl. Spectrosc. Rev.* **1992**. 27, 67–124.
- [178] U. Neugebauer, P. Rösch, M. Schmitt, J. Popp, C. Julien, A. Rasmussen, C. Budich, & V. Deckert. 'On the way to nanometer-sized information of the bacterial surface by means of tip-enhanced Raman spectroscopy (TERS)'. *ChemPhysChem* **2006**. 7, 1428–1430.
- [179] U. Neugebauer, U. Schmid, K. Baumann, U. Holzgrabe, W. Ziebuhr, S. Kozitskaya, W. Kiefer, M. Schmitt, & J. Popp. 'Characterization of Bacterial Growth and the Influence of Antibiotics by Means of UV Resonance Raman Spectroscopy'. *Biopolymers* **2006**. 82, 306–311.
- [180] U. Neugebauer, U. Schmid, K. Baumann, W. Ziebuhr, S. Kozitskaya, V. Deckert, M. Schmitt, & J. Popp. 'Towards a detailed understanding of the bacterial metabolism - A comprehensive vibrational spectroscopic characterization of Staphylococcus epidermidis'. *ChemPhysChem* **2006**. accepted.
- [181] A. Nicholls. 'Graphical representation and analysis of surface properties', **1992**.
- [182] S. Nie & S. R. Emory. 'Probing Single Molecules and Single Nanoparticles by Surface-Enhanced Raman Scattering'. *Science* **1997**. 275, 1102–1106.
- [183] Y. Nishimura, M. Tsuboi, & T. Sato. 'Structure-spectrum correlation in nucleic acids. I. Raman lines in the 600-700 cm<sup>-1</sup> range of guanosine residue'. *Nucleic Acids Res.* **1984**. 12(17), 6901–6908.
- [184] I. Nottingher & A. Elfick. 'Effect of Sample and Substrate Electric Properties on the Electric Field Enhancement at the Apex of SPM Nanotips'. *J. Phys. Chem. B* **2005**. 109, 15 699–15 706.

- [185] I. Notingher, S. Verrier, H. S., J. M. Polak, & L. L. Hench. 'Spectroscopic Study of Human Lung Epithelial Cells (A549) in Culture: Living Cells Versus Dead Cells'. *Biopolymers (Biospectroscopy)* **2003**. 72, 230–240.
- [186] M. J. Nowak, L. Lapinski, J. S. Kwiatkowski, & J. Leszczynski. 'Molecular Structure and Infrared Spectra of Adenine. Experimental Matrix Isolation and Density Functional Theory Study of Adenine <sup>15</sup>N Isotopomers'. *J. Phys. Chem.* **1996**. 100, 3527–3534.
- [187] M. E. Nunez, M. O. Martin, P. H. Chan, L. K. Duong, A. R. Sindhurakar, & E. M. Spain. 'Atomic Force Microscopy of Bacterial Communities'. *Methods in Enzymology* **2005**. 397, 256–268.
- [188] G. Orphanides & A. Maxwell. 'Evidence for a conformational change in the DNA gyrase-DNA complex from hydroxyl radical footprinting'. *Nucleic Acids Res.* **1994**. 22, 1567–1575.
- [189] A. Otto. 'The 'chemical' (electronic) contribution to surface-enhanced Raman scattering'. *J. Raman Spectrosc.* **2005**. 36, 497–509.
- [190] A. Otto, I. Mrozek, H. Grabhorn, & W. Akemann. 'Surface-enhanced Raman scattering'. *J. Phys.: Condens. Matter* **1992**. 4, 1143–1212.
- [191] S. A. Overman & G. J. Thomas Jr. 'Raman Markers of Nonaromatic Side Chains in an alpha-Helix Assembly: Ala, Asp, Glu, Gly, Ile, Leu, Lys, Ser, and Val Residues of Phage fd Subunits'. *Biochemistry* **1999**. 38, 4018–4027.
- [192] P. G. Pappas. 'Laboratory in the diagnosis and management of urinary tract infections'. *Med. Clin. N. Am.* **1991**. 75(2), 313–325.
- [193] J. P. Perdew, J. A. Chevary, S. H. Vosko, K. A. Jackson, M. R. Pederson, D. J. Singh, & C. Fiolhais. 'Atoms, molecules, solids, and surfaces: Applications of the generalized gradient approximation for exchange and correlation'. *Phys. Rev. B: Condens. Matter Mater. Phys.* **1992**. 46(11), 6671–6687.
- [194] U. Petersen. 'Von der Nalidixinsäure zu den Chinolonen der dritten Generation'. *Pharmazie in unserer Zeit* **2001**. 5(376-380).
- [195] R. Petry, M. Schmitt, & J. Popp. 'Raman spectroscopy-a prospective tool in the life sciences'. *ChemPhysChem* **2003**. 4(1), 14–30.
- [196] B. Pettinger, G. Picardi, R. Schuster, & G. Ertl. 'Surface-enhanced and STM tip-enhanced Raman spectroscopy of CN-ions at gold surfaces'. *J. Electroanal. Chem.* **2003**. 554-555, 293–299.
- [197] B. Pettinger, B. Ren, G. Picardi, R. Schuster, & G. Ertl. 'Nanoscale Probing of Adsorbed Species by Tip-Enhanced Raman Spectroscopy'. *Phys. Rev. Lett.* **2004**. 92, 096 101–096 101–096 104.
- [198] B. Pettinger, B. Ren, G. Picardi, R. Schuster, & G. Ertl. 'Tip-enhanced Raman spectroscopy (TERS) of malachite green isothiocyanate at Au(111): bleaching behavior under the influence of high electromagnetic field'. *J. Raman Spectrosc.* **2005**. 36, 541–550.
- [199] W. G. Pitt & S. A. Ross. 'Ultrasound Increases the Rate of Bacterial Cell Growth'. *Biotechnol. Prog.* **2003**. 19, 1038–1044.
- [200] Y. Pommier, P. Pourquier, Y. Fan, & D. Strumberg. 'Mechanism of action of eukariotic DNA topoisomerase I and drugs targeted to the enzyme'. *Biochim. Biophys. Acta, Gene Struct. Expression* **1998**. 1400(1-3), 83–105.
- [201] L. H. Pope, M. C. Davies, C. A. Laughton, C. J. Roberts, S. J. B. Tendler, & P. M. Williams. 'Intercalation-induced changes in DNA supercoiling observed in real-time by atomic force microscopy'. *Anal. Chim. Acta* **1999**. 400, 27–32.
- [202] W. R. Premasiri, D. T. Moir, M. S. Klemperer, N. Krieger, G. Jones, & L. D. Ziegler. 'Characterization of the Surface Enhanced Raman Scattering (SERS) of Bacteria'. *J. Phys. Chem. B* **2005**. 109, 312–320.

## Bibliography

- [203] R. Purrello, M. Molina, Y. Wang, G. Smulevich, J. R. Fresco, T. G. Spiro, & J. Fossella. 'Keto-iminol tautomerism of protonated cytidine monophosphate characterized by ultraviolet resonance Raman spectroscopy: implications of C<sup>+</sup> iminol tautomer for base mispairing'. *J. Am. Chem. Soc.* **1993**. 115(2), 760–767.
- [204] A. Rasmussen & V. Deckert. 'New dimension in nano-imaging: breaking through the diffraction limit with scanning near-field optical microscopy'. *Anal. Bioanal. Chem.* **2005**. 381, 165–172.
- [205] A. Rasmussen & V. Deckert. 'Surface- and tip-enhanced Raman scattering of DNA components'. *J. Raman Spectrosc.* **2006**. 37(1-3), 311–317.
- [206] G. Rauhut & P. Pulay. 'Transferable Scaling Factors for Density Functional Derived Vibrational Force Fields'. *J. Phys. Chem.* **1995**. 99, 3093–3100.
- [207] R. P. Rava & T. G. Spiro. 'Resonance Enhancement in the Ultraviolet Raman Spectra of Aromatic Amino Acids'. *J. Phys. Chem.* **1985**. 89, 1856–1861.
- [208] R. J. Reece & A. Maxwell. 'The C-terminal domain of the Escherichia coli DNA gyrase A subunit is a DNA-binding protein.' *Nucleic Acids Res.* **1991**. 19, 1399–1405.
- [209] M. Refregiers, A. Laigle, B. Jolles, G. V. Wheeler, & L. Chinsky. 'Resonance Raman analysis of a fluorescently labeled oligonucleotide forming a very stable hairpin'. *Eur. Biophys. J.* **1997**. 26, 277–281.
- [210] B. Ren, G. Picardi, B. Pettinger, R. Schuster, & G. Ertl. 'Tip-enhanced Raman spectroscopy of benzenethiol adsorbed on Au and Pt single-crystal surfaces'. *Angew. Chem., Int. Ed. (2004)* **2005**. 44(1), 139–142.
- [211] D. Richards, R. G. Milner, F. Huang, & F. Festy. 'Tip-enhanced Raman microscopy: practicalities and limitations'. *J. Raman Spectrosc.* **2003**. 34, 663–667.
- [212] N. A. Richardson, S. S. Wesolowski, & H. F. Schaefer. 'Electron Affinity of the Guanine-Cytosine Base Pair and Structural Perturbations upon Anion Formation'. *J. Am. Chem. Soc.* **2002**. 124, 10 163–10 170.
- [213] K. Ritchie, X.-Y. Shan, J. Kondo, K. Iwasawa, T. Fujiwara, & A. Kusumi. 'Detection on Non-Brownian Diffusion in the Cell Membrane in Single Molecule Tracking'. *Biophys. J.* **2005**. 88, 2266–2277.
- [214] P. Rösch, M. Harz, M. Krause, R. Petry, K.-D. Peschke, H. Burkhardt, O. Ronneberger, A. Schüle, G. Schmauz, R. Riesenberger, A. Wuttig, M. Lankers, S. Hofer, H. Thiele, H.-W. Motzkus, & J. Popp. 'Online Monitoring and Identification of Bioaerosols (OMIB)'. In J. Popp & M. Strehle (eds.), *Biophotonics*. Wiley-VCH Verlag GmbH & C. KGaA, Weinheim, **2006** 89–165.
- [215] P. Rösch, M. Harz, K.-D. Peschke, O. Ronneberger, H. Burkhardt, & J. Popp. 'Identification of Single Eukaryotic Cells with Micro-Raman Spectroscopy'. *Biopolymers* **2006**. 82, 312–316.
- [216] P. Rösch, M. Harz, K.-D. Peschke, O. Ronneberger, H. Burkhardt, A. Schüle, G. Schmauz, M. Lankers, S. Hofer, H. Thiele, H.-W. Motzkus, & J. Popp. 'On-Line Monitoring and Identification of Bioaerosols'. *Anal. Chem.* **2006**. 78, 2163–2170.
- [217] P. Rösch, M. Harz, M. Schmitt, K.-D. Peschke, O. Ronneberger, H. Burkhardt, H.-W. Motzkus, M. Lankers, S. Hofer, H. Thiele, & J. Popp. 'Rapid Identification of Single Microbes by various Raman spectroscopic techniques'. *Proc. SPIE-Int. Soc. Opt. Eng.* **2006**. 6093, 78.
- [218] P. Rösch, M. Harz, M. Schmitt, K.-D. Peschke, O. Ronneberger, H. Burkhardt, H.-W. Motzkus, M. Lankers, S. Hofer, H. Thiele, & J. Popp. 'Chemotaxonomic Identification of Single Bacteria by Micro-Raman Spectroscopy: Application to Clean-Room-Relevant Biological Contaminations'. *Appl. Environ. Microbiol.* **2005**. 71(3), 1626–1637.
- [219] D. L. Ross & C. M. Riley. 'Physicochemical properties of the fluoroquinolone antimicrobials. II Acid ionization constants and their relationship to structure'. *Int. J. Pharm.* **1992**. 83, 267–272.

- [220] I. Sadovskaya, E. Vinogradov, S. Flahaut, G. Kogan, & S. Jabbouri. 'Extracellular Carbohydrate-Containing Polymers of a Model Biofilm-Producing Strain, *Staphylococcus epidermidis* RP62A'. *Infect. Immun.* **2005**. 73(5), 3007–3017.
- [221] I. Sadovskaya, E. Vinogradov, J. Li, & S. Jabbouri. 'Structural elucidation of the extracellular and cell-wall teichoic acids of *Staphylococcus epidermidis* RP62A, a reference biofilm-positive strain'. *Carbohydr. Res.* **2004**. 339, 1467–1473.
- [222] W. Saenger. *Principles of Nucleic Acid Structure*. Springer, New York, **1984**.
- [223] L. R. Santamaria, E. Charro, A. Zacarias, & M. Castro. 'Vibrational spectra of nucleic acid bases and their watson-crick pair complexes'. *J. Comput. Chem.* **1999**. 20(5), 511–530.
- [224] C. Santos Nuno & A. R. B. Castanho Miguel. 'An overview of the biophysical applications of atomic force microscopy'. *Biophys. Chem.* **2004**. 107(2), 133–149.
- [225] S. Sasic, T. Itoh, & Y. Ozaki. 'Detailed analysis of single-molecule surface-enhanced resonance Raman scattering spectra of Rhodamine 6G obtained from isolated nano-aggregates of colloidal silver'. *J. Raman Spectrosc.* **2005**. 36, 593–599.
- [226] H. G. Schlegel. *Allgemeine Mikrobiologie*. 7th ed. Georg Thieme Verlag, Stuttgart, **1992**.
- [227] F. J. Schmitz, P. G. Higgins, S. Mayer, A. C. Fluit, & A. Dalhoff. 'Activity of Quinolones Against Gram-Positive Cocci: Mechanisms of Drug Action and Bacterial Resistance'. *Eur. J. Clin. Microbiol. Infect. Dis.* **2002**. 21(9), 647–659.
- [228] B. Schrader. *Infrared and Raman Spectroscopy - Methods and Applications*. VCH, Weinheim, **1995**.
- [229] K. C. Schuster, I. Reese, E. Urlaub, J. R. Gapes, & B. Lendl. 'Multidimensional Information on the Chemical Composition of Single Bacterial Cells by Confocal Raman Microspectroscopy'. *Anal. Chem.* **2000**. 72, 5529–5534.
- [230] K. C. Schuster, E. Urlaub, & J. R. Gapes. 'Single-cell analysis of bacteria by Raman microscopy: spectral information on the chemical composition of cells and on the heterogeneity in a culture'. *J. Microbiol. Methods* **2000**. 42, 29–38.
- [231] R. Schweitzer-Stenner. 'Visible and UV-resonance Raman spectroscopy of model peptides'. *Journal of Raman Spectroscopy* **2001**. 32(9), 711–732.
- [232] R. Schweitzer-Stenner, F. Eker, Q. Huang, K. Griebenow, P. A. Mroz, & P. M. Kozlowski. 'Structure Analysis of Dipeptides in Water by Exploring and Utilizing the Structural Sensitivity of Amide III by Polarized Visible Raman, FTIR-Spectroscopy and DFT Based Normal Coordinate Analysis'. *J. Phys. Chem. B* **2002**. 106, 4294–4304.
- [233] A. P. Scott & L. Radom. 'Harmonic Vibrational Frequencies: An Evaluation of Hartree-Fock, Moller-Plesset, Quadratic Configuration Interaction, Density Functional Theory, and Semiempirical Scale Factors'. *J. Phys. Chem.* **1996**. 100(41), 16 502–16 513.
- [234] S. Segev, I. Yaniv, d. Haverstock, & H. Reinhart. 'Safety of long-term therapy with ciprofloxacin: data analysis of controlled clinical trials and review'. *Clin. Infect. Dis.* **1999**. 28, 299–308.
- [235] D. Serban, F. Arcineigas Sandra, E. Vorgias Constantinos, & J. Thomas George, J. 'Structure and dynamics of the DNA-binding protein HU of *B. stearothermophilus* investigated by Raman and ultraviolet-resonance Raman spectroscopy'. *Protein Sci.* **2003**. 12(4), 861–870.
- [236] D. Serban, J. M. Benevides, & G. J. Thomas Jr. 'DNA Secondary Structure and Raman Markers of Supercoiling in *Escherichia coli* Plasmid pUC19'. *Biochemistry* **2002**. 41, 847–853.
- [237] Z. Shao, J. Yang, & A. P. Somlyo. 'Biological atomic force microscopy: from microns to nanometers and beyond'. *Annu. Rev. Cell Dev. Biol.* **1995**. 11, 241–265.

## Bibliography

- [238] L. L. Shen, J. Baranowski, & A. G. Pernet. 'Mechanism of inhibition of DNA gyrase by quinolone antibacterials: specificity and cooperativity of drug binding to DNA'. *Biochemistry* **1989**. 28(9), 3879–3885.
- [239] L. L. Shen, L. A. Mitscher, P. N. Sharma, T. J. O'Donnell, D. W. T. Chu, C. S. Cooper, T. Rosen, & A. G. Pernet. 'Mechanism of inhibition of DNA gyrase by quinolone antibacterials: a cooperative drug–DNA binding model'. *Biochemistry* **1989**. 28(9), 3886–3894.
- [240] E. V. Shevchenko, D. V. Talapin, N. A. Kotov, S. O'Brien, & C. B. Murray. 'Structural diversity in binary nanoparticle superlattices'. *Nature* **2006**. 439, 55–59.
- [241] M. N. Siamwiza, R. C. Lord, M. C. Chen, T. Takamatsu, I. Harada, H. Matsuura, & T. Shimanouchi. 'Interpretation of the Doublet at 850 and 830 cm<sup>-1</sup> in the Raman Spectra of Tyrosyl Residues in Proteins and Certain Model Compounds'. *Biochemistry* **1975**. 14(22), 48704 876.
- [242] A. C. Singer, W. E. Huang, J. Helm, & I. P. Thompson. 'Insight into pollutant bioavailability and toxicity using Raman confocal microscopy'. *J. Microbiol. Methods* **2005**. 60, 417–422.
- [243] G. D. Sockalingum, H. Lamfarraj, A. Beljebbar, P. Pina, M. Delavenne, F. Witthuhn, P. Allouch, & M. Manfait. 'Vibrational spectroscopy as a probe to rapidly detect, identify and characterize microorganisms'. *Proc. SPIE* **1999**. 3608, 185–194.
- [244] C.-H. Song, H.-W. Ryu, J.-K. Park, & T.-S. Ko. 'Mechanism of DNA Gyrase Inhibition by Quinolones: I. Spectral Analysis for Nalidixic Acid Polymorphism'. *Bull. Korean Chem. Soc.* **1999**. 20(6), 727–730.
- [245] T. G. Spiro. 'Resonance raman spectra of heme and metalloproteins'. In T. G. Spiro (ed.), *Biological Applications of Raman spectroscopy*, vol. 3. John Wiley and Sons, New York, **1987**.
- [246] T. G. Spiro & C. A. Grygon. 'Applications of ultraviolet resonance Raman spectroscopy to proteins'. *Journal of Molecular Structure* **1988**. 173, 79–90.
- [247] R. M. Stöckle, Y. D. Suh, V. Deckert, & R. Zenobi. 'Nanoscale chemical analysis by tip-enhanced Raman spectroscopy'. *Chem. Phys. Lett.* **2000**. 318, 131–136.
- [248] K. Störl, J. Störl, M. Roth, & C. Zimmer. 'DNA topoisomerases from *Streptomyces noursei*: Influence of coumarins and quinolones on the enzymic activity'. *Biochim. Biophys. Acta* **1994**. 1199(2), 143–148.
- [249] U. Strausfeld & A. Richter. 'Simultaneous purification of DNA topoisomerase I and II from eukaryotic cells'. *Preparative biochem.* **1989**. 19(1), 37–48.
- [250] J. S. Suh & M. Moskovits. 'Surface-Enhanced Raman Spectroscopy of Amino Acids and Nucleotide Bases Adsorbed on Silver'. *J. Am. Chem. Soc.* **1986**. 108, 4711–4718.
- [251] J. G. Sutcliffe. 'Complete nucleotide sequence of the *Escherichia coli* plasmid pBR322'. *Cold Spring Harbor Symposia on Quantitative Biology* **1979**. 43(1), 77–90.
- [252] G. J. Thomas Jr. 'Raman Spectroscopy of Protein and Nucleic Acid Assemblies'. *Annu. Rev. Biophys. Biomol. Struct.* **1999**. 28, 1–27.
- [253] H. Tomioka, K. Sato, T. Akaki, H. Kajitani, S. Kawahara, & M. Sakatani. 'Comparative in vitro antimicrobial activities of the newly synthesized quinolone HSR-903, sitafloxacin (DU-6859a), gatifloxacin (AM-1155), levofloxacin against *Mycobacterium tuberculosis* and *Mycobacterium avium* complex'. *Antimicrob. Agents Chemother.* **1999**. 43, 3001–3004.
- [254] H. Tomioka, K. Sato, H. Kajitani, T. Akaki, & S. Shishido. 'Comparative Antimicrobial Activities of the Newly Synthesized quinolone WQ-303, Levofloxacin, Sparfloxacin, and Ciprofloxacin against *Mycobacterium tuberculosis* and *Mycobacterium avium* complex'. *Antimicrob. Agents Chemother.* **2000**. 44(2), 283–286.

- [255] A. Torrecillas, S. Corbalan-Garcia, & J. C. Gomez-Fernandez. 'An Infrared Spectroscopic Study of the Secondary Structure of Protein Kinase Calpha and Its Thermal Denaturation'. *Biochemistry* **2004**. 43, 2332–2344.
- [256] A. Toyama, N. Fujimoto, N. Hanada, J. Ono, E. Yoshimitsu, A. Matsubuchi, & H. Takeuchi. 'Assignments and hydrogen bond sensitivities of UV resonance Raman bands of the C8-deuterated guanine ring'. *J. Raman Spectrosc.* **2002**. 33, 699–708.
- [257] A. Toyama, H. Takeuchi, & I. Harada. 'Ultraviolet Resonance Raman Spectra of Adenine, Uracil and Thymine Derivatives in Several Solvents. Correlation Between Band Frequencies and Hydrogen-Bonding States of the Nucleic Acid Bases'. *J. Mol. Struct.* **1991**. 242, 87–98.
- [258] A. T. Tu. *Raman Spectroscopy in Biology: Principles and Applications*. John Wiley & Sons, Inc., **1982**.
- [259] I. Tumanova, J. Boyer, S. F. Ausar, J. Burzynski, D. Rosencrance, J. White, J. Scheidel, R. Parkinson, H. Maguire, C. R. Middaugh, D. Weiner, & A. P. Green. 'Analytical and Biological Characterization of Supercoiled Plasmids Purified by Various Chromatographic Techniques'. *DNA Cell Biol.* **2005**. 24(12), 819–831.
- [260] I. Turel. 'The Interactions of Metal Ions with Quinolone Antibacterial Agents'. *Coord. Chem. Rev.* **2002**. 232, 27–47.
- [261] I. Turel, P. Bukovec, & M. Quiros. 'Crystal structure of ciprofloxacin hexahydrate and its characterization'. *Int. J. Pharm.* **1997**. 152, 59–65.
- [262] I. Turel, K. Gruber, I. Leban, & N. Bukovec. 'Synthesis, Crystal Structure, and Characterization of Three Novel Compounds of the Quinolone Family Member (Norfloxacin)'. *J. Inorg. Biochem.* **1996**. 61, 197–212.
- [263] U. Uhlemann. 'Interpretation von Raman-Spektren biologisch relevanter Moleküle mit Hilfe Dichtefunktional-theoretischer Simulation'. Diplomarbeit, Friedrich-Schiller-Universität Jena, **2003**.
- [264] H. Vasmel. 'Influence of supercoiling on DNA structure: laser Raman spectroscopy of the plasmid pBR322'. *Biopolymers* **1985**. 24(6), 1001–1008.
- [265] T. Vo-Dinh, K. Houck, & D. L. Stokes. 'Surface-Enhanced Raman Gene Probes'. *Anal. Chem.* **1994**. 66, 3379–3383.
- [266] T. Vo-Dinh, F. Yan, & M. B. Wabuyele. 'Surface-enhanced Raman scattering for medical diagnostics and biological imaging'. *J. Raman Spectrosc.* **2005**. 36(6-7), 640–647.
- [267] M. B. Wabuyele & T. Vo-Dinh. 'Detection of Human Immunodeficiency Virus Type 1 DNA Sequence Using Plasmonics Nanoprobes'. *Anal. Chem.* **2005**. 77, 7810–7815.
- [268] J. C. Wang. 'Cellular Roles of DNA Topoisomerases: A Molecular Perspective'. *Nature* **2002**. 3, 430–440.
- [269] R. M. Wartell & J. T. Harrell. 'Characteristics and Variations of B-Type DNA Conformations in Solution: A Quantitative Analysis of Raman Band Intensities of Eight DNAs'. *Biochemistry* **1986**. 25, 2664–2671.
- [270] H. Watanabe, N. Hayazawa, Y. Inouye, & S. Kawata. 'DFT Vibrational Calculations of Rhodamine 6G Adsorbed on Silver: Analysis of Tip-Enhanced Raman Spectroscopy'. *J. Phys. Chem. B* **2005**. 109(11), 5012–5020.
- [271] Z. Q. Wen, S. A. Overman, P. Bondre, & G. J. Thomas Jr. 'Structure and Organization of Bacteriophage PF3 Probed by Raman and Ultraviolet Resonance Raman Spectroscopy'. *Biochemistry* **2001**. 40, 449–458.
- [272] Z. Q. Wen, S. A. Overman, & G. J. Thomas Jr. 'Structure and Interactions of the Single-Stranded DNA Genome of Filamentous Virus fd: Investigation by Ultraviolet Resonance Raman Spectroscopy'. *Biochemistry* **1997**. 36, 7810–7820.

## Bibliography

- [273] Z. Q. Wen & G. J. Thomas Jr. 'UV Resonance Raman Spectroscopy of DNA and Protein Constituents of Viruses: Assignments and Cross Sections for Excitations at 257, 244, 238, and 229 nm'. *Biopolymers* **1998**. 45, 247–256.
- [274] J. H. White. 'Self-linking and the Gauss integral in higher dimensions'. *Am. J. Math.* **1969**. 91, 693–738.
- [275] D. B. Wigley, G. J. Davies, E. J. Dodson, A. Maxwell, & G. Dodson. 'Crystal structure of an N-terminal fragment of the DNA gyrase B protein'. *Nature* **1991**. 351, 624–629.
- [276] A. C. Williams & H. G. M. Edwards. 'Fourier Transform Raman Spectroscopy of Bacterial Cell Walls'. *J. Raman Spectrosc.* **1994**. 25, 673–677.
- [277] R. Withnall. 'Protein-ligand interactions studied by Raman and resonance Raman spectroscopy'. *Protein-Ligand Interactions: Structure and Spectroscopy* **2001**. 265–310.
- [278] K. Wojtuszewski & I. Mukerji. 'The HU-DNA binding interaction probed with UV resonance Raman spectroscopy: Structural elements of specificity'. *Protein Sci.* **2004**. 13, 2416–2428.
- [279] D. H. Wolpert & W. G. Macready. 'An Efficient Method to Estimate Bagging's Generalization Error'. *Mach. Learn.* **1999**. 35, 41–55.
- [280] Q. Wu, T. Hamilton, W. H. Nelson, S. Elliott, J. F. Sperry, & M. Wu. 'UV Raman Spectral Intensities of E. Coli and Other Bacteria Excited at 228.9, 244.0, and 248.2 nm'. *Anal. Chem.* **2001**. 73(14), 3432–3440.
- [281] Q. Wu, W. H. Nelson, S. Elliot, J. F. Sperry, M. Feld, R. Dasari, & R. Manoharan. 'Intensities of E. coli nucleic acid Raman spectra excited selectively from whole cells with 251-nm light'. *Anal. Chem.* **2000**. 72(13), 2981–2986.
- [282] W. Wu, B. Walczak, D. L. Massart, K. A. Prebble, & I. R. Last. 'Spectral transformation and wavelength selection in near-infrared spectra classification'. *Anal. Chim. Acta* **1995**. 315, 243–255.
- [283] C. Xie, Y.-q. Lie, W. Tang, & R. J. Newton. 'Study of dynamical process of heat denaturation in optically trapped single microorganisms by near-infrared Raman spectroscopy'. *J. Appl. Phys.* **2003**. 94(9), 6138–6142.
- [284] C. Xie, J. Mace, M. A. Dinno, Y. Q. Li, W. Tang, R. J. Newton, & P. J. Gemperline. 'Identification of Single Bacterial Cells in Aqueous Solution Using Confocal Laser Tweezers Raman Spectroscopy'. *Anal. Chem.* **2005**. 77, 4390–4397.
- [285] H. Xu, J. Aizpurua, M. Käll, & P. Apell. 'Electromagnetic contributions to single-molecule sensitivity in surface-enhanced Raman scattering'. *Phys. Rev. E: Stat., Nonlinear, Soft Matter Phys.* **2000**. 62(3), 4318–4324.
- [286] Y. Yamaguchi, M. Frisch, J. Gaw, H. F. Schaefer III, & J. S. Binkley. 'Analytic evaluation and basis set dependence of intensities of infrared spectra'. *J. Chem. Phys.* **1986**. 84(4), 2262–2278.
- [287] L. Zeiri, B. V. Bronk, Y. Shabtai, J. Eichler, & S. Efrima. 'Surface-Enhanced Raman Spectroscopy as a Tool for Probing Specific Biochemical Components in Bacteria'. *Appl. Spectrosc.* **2004**. 58(1), 33–40.
- [288] L. Zeiri & S. Efrima. 'Surface-enhanced Raman spectroscopy of bacteria: the effect of excitation wavelength and chemical modification of the colloidal milieu'. *J. Raman Spectrosc.* **2005**. 36(6/7), 667–675.
- [289] S. M. Zeman, K. M. Depew, S. J. Danishefsky, & D. M. Crothers. 'Simultaneous determination of helical unwinding angles and intrinsic association constants in ligand-DNA complexes: The interaction between DNA and calichearubicin B'. *Proc. Natl. Acad. Sci. USA* **1998**. 95, 4327–4332.
- [290] X. Zhang, J. Zhao, A. V. Whitney, J. W. Elam, & R. P. Van Duyne. 'Ultrastable Substrates for Surface-Enhanced Raman Spectroscopy: Al<sub>2</sub>O<sub>3</sub> Overlayers Fabricated by Atomic Layer Deposition Yield Improved Anthrax Biomarker Detection'. *J. Am. Chem. Soc.* **2006**. 128, 10304–10309.



## Publication list

During the dissertation the following papers have been published in refereed scientific journals:

1. U. Neugebauer, U. Schmid, K. Baumann, W. Ziebuhr, S. Kozitskaya, V. Deckert, M. Schmitt, J. Popp, *Towards a detailed understanding of the bacterial metabolism - A comprehensive vibrational spectroscopic characterization of Staphylococcus epidermidis*. *ChemPhysChem* **2007**, *8*, 124–137.
2. U. Neugebauer, P. Rösch, M. Schmitt, J. Popp, C. Julien, A. Rasmussen, C. Budich, V. Deckert, *On the way to nanometer-sized information of the bacterial surface by means of tip-enhanced Raman spectroscopy (TERS)*., *ChemPhysChem* **2006**, *7*, 1428–1430.
3. C. Budich, U. Neugebauer, J. Popp, V. Deckert, *Cell Wall Investigations Utilizing Tip-Enhanced Raman Scattering*, *Journal Optical Microscopy* **2006**, submitted
4. U. Neugebauer, A. Szeghalmi, M. Schmitt, W. Kiefer, J. Popp, U. Holzgrabe, *Vibrational spectroscopic characterization of fluoroquinolones*, *Spectrochimica Acta Part A* **2005**, *61*, 1505–1517.
5. U. Neugebauer, U. Schmid, K. Baumann, U. Holzgrabe, W. Ziebuhr, S. Kozitskaya, W. Kiefer, M. Schmitt, and J. Popp, *Characterization of Bacterial Growth and the Influence of Antibiotics by Means of UV Resonance Raman Spectroscopy*., *Biopolymers* **2006**, *82*, 306–311.
6. U. Neugebauer, U. Schmid, K. Baumann, W. Ziebuhr, S. Kozitskaya, U. Holzgrabe, M. Schmitt, J. Popp, *Vibrational Spectroscopic Characterization of the Influence of Fluoroquinolone Drugs on the Bacterial Growth*. *J. Phys. Chem. A* **2006**, accepted.
7. U. Neugebauer, U. Schmid, K. Baumann, H. Simon, M. Schmitt, J. Popp, *UV-resonance Raman spectroscopy of DNA supercoiling and ethidium bromide intercalation*. **2006**, submitted.

The following paper was published in an unrefereed journal:

8. M. Harz, U. Neugebauer, P. Rösch, J. Popp, *Raman spectroscopy: A powerful tool for the investigations and identification of bacterial cells*., *G.I.T. Laboratory Journal Europe* **2006**, *3*, 26–28.



# Conference Contributions

## Poster

1. International Conference on Raman Spectroscopy, ICORS, 20.-25.08.2006, Yokohama, Japan, U. Neugebauer, U. Schmid, K. Baumann, V. Deckert, M. Schmitt, J. Popp *Characterization of bacteria and bacterial growth by means of vibrational spectroscopy*
2. Spec 2006, 19.-23.05.2006, Heidelberg, Germany, U. Neugebauer, U. Schmid, K. Baumann, W. Ziebuhr, S. Kozyskaya, U. Holzgrabe, W. Kiefer, J. Popp *Vibrational Spectroscopic Study of Gyrase Inhibitors and Their Biological Targets*
3. Biophotonik Symposium, 27.-29.04.2006, München, Germany, U. Neugebauer, C. Julien, V. Deckert, P. Rösch, M. Schmitt, J. Popp *Hochauflöste Informationen der äußeren Bakterenschicht mittels spitzenverstärkter Raman-Spektroskopie (TERS)*
4. International Symposium on Novel Agents against Infectious Diseases, 12.-15.02.2006, Würzburg, Germany, U. Neugebauer, W. Ziebuhr, S. Kozitskaya, U. Holzgrabe, W. Kiefer, M. Schmitt, J. Popp *Characterization of Bacterial Growth and the Influence of Antibiotics by Means of Vibrational Spectroscopy*
5. European Conference on Spectroscopy of Biological Molecules, ECSBM 3.-8.09.2005, Aschaffenburg, Germany, U. Neugebauer, W. Ziebuhr, S. Kozyskaya, U. Holzgrabe, W. Kiefer, J. Popp *Characterization of Bacterial Growth and the Influence of Antibiotics by Means of Vibrational Spectroscopy*
6. German-Canadian Workshop, 11./12.06.2005, Munich, Germany, U. Neugebauer, A. Szeghalmi, W. Ziebuhr, S. Kozyskaya, U. Holzgrabe, M. Schmitt, W. Kiefer, J. Popp *Raman Spectroscopic Characterization of Gyrase Inhibitors and Their Influence on Bacteria*
7. Bunsentagung, 5.-7.05.2005, Frankfurt, Germany, U. Neugebauer, A. Szeghalmi, W. Ziebuhr, U. Holzgrabe, M. Schmitt, W. Kiefer, J. Popp *Schwingungsspektroskopische Charakterisierung von Gyrasehemmstoffen und ihren Wechselwirkungen mit dem biologischen Target*
8. Biophotonik-Symposium 18.02.2005, Jena, Germany, U. Neugebauer, W. Ziebuhr, S. Kozyskaya, U. Holzgrabe, J. Popp *Raman-Spektroskopische Charakterisierung von Bakterienwachstum und Einfluss von Antibiotika*

## Conference Contributions

9. FT-IR Spectroscopy in Microbiological and Medical Diagnostic, 21./22.10.2004 Berlin, Germany, U. Neugebauer, P. Rösch, U. Holzgrabe, J. Popp *Spectroscopic Investigation of the Influence of Norfloxacin and Ciprofloxacin on Bacillus pumilus*
10. World Conference on Magic Bullets, 6.-8.09.2004, Nürnberg, Germany, U. Neugebauer, U. Holzgrabe, J. Popp *The Application of Raman Spectroscopy for the Investigation of the Impact of Antiinfective Agents*
11. ICORS 2004, Brisbane, Australia, U. Neugebauer, A. Szeghalmi, T. Frosch, M. Schmitt, W. Kiefer, J. Popp *Raman spectroscopic studies of the interaction of quinolones with the biological targets DNA and bacterial gyrase*
12. Bunsentagung 2003, Dresden, Germany, T. Frosch, U. Neugebauer, J. Popp, M. Schmitt, U. Uhlemann, W. Kiefer, A. Szeghalmi, U. Holzgrabe, T. Schirmeister, G. Bringmann *Schwingungsspektroskopische Charakterisierung von pharmazeutischen Wirkstoffen und deren Wechselwirkung mit biologischen Zielstrukturen*
13. Jahrestagung der Deutschen Pharmazeutischen Gesellschaft 2003, Würzburg, Germany, A. Szeghalmi, R. Geßner, B. Küstner, M. Schmitt, W. Kiefer, T. Frosch, U. Neugebauer, U. Uhlemann, J. Popp, T. Schirmeister, U. Holzgrabe, G. Bringmann *The Characterization of Active Agents and Their Interactions by Means of Raman Spectroscopy*
14. RISBM 2003 (Raman and IR Spectroscopy in Biology and Medicine), Jena, Germany, U. Neugebauer, T. Frosch, A. Szeghalmi, M. Schmitt, U. Holzgrabe, J. Popp *Spectroscopic Characterization of Fluoroquinolones*
15. RISBM 2003 (Raman and IR Spectroscopy in Biology and Medicine), Jena, Germany, T. Frosch, U. Neugebauer, U. Uhlemann, B. Küstner, A. Szeghalmi, R. Geßner, S. Schlücker, M. Schmitt, J. Faber, G. Bringmann, J. Popp *The Characterization of Anti-Malaria Active Agents and Their Interactions by Means of IR and Raman Spectroscopy*
16. RISBM 2003 (Raman and IR Spectroscopy in Biology and Medicine), Jena, Germany, A. Szeghalmi, M. Schmitt, W. Kiefer, T. Frosch, U. Neugebauer, U. Uhlemann, J. Popp, T. Schirmeister, U. Holzgrabe, G. Bringmann *The Characterization of Active Agents and Their Interactions by Means of Raman Spectroscopy*

## Talks

1. The Full Spectrum - Biology between Infrared and Hard X-Rays - and beyond, 26./27.09.2006, Wettingen, Switzerland, *Raman and resonance Raman spectroscopy of biomolecules*
2. SFB-Meeting, 09.12.2005, Würzburg, Germany, *Raman Spectroscopic Characterization of Gyrase Inhibitors and their Influence on Bacteria*
3. GDCh Shorttalk, 14.12.2005, Jena, Germany, *Raman-Spektroskopische Charakterisierung von Gyrasehemmstoffen, ihren biologischen Targets und ihre Wechselwirkung mit Bakterien*
4. XIV. Krakow-Jena Symposium on Physical Chemistry 4.-7.10.2005, Dornburg, Germany, *Spectroscopic characterization of gyrase inhibitors and their influence on bacteria*
5. SERS-Meeting, 17.01.2005, Dresden, Germany, *Nanometer-sized Information of the outer bacterial layer of Staphylococcus by means of tip-enhanced Raman spectroscopy (TERS)*
6. SFB-Symposium 10.-12.11.2004, Würzburg, Germany, *Raman Spectroscopical Studies of the Interaction of Active Agents with Biological Targets*



## List of Figures

2.1	Energy levels and transitions for an anharmonic oscillator . . . . .	9
2.2	Energy level diagram showing the basic transitions involved in the spontaneous Raman scattering . . . . .	10
2.3	Energy level diagram illustrating the sum-over-state description of the Raman scattering . . . . .	14
2.4	Time dependent picture of resonance Raman scattering . . . . .	15
2.5	Selectivity of resonance Raman spectroscopy . . . . .	16
2.6	Resonance Raman spectroscopy and fluorescence . . . . .	17
2.7	Tip-enhanced Raman spectroscopy (TERS) configuration . . . . .	21
2.8	Atomic force microscopy . . . . .	23
2.9	Imaging modes of an atomic force microscope . . . . .	24
3.1	Experimental setup of the resonance Raman experiments when cooling the sample	30
3.2	Experimental set-up of the TERS experiments . . . . .	32
3.3	SEM images of the silver-coated AFM-tips for the TERS experiments . . . . .	34
3.4	Plasmon resonance of the silver-coated AFM-tips for the TERS experiment . . . . .	35
3.5	Tuning curve of the non-contact AFM tips . . . . .	35
3.6	Optical response when scanning the silver-coated AFM tip through the laser focus	36
3.7	Raman spectrum of BSB (Bis-2-methylstyryl-1,4-benzene) . . . . .	37
3.8	Antibiotic susceptibility test . . . . .	39
3.9	PAGE of extracted gyrase . . . . .	44
4.1	Biofilm of <i>S. epidermidis</i> . . . . .	55
4.2	Pseudo 3D topographic AFM image of a cluster of single <i>S. epidermidis</i> cells on a glass surface . . . . .	55
4.3	Vibrational spectra (IR absorption, micro-Raman and UV-resonance Raman) of bulk <i>S. epidermidis</i> . . . . .	56
4.4	Raman spectra ( $\lambda_{ex} = 532$ nm) of <i>B. pumilus</i> , <i>B. subtilis</i> , <i>S. epidermidis</i> and <i>E. coli</i> and hierarchical cluster analysis . . . . .	61
4.5	Pseudo 3D AFM image of <i>E. coli</i> . . . . .	62
4.6	Growth curve of <i>S. epidermidis</i> under batch conditions . . . . .	64

List of Figures

4.7	IR absorption spectra of <i>S. epidermidis</i> at different growth times; and HCA and PCA of those spectra . . . . .	65
4.8	Micro-Raman spectra of single <i>S. epidermidis</i> cells at different growth times; and HCA and PCA of those spectra . . . . .	67
4.9	UV-resonance Raman spectra of <i>S. epidermidis</i> at different growth times; and HCA and PCA of those spectra . . . . .	69
4.10	Relative ratio of nucleic acid and proteins during the different growth phases . . .	70
4.11	Growth curve of <i>B. pumilus</i> under batch conditions . . . . .	72
5.1	Scheme of the structure of the cell wall of Gram-positive bacteria . . . . .	76
5.2	Pseudo three-dimensional topographic image of single <i>S. epidermidis</i> cells on a glass surface and TERS spectra . . . . .	77
5.3	TERS spectra of <i>S. epidermidis</i> recorded at selected points on the cell surface . .	79
5.4	TERS spectra of <i>S. epidermidis</i> with the enhancing tip being approached to the sample surface and retracted . . . . .	80
5.5	TERS spectra of <i>S. epidermidis</i> from different individual cells . . . . .	81
5.6	Evolution of the TERS signal on one spot of the bacterial surface with time . . .	85
5.7	Pseudo-3D-image and TERS spectra of <i>S. epidermidis</i> under argon . . . . .	86
5.8	<i>S. epidermidis</i> moved on the glass plate by the AFM tip . . . . .	88
5.9	REM image of contaminated AFM tips . . . . .	89
6.1	Chemical structure of the investigated quinolones . . . . .	93
6.2	Chemical structure of five precursors for moxifloxacin . . . . .	93
6.3	UV/vis absorption spectra of the quinolones in water . . . . .	96
6.4	UV/vis absorption spectra of norfloxacin at different pH and the corresponding structures . . . . .	98
6.5	Calculated and experimental Raman spectrum of norfloxacin . . . . .	99
6.6	Some characteristic vibrations of norfloxacin and its anion . . . . .	99
6.7	Calculated Raman spectra of different conformation of cinoxacin . . . . .	101
6.8	Raman spectra of different quinolone derivatives . . . . .	102
6.9	IR absorption spectra of the quinolones . . . . .	104
6.10	FT-Raman spectra of anhydrous and hydrated norfloxacin and ciprofloxacin . . .	105
6.11	Raman spectra of solution of ciprofloxacin at different pH, and SERS spectra of some fluoroquinolones . . . . .	108
6.12	Resonance Raman spectra of norfloxacin . . . . .	111
7.1	Structures of the nucleic acid bases . . . . .	114
7.2	Micro-Raman spectra ( $\lambda_{ex}= 532$ nm) of the nucleic acid bases . . . . .	115
7.3	Calculated micro-Raman spectra of cytosine tautomers . . . . .	117
7.4	The Watson-Crick DNA base pairs: calculated micro-Raman spectra and geometry	123



7.5	Optimized structure of deoxyadenosine-5'-monophosphate as obtained from DFT calculations . . . . .	125
7.6	Raman spectra of guanine, guanosine and GMP . . . . .	127
7.7	UV absorption spectra of the deoxynucleotides . . . . .	129
7.8	UV-resonance Raman spectra of the DNA building blocks . . . . .	131
7.9	Raman spectrum of the plasmid DNA pBR322 . . . . .	137
7.10	UV absorption spectra of plasmid DNA and the individual nucleotides . . . . .	139
7.11	UV-resonance Raman spectra of plasmid pBR322 and the individual nucleotides. . . . .	140
7.12	Agarose gel of supercoiled and relaxed plasmid DNA pBR322 . . . . .	143
7.13	UV-resonance Raman spectra of plasmid pBR322 in the superhelical and relaxed form . . . . .	143
7.14	UV-resonance Raman spectra ethidium bromide, supercoiled DNA and the DNA-ethidium bromide complex . . . . .	146
7.15	Amount of ethidium bromide subtracted by orthogonalization from the UV-resonance spectra . . . . .	148
7.16	PCA of the UV-resonance Raman spectra of relaxed DNA, supercoiled DNA and the DNA-ethidium bromide complex . . . . .	148
8.1	Breakage reunion domain of the GyrA59 domain of gyrase . . . . .	152
8.2	Schematic view of supercoiling by DNA gyrase . . . . .	153
8.3	UV absorption and Raman spectra of amino acids . . . . .	155
8.4	Vibrational modes of the peptide bond . . . . .	158
8.5	Raman and resonance Raman spectra of gyrase . . . . .	159
8.6	UV-resonance Raman spectra of GyrA, relaxed pBR322 and the mixture of both . . . . .	161
8.7	UV-resonance Raman spectra of GyrA, pBR322 and the mixture of both . . . . .	162
8.8	UV-resonance Raman spectra of GyrA, moxifloxacin and the mixture of both . . . . .	164
9.1	Growth curve of <i>S. epidermidis</i> under the influence of moxifloxacin . . . . .	168
9.2	IR absorption spectra of <i>S. epidermidis</i> with different moxifloxacin concentrations and HCA . . . . .	169
9.3	PCA and REM-TS/LDA of the IR spectra of <i>S. epidermidis</i> with different moxifloxacin concentrations . . . . .	170
9.4	Micro-Raman spectra of <i>S. epidermidis</i> with different moxifloxacin concentrations and HCA . . . . .	173
9.5	PCA and REM-TS/LDA of the micro-Raman spectra of <i>S. epidermidis</i> with different moxifloxacin concentrations . . . . .	174
9.6	UV-resonance Raman spectra of <i>S. epidermidis</i> with different moxifloxacin concentrations and HCA . . . . .	176
9.7	PCA and REM-TS/LDA of the UV-resonance Raman spectra of <i>S. epidermidis</i> with different moxifloxacin concentrations . . . . .	177

## List of Figures

9.8	Growth curve of <i>B. pumilus</i> under the influence of ciprofloxacin . . . . .	178
10.1	Characterization of bacteria by means of different vibrational spectroscopic techniques . . . . .	181
11.1	Charakterisierung von Bakterien mit Hilfe verschiedener schwingungsspektroskopischer Methoden . . . . .	188
B.1	Micro-Raman spectra of adenine, adenosine and AMP . . . . .	203
B.2	Micro-Raman spectra of thymine, thymidine and TMP . . . . .	204
B.3	Micro-Raman spectra of cytosine, cytidine and CMP . . . . .	205
B.4	IR absorption spectra of adenine, adenosine and AMP . . . . .	214
B.5	IR absorption spectra of cytosine, cytidine and CMP . . . . .	215
B.6	UV absorption spectra of adenine, adenosine and AMP in aqueous solution . . .	216
B.7	UV absorption spectra of guanine, guanosine and GMP in aqueous solution . . .	216
B.8	UV absorption spectra of thymine, thymidine and TMP in aqueous solution . . .	217
B.9	UV absorption spectra of cytosine, cytidine and CMP in aqueous solution . . . .	217
B.10	Raman and UV-resonance Raman spectra of aliphatic amino acids . . . . .	218
B.11	Raman and UV-resonance Raman spectra of aromatic and heterocyclic amino acids	219

## List of Tables

3.1	Temperature program for the PCR . . . . .	43
4.1	Tentative assignment of the Raman and IR absorption bands of <i>S. epidermidis</i> . .	57
4.2	Assignment of the UV-resonance Raman bands of <i>S. epidermidis</i> . . . . .	59
4.3	Relative intensity change of the amide I and DNA band in the IR absorption spectra with growth time . . . . .	66
4.4	Wavenumbers showing the largest variance and the highest discriminative power for the bacterial spectra of <i>S. epidermidis</i> at different growth times . . . . .	73
5.1	Tentative band assignment of the TERS bands of <i>S. epidermidis</i> . . . . .	83
6.1	Absorption maxima (in nm) of the quinolones in aqueous solutions . . . . .	97
6.2	Detailed vibrational analysis of norfloxacin . . . . .	100
6.3	Some characteristic Raman wavenumbers of the quinolone in the solid state . . .	103
7.1	Comparison of the geometry parameters of the nucleic acid bases obtained by DFT calculations with experiment . . . . .	116
7.2	Assignment of the Raman bands of the DNA bases . . . . .	119
7.3	Geometry changes in the nucleic acid bases upon base pairing . . . . .	122
7.4	Vibrational band assignment of the UV-resonance Raman spectra of the DNA building blocks . . . . .	132
7.5	Torsional angles for A-, B- and Z-DNA . . . . .	135
7.6	Complete nucleotide sequence of the <i>Escherichia coli</i> plasmid pBR322 . . . . .	136
7.7	Vibrational band assignment of the Raman spectrum of pBR322 . . . . .	138
7.8	Assignment of the UV-resonance Raman bands of DNA . . . . .	141
7.9	Assignment of the UV-resonance Raman bands of ethidium bromide . . . . .	147
8.1	Assignment of the vibrational Raman bands of tyrosine . . . . .	156
8.2	Structure dependence of the amide vibration . . . . .	158
9.1	Minimal inhibition concentration of norfloxacin, ciprofloxacin, moxifloxacin and vancomycin on <i>B. pumilus</i> and <i>S. epidermidis</i> . . . . .	165

*List of Tables*

9.2	Wavenumbers showing the highest discriminative power for the spectra of <i>S. epidermidis</i> experiencing different moxifloxacin concentrations . . . . .	171
B.1	Assignment of the Raman bands of guanine, guanosine and GMP . . . . .	206

# Danksagung

An erster Stelle danke ich Herrn Prof. Dr. Jürgen Popp, für die Aufnahme in seine Arbeitsgruppe, für das interessante Thema, die bereichernden und produktiven Anregungen, sowie die Möglichkeit eigene Ideen umzusetzen und in seinen reich ausgestatteten Laboren arbeiten zu können. Ich danke ihm außerdem, dass er es mir ermöglichte an zahlreichen Tagungen im In- und Ausland teilzunehmen, sowie für die Forschungsaufenthalte bei Kooperationspartnern in Würzburg und Dortmund.

Mein besonderer Dank gilt auch Herrn Priv.-Doz. Dr. Micheal Schmitt für die Beratung und Unterstützung im Forscheralltag. Auch wenn die Aufgaben sich auf seinem Tisch stapelten, nahm er sich stets Zeit, um fachliche und organisatorische Dinge zu diskutieren. Ebenso danke ich Frau Dr. Petra Rösch für die Einweisung ins Biolabor und in die Spektrometer.

Allen Mitarbeitern der Arbeitsgruppe Popp (Dana Cialla, Claudiu Dem, Thomas Dörfer, Torsten Frosch, Katharina Gaus, Michaela Harz, Katharina Hering, Mario Krause, Antje Kritz, Michael Kühnert, Susanne Liedtke, Marion Ludwig, Tobias Meyer, Thomas Mayerhöfer, Renate Petry, Martin Presselt, Petra Rösch, Katrin Strehle, Marion Strehle, Michael Schmitt, Beate Truckenbrodt, Stefanie Tschierlei, Ute Uhlemann, Angela Walter) danke ich für die gute Zusammenarbeit und das freundschaftliche Klima. Die Vielfalt der Projekte innerhalb der Arbeitsgruppe schuf eine reiche Arbeitsatmosphäre und ermöglicht den Gedankenaustausch über das eigene Thema hinaus.

In Würzburg danke ich Prof. Dr. Wolfgang Kiefer und seiner Arbeitsgruppe, besonders Adriana Szeghalmi, Benjamin Dietzek, Bernd Küstner und Belinda Böhm, für die Aufnahme in die Labore für einige Messungen und fruchtbare Diskussionen.

Innerhalb des Sonderforschungsbereich 630 „Erkennung, Gewinnung und funktionale Analyse von Wirkstoffen gegen Infektionskrankheiten“ danke ich besonders Wilma Ziebuhr, Svetlana Kotziskaya and Knut Olsen für the Einführung in die biologischen Arbeitstechniken, für die Staphylokokken-Bakterienstämme und die Bereitstellung der REM-Bilder von Biofilmen von *Staphylococcus epidermidis*. Ein grosses Dankeschön gilt Ulrike Schmid und Knut Baumann für die sehr gute Kooperation. Auf sie geht die Programmentwicklung zur multivariate Datenanalyse (REM-TS, Orthogonalisierung, B/W-Verhältnis) zurück. Frau Prof. Dr. U. Holzgrabe und ihrer Arbeitsgruppe danke ich für die Bereitstellung und Synthese von Moxifloxacin und den Vorstufen, sowie für interessante und aufschlussreiche Gespräche zur Pharmakokinetik und Pharmakodynamik. Tanja Gronauer danke ich für das Messen von CD-Spektren. In Jena gilt dafür Matthias Görlach und Yvonne Ihle mein Dank. Auch die regelmäßigen Seminare innerhalb

## *Danksagung*

des SFB630 haben meine Blick auf die biologischen und medizinischen Zusammenhänge sehr geweitet. Catharina Hippius danke ich für die in Würzburg gewährte Gastfreundschaft.

Ein herzliches Dankeschön gilt Frau Dr. Hannelore Simon für die Einführung in die experimentellen Fertigkeiten der DNA- und Proteinextraktion, für die Bereitstellung der Topoisomerase I und ihr immer offenes Ohr bei biologischen Fragen. Für angenehme Laborgesellschaft am Lehrstuhl für Genetik danke ich Pia Nutt, Ulrike Wrazidlo, Maren Hintz und Rainer Melzer. Für fruchtbare und interessante Diskussionen bei biologischen Problemen danke ich weiterhin Prof. Zimmer, Walther Pohle, Ludwig Martins, Matthias Gube und Wolfgang Fritzsche.

Herrn Prof. Dr. Peter Zipfel, Andrea Hartmann und Anja Kuhnert danke ich für die Bereitstellung der Ultrazentrifuge. Dr. Tim Liebert, Dominik Fenn, Prof. Dr. Gerd Buntkowsky und Daniel Tietze danke ich für die Benutzung der Lyophylle. Herrn Dr. Hans Krügel gilt mein Dank für die DNA-Proben mit verschiedenem GC-Gehalt und PD Dr. Karl-Hermann Schmidt für Anleitung und Durchführung der PCR in seinem Labor. Andrea Steinbrück danke ich für die Absorptionsmessung der TERS-Spitzen.

Vielen Dank an PD Dr. Volker Deckert, für die Möglichkeit in seiner Arbeitsgruppe zu arbeiten und zu lernen. Ein herzliches Dankeschön an Akiko Rasmussen, Carine Julien und Christian Budich für die vielen Gespräche über TERS und SERS und AFM, und die Gesellschaft bei langen Messungen. Herrn Gosciniak danke ich für das Beschichten der AFM-Spitzen, Erika Pulvermacher für die REM-Messungen und Herrn Herzog für Unterstützung bei technischen, organisatorischen und sonstigen Fragen. Allen Mitarbeitern des ISAS danke ich für die freundliche Atmosphäre.

Für Hilfe, Tricks und Kniffe bei Computerproblemen und Softwarefragen danke ich besonders Dirk Bender, aber auch Thomas Dörfer, Petra Rösch, Michael Schmitt, Stephanie Tschierlei, und Ute Uhlemann sowie außerhalb der eigenen Arbeitsgruppe Stephan Schenk, Andreas Plank, Jan-Martin Wagner, Theodor Alpermann, Georg Bergner und Tillmann Gebauer.

Torsten Frosch danke ich für die angenehme Zimmergesellschaft. Frau Inge Weber und Frau Marion Ludwig danke ich für das Aufnehmen einiger IR Spektren, Kerstin Langgut für die Unterstützung bei der „Mediengroßproduktion“ im Biolabor und Dana Cialla für ihre engagierte Arbeit als F-Praktikant und HiWi.

Weiterer Dank gilt den Mitarbeitern des Institutes für Physikalische Chemie für das angenehme Arbeitsklima und gemeinsame Praktikumsstunden, der Werkstatt (einschließlich Elektrowerkstatt und Glasbläserei) für die tatkräftige Hilfe bei apparativen Problemen und den beiden Sekretärinnen Frau Krause und Frau Zeise für Unterstützung bei bürokratischen Angelegenheiten.

Für das Korrekturlesen dieser Arbeit danke ich Michael Schmitt, Petra Rösch, Dana Cialla und Angela Walther, die auch Tippfehler in langen Tabellen entdeckte. Für Designunterstützung bei den Grafiken geht mein herzlicher Dank an Konrad Schöller.

Ein herzliches Dankeschön auch an meinen Vater, sowie meine Freunde und Kommilitonen, die mich während der Promotion begleitet haben und diese Zeit zu einer sehr schönen gemacht haben.

# **Selbständigkeitserklärung**

Ich erkläre, dass ich die vorliegende Arbeit selbständig und unter Verwendung der angegebenen Hilfsmittel, persönlichen Mitteilungen und Quellen angefertigt habe.

Jena, den 9. Februar 2007





## Lebenslauf

- seit März 2003 wissenschaftlicher Mitarbeiter an der Friedrich-Schiller-Universität Jena, Institut für Physikalische Chemie, AK Prof. Dr. J. Popp mit Forschungsaufenthalten in Dortmund (ISAS, Institute for Analytical Sciences) und Würzburg (Universität)
- 11.2002 Abschluß des Studiums mit dem akademischen Grad „Diplom-Chemiker“ an der Friedrich-Schiller-Universität Jena, Titel der Diplomarbeit: *Zur Photophysik von Poly(phenylen-ethinylenbipyridylen) und seinen Modellverbindungen*. Betreuer: Prof. Dr. U.-W. Grummt
- 07.2001 – 08.2001 Forschungsaufenthalt am Institut Laue-Langevin (ILL) in Grenoble, Frankreich, *Untersuchung von Scherkraft- induzierten Übergängen von lamellaren Phasen mit Hilfe von Kleinwinkelneutronenstreuung (SANS)*. Betreuer: Johannes Zipfel, Peter Lindner
- 11.2000 – 03.2001 Studentische Hilfskraft bei DC Hartmut Knoll (AK Prof. Vogelsberger) an der Friedrich-Schiller-Universität Jena, *Herstellung von organischen Nanopartikeln aus der Lösung*.
- 10.2000 – 11.2002 Hauptstudium im Fach Chemie an der Friedrich-Schiller-Universität Jena, Spezialisierung in physikalischer Chemie und Grenzflächenchemie
- 06.2000 – 10.2000 Forschungsaufenthalt an der University of North Carolina at Chapel Hill, NC, USA *Zeitaufgelöste EPR-Spektroskopie an Phenoxiden und Guanin, Photoionisation mit gepulsten Laserblitzen*. Betreuer: Prof. Malcolm Forbes
- 08.1999 – 05.2000 Science Exchange Student an der University of North Carolina at Chapel Hill, NC, USA
- 10.1997 – 08.1999 Grundstudium im Fach Chemie an der Friedrich-Schiller-Universität Jena
- 09.1991 – 07.1997 Gymnasium: Johann-Wilhelm-Häßler-Gymnasium Erfurt, Abschluss mit der allgemeinen Hochschulreife (Abitur)
- 09.1985 – 08.1991 Grundschule, Erfurt